upna Universidad Pública de Navarra
Nafarroako Unibertsitate Publikoa

THESIS FOR THE DEGREE OF DOCTOR OF PHILOSOPHY

Dual-Band and Integrated Detectors for Submillimetre Applications

Alicia Elena Torres García

Director: Ramón Gonzalo García
Director: Iñigo Ederra Urzainqui

Grupo de Antenas
Departamento Ingeniería Eléctrica, Electrónica y de las Comunicaciones
Universidad Pública de Navarra
Pamplona, España, 2020

https://doi.org/10.48035/Tesis/2454/41083

Agradecimientos

Se me hace realmente difícil resumir y expresar el agradecimiento que merecen todas las personas que de una manera u otra me han ayudado a realizar esta tesis. Espero en estas líneas no olvidar a nadie, y de ser así, les pido disculpas.

Quisiera agradecer en primer lugar a mis directores Ramón e Iñigo. Gracias a Ramón por darme esta oportunidad, por la confianza depositada y por toda la ayuda. Gracias a Iñigo por estar siempre dispuesto a enseñarme, a debatir ideas, por aprender el dialecto "cubano" y por la paciencia. Sois unos magníficos profesionales y unas excelentes personas. Es un verdadero placer haber podido contar con vuestra supervisión y vuestra amistad.

Gracias a todo el grupo de Antenas, que tanto me han ayudado en el plano profesional y personal desde el primer momento que llegué a Navarra, a Miguel, Juan Carlos, Carlos del Río. Gracias en especial a Jorge por la oportunidad de aprender a fabricar en sala limpia y a medir. Gracias a su familia por preocuparse y ayudarnos tanto en el embarazo.

Durante estos años en la "uni" he tenido la oportunidad de conocer gente maravillosa que ahora tengo el placer de llamar amigos y "titos". Gracias a Unai, Baha, Pacheco, Pablo, Carlos Quemada, Lex, Liberal, Irati, Dayan, Biurrun, gracias por tantos buenos cafés, por los debates en la pizarra, por todo.

Special thanks to Jan, Peter, Vladimir, Helena, Thomas and the THz and MM-Wave Laboratory from Chalmers Technology University. Thanks for the help and for teaching us so many things in such a short time, it has been a pleasure to work and learn with you all. Also thanks to the "young ones" for those nice "fika" moments.

Quiero agradecer también a todos mis amigos cubanos "desperdigados" por el mundo, por el apoyo, por el ánimo, porque me demuestran cada día que la amistad no conoce fronteras.

Por último, y estos quizás deberían ser los agradecimientos más largos, pero son de los que no alcanza ninguna palabra y solo se pueden dar con abrazos, quiero agradecer a mi familia. Gracias por alentarme siempre, aun cuando perseguir mi sueño significara alejarme de ustedes. A mis padres por todo el sacrificio, por guiarme siempre. A mi madre por el apoyo incondicional, a mi padre por enseñarme el amor por la investigación y la docencia. A mis titas, que consiguen siempre dibujarme una sonrisa. A mi familia adoptiva de Murcia, que me hacen sentir siempre como en casa, no tengo palabras para agradecer tanto cariño.

Por último, a mis Joses. Jose, a ti te debo poner en mayúsculas, cursiva y con comillas en estos agradecimientos. Gracias por estar siempre, por ser mi amigo, mi compañero de fabricación, de medidas, de vida, mi revisor más duro, y el mejor papi. Gracias a mi niño, mi pequeño príncipe, mi motor impulsor, gracias por enseñarme el mayor amor del mundo.

Resumen

En el transcurso de las últimas décadas, los terahercios han pasado de ser un campo de investigación limitado, debido a la dificultad en su generación y detección, a ser un área proactiva con disímiles aplicaciones en muchos y nuevos campos. Las características únicas y distintivas de la radiación en la banda de los terahercios, combinado con el desarrollo reciente de detectores y fuentes de alta calidad han impulsado su aplicación en diversos sectores como son: imágenes médicas y de seguridad, estudios atmosféricos y radioastronomía, comunicaciones inalámbricas de alta velocidad, entre otros. Sin embargo, la expansión de dicho potencial está actualmente limitada por la necesidad de tecnologías que combinen el bajo coste, la portabilidad y la eficiencia. A lo anterior se debe añadir que, para aplicaciones no refrigeradas, las características excepcionales de los terahercios pueden verse fuertemente afectadas por las variaciones de las condiciones atmosféricas. Por tanto, la combinación de detectores en la banda de los terahercios con sensores que operen simultáneamente en otras bandas de frecuencia puede ser muy útil en el desarrollo de receptores confiables y consistentes que brinden información adicional y complementaria sobre el objeto o fenómeno que se estudia.

La primera parte de este trabajo está enfocada en el diseño de detectores multibanda asequibles e integrados en el rango de los terahercios. De esta manera se puede obtener información de diferentes rangos espectrales en una sola medida reduciendo así el costo, las dimensiones, el peso y el consumo energético del receptor. Con este objetivo se diseñaron concretamente dos detectores doble banda. El primero de ellos opera simultáneamente en la banda submilimétrica y en el infrarrojo. El segundo detector se diseñó para trabajar en las bandas milimétrica y submilimétrica. Ambos detectores están basados en lentes planares de Fresnel impresas en un bloque de silicio de alta resistividad. Las lentes planares se diseñaron para operar en la banda alta de frecuencia (como lentes), enfocando la radiación en un detector de alta frecuencia ubicado en el lado opuesto del dieléctrico. Al mismo tiempo, estas lentes fueron parcialmente modificadas para convertirse en antenas operando como detectores para la banda baja de frecuencia. A pesar de la baja eficiencia y ancho de banda (comparado con diseños basados en lentes refractivas), los diseños basados en elementos ópticos difractivos, como son las lentes utilizadas, son de gran interés por su potencial para crear dispositivos ligeros y simplificar el proceso de fabricación. Tres modificaciones diferentes de lentes planas, inspiradas en antenas convencionales, fueron evaluadas: espirales, bow-tie, y meander. El funcionamiento de los detectores en las bandas milimétrica y submilimétrica

se basó en detección directa, empleando diodos Schottky. Consecuentemente, se evaluó el funcionamiento de estos detectores en términos de acoplamiento, responsividad y potencia equivalente de ruido.

Por otro lado, es incluso mayor la necesidad de implementar receptores integrados para la detección heterodina en la banda de los terahercios. Las agrupaciones de muchos elementos están condicionadas por las limitaciones en el acoplamiento de la potencia del oscilador local (OL), los circuitos de distribución de la señal de salida de frecuencia intermedia (IF) y del OL, así como la disponibilidad de fuentes de alta potencia para este último. En este contexto, las guías de onda metálicas, que son la solución mas empleada, incrementan el costo y la complejidad y las dimensiones, al mismo tiempo que restringen la compactibilidad de los sistemas. El apilado o montaje de varias capas de obleas de silicio, excavadas con alta precisión ha surgido como una alternativa muy prometedora. Sin embargo, su alineamiento y montaje manual son todavía una limitación para el desarrollo de esta tecnología.

En los últimos años han surgido nuevas soluciones que integran la fotónica y la electrónica en el campo de los terahercios, lo cual ha conllevado al surgimiento de novedosos y avanzados dispositivos basados en diseños híbridos. La segunda parte de esta tesis combina conceptos y tecnologías de ambos dominios (electrónico y fotónico) y puede constituir un punto de partida para la creación de una nueva forma de detectores heterodinos integrados en silicio. El prototipo que se propone para demostrar el concepto es el de un mezclador subarmónico que integra una antena planar en una plataforma fotónica de silicio. La señal del oscilador local es guiada y se acopla al par de diodos (en configuración antiparalela) mediante una guía de cristal fotónico. El proceso de fabricación de este cristal fotónico es completamente compatible con la fabricación de muchos componentes activos, posibilitando un nivel superior de integración, añadido a la posibilidad de extender este concepto a diseños multi-pixel en 2D. Las prestaciones de un prototipo de un elemento fueron experimentalmente demostradas en este trabajo, obteniéndose una buena concordancia entre los resultados simulados y las medidas. Además, las prestaciones del diseño presentado son comparables con el estado del arte de los mezcladores basados en antenas planares.

Abstract

During the last decades, terahertz science has gradually been converted from a limited research field, due to the difficulties in its generation and detection, to become a proactive field with application in many new research areas. The unique and distinctive characteristics of terahertz radiation, combined with the development of high-quality sources and detectors, have boosted its opportunities of applications in such diverse fields as: medicine, security imaging, atmosphere study or radioastronomy, high-data rate wireless communications, etc. However, the widespread deployment of such potential is still limited due to the lack of low-cost, portable, efficient technologies. Furthermore, for uncooled Earth applications, the exceptional features of imaging and sensing in the terahertz range are strongly affected by variations of the atmospheric conditions. The combination of terahertz detectors with sensors at other frequency ranges can be highly desirable for the development of consistent and reliable receivers in order to have complementary and additional information about the object or phenomenology under study.

The first part of this work is focused on the design of compact and affordable integrated multi-band detectors in the terahertz range. The proposed receivers are designed to obtain information of different spectral ranges in a single measurement, reducing instrument cost, size, weight, and power consumption. To this aim, two dual-band direct detectors are proposed. The first one integrates the submillimetre wave range and the IR range, whilst the second one is intended to operate at the millimetre and submillimetre wave ranges. Both detectors are based on Fresnel zone plate lenses (FZPL) printed on a high resistivity silicon slab. The planar lens is designed to operate in the higher-frequency range, focusing the incoming radiation into a high frequency detector placed on the opposite side of the slab. At the same time, the planar lens is modified to perform as an antenna for the lower-frequency detector. Despite the lower efficiency and bandwidth, compared with the classical refractive lens approach, a design based on a diffractive optical element, as is the FZPL, is of great interest because of its potential to create thin and lightweight devices and simplify their manufacturing process. Three different modifications of the FZP lens have been evaluated, namely spiral, bow-tie, and meander modifications. The direct detection of the millimetre and submillimetre ranges relies on a Schottky diode, for which, the detector performance in terms of RF coupling, responsivity and noise equivalent power has been assessed.

For THz heterodyne detection the need to find compact and integrated solutions is even greater. Large multi-pixel heterodyne arrays are limited because

of the constraints in LO power coupling, IF layout, LO distribution network and the availability of high power LO sources. In this context, hollow metallic waveguides increase the complexity and cost whilst restrict the compactness of the arrays. Silicon micromachining of vertical stacked layers has arisen as an alternative, although the alignment and manual assembly is a limitation on the large-scale deployment of this technology.

Since few years ago, the integration of a photonic and electronic solution has undergone significant development and innovative hybrid approaches have been proposed. The second part of this work merge concepts and technologies from both, electronics and photonics domains and may be a good starting point for the creation of new silicon integrated heterodyne detectors. The proposed prototype is a subharmonic mixer that integrates a planar antenna on a photonic silicon platform. The local oscillator signal is guided and coupled to the diode-pair within a photonic crystal (PC) waveguide. The fabrication process of this PC is fully compatible with the manufacturing of many active components leading to a further level of integration, along with the possibility of extending the concept to a 2D multi-pixel approach. The performance of a single-pixel prototype has been experimentally demonstrated showing good agreement with the simulation and is comparable with the state-of-the-art of planar-antenna based mixers.

Contents

List of Figures

List of Tables

Abbreviations and Acronyms

ADS	Advanced Design System
ACST	Advanced Compound Semiconductor
APD	Antiparallel Diode
CL	Conversion Loss
ENT	Equivalent Noise Temperature
FPA	Focal Plane Array
FZP	Fresnel Zone Plate
HFSS	High Frequency Structure Simulator
IF	Intermediate Frequency
KDT	Kirchhoff Diffraction Theory
LO	Local Oscillator
MMIC	Monolithic Microwave Integrated Circuits
MMW	Millimetre Wavelengths
NEP	Noise Equivalent Power
PC	Photonic Crystal
PBG	Photonic Band Gap
RF	Radio Frequency
SBD	Schottky Barrier Diode
SubMMW	Submillimetre Wavelengths
TE	Transverse Electric
TEM	Transverse Electromagnetic
THz	Terahertz
UMS	United Monolithic Semiconductors
VDI	Virginia Diodes Incorporation

Chapter 1

Introduction

The terahertz band has remained underdeveloped for many years, between the well-established highest frequency microwave technologies and the well-developed optical engineering of infrared (IR) detectors. However, recent breakthroughs in the fabrication processes and progress in electronic and optics technologies have boosted the terahertz field.

Depending on the bibliographic references consulted, the THz radiation is defined either as the radiation between 100 GHz and 10 THz [Hea18, Son15, Car15], 100 GHz to 30 THz [Dhi17] or the radiation from 300 GHz to 3 THz [ITU16]. Conversely, there is a major consensus in the definition of millimetres (MMW) and submillimetres waves (SubMMW). The first ones are electromagnetic signals between 30 GHz and 300 GHz, whilst the SubMMW range is defined from 300 GHz to 3 THz. These frequencies ranges have in common that they present interesting properties which make them very suitable for multiple and dissimilar applications such as space science applications [Phi92, Mel00, Wat06], gas spectroscopy and quantum physics [Win96, Uen08], non-destructive evaluation [Fuk15], security and medical imaging [Mit18], among others.

Reviewing some of the distinctive and advantageous characteristics that have led the development of millimetre and submillimetre waves technologies, we can mention that the wavelengths within those frequency ranges have good penetration through many materials, which are opaque in the visible range and become almost "transparent" at MMW or SubMMW, e.g. clothes, paper and envelopes. Moreover, metallic objects can be easily discriminated from other dielectric ma-

terials [Fed05]. Based on that, security systems for the detection of concealed objects, manufacturing process monitoring and non-destructive testing in quality controls can be developed. Additionally, THz waves can provide images with a better resolution (submillimetre resolution) than the microwave ones [Mit18]. Another potential imaging application where THz band may be superior is in environments with high concentration of suspended dust or particles such as smoke or wind dust environments; as wavelengths are longer than that of the suspended micro-scale particles in the air, they are absorbed in a lesser degree and transmitted more readily through it (compared to the IR) [Bro03]. Medical and biological applications may also benefit from the use of the THz range mainly because of two special characteristics, namely, the non-ionizing nature of the radiation [Wal02] and the rapid attenuation in the water. For example, as the water content in tumour tissues is significantly different from the normal tissue cells, it may be possible to identify them even in an early stage [Woo03].

THz spectroscopy also takes advantage from the distinctive response of the materials to THz radiation. Some solid materials show characteristic spectral features in the 0.5 THz - 10 THz range, which allows the detection and discrimination of different chemical substances [Fed05]. Regarding this property, THz technology may be used in drug detection and in the detection of harmful compounds, antibiotics, and microorganisms [Afs19].

Along with spectroscopy [Luh79, Luc10, Sie12], space science has historically been the main driving force and the more consolidated developer of terahertz technology. Almost half of the energy generated by the visible stars and galaxies is absorbed by the surrounding dust and re-emitted at far-infrared and submillimetre frequencies [Tan15]. When a star is born, the process implies the presence of great quantities of dusty material so visible-light telescopes are not so useful. However, at the infrared, submillimetre and millimetre wavelength regions, where the effects of this obscuration are nearly negligible, the phenomenology can be properly studied. Many ground and space missions can be cited as references of the efforts dedicated to the study of atmospheric and cosmological phenomena in the THz range [Blu92, Pag03, Sie07, Gra13, Bas17]. For these applications where extreme sensitivities is required, the instruments must be often cryogenically cooled.

1.1 Motivation

Despite of all these outstanding characteristics of the THz range, there are some drawbacks that must be mentioned. Atmospheric attenuation at these frequencies is really high, which is a critical limitation for THz sensors in Earth applications. It is important to say that, within the overall high attenuation, there are certain frequencies where the transmission is higher, which are known as THz windows [Yua03]. Nevertheless, Earth uncooled THz detection is very sensitive to all atmospheric fluctuations (specially those related to water) as well as temperature variations. Therefore, although THz wavelengths bring useful and unique features, in many applications this information must be complemented with additional images or measurements in other frequency ranges such as the IR or visible. This could be the case of a stand-off detection system as the one presented in Figure 1.1 (a) (after [Kow14]). The complementary information obtained by using various cameras operating in different spectral ranges (i.e. Long wave–IR, Middle-IR, THz (250 GHz) and visible) has proved to be very useful for the detection of concealed objects in security applications [Kow14, Kow19].

Furthermore, even within the SubMM frequency range, not all frequencies provide the same information. Figure 1.1 (b) shows the results presented in [Zho18] where multi-frequency terahertz imagines are used for effective diagnosis of cancerous brain tissues. The images were obtained by combining conventional terahertz time domain spectroscopy with a tunable multispectral Metamaterial-FPA. The metastatic brain tumour is indistinguishable from the health brain tissue in an optical image. However, by contrasting the THz imaging from the normal tissue and the tumour, the areas with metastasis can be clearly distinguishable. Nevertheless, not all the T-images exhibited the same contrast. Within the range from 1 to 5 THz, some frequencies were able to differentiate better the tumour than others.

Another example can be found in Figure 1.1(c), where the images obtained after the study of an ancient Egyptian vertebral body using terahertz TDS in [Öhr10] are presented. The series of studies carried out by this research group confirmed that images obtained at lower terahertz frequencies (0.24 THz) displayed overall structures while the higher terahertz frequencies (0.54 THz) showed more details since they exhibit higher resolution. In the same study it was pointed out that broadband terahertz TDS used for imaging applications leads to long acquisition time. Therefore, a multiband multipixel system operating in defined frequencies could be very useful in order to reduce the acquisition

times and widen the scanned area.

Finally, 1.1(d) shows the information from different instruments mapping the Centaurus A galaxy. Radioastronomy applications have a long background in the combination of several spectral ranges. It is widely accepted that much better understanding from the observed object or phenomena can be obtained by including information from different instruments. Particularly, the combination of the terahertz with other frequency ranges could be significantly attractive for some applications such as the study of stars formation process. A detector that can work simultaneously at mid-infrared wavelengths, around 10 μm, and at submillimeter wavelengths, around 300-750 μm (∼0.4-1 THz), would be very useful to study the physical conditions in the different stages of the star development. These two wavelength regimes provide complementary information on the emitting material, which is most useful for the models to better constrain the physical parameters of the objects. Space observatories, such as Planck [Ade14], and the biggest space observatory under construction, James Webb Space Telescope (JWST) [Rie15], are examples of the potential currently offered by the combination of these and others frequency ranges in radioastronomy.

As has been mentioned, for some applications, the combination of several detectors with high spectral resolution facilitates fine discrimination between different targets based on their spectral response in each of the narrow bands. In that sense, if the frequency ranges of interest are very distant, the typical solution is to use separated Focal Plane Array (FPA) detectors with fixed or mobile splitters, mirrors and alignment elements. This approach usually requires long-time for sequential scanning at different frequencies. In many cases this is the only suitable solution, but it drives to bulky systems and increases their cost. Moreover, multi-band systems that use separate lens systems and detectors to acquire different spectral bands may present problems to ensure that the frequency bands are comparable both spatially and radiometrically. Another found solution is the 2-D detector array of antennas operating at different frequencies employing the same quasi-optical system. The array of different size antennas occupies much more chip area [Sim17] at the same time that the positioning and alignment to focus the radiation in a common quasi-optical system is very challenging [Lam03].

Therefore, finding compact integrated multi-band detectors in the terahertz range is of great interest to obtain information of different spectral ranges in a single measurement, reducing instrument cost, size, weight, and power consumption. Notwithstanding the developments in uncooled THz detection technologies, most of the state-of the-art devices are based on volumetric concepts that increase the cost and limit the integration in large arrays. The high atmo-

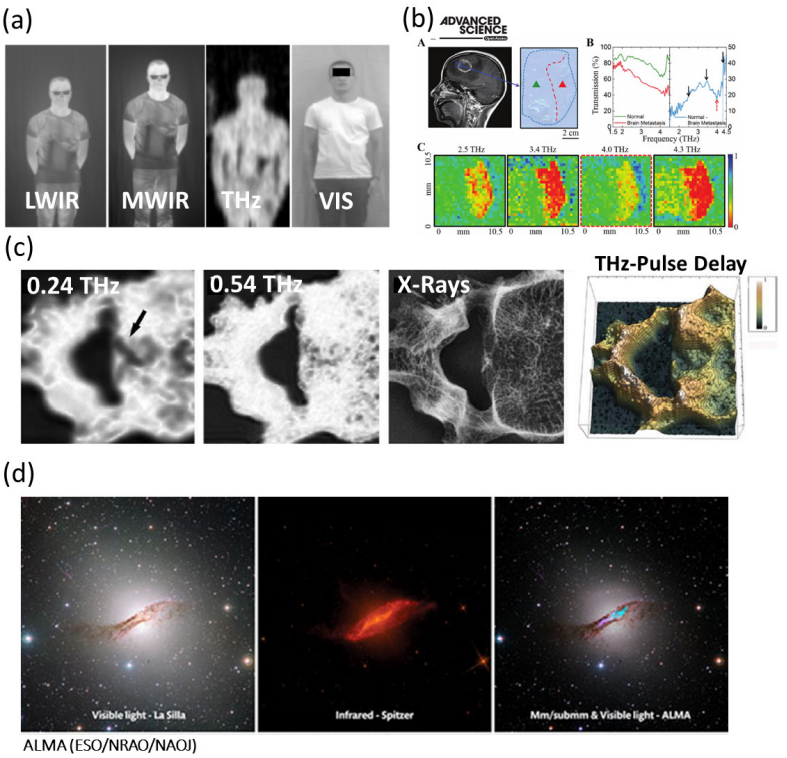

Figure 1.1: Examples of multi-band terahertz applications. (a) Concealed objects detection in log-wave IR, mid-IR, THz (250 GHz) and visible ranges, after [Kow14]. (b) Multi-frequency THz imaging for effective diagnosis of cancerous brain tissues, after [Zho18]. (c) 0.24 THz, 0.54 THz, and conventional X-ray and terahertz pulse delay image (with false colors) corresponding to terahertz optical density of an Ancient Egyptian vertebral body [Öhr10]. (d) Visible, IR and combined MM-SubMMW-Visible images from the the Centaurus A galaxy [ALMA].

spheric attenuation, together with the high losses associated with the excitation of surface waves in electrically thick substrates and the high losses of the metal conductors have forced the use of bulky quasi-optical elements such as silicon lenses and metallic waveguide based components. Thin, lightweight and reduce the volume of the elements; alongside with new compact fully planar and portable approaches, have become very desirable for most new THz components.

For THz heterodyne detection, the eagerness to find compact and integrated solutions are even majors. Heterodyne detection above 100 GHz is usually performed by the combination of hollow metallic waveguides and suspended microstrip based circuits. Until now, hollow metallic waveguides have been the best proven solution to compensate the ohmic losses from metal-based transmission lines and passive components at high frequencies. However, such implementations increase the complexity and cost and restrict the compactness and reliability of terahertz integrated circuit. Additionally, most of the implemented devices consist of either a single pixel or low number of pixels. The development of large multi-pixel heterodyne arrays is still a challenge, limiting the mapping ability and scanning velocity of these systems. Recent research works have shown some promising results [LLo13, Rec15, Gra15]. Nevertheless, they are based on either bulky structures or multilayer silicon structures, where the fabrication and alignment requirements increase exponentially with the frequency up scaling (dimensions down scaling). Thus, high level component integration with efficient LO power distribution and coupling are key factors in the development of new heterodyne detectors.

Recently, several studies dealing with electronic devices on silicon-based platforms have been reported as an alternative for highly integrated devices. The integration of electronic and photonic solutions has arisen in the last years as a very promising field to close even more the "terahertz gap" [Sen18, Wit18]. In this context, novel integrated silicon systems would be necessary in the next generation of terahertz devices to achieve compacts architectures with multifunctional and reconfigurable capabilities. An integrated heterodyne receiver that integrates a planar antenna and a mixer on a photonic silicon platform may allow the realization of two-dimensional multi-pixel array with very attractive potentialities.

1.2 Background

1.2.1 Terahertz Detection

Terahertz detection can be broadly divided into two approaches, namely, coherent and incoherent (direct) detectors. Coherent detection is based on heterodyne receivers, which are basically down-converting mixers. The THz signal (usually with very low power) is received by an RF antenna and it is guided to a non-linear device (e.g. diode, transistor) where is mixed with a local oscillator signal (higher power). The down–conversion mixing results in an intermediate frequency (IF), which is a replica of the original RF spectrum with both the phase and amplitude information in a much lower frequency range, where there is availability of components for amplification and processing. Furthermore, heterodyne detectors typically provide high spectral resolution. The main drawback for the coherent SubMMW receivers is the requirements of LO sources, whose availability and power capacity decrease when frequency increases. Besides, the need of a LO distribution network and other circuit elements (e.g. filter, matching sections) limits the large FPA feasibility of heterodyne detectors. Currently, superconductor insulator semiconductors (SIS) are the most sensitive mixers available. For frequencies above 1 THz, hot electron bolometer (HEB) mixers is another competitive technology although, as the SIS mixers, they typically operate at temperature below 4 K. Oppositely, Schottky diode mixers can work at room temperature; however, they require higher local oscillator pump power.

On the other hand, a direct detector is a simple device consisting on an antenna that collects the terahertz radiation and is directly connected to a detection element where the terahertz signal is rectified to baseband (either DC or very low frequency) and no phase information is recovered. Such detectors can be broadly classified in three groups: thermal detectors (e.g. bolometers, Gollay cells, pyroelectric detector), photoconductive detectors and electronic rectifiers (e.g. Schottky diodes, FETs) [Car15]. Incoherent detectors, as a general rule, are broadband devices and they are preferred over coherent detectors when sensitivity is more critical than spectral resolution. Furthermore, their simplicity makes them easy to scale in 2D arrays.

There is a wide variety of devices and technologies, in addition to the above mentioned, that have been studied and used for THz either coherent or incoherent detection. A recent review of all these technologies has been presented in [Lew19] where they were summarized and classified according to the physical mechanism employed.

Certainly, Schottky diode-based devices have been among the most studied and applied detectors for direct and heterodyne receivers below 1 THz for uncooled application. This may be due to many reasons, but mainly because of its high cut-off frequency and relatively simple and versatile structure. Current Schottky diode-based direct detectors are cost-effective uncooled detectors, easy to manufacture and integrate on array configuration. Therefore, the designs proposed in this thesis will be based on Schottky diodes for both direct and heterodyne detection.

1.2.2 Diffractive Optical Terahertz components

Conventional refractive lenses are key components for many terahertz applications. Notwithstanding the important results achieved in the fabrication of large array of Silicon micro-lenses [Alo13], they are still volumetric components. Moreover, classical silicon lenses are difficult to fabricate, especially for short-focal lengths [Wil04]. In this scenario, diffractive optical elements have become of great interest because of their potential to create thin and lightweight devices and simplify their manufacturing process.

Diffractive optical elements in the THz range have been designed not only based on geometrical optics, but also on wave optics. This last approach is the one used when the feature size of the conforming elements is on the order of the wavelength. Thus, the phase of each element can be individually controlled to achieve a certain beam behaviour, namely, focusing, shaping, redirecting, etc. The same dedicated design procedure leads to the possibility of achieving systems with short focal length and large diameter (i.e. short Focal number $F_{\#}$) [Sie19]. Historically, the main drawback of diffractive optics has been its intrinsic narrowband operation combined with off-axis and chromatic aberration and low broadband focusing efficiency. However, recent investigations have overcome such limitations. Regarding this, we can cite the broadband behaviour obtained with a lens based on a kinoform structure of high order [Sus14], a lens based on transformation optics [Yan11] and planar lenses based on multi-level microstructures [Wan16, Moh16].

1.2.3 Photonic Crystal-Electronic Integration in the Submillimetre Frequency Range

For many years, the solutions to fill the so-called "terahertz gap" came up separately from the frequency up-converting of microwave electronic or from the down-conversion in optics and photonic. Both solutions were developed without interaction between them until the past decade. However, recent breakthroughs in the fabrication process and the progress in both, electronic and photonic technologies, has boosted the development of compact integrated electronic solution as well as hybrid electronic–photonic systems [Wit18, Sen18].

In the last years, several studies where electronic devices are coupled with silicon-based platforms have been reported as an alternative for highly integrated devices. The basic concept behind these studies comes from the photonic domain where optical waveguides based on Silicon-on-Insulator (SOI) technology, including optical Photonic-Crystal waveguides, have been widely investigated [Joa08]. Within this framework, high-resistivity silicon (HR–Si) has been successfully used as an efficient platform for passive Photonic-Crystal-based devices, namely, dielectric PC waveguides for applications at frequencies up to 600 GHz [Tsu15, Ama17, Ede10], diplexers for terahertz-wave integrated communication circuits [Yat16] and high Q-factor Photonic-Crystal resonators for sensing [Ott14, Oka17].

The fabrication of Photonic-Crystal platforms is compatible with the manufacturing process of many active components. The sacrificial dielectric layer, which is commonly used to support the epitaxial semiconductor layers that perform the active junctions, could be used as a PC platform (i.e. etching the dielectric with dry or chemical etching). The first steps for active components integration have been mainly focused on resonant-tunnelling diodes (RTDs). In [Oka17], a Resonant-Tunnelling Diode (RTD) chip was mounted directly onto a PC waveguide where evanescent coupling takes place, resulting in coupling efficiency lower than 0.1 %. The same research group presented a RTD detector attached to a PC waveguide connected to a THz fibre demonstrating a 10 Gbit/s error-free data rate communication at 300 GHz [Yu19a]. In order to improve mode and impedance matching between the RTD and the PC waveguide, a tapered-slot mode converter printed on an external InP substrate connected to the RTD was used. This showed coupling efficiency higher than 90 % with 50 GHz 3-dB bandwidth and achieved real-time error-free data transmission at 32 Gbit/s [Yu19b]. In all these approaches, the coupling element and the output lines (read-out lines) were fabricated as separated components and then, welded or attached to the PC slab.

In previous works several mixer configurations using PC substrates were proposed [Ede07, Khr13]. However, in both cases the PC was used to improve the radiating performance of the radiating element, a dipole antenna. The LO injection was based on a conventional waveguide [Ede07] or quasi-optically fed through the PC [Khr13], with low efficiency. A recent research proposed a metallic waveguide-input three terminal RTD fundamental mixer based on a PC waveguide platform operating at 0.3 THz [Yu20]. The device demonstrated 20 dB conversion loss and >10 Gbit/s error-free transmission operating as coherent THz receiver. However, it exhibited low RF-LO isolation (6 dB) and required external bias.

1.3 Objectives and outline of the Thesis

Based on all the previously exposed, **the main goal** in this thesis is the design and implementation of integrated and compact terahertz detectors based on planar configurations. To this aim, the thesis is divided into two major topics to cover the applications for both direct and heterodyne detectors:

- **Dual-Band direct detectors**. The first part of the thesis focuses on the development of compact dual-band direct detectors based on planar diffractive optical lenses. Two different approaches based on modified Fresnel zone plate (FZP) lenses have been proposed. A dual-band detector where the operational bands are largely separated in the spectrum (i.e. $f_h/f_l > 70$) and another one where the working frequencies are closer (i.e. $f_h/f_l < 10$).
- **Silicon integrated planar heterodyne detector**. The second part of the thesis is committed to the implementation of an integrated planar subharmonic mixer on a silicon photonic crystal platform.

The contents of the thesis are organized as follows:

- In Chapter 2, the main features of SubMMW direct detectors based on Schottky diode technology compatible with the dual-band integrated approach are discussed. To this aim, a general overview of Schottky diode technology and specifically, the planar and quasi-vertical approaches are summarized. Afterwards, the performance of three diodes is assessed to be used in direct detection architectures integrated with a planar antenna. The figures of merit for the detectors namely, responsivity and noise equivalent power, are derived from the referred comparison. The measured flicker noise was included in the assessment of the NEP proving its relevance in the accurate prediction of the detector performance.
- Chapter 3 presents the development of an integrated dual-band direct detector for subMM (300-500 GHz) and mid-IR range (28 THz) based on FZP lenses. Firstly, the study and evaluation of different modified SubMMW wave antennas suitable to act as a Fresnel zone plate lens in the IR range is performed. Afterwards, both concepts are brought together to create the dual-band design. Finally, a PBG based solution is introduced to avoid the surface wave excitation and improve the radiation performance of the device.

- Chapter 4 provides an alternative with respect to the design presented in Chapter 3 in order to develop a dual-band detector, but in this case working at two closer frequencies. Therefore, the implementation of the proof of concept of an integrated dual-band direct detector at W-band (75-110 GHz) and 850 GHz based on Fresnel zone plate lenses is presented. Like in the previous design, different modified SubMMW antennas suitable to act as a Fresnel zone plate lens at 850 GHz are assessed, whereas both, fast scalar Kirchhoff's diffraction and FDTD 3D EM simulations are employed and compared. Experimental validation of the focusing behaviour of the modified FZP lenses are also included in the chapter.

- Chapter 5 deals with the second general goal of the thesis, which consists in the design and implementation of an integrated planar subharmonic mixer on a silicon photonic crystal platform. The first part of the chapter presents the study and design of a photonic crystal silicon platform consisting of a PC waveguide and a PC cavity that will serve to guide and couple the LO signal to a planar antenna connected with the mixing diode element. The Load-Pull analysis of the mixer topology is performed to find the minimum achievable CL and the optimum embedding impedances. The same planar antenna is simultaneously optimized for coupling with the LO signal and with the RF radiation, at the same time that presents a matching impedance condition for the anti-parallel diodes. Additionally, the development of in-house fabrication techniques to manufacture the silicon photonic crystal platform covered by a 3 μm SiO_2 membrane is briefly described, since the complete fabrication process is explained in Appendix A. Finally, the assembly and measurement of the prototype in terms of noise temperature and conversion loss are detailed.

- Chapter 6 summarizes the main results and some guidelines for future research are given.

Chapter 2

Submillimetre Wave Direct Detectors Based on Schottky Diode Technology

2.1 Introduction

The main goal of this first part of the thesis is the design of compact dual-band detectors intended to work in an incoherent (direct) architecture. To this aim, the selection of the detection elements is the first step. The main features of a solution based on Schottky diodes are studied. Afterwards, the proposed planar antennas will be designed accordingly to fulfil its requirements.

This chapter starts with a brief summarize of the main features of Schottky diode technology and the state-of-the-art of planar and quasi-vertical direct detector approaches. Then, three diodes based on different fabrication technologies and therefore, different barrier height and flicker noise response, are studied. This study allows us to evaluate and compare the benefits and limitations of each technology under the same conditions (i.e. same input power, bias current, RF and low modulation frequencies and load impedance).

The predicted performance of the direct detectors in terms of intrinsic and loaded responsivities, as well as the low-frequency and RF-frequency matching conditions were evaluated. Afterwards, special attention has been given to the

study of the Noise Equivalent Powers (NEP), since this is a parameter widely employed in the evaluation of the direct detectors. However, we can find different definitions for the same parameter in the literature. Furthermore, it is variable with the forward current flowing in the diode and with the modulation frequency since it is affected by the flicker noise. Therefore, the study of the flicker noise was included in the presented analysis and the diodes were also compared in terms of its noise frequency corner. Finally, the study of the Noise Equivalent Power of the three assessed devices under different bias conditions and modulation frequency will be presented.

2.2 Review of Schottky Diode Technology

Planar Schottky diode technology is a mature field with more than 30 years of development and numerous dedicated studies. Even when the scope of this thesis is not directly focused on the development of the semiconductor device, some of the basic characteristics and operating principle of the Schottky diode are described in this section. This way, the further developed devices will be optimized considering the most suitable Schottky diode properties and configuration.

A Schottky diode is based on the junction created between a semiconductor and sputtered or evaporated metal on its surface. The major advantage of this junction is that it is based on the flow of only majority carriers. That is, electrons flowing from the semiconductor to the metal in forward regime if an n-type semiconductor is employed; whereas in p-type Schottky junctions the forward currents results from holes flowing from the semiconductor to the metal. This operational principle results in a very fast switching device [Bah03].

When the metal and semiconductor are brought together during fabrication, a potential barrier is created. The zone of the semiconductor closest to the metal becomes depleted from charge carriers leaving spaces with opposite charge until dynamic equilibrium is reached. The created potential barrier (Ψ_{bi}) prevents the electrons to flow from the semiconductor to the metal. If a forward voltage is applied to the junction (V_j), the potential barrier is lowered allowing the electrons flow into the metal. Thus, the resistance of the junction is function of the junction voltage (i.e. variable resistor or varistor): a higher voltage gives a lower resistance. On the other hand, if a reverse voltage is applied the potential barrier and the depletion width are increased. Thus, the junction acts as a voltage controlled capacitor (i.e. variable reactor or varactor) [Nea12].

The barrier height (Φ_B) is determined by the metal and the type of semiconductor used (n or p). Different materials and doping create different barrier height, which is usually between 0.2-0.9 eV for most Schottky diodes. For an ideal contact, the barrier height can be calculated as the difference between the metal work-function(ϕ_m) and the semiconductor electron-affinity (χ). Nevertheless, the estimation of a practical barrier height, including the non-ideal interface phenomena, is rather complicated [Cow65]. In practice, its calculation relies on measurements.

For millimetre and higher frequency operation the optimization of the barrier and parasitic impedances is crucial. The semiconductor thickness, doping concentration and contact size are optimized depending on the application. Gal-

lium arsenide (GaAs), silicon (Si), gallium nitride (GaN) and indium phosphide (InP) are examples of commonly used semiconductors. The metal can be titanium (Ti), platinum (Pt), chromium (Cr) and various alloys [Tan13].

For practical reasons, Schottky diodes can be classified in four types depending on the barrier height: high-barrier, medium-barrier, low-barrier and zero-bias-barrier. The first three types are made with n-type semiconductor and the appropriate metal; whereas zero-bias diodes are normally built with p-type semiconductor material [Cor09]. The term "zero-bias" is used to refer to diodes with the lowest barrier height. Due to its very low forward voltage, these diodes perform the most sensitive detectors.

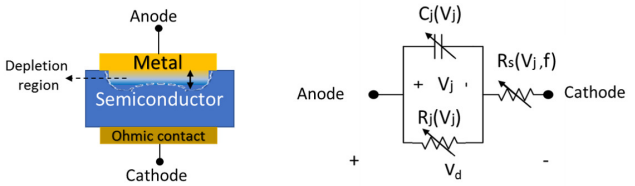

Figure 2.1: Schottky diode equivalent circuit.

A typical Schottky diode junction is modelled with a junction resistor, $R_j(V_j)$, a junction capacitor, $C_j(V_j)$, and a series resistor R_s, as shown in Figure 2.1. The junction capacitance is determined by the physical dimensions of the junction and the doping profile of the semiconductor layer. The series resistor includes the total resistance from the undepleted semiconductor to the cathode ohmic-contact. That is the epitaxial layer and the resistance due to the substrate [Tan13]. The modelling equation of the current for a Schottky junction, regardless of the technology in which it has been implemented, is given by equation 2.1.

$$I_j(V_j, T) = I_{sat}\left(e^{\frac{q(V_d - R_s I_d)}{\eta k_B T}} - 1\right) \tag{2.1}$$

where

k_B = Boltzmann's constant$\sim 1.38 \times 10^{-23} J/K$
q = electron charge, $1.60206 \times 10^{-19} C$
T = absolute temperature, K
R_s = series resistance, Ω
η = ideality factor
I_{sat} = saturation current, A

$$I_{sat} = AA^{**}e^{(\frac{-q\Phi_b}{k_B T})} \tag{2.2}$$

where
A = effective diode area, cm^2
$A**$ = modified Richardson constant, $(A/K)^2/cm^2$
Φ_b = barrier height, V

As well, the cut-off frequency is computed as the frequency at which the reactance of the diode equals the series resistance:

$$f_c = \frac{1}{2\pi R_s C_j}. \tag{2.3}$$

As a matter of fact, to achieve good performance at high frequencies, the diode junction area should be small. By reducing the junction area, the junction capacitance is also reduced so that the operating frequency is, therefore, increased. However, this capacitance reduction usually leads to a trade-off because at the same time, the series resistance increases.

In the frequency range up to 1 THz, the operation of Schottky diodes is well understood and planar Schottky diodes have been accurately modelled with lumped equivalent circuits that includes all the parasitic components. Several studies have been dedicated to improve and optimize the diode modelling in terms of frequency, power, temperature and noise response [Tan13, Wan09, Gut19a]. Finally, depending on the application, Schottky diodes can be arranged in different configurations. In such way, direct detectors are typically based on single, parallel or series diode approaches, whereas for mixing and multiplier applications in the SubMMW range it is usual to find anti-parallel and anti-series configurations [Mae10, Per19, Ji20]. Anti-parallel configurations are used to generate and increase the efficiency of only the odd harmonics by suppressing the even harmonics; whereas for the anti-series configuration it is just the other way around, the odd harmonics are cancelled and the even harmonics are more efficient.

2.2.1 Noise in Schottky Diodes

The noise mechanics existing in a Schottky diode have been extensively investigated [Zie70, Sat98, Zel13]. Modelling and optimization of low frequency (LF) noise is essential for predicting the noise system limitations. The main contributors to LF noise in Schottky diodes are:

- **Thermal Noise (White Noise, Johnson or Nyquist Noise):** It is due to the random motion of charge carriers in any conductive material above 0 K. For a diode, the mean square thermal current is:

$$< i^2_{nThermal} >= 4k_BTB/R_s \tag{2.4}$$

  This is a white noise since the noise power density presents a uniform distribution in the low frequency range up to the THz range.

- **Shot Noise:** In every diode junction, when electrons or holes exceed the potential barrier, the current does not flow as a constant value. The discontinuous nature of this current is the shot noise. This noise also presents a uniform power spectral density distribution. The mean [Bah03]. The mean square shot noise current density is:

$$< i^2_{nShot} >= 2q(I_D)B \tag{2.5}$$

  where I_D is the forward current flowing in the diode.

- **Flicker noise (1/f, pink noise):** It is due to imperfections at the metal-semiconductor interfaces formed during the fabrication process. These crystal defects create traps for the carriers which lead to a fluctuating number of carriers when the diode is biased. The probability of trapping increases with time; thus, the noise level is inversely proportional to the frequency. When plotted on a logarithmic graph, the 1/f power spectral density looks extremely straightforward since it reduces to a straight line with slope approximately equal to –1. The flicker noise current can be modelled by:

$$< i^2_{nFlicker} >= K_f \frac{I_D^{a_f}}{f^{b_f}} \tag{2.6}$$

  Where K_f is the flicker noise constant, a_f is the flicker noise current exponent and b_f is the flicker noise frequency exponent. The values of K_f,

a_f and b_f are obtained from a curve fitting procedure from low frequency noise direct measurements of the device [Zel13]. In real measurements the usual is to find $1/(f^{b_f})$ with $0.8 > bf > 1.4$.

- **Burst Noise (Generation recombination, popcorn noise, red noise):** The root cause is the same of the flicker noise, namely trapping (capture) and de-trapping (emission) of carriers. It follows a Lorentz function and its contribution is difficult to appreciate isolated in Schottky diodes because the 1/f noise is considered as gathering of generation-recombination noise.

2.2.2 Planar and Quasi-Vertical Schottky Diode Technology

First high frequency Schottky diodes were based on whisker technology, which consisted of pointed contacts of tapered metal wires with a semiconductor surface [You65, Cro91]. Although parasitic losses such as the series resistance and the shunt capacitance are minimized, this technology suffered limitations on fabrication and repeatability. In 1993, a research group of the University of Virginia demonstrated the first planar Schottky diode competitive with whisker contacted diodes [Riz93]. Previously, in 1990, the same group, had proposed the planar surface channel diode for terahertz application with theoretical minimum parasitic capacitance [Bis90].

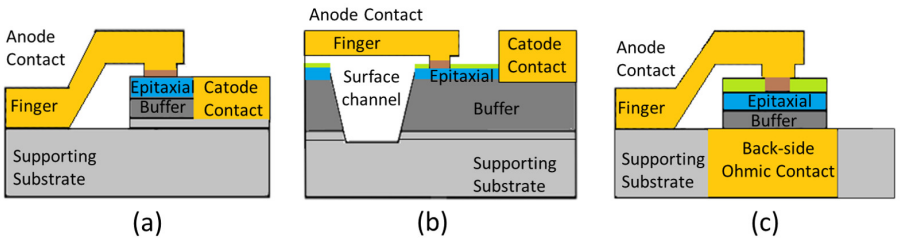

Figure 2.2: Schematic cross-section of planar Schottky diodes: (a) air-bridged diode, (b) surface channel and (c) quasi-vertical diode.

Figure 2.2 shows the schematic cross-section layouts around the anode contact of the currently most employed subMMW Schottky diodes.

- The first structure (Figure 2.2 (a)) is the air bridge diode. It can be also found in the literature as mesa diode. The key implementation phase for the success of this diode is the fabrication of a robust air bridge. This may represent a problem when it is necessary to reduce the size of the active area of the diode to a small fraction of a square micron.

- The second one, shown in Figure 2.2(b), is the surface-channel planar diode. A channel is etched across the width of the diode isolating the anode from the cathode. The channel etching is one of the last steps in the fabrication, guaranteeing a planar wafer surface during the most critical steps in the fabrication. One of the major concerns of this technology is the large pad to pad capacitance. A lot of effort has been made in order to reduce this parasitic impedance. The solutions have arisen from removing or thinning the supporting substrate as well as tailoring the surface channel dimensions. This technology provides a good trade-off between fabrication complexity and detrimental effects of parasitic elements, while is the most employed for high frequency Schottky diode applications.

  Another completely planar Schottky technology is the used by the company United Monolithic Semiconductors (UMS) [UMS]. This one does not include the surface channel, neither any air bridge for the anode finger. The parasitic effects are much more pronounced limiting its use for very high sub-millimetre frequencies [Wan09].

- The third and last structure, shown in Figure 2.2(c), is the quasi-vertical diode structure [Sim93]. During the last years a lot of effort was dedicated to reach the advantages of the whisker diode in a feasible planar approach [Ali15]. In the quasi-vertical approach, the Schottky contact is formed on the front side of the epitaxial layer, whereas the ohmic contact cathode is formed on its backside directly below; thus, vertical current flow is ensured. This way, the lateral currents flowing near the diode surface (crowding currents), which affect surface channel diodes, increasing its ohmic losses, are avoided [Tan11]. The quasi-vertical design has been boosted in the last years thanks to the advances in fabrication technologies. Nevertheless, the main constrain of this technology is still the difficulty in the fabrication that implies two-side processing of the semiconductor wafer and a robust air bridges.

Nowadays, planar Schottky diodes can be found either as flip-chip discrete diodes or as integrated components. The flip-chip discrete diodes may be mounted into the circuit with either solder or conductive epoxy. The last approach may present constraints on the assembly; at the same time, it may have poor mechanical toughness. Nevertheless, the state-of-the-art of fabrication technology allows that current diodes can be integrated with many passive and active elements onto the same substrate. Thus, integrated planar technology has been well proven beyond 300 GHz up to several THz [Mae10].

2.3 Schottky Barrier Diode Direct Detectors

As mentioned above, Schottky diode based direct detectors are one of the most popular and cost-effective solutions in the THz and sub-THz frequency band. Their acceptance is because they are simple and versatile devices able to operate cooled or uncooled and with or without biasing (zero-bias Schottky diodes). Besides, Schottky diode technology has been integrated with CMOS process opening up a very promising field for affordable THz devices [Han13]. Table 2.1 summarizes the state-of-the-art of Schottky Barrier Diode (SBD) direct detectors based on its most important figures of merit, namely, responsivity and NEP.

Table 2.1: Comparison of the State-of-the-Art of SBD Detectors.

Ref.	Technology	Resp (V/W)	NEP (pW/$\sqrt{Hz}$)	Frequency (GHz)
[VDIa]	WG ZBD	2800 typ.	9.5 typ.	75-110
[VDIa]	WG ZBD	1600 typ.	7.2 typ.	330-500
[Gut19b]	MIC ZBD	11000	2.65	82 (BW 17.83 GHz)
[Hro13]	MIC ZBD	2000-6000	14.5-307.5	60-110
[VDIa]	QO ZBD	80-200	12-30	100-1000
[ACS]	QO ZBD	22@70GHz 0.12@1THz	3 min.	50-2500
[Han13]	CMOS-SBD	336	29	280
[Han13]	CMOS-SBD	273	42	860

Waveguide and MIC packaged SBD detectors have reported the highest responsivity and best NEP values [VDIa, ACS]. Nevertheless, they are all based on horns or external antennas and waveguide solutions, which are bulky and difficult to integrate in a planar array. Conversely, Quasi-Optical SBD detectors present lower performance due to the difficulty to have a good antenna-diode matching. Besides, the antenna and lens efficiencies are included in the overall circuit performance. Nevertheless, this approach is more suitable for multi-pixel integration. Recent progress in CMOS (Complementary Metal Oxide Silicon) integrated circuit technology has made possible the integration with Schottky diodes, which means an alternative for the implementation of affordable systems [Zha13]. However, CMOS Schottky diodes are necessarily high barrier diodes that must be biased, which implies a increase in the NEP due to the flicker

noise contribution. Recent research have reported solutions to overcome the NEP variations [Han13, Kim17, Kim17]; however, they are still not competitive with the high performance of GaAs or SiGe technologies [Kim17].

For highly sensitive direct detection applications, the best current solution is to use a zero-bias (ZB) or very low-barrier diode. These diodes feature extremely non-linear IV-behaviour around zero-voltage, which is essential for low-noise electronics [Hes07, Hoe11]. Moreover, ZB diode implies a low R_j value; thus, best coupling can be obtained, which translates into better responsivity and higher video bandwidths. Nevertheless, any Schottky diode could be potentially used as zero-bias detector taking into account that the higher the barrier height, the less sensitive the detector will be to low power input signals. Nonetheless, if the diode is externally slightly forward biased, the barrier height is reduced and the responsivity to small-signals can be improved.

The introduction of a bias control entails a cumbersome inconvenient for the direct detector, in which the main advantages are the simplicity and versatility. However, there are some situations where introduction of a bias circuit is justified. The first one is in high-power applications. When the detector is to be used under high power conditions, the excess noise sources beyond thermal and/or shot noise, such as 1/f or flicker noise must be carefully considered. Low barrier diodes cannot generate significant excess noise at very low input power levels. Notwithstanding, as the input power increases, flicker noise also increases and eventually becomes the dominant noise mechanism [Hes07]; therefore, a barrier diode with external bias may be a comparable option. Still, it is true that this is an unusual scenario for millimetre and sub-millimetre applications where very low radiated powers and very high free space losses are handled. Another case where external bias may be advantageous is in applications with extreme temperature variations. The differential resistance of the Schottky diode is temperature dependent, as well as the saturation current. Zero-bias diode detectors are particularly affected for the temperature variations. A very small bias current may be applied to compensate the decrease in responsivity for very low temperatures. A deeper study of this solution can be found in [Wau96].

For heterodyne detection, Schottky diodes have also been proved to be among the best options for room temperature operation. We can find reference for low-noise Schottky diode THz mixers up to 2.5 THz for planetary and atmospheric science studies [Sob11, Mae10], and high data rate communication system at 300 GHz [Per19]. A comparative table of some room-temperature sub-harmonic mixer performance is given in Chapter 5.

2.4 Submillimetre Direct Detectors based on GaAs Schottky Diodes

There are several research groups engaged in the development of Schottky diodes for diverse uses. However, there are only a few commercial companies able to sell this technology for terahertz range applications. Besides, usually only general characteristics of the fabricated devices are available in the literature. All this complicated the task of assuring a valid comparison between the different technologies.

In this section, the performance of three different planar Schottky diodes will be assessed as possible detector element for the presented dual-band integrated detector. The diodes were selected to cover the diversity of existing technologies. Moreover, the selection criteria were the availability of the information of its lumped elements modelling components as well as the noise power spectral characteristic and flicker noise modelling variables. Two ZB commercial GaAs diodes and a high barrier diode originally designed for mixer applications on a 3 μm GaAs membrane substrate have been considered in the study:

- The first planar Schottky diode chosen for evaluation is the **zero-bias Schottky barrier based on a quasi-vertical structure** that mimics the whisker-contact diodes described in Section 2.2.2. This technology was initially developed at the Technical University of Darmstadt and, afterwards, by the Advanced Compound Semiconductor Technologies GmbH (ACST, Hanau,Germany) [Coj05]. The diode intrinsic parameters used for the analysis are those reported in [Hoe11], which are listed in Table 2.2.

- The second one is a very **low-barrier diode based on VDI technology** [VDIa]. High quality planar Schottky diodes working at millimetre and sub-millimetre wavelength have been fabricated for more than two decades at the University of Virginia, and now at Virginia Diodes Inc. The VDI zero-bias commercial diodes employed is a planar surface etched Schottky barrier diode fabricated in a flip-chip configuration. Available manufacturer information is limited. The parameters for the simulation were obtained from [Hes07, Hro13, Zel13] and are also shown in Table 2.2.

- Finally, the third studied diode is a **surface etched Schottky barrier diode (SC-B) on a 3 μm GaAs membrane** fabricated at the Terahertz and Millimetre Wave Laboratory at the Department of Microtechnology and Nanoscience from Chalmers Technological University. The referred

group has vast experience and relevant research results in the design and fabrication of Schottky diodes, fundamentally for mixer and multiplier applications. A Schottky barrier diode, originally designed for mixer application (varistor diode) will be assessed as SubMMW direct detector. The layout and fabrication technology for this diode can be found in [Dra13]. The 3 μm GaAs membrane technology allows the possibility to fabricate the antenna and the diode integrated on the same substrate and shaping the membrane with any geometry to facilitate the device assembly. Related to this, more information on the membrane shaping is given in Section 3.6. The internal diode parameters employed in the simulations for the three evaluated diodes are summarized in Table 2.2.

Table 2.2: Internal diode parameters for the three assessed Schottky diodes.

Technology	Rs[Ω]	Cj[fF]	n	Is[A]
Quasi-vertical Zero-Bias(QV-ZB)	5.5	31.2	1.21	54×10^{-6}
Low Barrier Surface Channel (SC-ZB)	6	26	1.31	27×10^{-6}
Surface Channel Barrier Diode on 3 μm GaAs membrane (SC-B)	5	56	1.3	24×10^{-14}

2.4.1 Direct Detector Configuration

The schematic circuit for a simple planar SubMMW square-law detector is shown in Figure 2.3. The diode is connected to the antenna terminals in the centre of the antenna-lens. The antenna-lens approach will be introduced in the next chapter. However, the presented analysis is suitable to any planar antenna. A low-pass high/low stepped-impedance filter acts as RF-Choke isolating the RF from the Quasi-DC part of the circuit. For the RF frequencies, the RF-Choke appears as a virtual short circuit providing RF ground to the diode and filtering the harmonics and spurious signals. The antenna with a certain efficiency ($\eta_{ant}(f)$) couples part of the incident RF power received to the diode (P_{in}) as can be seen in the equivalent circuit for RF shown in 2.3(b). Maximum power transfer is achieved when the antenna impedance is the complex conjugate of the diode impedance. The influence of the possible bias circuit is included in the variation of the diode junction resistance.

The equivalent circuit for DC and quasi-DC frequencies can be seen in Figure 2.3(c). Due to the non-linear current-voltage characteristic of the diode, the input power induces a proportional output voltage, which is then recovered through the load resistance, R_L. Finally, these direct detectors are connected to a low-noise amplifier since the level of the detected signals are usually too low. The low frequency bandwidth of the detector is determined by the output low-pass filter network consisting of a shunt capacitor C_L and the output resistance R_L. To evaluate the detector performance, DC and Harmonic Balance simulations with order 3 were performed in ADS [ADS].

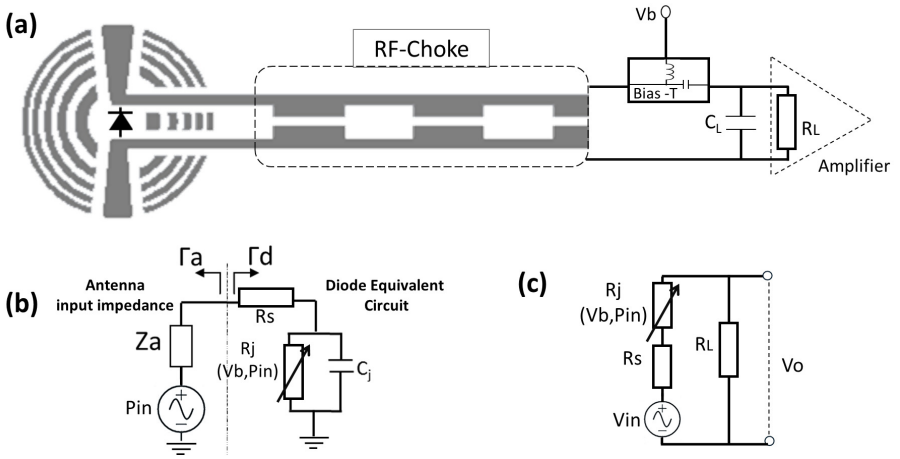

Figure 2.3: (a) Schematic circuit for the direct detector with a single Schottky diode. (b) RF equivalent circuit and (c) quasi-DC equivalent circuit.

2.4.2 I-V Diodes Characteristic

The I-V characteristic curve for the three analysed diodes and the corresponding differential resistance (R_j) are shown in Figure 2.4, where I_D is the forward current flowing through the diodes and V is the applied voltage. The strong nonlinear I-V characteristic at low voltages for both zero-bias Schottky diodes can be observed. Oppositely, for the GaAs membrane diode, the turn-on forward voltage is above 0.8 V as expected from a high barrier Schottky diode.

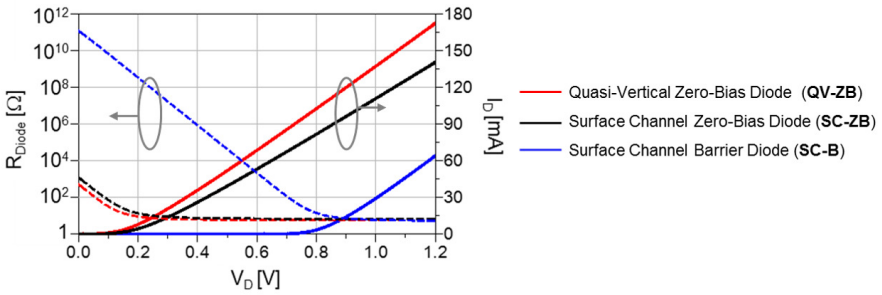

Figure 2.4: DC current (right axis) and diode resistance (left axis) for the three type of Schottky diodes *vs* bias voltage.

The Junction Resistance (R_j), also known as Differential Resistance (R_{diff}), is the relation between the applied voltage and the obtained current in the diode's junction. This is a crucial parameter, which determines the matching capability and the voltage responsivity when loaded by the video circuit. It is derived by simply differentiating the diode I-V response:

$$R_{Diode} = R_s + R_j = \frac{1}{\frac{\partial I_D}{\partial V_D}} = \frac{\partial V_D}{\partial I_D} \qquad [\Omega] \tag{2.7}$$

The QV-ZB Schottky diode exhibits the lowest R_j, which is in the order of 500 Ω for $V = 0$, while for the SC-ZB it is about 1200 Ω for the same voltage. On the other hand, the SC-Barrier diode presents a very high junction resistance (higher than 10^{10} Ω) for low voltages. Nevertheless, applying a forward bias the junction resistance is lowered to values below 1 MΩ for voltages higher than 0.4 V. It is important to highlight that the diode resistance is a function of the current flow through the junction but also depends on the anode size and the Schottky interface. This dependence can be better seen by differentiating

equation 2.1. The larger the anode area, the higher the saturation current (I_s) and the lower R_j. At the same time, bigger anodes lead to lower R_s and higher junction capacitance (C_j).

2.4.3 Responsivity

The responsivity is the ratio between the average increment in the current flowing through the diode (or voltage at the output) due to the application of an RF power to the power that arrives to the detection circuit (P_{in}):

$$\Re_I = \frac{\Delta I_o}{P_{in}} \qquad [A/W] \tag{2.8}$$

$$\Re_V = \frac{\Delta V_o}{P_{in}} \qquad [V/W] \tag{2.9}$$

Low-Frequency Responsivity

The intrinsic RF-to-DC conversion in a diode under low-frequency and low power level, is quantified by the short circuit current responsivity ($\Re_I$). Under square law detection this is defined as half the second derivative of the diode I-V response curvature [Car15]:

$$\Re_I = \frac{\frac{\partial^2 I_D}{\partial {V_D}^2}}{2\frac{\partial I_D}{\partial V_D}} \qquad [A/W] \tag{2.10}$$

This result is derived after some mathematical manipulation of the Taylor expansion of the IV-function (equation:2.1). The demonstration can be found elsewhere [Cow66].
Likewise, the **intrinsic low frequency, low power open circuit voltage responsivity** ($\Re_V$) relates the variation in the diode voltage to the applied power level and the intrinsic short circuit current responsivity:

$$\Re_V = \Re_I R_j = \Re_I \frac{\partial V_D}{\partial I_D} = \frac{\frac{\partial^2 I_D}{\partial {V_D}^2}}{2(\frac{dI_D}{dV_D})^2} \qquad [V/W] \tag{2.11}$$

Figure 2.5 shows the maximum intrinsic current and open voltage responsivities from equations 2.10 and 2.11 for the three evaluated diodes. The current responsivity (Figure 2.5(a)), in an ideal Schottky diode without external bias at 300 K is obtained with $\eta = 1$ and it is $\Re_I = q/(2\eta k_B T) = 19.3\ A/W$. Consequently, since the diodes studied here present similar η values (1.21 and 1.3), comparable current responsivities about 15 A/W are obtained. Moreover, for the Zero-Bias diodes the maximum current responsivity is achieved at values near 0 V, whereas for the SC-Barrier diodes it can be obtained in a wide voltage range.

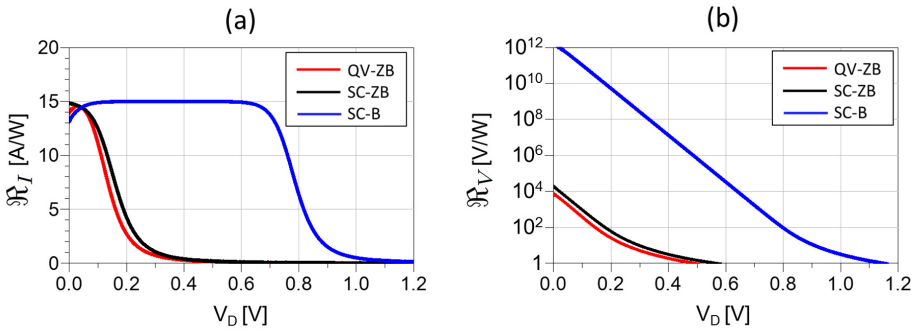

Figure 2.5: Low frequency, low power (a) Internal current responsivity. (b) Internal voltage responsivity.

The open circuit voltage responsivity (as its name implies) assumes that the rectifier circuit is loaded with an impedance much higher than R_j. This parameter can be seen in Figure 2.5(b) where intrinsic responsivities higher than 10^9 are obtained for the SC-Schottky barrier diode with low voltage values. Nevertheless, this is not a realistic approach. The input impedance of the voltage amplifier that must be connected at the detector output rather can be higher than 10 MΩ, and in that case, the bandwidth of the detector output will be very limited.

High-Frequency Responsivity

The definition of $\Re_I$ given in equation (2.10)was driven from the DC I-V response and assumes that all the input RF power is absorbed by R_j. However, a portion of this power is dissipated in the parasitic impedance C_j and R_s and only the high frequency power absorbed in the junction is the one that contributed to the increment in the output current (or voltage difference). Taking into account this RF power transfer degradation, the low level current responsivity of a Schottky diode was found to be [Cow66]:

$$\Re_{I_{RF}} = \Re_I \frac{1}{(1+\frac{R_s}{R_j})(1+(f_{RF}/f_c)^2)} \tag{2.12}$$

By including the RF power transfer degradation some interesting results can be noted. The last term (f_{RF}/f_c^2) contains the frequency dependence. The responsivity decreases with the increase of the RF frequency. It seems logical, since the impedance of the parasitic junction capacitance decrease inversely with the increase of the frequency up to a point where it will short-circuit the junction. In the same way, an increase of the parasitic impedances R_s and C_j result in a degradation of the responsivity.

For a detector as the one presented in Figure 2.3, based on voltage read-out the representative measurable value is the loaded voltage responsivity, which is the ratio of the increase in the video output voltage (ΔV_{OL}) to the input power in the detection circuit (P_{in}) for a certain output load (R_L):

$$\Re_{V_L} = \frac{\Delta V_{OL}}{P_{in}} \qquad [V/W] \tag{2.13}$$

The relation between these parameters leads to the typical output voltage *vs* input power transfer curves shown in Figure 2.6 for two output load impedances (1 kΩ and 1 MΩ). The square-law detector regimen implies that the output voltage is directly proportional to the input power. From Figure 2.6 it can be seen that the ZB Schottky diodes work in square law detection regimen for input powers below -20 dBm. Conversely, the high barrier diode must be biased to obtain measurable output voltage values working as square-law detector. Besides, from comparison between Figure 2.6 (a) and (b) it can be intuited that the loaded voltage responsivity also depends on the output load (R_L). Further analysis about this behaviour are presented in next sections.

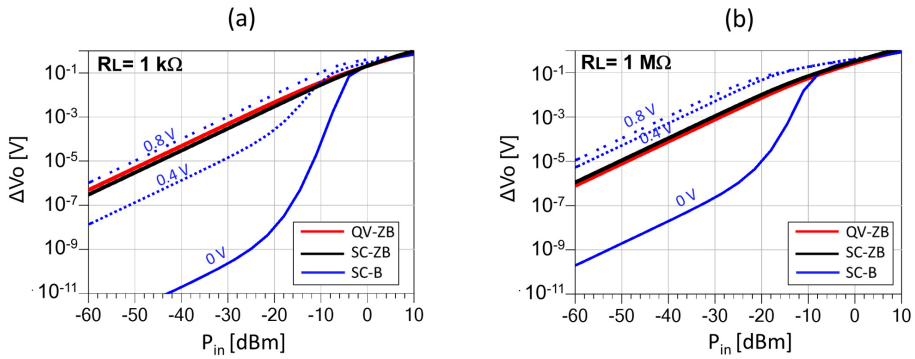

Figure 2.6: Detector transfer curve. (a) Output load impedance equal to 1 kΩ and (b) 1 MΩ.

2.4.4 Low-Frequency Matching

To maximize the loaded voltage responsivity two impedance matchings must be considered. The first one is the RF matching, which allows all the input power available at the antenna terminals to be delivered to the diode. Detailed explanation of this matching can be found in Section 2.4.5. The second one is the low frequency amplifier section matching. For DC or low frequency detection, the output voltage will be the result of a voltage divider between the diode resistance and the output load resistance (see Figure 2.3(c)). Thus, to maximize the output voltage, the video resistance must be higher than the junction resistance.

Figure 2.7 presents the loaded voltage responsivities for different output loads (R_L) sweeping the input power from -60 dBm to 0 dBm without external bias for the three analysed Schottky diodes with 300 GHz RF frequency and assuming perfect RF matching.

For the ZB diodes (Figure 2.7 (a and b)), the responsivity exhibits a linear response, with constant responsivity for input powers below -20 dBm. This is an indirect verification of the square-law detector transfer curve where the magnitude of the output voltage is proportional to the magnitude of the RF input power. Above -20 dBm, the ZB detectors start to work in the linear regimen and the responsivity decreases. On the contrary, the surface channel barrier diode cannot be used without external bias for signals lower than -20 dBm as can be seen in (Figure 2.7 (c)).

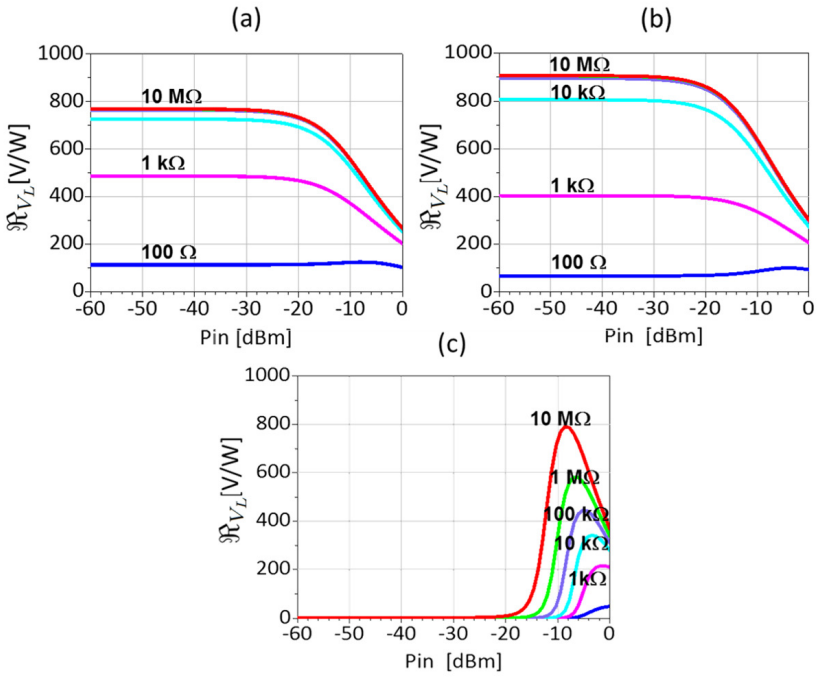

Figure 2.7: Loaded voltage responsivity *vs* input power (P_{in}) assuming RF matching with f_{RF}=300 GHz and $V_b = 0$. (a) QV-ZB. (b) SC-ZB. (c) SC-B.

If the final detector application requires recovering of large video bandwidth, such as the detectors presented in [Mon13], the R_j impedance must be lower than the one of a low impedance amplifier (i.e 10 kΩ). For those applications, the low R_j of low-barrier and zero-bias diodes, namely the zero-bias ACST and VDI diodes, offers much better coupling possibilities as can be seen in Figure 2.7(a and b). Nevertheless, the differential resistance of the SC-barrier diode can be lowered by applying an external DC bias. The loaded voltage responsivity for the SC GaAs membrane diode-based detector can be optimized for a certain forward bias and for an output load as can be seen in Figure 2.8. In contrast, for the ZB diode the best responsivity results are achieved without external bias.

From Figure 2.8 we can be also seen that biasing the detector, the voltage responsivity may be raised to be ten times higher than the one obtained with zero-bias detectors.

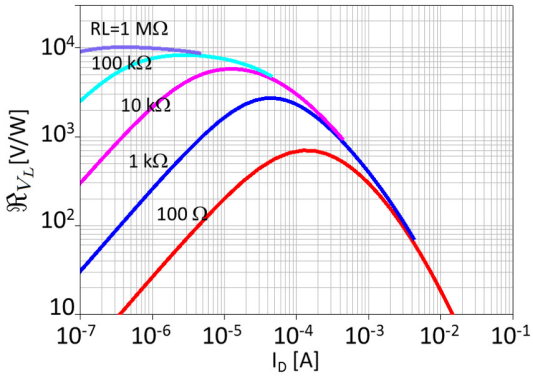

Figure 2.8: Loaded voltage responsivity *vs* I_D at f_{RF} = 300 GHz (with RF matching condition) and P_{in}=-30 dBm for the SC-barrier GaAs membrane diode-based detector.

However, optimization of the responsivity implies a trade-off since it is proportional to the resistance, and so is the white noise [Dec16]. As it is known, introduction of a bias current implies the outcome of the flicker noise, which degrades the final noise detector performance. The analysis of the noise in the detector is given in Section 2.4.6.

2.4.5 RF-Frequency Matching

Getting back to the RF analysis of the submillimetre Schottky diode-based detector, the equivalent circuit for the antenna connected to the diode for RF frequencies was shown in Figure 2.3(b). The optimum condition (i.e maximum responsivity) is achieved when the antenna impedance (Z_a) compensates the real and imaginary part of the diode impedance. This is the conjugate matching condition, which states that the maximum power transferred to the load is achieved when $Z_a = Z_d^*$. The parameter that characterizes the mismatching factor is known as M-factor and is defined as the ratio between the power delivered to a load (P_L) and the maximum power available from a generator (P_{avs}) [Col07], equation 2.14

$$M = \frac{4R_d R_a}{(R_a + R_d)^2 + (X_a + X_d)^2} \tag{2.14}$$

where $Z_a = R_a + jX_a$ is the antenna input impedance and $Z_d = R_d + jX_d$ is the diode impedance.

For the three Schottky diodes exemplifications the input impedance can be seen in the Smith Chart in Figure 2.9. The plotted impedances only take into account the parameters directly associated with the Schottky junction (R_s, C_j and R_j). The submillimetre frequency range is plotted from 300 to 500 GHz for a fixed P_{in} = -30 dBm. Besides, for the GaAs membrane diode, the impedances are plotted including different bias voltages in the range from 0 to 0.8 V. It can be seen the reactive behaviour in all diode impedances (very high capacitive impedance values) and the inductive input antenna impedances that satisfies the matching condition ($Z_a = Z_d*$).

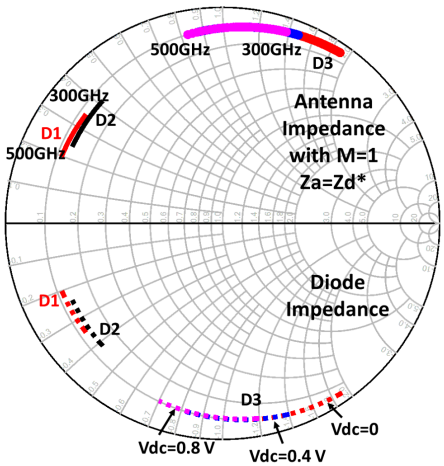

Figure 2.9: Diodes impedances (Z_d) and antenna input impedance ($Z_a = Z_d*$) for M=1. D1 represents the QV-ZB diode, D2 is the SC-ZB diode and D3 is the SC-B GaAs membrane diode.

Finally, another interesting study about the antenna input impedance requirements can be obtained from the Load-Pull analysis of the detector. The input impedance of the antenna can be swept in the Smith Chart to obtain circles with constant responsivity for different output load or different RF frequency as can be seen in Figure 2.10. This way it is easy to determine the range of variation in the input impedance of the antenna to achieve a certain required responsivity.

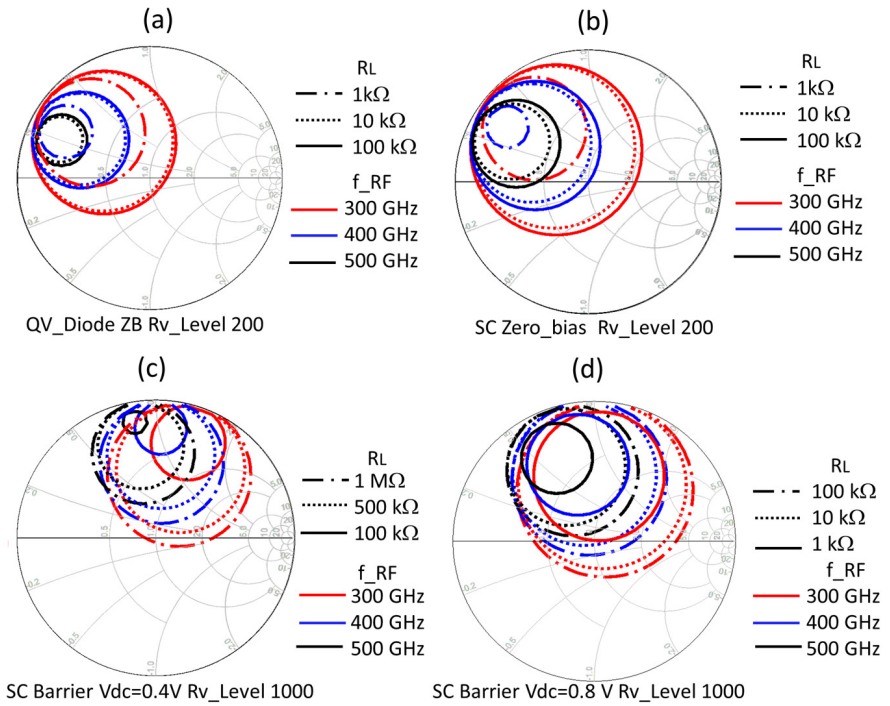

Figure 2.10: Load-pull analysis of the Schottky diode-based detectors for different RF frequencies and output load impedances (P_{in}=-30 dBm). (a) QV-ZB with constant responsivity equal to 200. (b) SC-ZB with constant responsivity equal to 200. (c and d) SC-B with constant responsivity equal to 1000 and bias voltages equal to 0.4 V and 0.8 V respectively.

The constant responsivity curves for the QV-ZB and the SC-ZB diodes shown in Figure 2.10 (a and b) describe the range of input impedances to obtain constant resonsivity equal to 200 V/W. It can be seen that for higher frequencies the circles become smaller, which is in line with the expected degradation of the responsivity with the frequency increase. Moreover, Figure 2.10 (c and b) present the 1000 V/W constant responsivities curves for the SC-B diode biased by 0.4 and 0.8 V respectively. As outlined above, higher responsivities can be obtained by properly biasing the diode. It can be observed that this approach could present responsivity higher than 1000 V/W in a broad frequency range.

2.4.6 Noise Equivalent Power

The parameter that is typically employed to characterize the minimum detectable power of a submillimetre direct detector is the Noise Equivalent Power (NEP), which can be defined as the incident power on the detector generating an output signal equal to the noise output (i.e. $S/N = 1$ for a bandwidth of 1 Hz or $S/N = 1$ after 0.5 second of integration time) [Bah03]. This normalization to 1 Hz bandwidth allows comparing different detector technologies for different applications. Nevertheless, even when it is a very common metric, there is some ambiguity given the different definitions and calculation methods used to describe it [Lec07].

Depending on the read-out circuit employed, i.e. whether the change in voltage or current is measured the NEP is defined as the ratio of the noise spectral density of the rectified signal (at DC or a low modulation frequency) expressed in units of $A/\sqrt{Hz}$ or $V/\sqrt{Hz}$, to the device responsivity expressed in units of A/W or V/W, respectively [Mac15].

$$NEP = \frac{i_N}{\Re_I} \qquad [W/\sqrt{Hz}] \tag{2.15}$$

$$NEP = \frac{v_N}{\Re_{V_L}} \qquad [W/\sqrt{Hz}] \tag{2.16}$$

Besides, Electrical NEP and Optical NEP must be distinguished. The electrical NEP refers to the signal power portion that is absorbed by the detector (power at the input of the detector (P_{in}) and it is determined by the noise sources (namely, thermal, shot and flicker noise). On the other side, the optical NEP (sometimes named system NEP) is equal to the ratio of the electrical NEP and the coupling efficiency of the detector system [Lec07]. Including the quasi-optical elements and the antenna in the NEP study, is evident that from the

available power of the signal (P_{av}) the power that is accepted by the detection circuit (P_{in}) depends on the antenna efficiency η_{ant} as well as the antenna-diode coupling factor (M). Further analysis will be focused on the Electrical NEP considering the antenna and the diode perfectly matched.

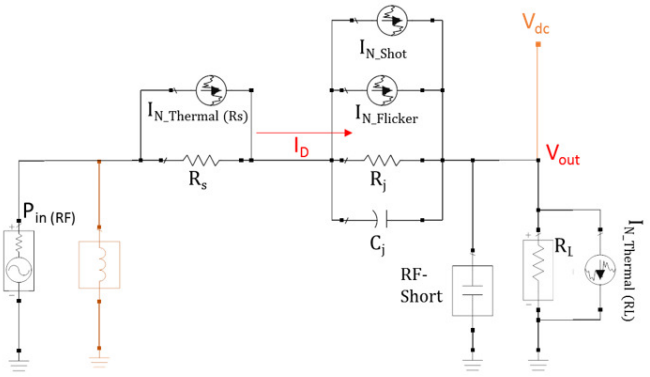

Figure 2.11: Simplified scheme of the Schottky diode based detector including the main noise current sources.

$$v_{out\ (Shot)} = \sqrt{2qI_D R_j^2}\frac{R_L}{R_{diode}+R_L} \tag{2.17}$$

$$v_{out\ (Thermal\rightarrow R_s)} = \sqrt{4k_B T R_s}\frac{R_L}{R_{diode}+R_L} \tag{2.18}$$

$$v_{out\ (Thermal\rightarrow R_L)} = \sqrt{4k_B T R_L}\frac{R_{diode}}{R_L+R_{diode}} \tag{2.19}$$

$$v_{out\ (Flicker)}(f) = \sqrt{K_f \frac{I_D^{a_f}}{f^{b_f}}}\frac{R_L}{R_{diode}+R_L} \tag{2.20}$$

$$v_{outTotal}(f) = \sqrt{|v_{Shot}|^2 + |v_{Ther\rightarrow R_s}|^2 + |v_{Ther\rightarrow R_L}|^2 + |v_{Flick.}(f)|^2)} \tag{2.21}$$

Figure 2.11 shows the schematic circuit with the corresponding dominant noise current sources that can be used to predict the low frequency noise response of a direct detector based on a Schottky diode.

The flicker and shot noises generated by the junction resistance, the thermal noise in the series resistance and an external thermal noise associated with the load resistance constitute the dominant noise contributors. The nature of these main noise mechanisms were explained in Section 2.2.1. Assuming all the noise mechanisms to be incoherent, the total voltage noise (v_{out}) at the output can be obtained from the individual evaluation of each source followed by the quadratic sum of all the isolated contributions (equations: 2.18-2.21).

For the ZB Schottky diodes, it is usually accepted that the noise voltage can be driven from the composition of only the shot-noise noise associated with R_j and the thermal noises [Bah03]. However, the previous assumption in only valid if the forward current flowing in the diode is so low that the shot noise dominates the overall noises or the low frequency detected signal (also video frequency or modulation frequency) is higher than the noise corner frequency.

In the same way, when the SC-B diode is biased the noise sources related with the fluctuation of the numbers of the forward current carriers due to imperfections in the junction materials cannot be obviated. On this matter, the flicker noise (or $1/f$ noise) contribution is particularly important. Seeing that, it is fair to say that the flicker noise also appears in the ZB detectors when the input power increases, which implies higher forward current flowing in the diode. And what is more, the flicker noise will become dominant for high input powers even for ZB diodes. That is why a NEP parameter characterization as a function of the forward current in the diode, including the contribution of this flicker noise may be far more useful than the normalized NEP with zero RF power, which is the most employed parameter in the literature for different SubMMW detector comparison.

The way of including the $1/f$ noise contribution in microwave detectors is by adding of the term f_n/f_V in the total spectral noise density [Cow66], where f_V is the low modulation frequency and the noise corner frequency (f_n) is the frequency at which the mean square shot and flicker noise are equal. This last one is an specific value difficult to find in any data-sheet of millimetre and submillimetre commercial diodes. Oppositely, it is a well-known magnitude in microwave applications. The reason may be that this magnitude depends on the intrinsic properties of the metal semiconductor junction, namely, the thickness of the layers, the doping and the impurities or defects in the structures, which may vary during fabrication. Different devices with the same layout may present variations in the corner frequency value. Finally, the estimation of the corner frequency lies in a direct measurement of the device, which requires a specific and advanced setup that may not be always available.

A modelling concept for the QV-ZB diode structure of ACST GmbH for prediction of the 1/f-noise in the millimetre-wave range was presented in [Hoe13]. The K_f and a_f values that characterize the 1/f noise (see equation 2.6) obtained from the spectral noise voltage density measured for different bias current applied to a discrete diode were 0.5 and 4 respectively. Moreover, in the cited investigation the b_f parameter was assumed to be equal to 1.

Similarly, the signal-to-noise ratio of VDI zero-bias detectors was measured as a function of input power and modulation rate in [Hes07]. The conclusions from this study are that the flicker noise factor increases roughly linearly with the applied power and in large signal applications this noise becomes increasingly significant. Then, modulation is required to achieve optimal sensitivity. Again, the results confirmed that measurements or calculation of zero-bias NEP is not sufficient to characterize their performance in the broad range of applications where higher power levels are likely to be encountered [Hes07]. Moreover, in [Zel13], a detailed study of the noise in VDI technology Schottky diodes and a modelling approach for its accurate simulation can be encountered. From the voltage noise spectrum presented in the referred work for a ZB-Schottky diode (i.e. which is the SC-ZB employed in the presented comparison), the K_f, a_f and b_f parameters that accurately predict the 1/f noise are 2.11×10^{-7}, 2.57 and 1.039, respectively.

Lastly, for the SC-B GaAs membrane diode technology, we did not have any previous references for the flicker noise frequency values. Thus, the noise spectral density was measured employing the Advanced Low-frequency Noise analyser E4727A from Keysight. The summarized result from the spectral current noise density versus modulation frequency, measured with different bias currents (I_{dc}) can be seen in Figure 2.12. As expected, the low frequency spectrum is dominated by the flicker noise presenting approximately a $1/f$ behaviour.

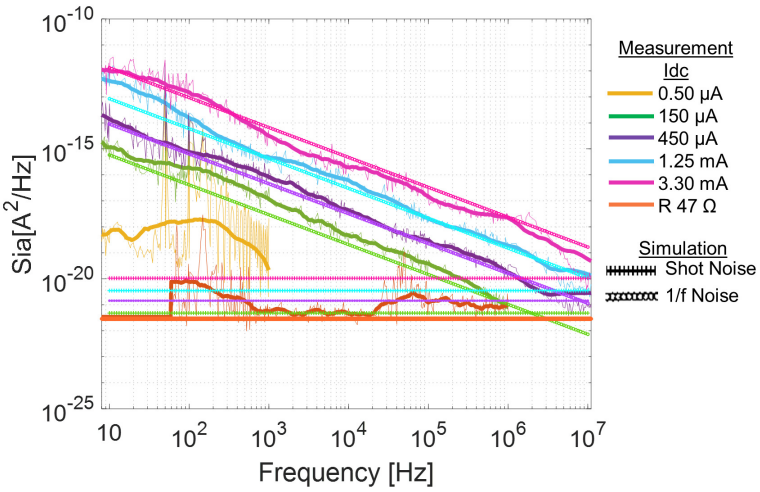

Figure 2.12: Measured current spectral density of the SC-B GaAs membrane Schottky diode with different DC bias currents (continuous line). Simulated results for the flicker noise (circle markers) and shot and thermal noises (plus symbol markers) are also included. A 47 Ω resistance was measured for reference and calibration (orange line).

From the previous measurement, the thermal and shot noise contributions were subtracted to the measured data to isolate the measured flicker noise ($i_{N_{Flicker}} = i_{N_{Total}} - i_{N_{White}}$). Afterwards, a curve fitting procedure was performed in Matlab to obtain the K_f, a_f and b_f parameters that better emulate the measured results. The simulated results for flicker noise with the best fitted values ($K_f = 2 \times 10^{-5}$, $a_f = 2.5$, and $b_f = 1.15$) can be also seen in Figure 2.12 (circle markers). Moreover, the simulated current spectral densities associated with the shot and thermal noises are shown as plus symbol markers.

Finally, for the three diodes, the noise corner frequency values (f_n) as a function of the current were obtained by equating the expressions for average flicker noise and shot noise densities:

$$< i^2_{N_{Flicker}} >= k_f \frac{I^{a_f}}{f^{b_f}} =< i^2_{N_{Shot}} >= 2q(I_D) \tag{2.22}$$

Figure 2.13(a) resumes the parameters used for modelling the flicker noise,

(a)

I_f Modelling Parameters

	k_f	a_f	b_f
QV_ZB	0.5	4	1
SC_ZB	2.11e-07	2.57	1.039
SC_B	3e-05	2.5	1.15

(b)

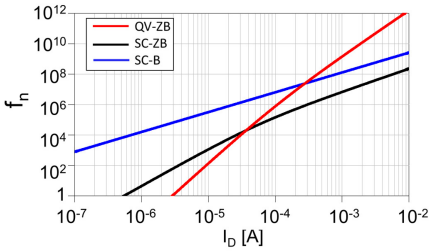

Figure 2.13: (a) Modelling parameters of the 1/f noise for the studied diodes. (b) Calculated noise frequency corner (f_n) *vs* I_D.

whilst Figure 2.13(b) shows the corner frequencies f_n dependence with the forward current for the three analysed diodes. It is interesting to note that the flicker noise behaves partly different in the multiple assessed technologies. The SC-B curve exhibits a lower slope since the b_f value is slightly higher than one. Similar results have been reported in [Zel13] where the $1/f$ noise in a VDI high barrier GaAs based diode was studied.

By including the modelling parameters of the flicker noise in equation 2.21, all the individual noise contributions can be assessed. Figure 2.14 shows the comparison of the isolated noise voltages contributions at the detector output, assuming a load resistor of R_L=10 kΩ, for the three studied diodes. Furthermore, the flicker noise frequency dependence is shown in Figure 2.14(c) where the spectral flicker noise density at the output of the detector is evaluated for different modulation frequencies. From this result, the inverse dependence of the flicker noise with the low frequency modulation can be also substantiated. On the other hand, the spectral voltage thermal and shot noises are frequency independent.

From the comparison of all the individual contributions it can be also seen that, for very low I_D values, the dominant noises are the thermal noise from the output load (green curve) and secondly, the shot noise. However, with the increase of the forward current the flicker noise quickly becomes the dominant contributor.

Lastly, the NEP as a function of the forward current in the diodes was also simulated and the results can be seen in Figure 2.15. The predicted NEP is obtained for the realistic voltage responsivity values derived in Figure 2.7 and 2.8 with a constant RF input power of -30 dBm and f_{RF} = 300 GHz. The

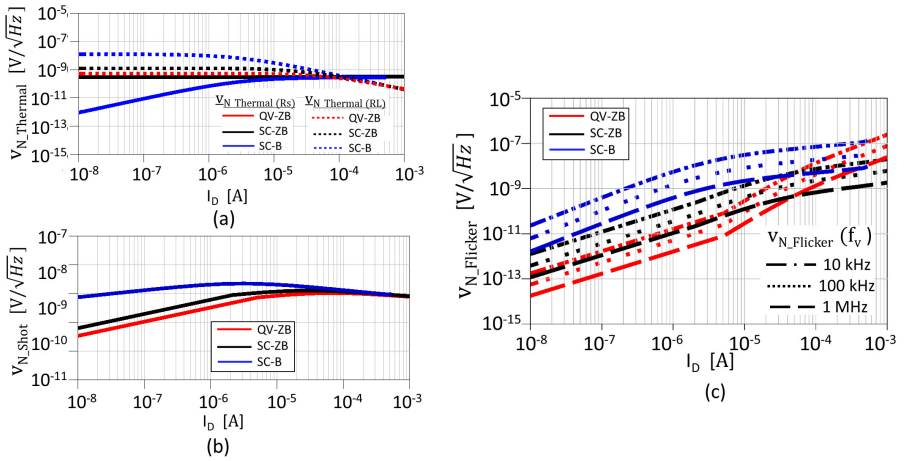

Figure 2.14: Individual contributions of the spectral noise voltage sources at the detector output with R_L=10 kΩ. Spectral noise voltage of the: (a) Thermal noise sources R_S and R_L. (b) Shot noise source, (c) Flicker noise source for three modulation frequencies: 10 kHz, 100 kHz, and 1 MHz.

external load impedance (R_L) is 10 kΩ, whilst the low frequency was evaluated for modulations of 10 kHz, 100 kHz, and 1 MHz. Under low bias current conditions (or for zero-bias with low input power), the simulated for the QV-ZB diode and for the SC-ZB is the same that the one obtained if only the white noise sources would be included. That is because the contribution of the flicker noise for very low forward current is negligible. Nevertheless, as previously noted, if the current flowing through the diode increases, the flicker noise contribution becomes the main noise source in the detector. Besides, in a ZB Schottky diode the responsivity decreases with the I_D increase. Thus, these two factors, when combined, translate in the observed fast NEP degradation for high power levels (or high forward rectified current).

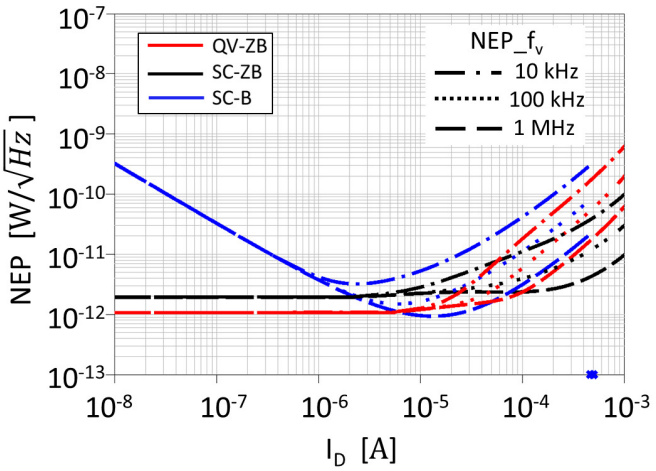

Figure 2.15: Estimated NEP *vs* I_D, f_{RF}=300 GHz, P_{in} = −30 dBm and R_L=10 kΩ at 0.1 kHz, 1 kHz, and 10 kHz modulation frequencies.

Other important interpretation is that the degradation of the NEP with the increase of I_D is higher for low modulation frequencies. From Figure 2.12 and 2.14 can be seen that the measured noise is lower at higher modulation frequency since the contribution of the 1/f noise is negligible for frequencies higher than the noise corner, where the noise is dominated for the shot and thermal noise.

For the SC-B GaAs membrane diode, the NEP follows the inverse of the voltage responsivity curve (see Figure 2.8). At 10 kHz modulation frequency, the high 1/f noise level considerably degrades the overall NEP. Conversely, for higher modulation frequencies and I_D values around the optimal bias point, which implies maximum responsivity, the 1/f noise is inconsequential leading to the NEP values even better than those obtained with the ZB diodes. Nevertheless, with the further increase of I_D above 20 μA, the decrease in responsivity and the increase of the flicker noise dominate again the overall NEP performance.

2.5 Conclusions

Among all the technologies used for uncooled MMW and SubMMW detection, those based on Schottky diodes are particular attractive due to their simplicity and versatility. In this chapter, three commercial GaAs Schottky diodes based on different fabrication technologies have been assessed as detector elements in a planar direct detector configuration. The comparison entails several fundamental parameters such as: loaded voltage responsivity, low-frequency and RF-frequency matching capabilities and variation of the NEP as a function of the input power (or the forward current) and the modulation frequency.

The diodes employed for the comparison were selected for the availability of its spectral noise information (either reported in the literature or measured by ourselves). This allows us to include the flicker noise contribution in the calculation of the NEP.

As expected, for a very low frequency modulation (as could be the case of a passive imaging application), the low-barrier (or the "zero-bias") diodes exhibit reasonable NEP values in the order of $pW/\sqrt{Hz}$. The high-barrier diode must be biased to operate as square-low detector under low input power condition. The flicker noise induced by this current is translated into a degradation of the NEP. However, in a high input power scenario, the NEP of low-barrier diodes could be even more affected by the flicker noise contribution. Conversely, for modulation frequencies higher than the noise corner frequency and for applications where high impedance output resistance and external bias can be employed, the superior loaded responsivity of the high-barrier diode implies that lower NEP could be obtained.

Chapter 3

Integrated Detectors for Submillimetre and Infrared Waves

3.1 Introduction

The possibility of integrating submillimetre and infrared detectors opens up new possibilities in different fields such as multispectral imaging, or simultaneous observation of different phenomena in radioastronomy, to name a few. Imaging applications would benefit from the higher resolution provided by the IR range, which will be complemented by the higher penetration through obscurations of the THz frequencies. This type of receiver would be the base for imaging cameras which would be the THz/IR counterpart of the Visible/IR cameras, where both types of images are fused. Finally, a single integrated device working at different wavelengths is widely desirable from the point of view of overall size and weight in any application.

Fresnel Zone Plate Lenses (FZPL) have been successfully employed to focus electromagnetic radiation over a wide frequency range from radio waves [Wil99, Hri00] to X rays [Nie74]. Specifically, in the IR range a conventional FZPL was designed to focus IR radiation onto a single antenna-coupled microbolometer enhancing its detection properties [Gon05]. Based on those results and taking advantage of the size of the FZPLs in the IR range, it was theoretical proposed that the IR lens could be reconverted in an spiral antenna working at

submillimetre waves [Ald09]. A variation of such detector configuration based on a square Fresnel lens-Square spiral antenna was latter studied in [Eta14].

The main objective of the presented study is the design and characterization of feasible subMMW wave antennas for a dual-band device with the double purpose of detecting THz radiation and acting as FZPL for an IR detector. For the study and characterization of the dual-band device, the combination of analytical and commercial software based solution was employed. The antenna-lens system at IR frequencies is an electrically very large structure ($> 120\lambda_{eff}$). That is why numerical analysis based on Kirchhoff Diffraction Theory was used for the lens analysis at IR frequencies, whereas a 3D full wave simulator (HFSS) was used for the SubMMW waves simulations. Final simulations of the sub-MMW detector were based in a combination of non-linear analysis in ADS with 3D full wave simulations (HFSS).

3.2 Proposed Approach

The proposed detector, shown in Figure 3.1, consists of a Si (silicon) slab where both detectors, namely the SubMMW and IR detectors, are printed on its opposite faces. On the top face, a detector based on a printed planar antenna working at SubMMW frequencies (300-500 GHz) acts as a modified FZPL in the IR band. The planar lens focuses IR radiation (∼28 THz) onto the IR detector , which is located on the opposite face, enhancing its detecting properties. The focal lens of the FZPL must correspond to the thickness of the silicon slab, in this case 380 μm. The IR detector can be an antenna-coupled micro-bolometer as the one shown in Figure 3.1. Nevertheless, the IR detector will be treated as a generic element whereas all the research and effort will be focused on the design and optimization of modified subMMW antennas able to serve the double function.

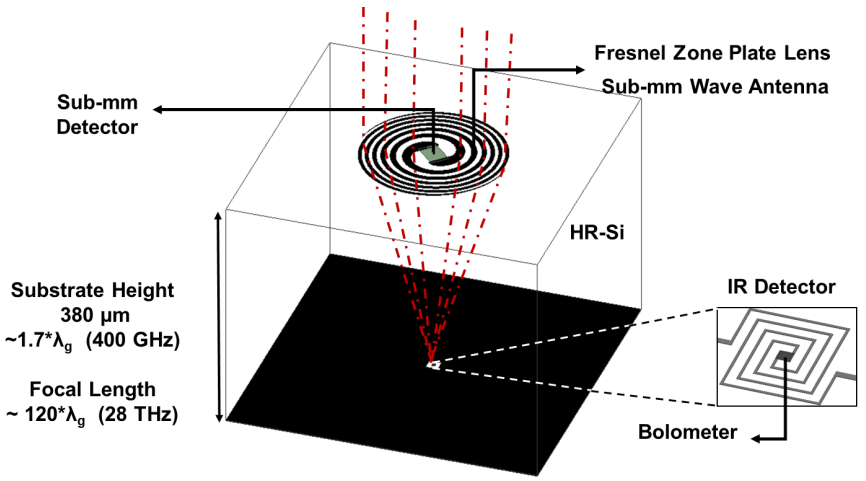

Figure 3.1: Schematic of the proposed SubMMW-IR detector.

In the final configuration, the modified antenna would be connected to a SubMMW detector element. The choice of the detection technology completely depends on the final application requirements. Nevertheless, both the analytical study of the IR lens and the characterization and simulation of different kinds of modified antennas suitable for the dual purpose operation can be applied

to several uncooled and cooled detectors (e.g. SIS, HEB, SBD, CMOS based technology). Finally, the subMMW detector presented as a proof of concept is a generic uncooled detector based on a Schottky diode.

The dimensions of the antenna and thus, its operational frequency, will be determined by the number of zones (M_t) and the focal length (F) of the lens. For a large number of Fresnel zones, we can obtain a higher efficiency lens and a lower frequency antenna; conversely, the smaller the number of zones, the higher the antenna frequency and the lower the focusing gain. However, since the metal zones become narrower when the lens order increases, the total number of zones will be limited by the resolution of the fabrication process. The focal length is chosen to be the thickness of the silicon slab. However, there is also a trade-off for this parameter between the best lens and antenna performance. For a fixed M_t, when F increases, the focus gain also improves, up to a limit given by the feed pattern properties. However, from the antenna point of view, the excitation of surface-wave modes in the substrate will be larger for thicker substrates and, hence, the radiation performance will worsen.

3.3 Fresnel Zone Plate Lenses Overview

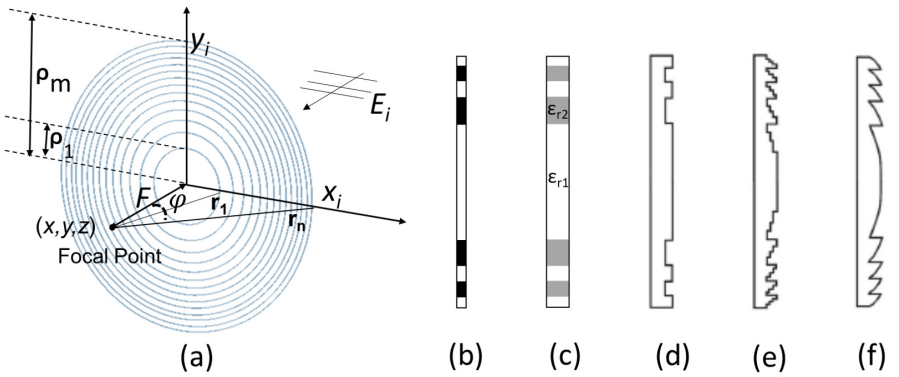

Figure 3.2: (a) 3D perspective view of the Fresnel zone rings. Profile (2D) views of: (b) Amplitude binary Fresnel zone plate (Soret Lens). (c) Multi-dielectric zone plate. (d-f) Phase—correcting zone plate lenses, (d) two-level (phase reversing zone plate) (e) Multi-level zone plate (the figure shows specifically the P=4 discretization level). (f) Kinoform-continuous phase profile (Fresnel diffractive lens).

Fresnel zone plate (FZP) lenses consist of a set of concentric annular zones where the successive radii are designed so that the distance from the focal point (F) to each ring increases by a value λ/P when going from the inner to the outer radius of any zone (Figure 3.2(a)). The variable P ($P \geq 2$) indicates the phase difference between two consecutive Fresnel zones, as in each subzone m, the phase is changed by $2\pi/P$ relative to the phase in the neighbouring subzone. The radius of the m^{th} ring (ρ_m) required to focus the radiation at a focal distance F can be determined from well-known geometric considerations [Hri00]:

$$\rho_m = \sqrt{\frac{2mF\lambda}{P} + \left(\frac{m\lambda}{P}\right)^2} \qquad m = 1, 2, ...M_t \tag{3.1}$$

where λ is the operational wavelength and M_t is the total number of zones.

Two general approaches can be distinguished to perform the Fresnel zones based on the modelling of two physical quantities: the amplitude $A(x, y)$ (Figure 3.2(b)) and the phase $\phi(x, y)$ (Figure 3.2(c-f)) of the electromagnetic field. Regarding the first one, amplitude modulation elements create binary amplitude profiles where the part of the radiation that does not contribute to constructive interference is blocked. The Soret Lens is the simplest one in this flat lens family. It consists of alternating opaque and transparent Fresnel zones which are obtained by printed metallic rings on a dielectric substrate. The main drawback of Soret lenses is their low transmission efficiency due to the high reflections caused by the opaque zones. These reflections reduce the focus intensity by a factor of π^2 (w.r.t a converging lens). Besides, they exhibit narrow bandwidth since this parameter is inversely related to the number of zones. Nevertheless, compared to conventional refractive focusing elements, there are plain benefits in their use, such as their low cost, ease of fabrication and reduced thickness. As a matter of fact, efficiency and bandwidth are exchanged for the improvement in size and weight.

Oppositely, in phase-correcting zones lenses, the opaque/transparent zones are replaced by configurations that introduce a certain phase delay whilst the radiation is transferred by all the zones (Figure 3.2 (c-f)). One way to obtain the phase correction is by combining different dielectrics materials (3.2 (c)) or, as in a more recent research [Pou18], by modifying the material porosity to change the effective material permittivity in a homogeneous medium, controlling the intended permittivity distribution in the lens surface. The phase delay can be also accomplished by removing dielectric rings from a dielectric slab as can be seen in Figure 3.2 (d-f). In each grooved full-wave zone a stair with equal steps (P steps) is created and the height (h_p) of each step is calculated by [Hri00]:

$$h_p = \frac{\lambda_0}{P(\sqrt{\epsilon_r} - 1)} \tag{3.2}$$

Compared with Soret lenses, phase lenses present much higher efficiency which increases with the number of phase correcting zones. For example, the aperture efficiency of the Soret lens is barely 10%, whereas for a reversal phase-lens($P = 2$) is 40.4% and for $P = 16$ it is 99% [Sie19]. Nevertheless, they are more sensitive to surface errors which cause phase disturbance, require a more difficult fabrication process and have higher production costs.

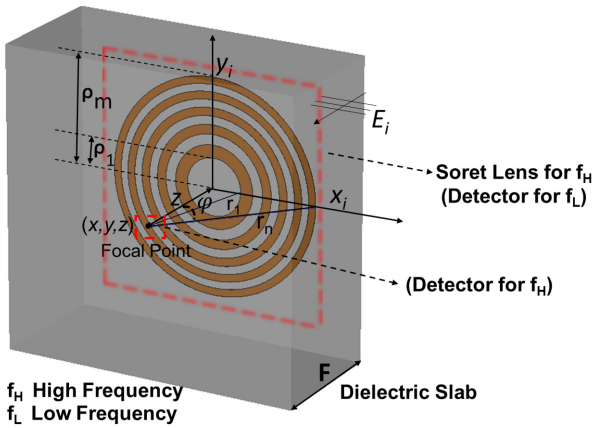

Figure 3.3: Geometrical configuration of the Amplitude Binary (Soret) Lens on a dielectric slab.

Planar Fresnel Lens Simulation Techniques

Different techniques have been proposed to study the Fresnel zone plate lenses, from the simplest geometric only based methods [Bus61] to full-wave electromagnetic analysis based solutions [Rei06]. The first approach is suitable for optics, where we deal with very large focal numbers ($f_{\#} = F/D$). However, this method does not provide an adequate answer for the microwave and millimetre wave ranges, where F/D tends to be smaller. An intermediate solution can be achieved by employing scalar Kirchhoff's diffraction (KD) theory [Hri00]. According to this, for the case illustrated in Fig. 3.3, when a plane wave impinges normally on the lens aperture the field contribution of the transmission from the transparent zones of the plate at a certain distance (z) can be obtained as:

$$\begin{aligned} E_n(x,y) &= \frac{i}{\lambda}\iint E_0(x_i,y_i)\frac{e^{-i\beta r}}{r}I(\phi)dx_i dy_i \\ r &= \sqrt{(x-x_i)^2+(y-y_i)^2+z^2} \end{aligned} \tag{3.3}$$

where $E_0(x_i, y_i, 0)$ is the electric field distribution at the plane of the lens, $I(\phi) = 0.5 * (1 + cos(\phi)) = 0.5(1 + z/r)$ is the Huygens's source inclination

factor, β is the propagation constant, and r is the ray coordinate (i.e. the distance from any point (x, y, z) in a z-plane with respect to another point in the lens plane $(x_i, y_i, 0)$). This solution assumes that the incident EM field is perfectly reflected in the opaque zones and transmitted in the transparent zones. This assumption might lead to an inaccurate solution for short focal lengths. A more rigorous result, which includes the polarization of the diffracted fields can be treated with the vectorial Kirchhoff's diffraction integral. However, it is far more complicated to solve analytically than the scalar version [Hri00]. Lastly, the most comprehensive analyses are those based on 3D Full-wave electromagnetic numerical modelling. For instance, Fresnel lens analysis at MMW range has been effectively performed with the Finite-Difference Time-Domain method (FDTD) and the Method of Moments (MoM) [Min11, Kim05].

The analysed dual band prototype is an electrically very large structure at the IR range. Specifically, the focal distance is $123\lambda_g$. Furthermore, non-symmetrical modifications are going to be included in the lens to perform the subMMW antenna. Consequently, the use of radial symmetries, commonly employed to reduce the computational resources in lens analysis, cannot be used. Even with an FDTD simulator enormous computational resources are needed for the full wave simulation. For these reasons, the study of the lenses was performed using a theoretical analysis based on scalar Fresnel-Kirchhoff diffraction, which simplifies and shortens the simulation times.

The IR Fresnel Lens is designed to operate at $\lambda = 10.7\ \mu m (\sim 28.2\ THz)$ with focal distance $F = 380\ \mu$m (i.e. a commercial slab thickness). The radius of the first 14 Fresnel Zones (from equation 3.3) are listed in Table 3.1. Figure 3.4 shows the distribution of the normalized E-field along the optical z-axis for the conventional FZPL from 2 to 14 Fresnel zones. The clearly defined foci appear at a distance of 380 μm, which is the thickness of the silicon substrate.

Table 3.1: Radius (ρ_m) of the FZPL designed for $\lambda_{Si} = 3.1\ \mu$m with $F = 380\ \mu$m.

ρ_1	ρ_2	ρ_3	ρ_4	ρ_5	ρ_6	ρ_7
34.67	49.08	60.17	69.55	77.84	85.35	92.28
ρ_8	ρ_9	ρ_{10}	ρ_{11}	ρ_{12}	ρ_{13}	ρ_{14}
98.75	104.85	110.63	116.14	121.43	126.51	131.41

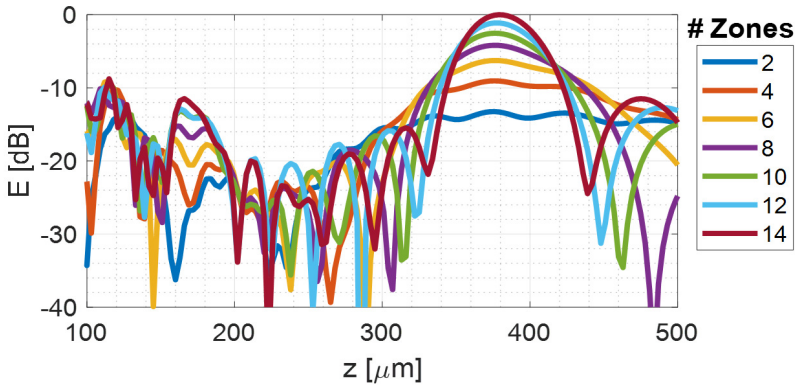

Figure 3.4: E-field along the z-axis for FZPL with a variation of the number of zones from 2 to 14. The graph is normalized with respect to the maximum of the 14-FZPL field.

The focusing properties of the planar lenses are usually expressed by the focusing gain (FG). This parameter is defined as the squared ratio of the magnitude of the focused field, $E(F)$, and the free-space electric field magnitude, $E_0(F)$, at the receiving point F (i.e. the field in the focus without the lens). This is:

$$FG = 20log\frac{|E(F)|}{|E_0(F)|} \qquad [dB] \tag{3.4}$$

Figure 3.5 (a) shows the calculated Focal Gain with different number of zones for the designed conventional FZPL. It can be seen that the focal gain increases very fast for the first numbers of zones, whereas for larger numbers the contribution of additional zones is smaller. The FG was also evaluated in a frequency bandwidth for planar lenses with 6, 10 and 14-FZPL and the results can be seen in Figure 3.5 (b). The bandwidth is inversely proportional to the number of zones. Focal gains higher than 20 dB can be obtained in less than 10 % fractional bandwidth, which is the main constrain of the planar lens.

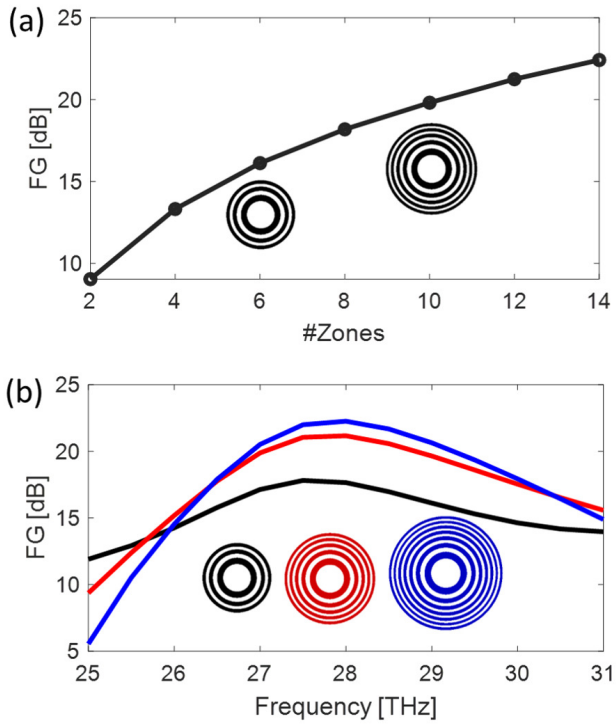

Figure 3.5: (a) Focal Gain *vs* number of Fresnel zones. (b) Focal Gain *vs* frequency for 6-FZPL (black), 10-FZPL (red) and 14-FZPL (blue).

3.4 Modified IR Lens-Antennas

Starting from the designed conventional FZPL, the structure can be modified to create a submillimetre wave antenna able to perform as a lens, focusing the IR radiation. In this work, we tried to cover the most common planar antenna topologies used in the subMM frequency range that can be obtained from direct modifications of the Fresnel plate lens. Thus, two possible variations of modified spiral antennas are studied in first place. Forward, resonant antennas such as dipoles, bow-tie and meander antennas are analysed. Besides, it is important to take into account in the analysis that the first zone of the modified lenses (possible antennas) will be partially obstructed by the submillimetre wave detector element. Consequently, the metal part of the Schottky diodes structure was included in the study of the modifies lenses. The goal is to find structures with good focusing properties in the IR range, while performing good impedance matching and radiation efficiency in the SMMW range.

Quasi-Spiral

As shown in [Ald09], taking advantage of the size of the IR FZPL, one suitable option may be to create a printed spiral antenna from the modification of the FZPL. However, the structure of a conventional spiral antennas (e.g. Archimedean, equiangular and log-periodic spirals), cannot be described as concentric rings and will have poor performance as a lens. In [Tor17] we analysed the focusing properties of an Archimedean spiral antenna designed following its typical equation $r = r_0 + (ExpantionCoefficient)\phi^{(1/SpiralCoefficient)}$ and optimized to resemble as much as possible the Fresnel Lens geometry.

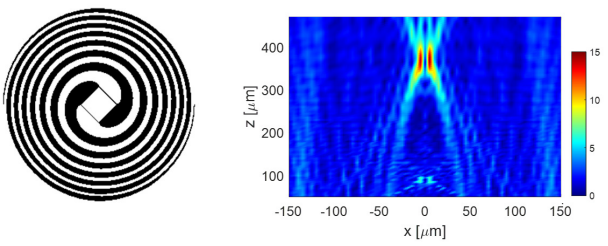

Figure 3.6: (a) Archimedean spiral antenna. (b) 2D E-Field magnitude in the xz-plane.

The result can be seen in Figure 3.6 where two foci shifted from the optical axis (x = 0) appear with low focusing gain level. It was concluded that this kind of approximation cannot be used as a planar lens.

Other approach consists in connecting the opaque (metal) areas of the designed Fresnel lens so that a type of quasi-spiral antenna is formed. It is important to note that this last design does not vary the radii of the Fresnel zones. Regarding to this, two ways of connecting the metal rings were studied, as can be seen in Figure 3.7 (a and b). The first one (QS-1) was proposed in the framework of this investigation whereas the second one (QS-2) is based in the theoretical model presented in [Ald09].

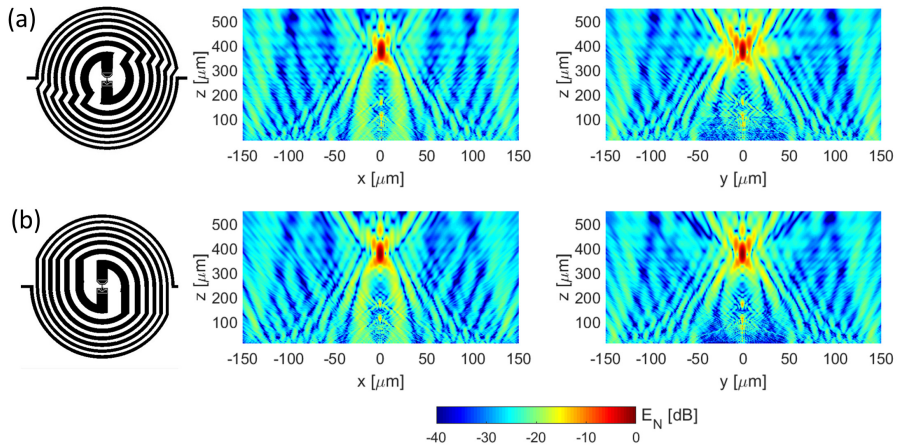

Figure 3.7: (a) Quasi-spiral 1 (QS1) (b) Quasi-spiral 2 (QS2). 2D E-Field magnitude in the xz-plane (centre figure) and in the yz-plane (right figure).

The focusing process can be visualized in the 2D colour map for E-field distribution on the xz and yz-planes. This is shown in Figure 3.7 (a) for the quasi-spiral type 1 and in Figure 3.7 (b) for the quasi-spiral type 2. From this analysis, any significant difference is appreciated between both approaches. If anything, slightly higher side-lobes in the yz-plane can be seen in the second variant with respect to the first one.

To evaluate the frequency bandwidth performance, the field distribution was simulated as a function of frequency. The E-field distribution along the optical axis (z) can be seen in Figure 3.8 for both quasi-spiral models. Besides, the

Focal Gain at the focal position ($z = 380\ \mu m, x = 0, y = 0$) was calculated and was compared with the conventional 14-FZP lens in Figure 3.9. The modification introduced in the lens to create the spirals represents a loss of 2 dB compared with the 14 FZPL at the design frequency (28.2 THz). The QS-2 model (represented in blue), exhibits slightly higher FG values than the QS-1. Even so, the performance of both models is almost the same.

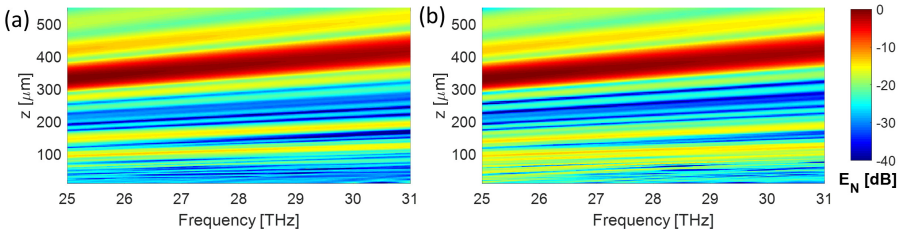

Figure 3.8: Normalized E-Field distribution along the z-axis for the frequency range 25-31 THz: (a) QS 1, (b) QS2.

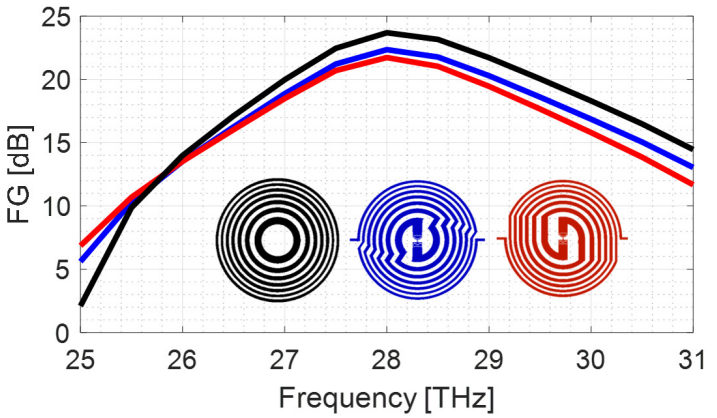

Figure 3.9: Focal Gain versus frequency for QS-1 (blue line) and QS-2 (red line). The FG of the conventional 14-FZPL is also included for comparison (black line).

Bow-Tie

As stated earlier, another lens modification may be performed. Figure 3.10 shows three variations from the dipole antenna with different taper angles (bow-tie dipoles) alongside their respective E-Field distributions when an IR plane wave illuminates them. In this case, the modifications are performed on a 10 zones Fresnel Lens. This is the minimum number of zones to achieve FG higher than 20 dB and results in a dipole length equal to $0.3\lambda_0$ at 400 GHz ($L_d = 2\rho_{10} = 220$ μm) which is approximately the typical dimension of a full-wave(λ) dipole printed on a silicon substrate.

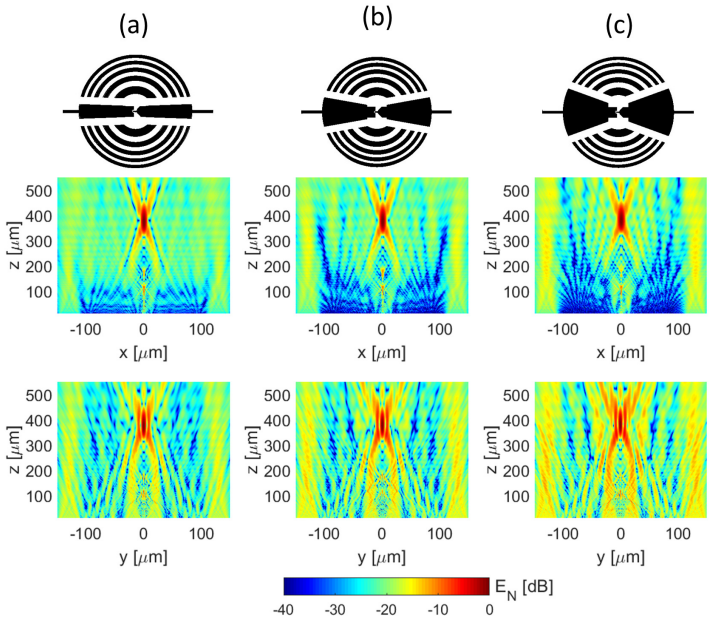

Figure 3.10: Bow-tie modified lens with different taper angles: (a) 0°, (b) 20°, (c) 40° with the respective 2D E-Field magnitude representation in the xz-plane and in the yz-plane below each one.

For the bow-tie type modified lenses, the degradation of the focusing properties with the increase of the taper angle is an expected consequence and can be corroborated in Figure 3.11. A 3-dB FG decay (w.r.t the 10 FZPL) happens

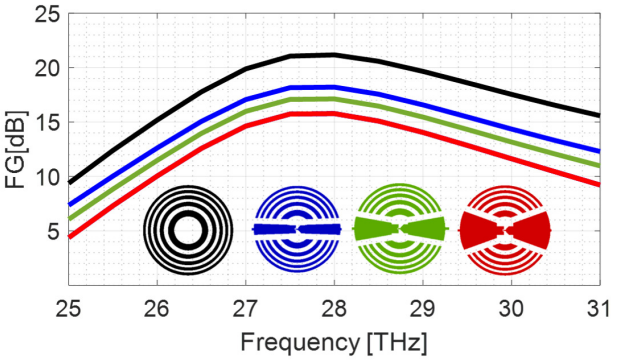

Figure 3.11: Focal Gain vs frequency for the quasi-bow-tie models with three different taper angles: 0° (blue line), 20° (green line) and 20° (red line). The FG of the conventional 10-FZPL is also included for comparison (black line).

with the simple dipole (0°) at the centre frequency. Moreover, the deterioration can be up to 6 dB for the extreme case of a very wide bow-tie (40°).

Quasi-Log and Quasi-Meander

Related with the last idea, another type of modified antenna, that we named quasi-log (Q-L), was tested and is presented in Figure 3.12(a). The name was given for the resemblance with a logarithmic planar antenna although the presented designs do not follow the design equation of a logarithmic model. Finally, another suitable modification in the lens to create another type of resonant sub-MMW antenna is the one showed in Figure 3.12 (b). This is the meander antenna, also known as folded dipole antenna.

Once again, the E-Field distribution of the quasi-log (Q-L) and quasi-meander (Q-M) models are presented in Figure 3.12. Additionally, the FG versus frequency response is showed in Figure 3.13. Compared with the 10-FZPL, the quasi-log and quasi-meander models present similar FG degradation, around 4.3 dB. The main difference in the behaviour of these modified lenses comes from the E-field distribution (Figure 3.12) where it can be seen that the quasi-log approach exhibits more pronounced undesired side lobes in the yz-plane.

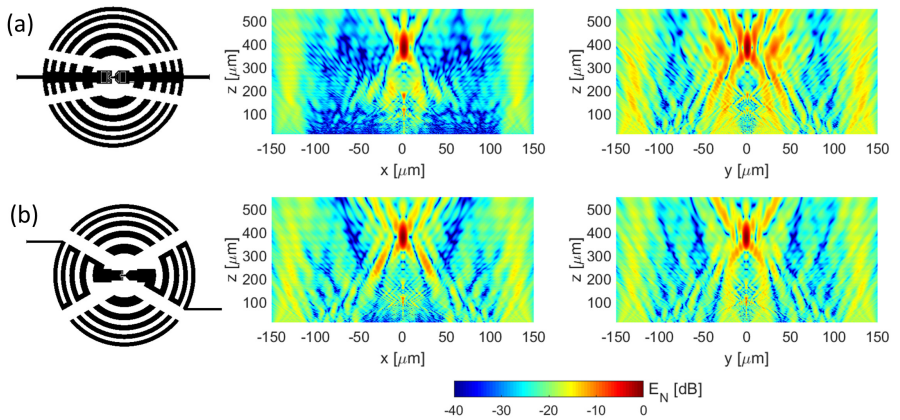

Figure 3.12: (a) Quasi-log modified lens and 2D E-Field magnitude representation in the xz-plane (left side) and in the yz-plane (right side). (b) Quasi-meander modified lens and 2D E-Field magnitude representation in the xz-plane (left side) and in the yz-plane (right side).

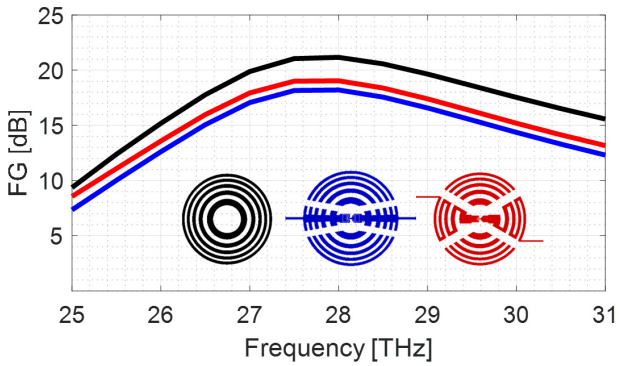

Figure 3.13: Focal Gain vs frequency for the quasi-log model (blue line) and for the quasi-meander model (red line). The FG of the conventional 10-FZPL is also included for comparison (black line).

Major modifications in Quasi-Log and Quasi-Meander models

Finally, last and major modifications of the quasi-log and quasi-meander designs were studied. The layout is the one presented in Figure 3.14 where it can be seen that the read-out lines are directly connected to the dipole port. By doing that, we extend the study to another group of antenna configurations widely used in direct detection. A deeper study of every model presented up to here and the advantages of this particular approach are given in Section 3.5.

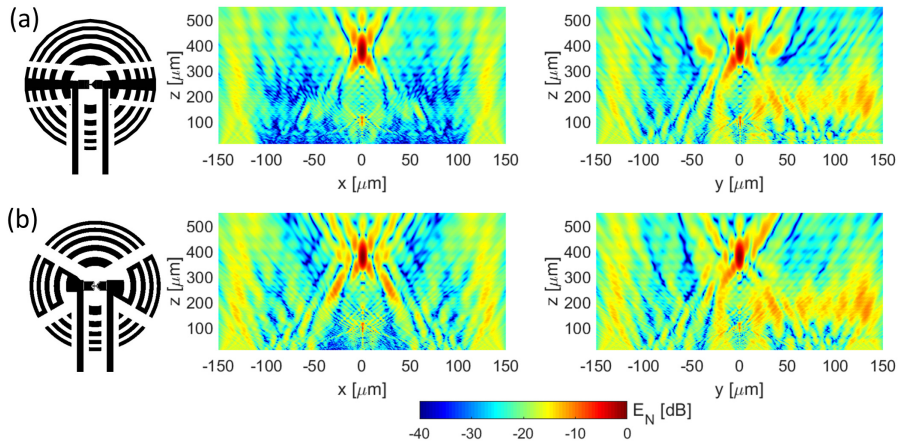

Figure 3.14: (a) Quasi-log with major modifications lens (MQ-L) and the 2D E-Field magnitude representation in the xz-plane (left side) and in the yz-plane (right side). (b) Quasi-meander (MQ-M) with major modifications lens and the 2D E-Field magnitude representation in the xz-plane (left side) and in the yz-plane (right side).

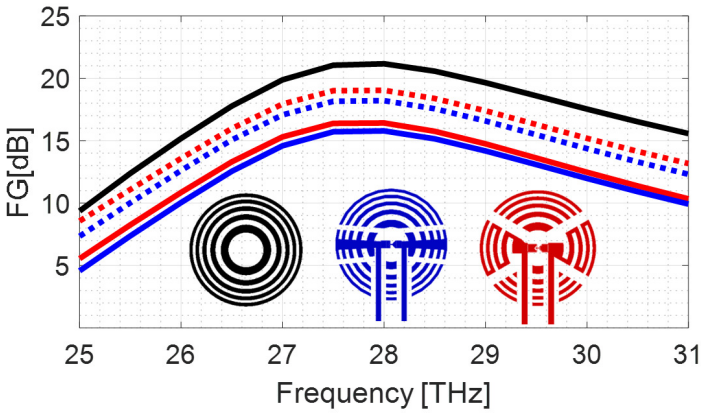

Figure 3.15: Focal Gain vs frequency for the modified quasi-log model (blue line) and for the quasi-meander model (red line). The discontinuous lines represent the respective FG previously obtained without the major modifications. The FG of the conventional 10-FZPL is also included for comparison (black line).

The influence of the feed lines crossing the lens can be observed in the 2D E-field distribution on the yz-plane (Figure 3.14). Major modifications results in an additional degradation of the FG of approximately 1.5 and 2 dB for the MQ-L and MQ-M antennas refereed to the previous Q-L and Q-M models (Figure 3.15). Even with this major modification, higher than 15 dB focusing enhancement can be obtained.

3.5 Submillimetre Wave Antennas

Once the modified antennas have been proved to act as IR planar lenses, their performance at the SubMMW range must be analysed. The impedance and radiation properties of the modified lens antennas are studied to meet the requirements of the SubMMW direct detector.

3.5.1 Input Impedance

Quasi-Spiral

The first modified lenses are shown in Figure 3.16. The presented approach is performed by connecting the Fresnel metallic rings and although is based on the printed spiral antennas, does not follow the spiral design equations. Thus, the impedance and radiation performance of the proposed quasi-spiral antennas must be studied.

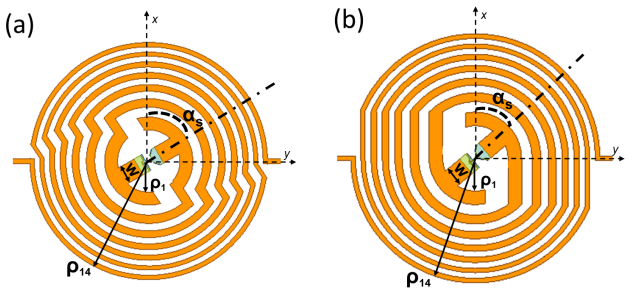

Figure 3.16: (a) Quasi-spiral 1 and (b) quasi-spiral 2 SubMMW antennas.

The conventional spiral design is a frequency independent antenna, introduced in the 1950s [Tur58], which presents constant input impedance, circular polarization and has been employed over a wide frequency range. In that conventional antenna the radiation will occur when the currents from nearby arms are in phase for constructive radiation, which happens at the radius corresponding to a circumference length of one wavelength ($C = \lambda$). The lowest and highest operational frequency will be determined by equation 3.5.

$$f_{low} = \frac{c}{2\pi R_{ext}\sqrt{\epsilon_{r,eff}}} \qquad f_{high} = \frac{c}{2\pi R_{int}\sqrt{\epsilon_{r,eff}}} \tag{3.5}$$

where $\epsilon_{r,eff}$ is the effective dielectric constant.
Back to the quasi-spiral design, the inner radius (R_{int}) is determined by the first Fresnel Zone (34.5 μm for the proposed design), whereas the outer radius (R_{ext}) depends on the number of zones selected for the lens. For 14 Fresnel Zones cases, the operational ranges of the quasi-spiral antenna using the equation of conventional spirals should go from 140 GHz to 550 GHz.

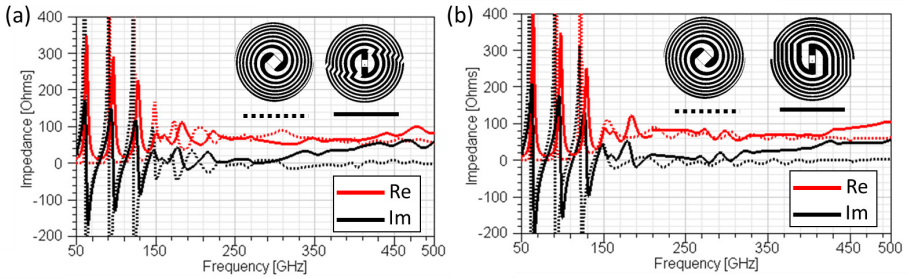

Figure 3.17: Simulated input impedance vs frequency for the quasi-spiral antennas and the equivalent Archimedean spiral (a) QS-1, (b) QS-2.

Figure 3.17 shows the input impedance for both quasi-spiral antennas simulated with the 3D full-wave electromagnetic solver Ansoft HFSS V.2018.2. An infinite wide substrate and ground plane with a slot where the IR detector will be placed were assumed in the simulation. For both cases, the comparison with an Archimedean spiral antenna with the same input and output radius was included (discontinue lines). In Figure 3.17 a ripple for the lowest frequency in the operational band can be observed in all the cases. The currents decay rapidly beyond the resonant rings due to radiations. As a rule of thumb, when the spiral aperture is 5/4 times the radius of the resonant ring, the input impedance is not affected by reflections from the truncation. However, at lower frequencies, a substantial proportion of the arm currents are reflected from the spiral ends [Wat08]. As can be seen in Figure 3.17 for the conventional spiral, above 200 GHz, when the aperture circumference is approximately 5/4 times of the wavelength, the impedance becomes mainly resistive and constant. For the modified spirals, the real part of the impedance is very similar to the one of the conventional spiral ($\sim$ 70Ω) whereas the imaginary part presents an in-

ductive ($\sim$ $50j$ Ω) behaviour emphasized in the upper part of the operational frequencies. This behaviour is very interesting to obtain good coupling with many types of detector elements.

To further maximize the antenna matching, there are few design variables that can be changed in these designs, since we must preserve the radii of the Fresnel zones. Therefore, only the angular position of the connection between the diode and the spiral (α_s) and the width of the central feed lines (w) (i.e. the ones connected to the diode) can be modified.

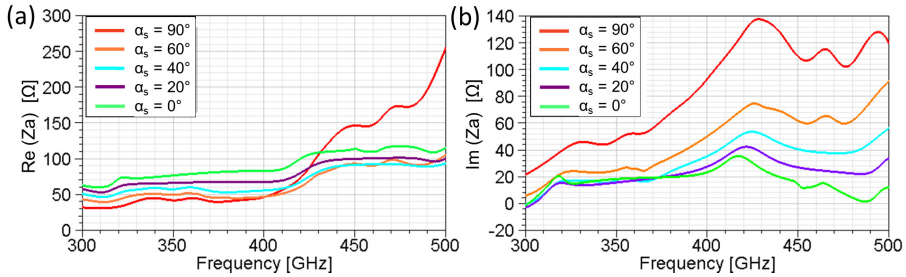

Figure 3.18: Simulated input impedance versus RF frequency for the quasi-spiral antenna type 1 (QS-1) as a function of the feed angle (α_s) with $w = 20$ μm. (a) Real part; (b) Imaginary part.

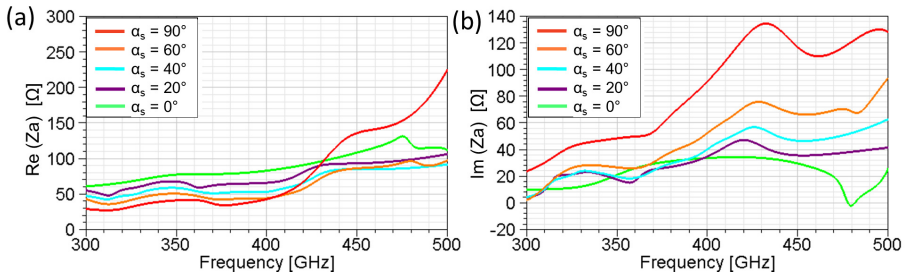

Figure 3.19: Simulated input impedance vs RF frequency for the quasi-spiral antenna type 2 (QS-2) as a function of the feed angle (α_s) with $w = 20$ μm. (a) Real part; (b) Imaginary part.

Figure 3.18 and Figure 3.19 show the variation of the input impedance for the QS1 and QS2 as a function of the feed angle (α_s). It can be seen that the referred parameter does significantly affect the input impedance. This is an expected result because a kind of stub is formed in the antenna feed point. For α_s smaller than 40° the antenna presents a stable performance in a wide frequency band. Nevertheless, for higher rotation values, which means longer stubs, the input impedance becomes very inductive. Moreover, from 300 to 400 GHz the input impedance real part exhibits low values.

The explained behaviour makes this antenna an ideal candidate to be coupled with the Schottky diode. Furthermore, the wide control of the input impedance with the variation of the rotational position of the feed predicts that good impedance matching can be obtained with many detector devices, just by adjusting this parameter. Lastly, both antennas, (QS-1 and QS-2), behave almost equally from the input impedance point of view.

Dipole and Bow Tie

The printed dipole antenna is one of the most studied radiation elements from microwave to optical frequencies. The input impedance and radiation behaviour are mainly governed by the length of the dipole. However, the feed separation and the width of the arms can be also modified to tune the input impedance in a narrower range. Two radiating lengths are the most commonly employed. In applications where impedances in the order of 50 Ω are required, $\lambda/2$ dipoles are the best candidates. Contrasting, when high input impedances are needed, λ dipoles are preferred.

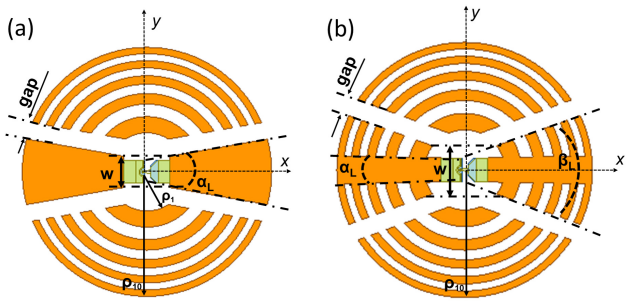

Figure 3.20: (a) Quasi-Bow-Tie and (b) quasi-log SubMMW antennas.

The presented prototypes are based on approximately λ dipoles with different taper angles of aperture (α_L) performed by the modification of the 10-FZPL as can be seen in Figure 3.20(a). The sections of the Fresnel lens isolated from the main dipole by a gap (*gap*) can be seen as parasitic radiators coupled to the main dipole. Figure 3.21(a) shows the input impedances of the modified dipole antenna with different taper angles (namely, 2°,10° and 20°).

Another possible approach, is the one presented in Figure 3.20(b). The initial objective with this configuration was to obtain the radiation due to the resonance of the array of vertical dipoles. Nevertheless, this was not the result achieved. The resonance of the horizontal dipole dominates the behaviour while the vertical dipoles act as parasitic loading elements. The variation of input impedance with the taper angle of the quasi-log antenna (β_L) from 2° to 60° can be seen in Figure 3.21(b).

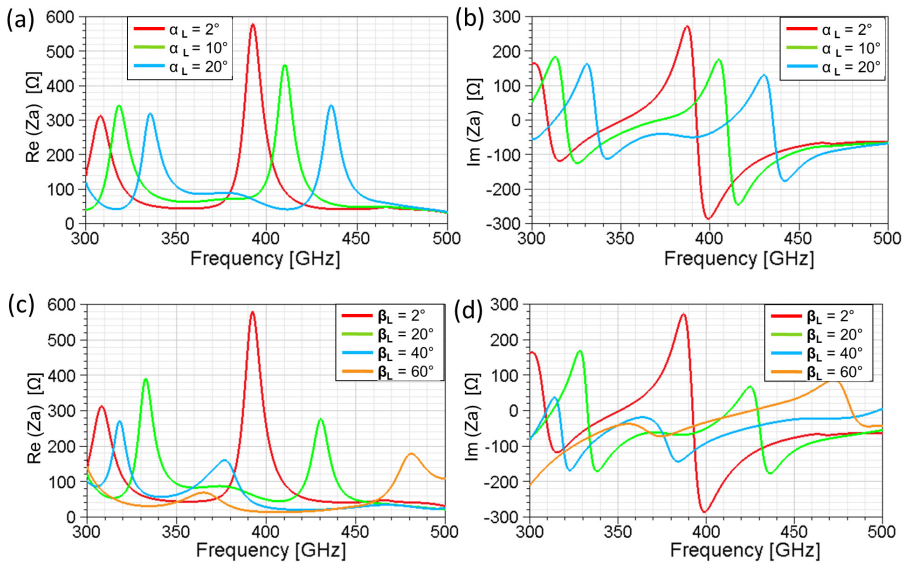

Figure 3.21: Simulated input impedance versus frequency for: (a-b) the quasi-bow-tie antenna as a function of the variation of the taper angle (α_L) with $w = 20$ μm and (c-d) quasi-log antenna as a function of the variation of the taper angle β_L with $\alpha_L = 2$ ° and $w = 20$ μm. (a-c) Real part; (b-d) Imaginary part.

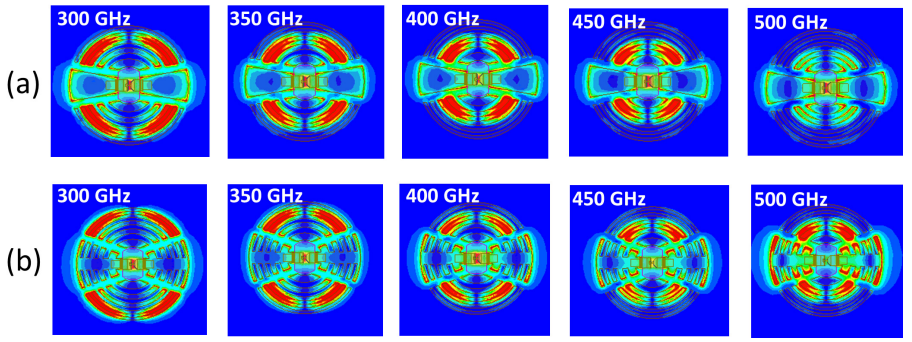

Figure 3.22: E-Field distribution of the (a) quasi-bow-tie ($\alpha_L = 20$ ° and $w = 20$ μm) and (b) quasi-log antennas ($\beta_L = 40$ ° and $w = 20$ μm).

Additionally, to clarify the origin of the resonances in both approaches, the E-Field distribution on the antenna plane is presented in Figure 3.22. The field distribution in the main dipole (i.e. the horizontal dipole) corresponds to the resonance of a lambda dipole. There is a maximum absolute value of the E Field at the centre and at the ends of the dipole and a null in the centre of the arms. Moreover, it is noticed the sections of the lens separated by the gap resonate when its length is $\lambda/2$. Accordingly, the resonance of the outer (longer) strips happens at 300 GHz whereas the $\lambda/2$ resonance of the inner strips appears at 500 GHz.

The conclusion is that strong resonant behaviour is obtained with all the variations of the modified bow-tie and quasi-log antennas. A wide range of input impedance either inductive or capacitive with very low or very high real part may be swept with the variation of the angles α_L and β_L. However, matching with the detector element can be optimized only for a narrow bandwidth.

Meander

The meander antenna is based on a dipole antenna where the arms have been folded in a certain way as shown in Figure 3.23, in order to either reduce the antenna size, or to obtain high values of input impedance, or both. Folded dipole antennas can be classified in the same group of the meander antennas and have been used as SubMMW antennas in applications where resonant matching or very large input impedances are needed. It was also set that at high frequencies almost not current is excited in the borders of the arms on the meander [Car15].

This allows to bias any active device placed in the centre without modifying the high frequency antenna performance.

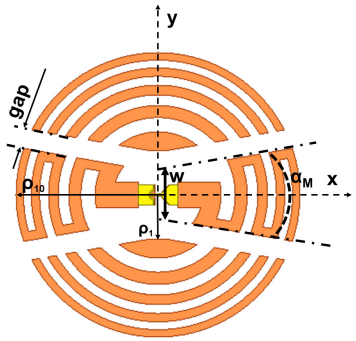

Figure 3.23: Quasi-meander SubMMW antenna.

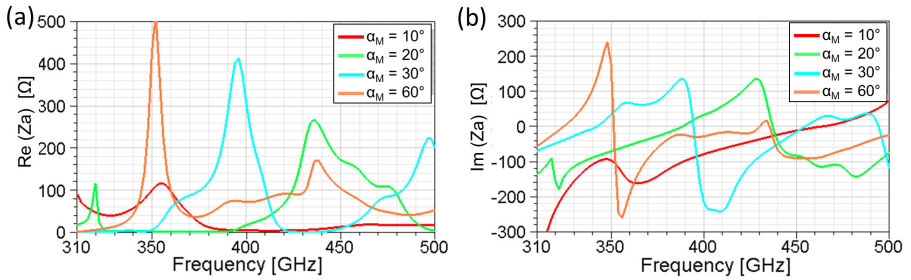

Figure 3.24: Simulated input impedance versus RF frequency for the quasi-meander antenna as a function of the variation of α_M with $w = 20\mu$m.

From the input impedance analysis (Figure 3.24) it can be seen that high real and imaginary components can be simultaneously obtained. Besides, the resonance frequency is widely tuneable with the variation of the taper angle (α_M).

RF Choke

Lastly, in a direct detector, the DC or very low frequency signal output component may be extracted through the read-out lines connected to the external terminals of the antennas as in the previously presented designs. Moreover, another possible approach consists in connecting the read-out circuit directly to the antenna RF input port through an RF Choke. This is normally a low-pass filter designed to "isolate" the RF from the low frequency parts of the detector. The configuration of this low-pass filter and its distance to the RF ports can be tuned to optimize the active element embedding impedance. For example, most millimetre and SubMMW detectors and emitters present a capacitive impedance behaviour. The distance from the active element to the filter can be designed to compensate this capacitive impedance. Afterwards, the antenna can be optimized to obtain the real part impedance matching. In any case, the overall dimensions of the low-pass filter must be minimized to avoid any influence on the RF antenna performance.

Finally, two new detector configurations based on the last presented concept have been proposed and can be seen in Figure 3.25 and Figure 3.27. The filter is composed of cascading alternated high and low impedance sections of coplanar stripline whose main dimensions are listed in Table 3.2. The design variable that shifts the distance from the antenna to the filter will be defined as d_f. However, the true distance from the diode to the filter includes the radius of the Fresnel Lens, which should not be modified.

Table 3.2: CPS stepped-impedance filter dimensions. See Figure 3.25 for reference.

Parameter	Description	Design
W_{hf}	Width of the high impedance sections	10 μm
s_{hf}	Separation of the high impedance sections	35 μm
W_{lf}	Width of the low impedance sections	25 μm
s_{lf}	Separation of the low impedance sections	5 μm
L_{LA}	Length of low/high impedance sections	80 μm

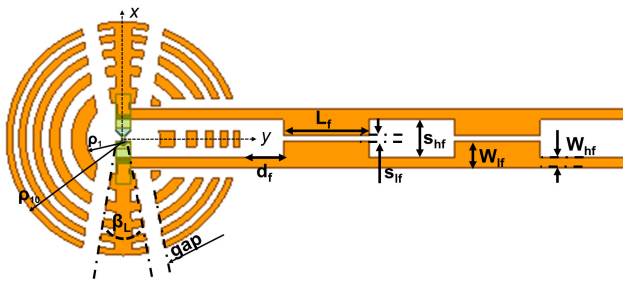

Figure 3.25: Modified quasi-log antenna with RF-Choke.

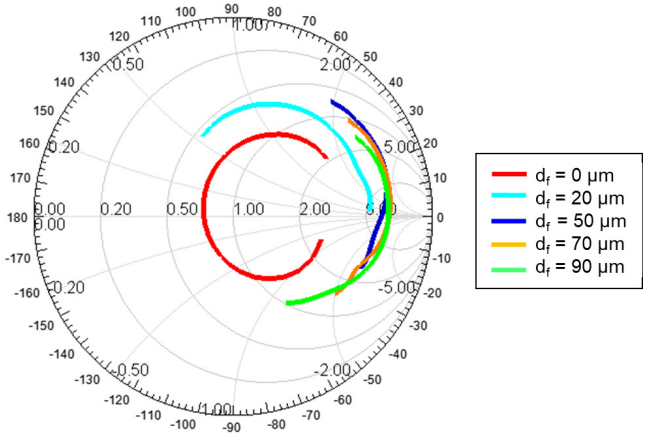

Figure 3.26: Smith chart representation of the input impedance of the modified bow-tie antenna connected to the RF-Choke for 370-430 GHz for different d_f values with $\beta_L = 5°$.

The input impedance variation of the quasi-log antenna connected to the RF-Choke can be seen in Figure 3.26. As was already exposed, the distance to the first filter section (d_f) can be optimized to compensate the reactive part of the input impedance. Afterwards, the antenna can be adjusted to be couple to the real part of the impedance.

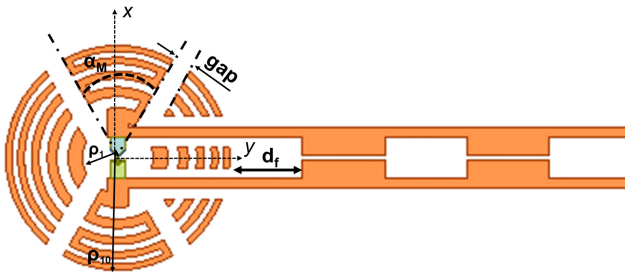

Figure 3.27: Modified quasi-meander antenna with the RF-Choke.

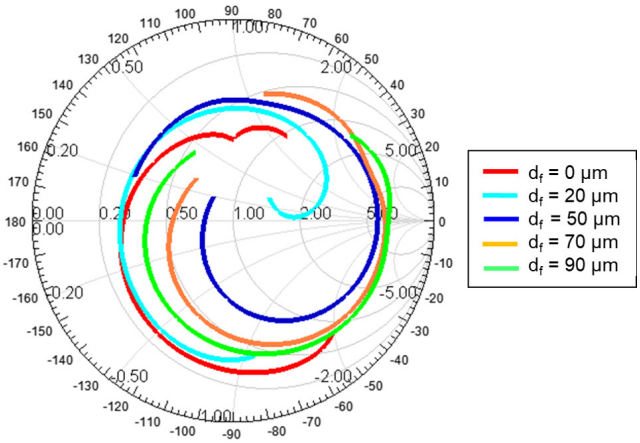

Figure 3.28: Smith chart representation of the input impedance of the modified meander antenna connected to the RF-Choke for 320-430 GHz for different d_f values with $\alpha_M = 15°$.

The last analysed modification is the quasi-meander antenna connected to the RF-Choke (Figure 3.27). Once again, d_f was modified and the input impedance variation can be seen in Figure 3.28. A wide range of impedances is swept by modifying d_f. Consequently, this design offers good chances to achieve good antenna-detector RF coupling.

3.5.2 Radiation Performance

The overall detector efficiency will be function of the impedance mismatch factor, as well as of the antenna radiation efficiency. In the presented designs it must be taken into account that the SubMMW antenna operates on a high relative permittivity substrate $1.8\lambda_{eff}$ (@400 GHz) thick. Thus, the design will be affected by the excitation of undesired surface-wave modes.

From a ray tracing point of view, the surface waves can be understood as rays incident on the back of the substrate at an angle larger than the critical angle which are reflected and remain trapped into the substrate. As these substrate modes do not contribute to the primary radiation pattern, they are considered a loss mechanism. The diffraction of surface waves at the edges of the antenna substrate will generate a drop of the antenna efficiency and the appearance or ripples and of side lobes. Furthermore, it is known that printed antenna on top of a dielectric media will radiate mainly into the dielectric, as this interface will offer a lower impedance medium. Based on that, one of the solutions found in the literature to overcome the surface-mode excitation is the inclusion of a lens on the backside of the substrate with the same dielectric constant. Nevertheless, in the presented dual band detector we may find an obstacle for the integration of a silicon lens on the back of the substrate due to the presence there of the IR detector. Moreover, one of the goals of the presented research is to preserve the planarity and low profile of the integrated detectors. Therefore, a different solution based on Photonic Band Gap technology will be studied.

Firstly, a ground plane with a small slot was placed on the back of the silicon substrate. This slot would emulate the IR antenna, which could be implemented in a complementary configuration (i.e. slot antenna). The ground plane is introduced to ensure the radiation to be towards the air side. As a rule of thumb, surface-mode excitation becomes appreciable in a grounded substrate for a substrate height over λ ratio (h/λ_{eff}) larger than 0.03 (with ϵ_r=10) [Jam79]. In the presented approach, this value is 0.5. Thus, the surface-wave contributions will not be negligible. The E-Field in two cuts, perpendicular and parallel to the plane of the substrate, for different values of interest of RF frequency is presented in Figure 3.29 where the excitation of substrate modes is clearly visible.

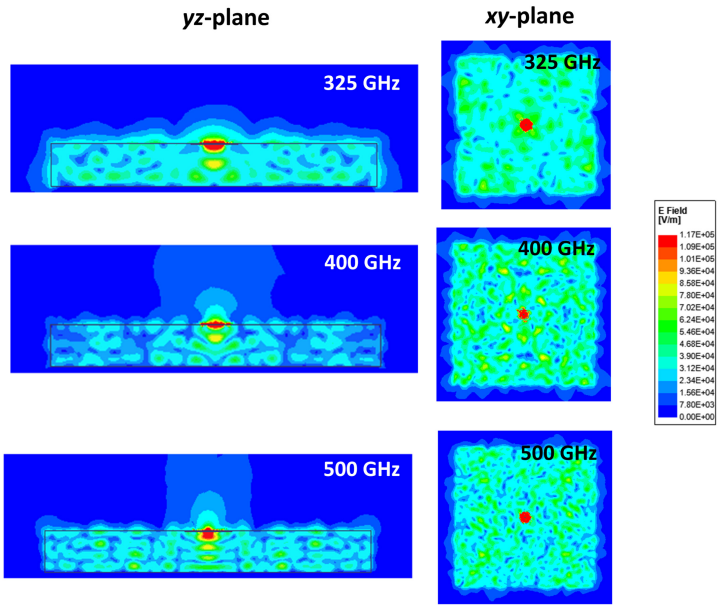

Figure 3.29: Electric field distribution in the yz-plane (perpendicular) and in the xz-plane (parallel) to the silicon slab in a finite grounded dielectric slab.

In order to evaluate the implications of the surface modes, the radiation pattern of one of the studied antennas (i.e. the QS1) was simulated (HFSS) in a finite square substrate with 3.5 mm length. An air box wider at $\lambda/2$ than the silicon substrate in all the axis was inluded in the simulation and PML radiation condition was applied to the air box. The radiation pattern obtained is shown in Figure 3.30 (a) for the same RF frequency values. It can be seen that the radiation pattern on a finite dielectric substrate presents very pronounced ripples and very poor radiation performance. To overcome this problem, we propose a solution based on Photonic Band Gap structures surrounding the antenna.

The use of PBG structures to improve the radiation performance of planar antennas has been extensively investigated. Numerous study of antennas lying on a EBG based substrate can be found [Maa03, Gon01]. However, the proposed solution must avoid the use of the PBG directly below the antenna to preserve the IR focusing performance. For this reason, the presented designs will be

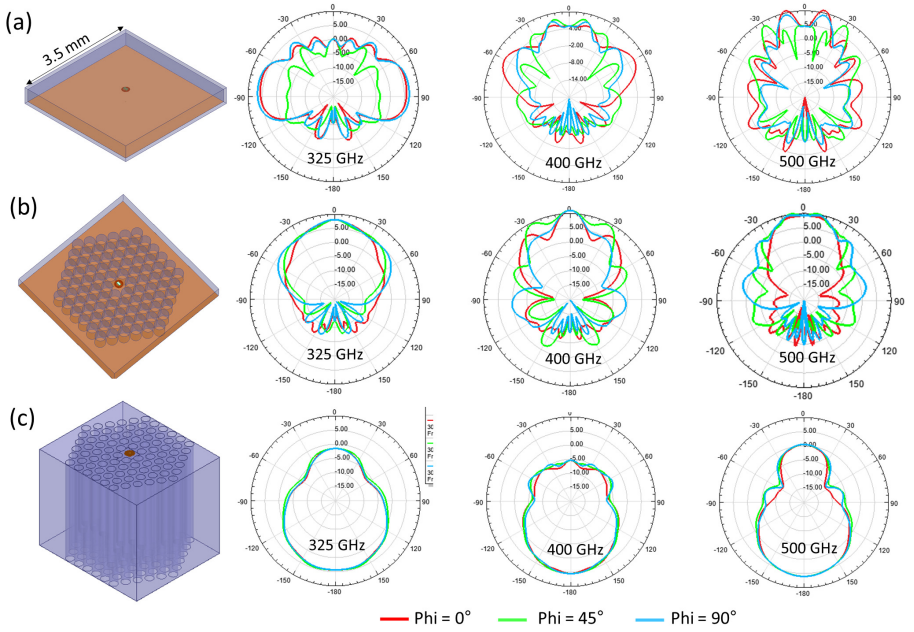

Figure 3.30: (a) Radiation pattern of the QS1 antenna on top of finite grounded silicon slab, (b) on top of finite grounded silicon slab including a PBG structure surrounding the antenna and (c) on top of an infinite silicon slab including a PBG structure surrounding the antenna.

based on the inclusion of PBG structures surrounding the antenna.

Figure 3.30 (b and c) shows the 3D views of the antenna surrounded by air columns etched in the dielectric substrate with a triangular lattice. In both approaches a single air cylinder is removed from the lattice and the antenna is placed in the centre of this defect. The band diagram for the mentioned PBG structure was obtained with the MIT photonic band software [Joh99] and can be seen in Figure 3.31. The selected dimensions are: lattice constant (a) 315 μm, air cylinder radio (r) 120 μm (0.38a), substrate height 380 μm (1.2a) and substrate dielectric constant ϵ_r=11.7. With these dimensions there is a gap for the even polarized modes from 0.26 to 0.36 normalized frequency values (a/λ). It is important to note that the even modes are the ones compatible with the ground plane.

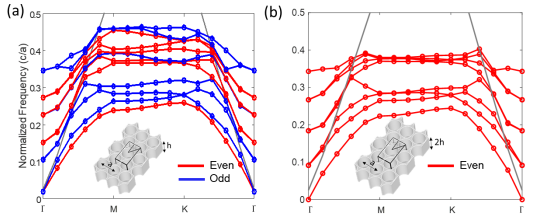

Figure 3.31: (a)Band diagram for a hexagonal lattice of air cylinders in silicon ($\varepsilon_r = 11.67$, $r = 0.38a, h_s = 1.2a$) for even (red lines) and odd (blue lines) polarizations and (b) even modes of the PBG structure on a grounded slab. The grey lines delimit the light cone.

For the first case presented in Figure 3.30 (b), the above mentioned ground plane is considered and the thickness of the silicon is the same that the IR focus length. The radiation patterns obtained exhibit the main radiation direction towards the air side and a clear reduction of the ripples. It must be pointed out that in this case, the PBG was simulated not going through the wafer, but leaving a 10 μm thick silicon at the top (on the antenna-side) to serve as support for the read out circuit. The E-Field simulations of this structure can be seen in Figure 3.32. The result confirms the surface wave suppression.

Another interesting solution is the one presented in Figure 3.30 (c). The substrate thickness is increased and for a thick enough substrate we may consider the cavity as a primitive dielectric rod antenna. In that case, the radiation pattern from the spiral is coupled to the cavity and radiated through the silicon side resulting in a very symmetric and "clean" radiation pattern for all the studied frequencies. The latter approach, although based in planar concepts, leads to assembly issues related with the presence of the IR detectors. A solution based on align and bounding two substrates could be investigated. Nonetheless for the presented dual-band device the final fabrication will be cumbersome. Notwithstanding all mentioned issues, the results presented in Figure 3.30 (c) may be an attractive planar solution in other scenarios.

Further presented solutions will be based on the grounded design presented in Figure 3.30 (b). Finally, some important details must be considered regarding the proposed approach. The first one is that the PBG is not a wideband solution. Thus, it may be optimized for a desired frequency. Besides, the modifications in the substrate introduce variations in the antenna input impedance. For this reason, to obtain accurate results, the final designs must be simulated including

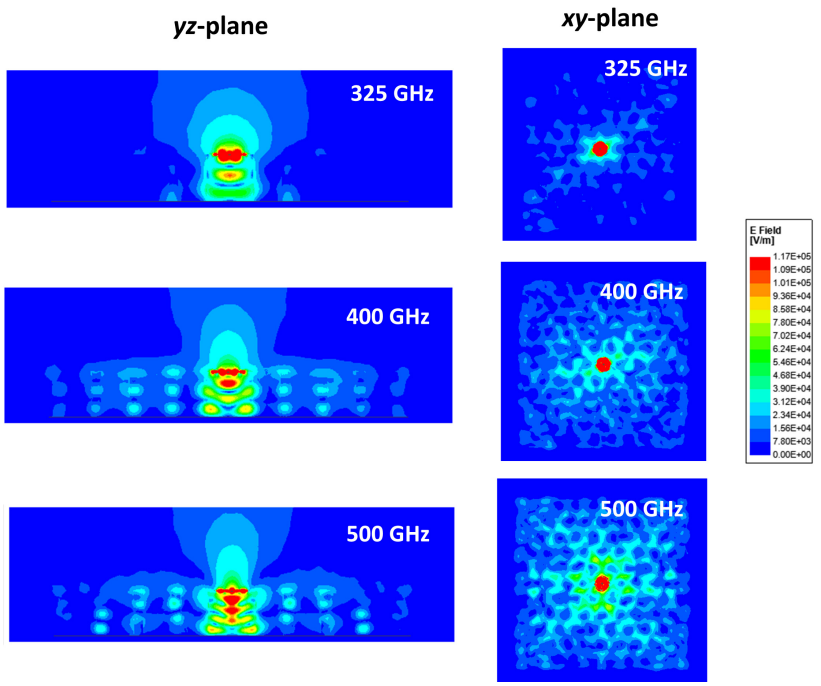

Figure 3.32: Electric field distribution in the yz-plane (perpendicular) and in the xz-plane (parallel) to the silicon slab in a finite grounded dielectric slab including a PBG structure surrounding the antenna.

the whole antenna, read-out circuit and PBG substrate.

In Section 3.5.1 it was demonstrated that the quasi-spiral antenna designs were the ones that offered better possibilities to maximize the mismatch factor. Therefore, major efforts in this section will focus on the study and optimization of the radiation of the mentioned prototypes. Regarding this, one of the main characteristics of the radiation of the conventional spiral antennas is the generation of circular polarization (CP). Moreover, for some applications it can be highly desirable to keep the CP behaviour in the proposed quasi-spiral designs. The simulation of the boresight axial ratio (AR) versus frequency for both models (QS1 and QS2) with extremes values of α_s variations (namely, 0° and 90°) can be seen in Figure 3.33. Even when the PBG was designed for the low band of the analysed frequency range (Figure 3.33 (a)), the upper band range (Figure 3.33 (b) shows promising results worth mentioning.

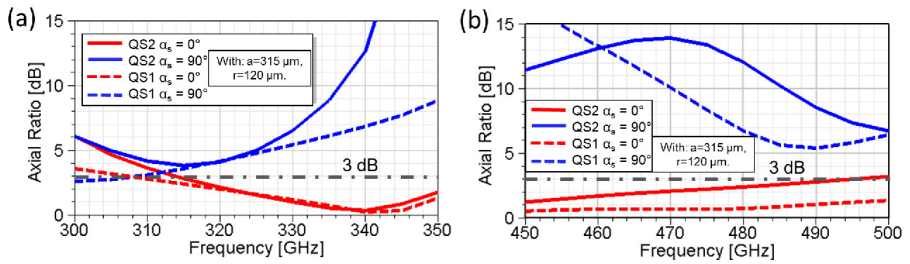

Figure 3.33: Simulated boresight Axial Ratio for the QS1 (discontinuous lines) and the QS2 (continuous lines) with $\alpha_s = 0°$ (red) and 90° (blue). The PBG dimensions are $a = 315$ μm and $r = 120$ μm. The horizontal 3 dB Axial Ratio level is highlighted. (a) 300-350 GHz and (b) 450-500 GHz)

Circular polarization ($AR < 3dB$) is obtained with $\alpha_s = 0°$ in a frequency bandwidth larger than 40 GHz for the low frequency band (Figure 3.33 (a)) and more than 50 GHz for the high frequency band (Figure 3.33 (b)) for both, QS1 and QS2 models. Nevertheless, the QS1 antenna (discontinuous lines) exhibits overall lower (better) AR values, particularly in the high frequency band.

On the other hand, with the increase of the angular position of the connection between the diode and the antenna (α_s parameter), the AR also increases; although, circular polarization within a narrower frequency bandwidth can be still obtained. For the limit case of $\alpha_s = 90°$, showed in blue lines, there is not effective CP over any frequency range. To sum up, in the presented quasi-spiral antennas axial ratios lower than 3 dB can be obtained despite the modifications.

The CP can be tuned by means of the angle α_s and the parameters related with the PBG. However, the higher α_s, the worse CP behaviour.

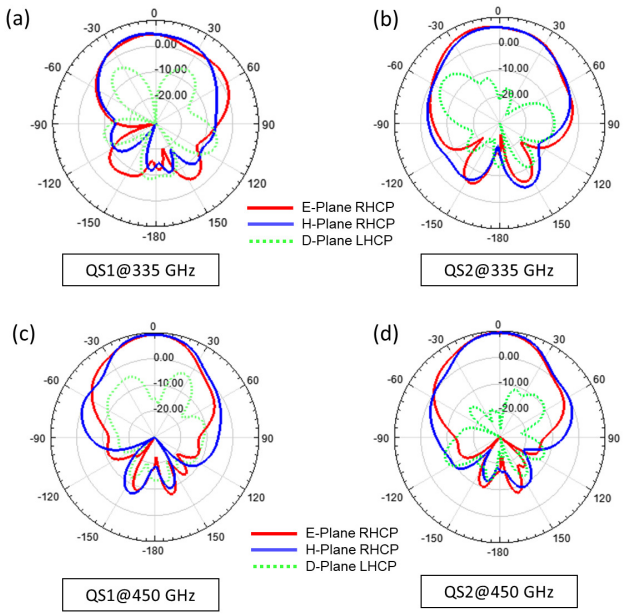

Figure 3.34: Directivity radiation pattern at 335 GHz for (a) QS1 and (b) QS2 antennas. Directivity radiation Pattern at 450 GHz for (c) QS1 and (d) QS2 antennas (with $\alpha_s = 0$).

Figure 3.34 shows the simulated directivity radiation patterns for the frequencies where best AR values was obtained at each analysed frequency bands. The polarization discrimination between RHCP and LHCP radiation patterns confirms the purity of the achieved CP. The referred patterns were obtained including the whole antenna environment, namely, the PBG structure, the Schottky diode as excitation element and the theoretical estimated losses of all materials.

Furthermore, Figure 3.35 presents the total directivity versus frequency performance for the same frequency ranges and parameters used in the CP study. From the directivity point of view, the QS1 model is superior for the lower frequency range which is presented in Figure 3.35 (a). For the higher frequency range (Figure 3.35 (b)), both spiral modifications behave similarly. Addition-

ally, the increase of α lowers the directivity of both models for both frequency ranges.

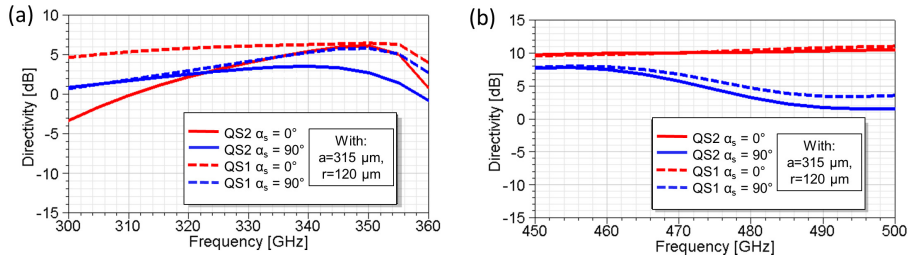

Figure 3.35: Simulated total directivity for the QS1 (discontinuous lines) and the QS2 (continuous lines) with $\alpha_s = 0°$ (red) and 90° (blue). The PBG dimensions are $a = 315$ μm and $r = 120$ μm.

Summarizing, in section 3.5.1 it was seen that the best antenna-detector coupling (using a Schottky diode as detector element) is obtained with high values of α. However, from the radiation analysis presented in this section, the overall conclusion is that a compromise must found. High values of α result in a degradation of the radiation and CP properties of the antenna but better mismatch factors.

3.6 Final Single Detector Assembly Simulation

The manufacture of the proposed device implies the use of complex fabrication techniques. We propose two different approaches for the manufacture and assembly; at the same time, the advantages and disadvantages of each one will be analysed.

3.6.1 Discrete Diode Stamping.

The first approach is the one presented in Figure 3.36 where he diode and the antenna are fabricated separately. The antenna is printed directly on the silicon wafer by means of a conventional photholitography process.On the other hand, the diode is fabricated on a 3 μm GaAs membrane, which is shaped in a way that fits in the centre of the antenna within the first Fresnel metal ring. Afterwards, the diode gold Beam Leads can be "stamped" to the antenna with the help of a high precision bounding equipment. The main advantage of this idea is that it does not affect the performance of the device at the IR range. However, for the presented frequencies, the discrete diode is too small, and the assembly will be in the limit of the discrete flip-chip mounting.

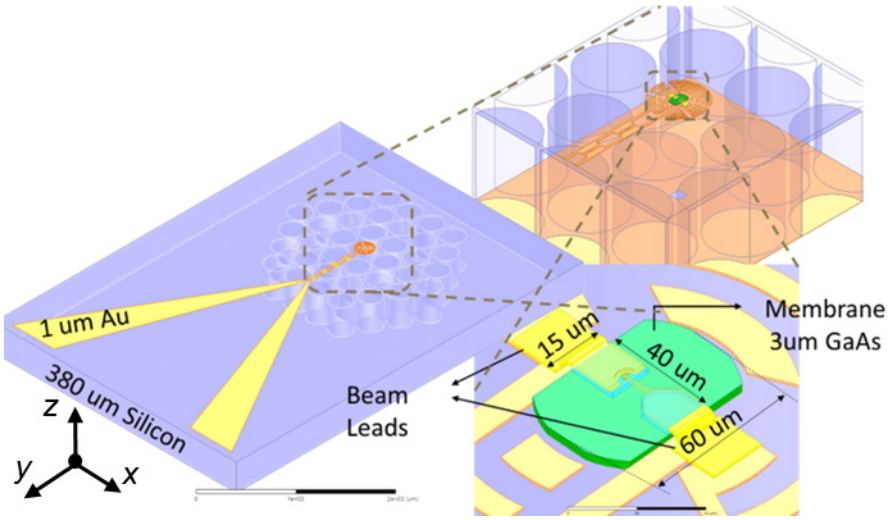

Figure 3.36: SubMMW detector with the Schottky diode stamped.

3.6.2 Integrated Detector (Antenna+Diode) in the 3 μm GaAs Membrane.

The second approach can be seen in Figure 3.37. In this case the antenna and the diode are both fabricated in the 3 μm GaAs membrane. To fix and align the antenna-diode on the slab that contains the PBG and the IR detector in the back side, a 3 μm trench with the same pattern that the membrane is etched on the top of the silicon. The read-out circuit can be connected to the output pads by stamping the beam-leads as can be seen in the image. This way, wire-bonding is avoided. Altogether, it presents a high integration level and easier assembly. Nevertheless, the performance of the IR lens can be affected if there is any air gap between the membrane and the silicon. The referred gap can be reduced with an optimum silicon etching process (i.e. no bottom roughness) and the use of silicon compression pins. The detailed microfabrication of silicon compression pins is explained in [Chat13].

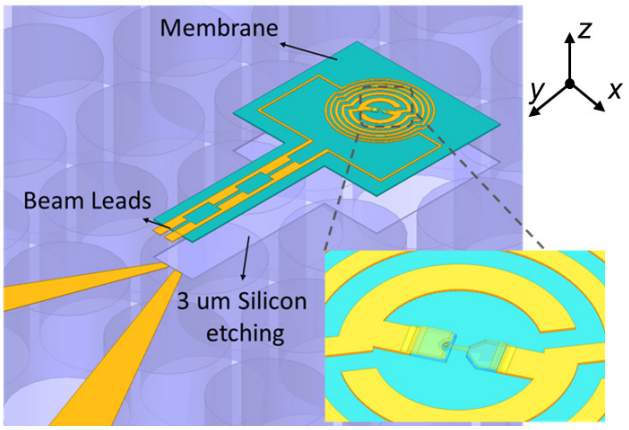

Figure 3.37: SubMMW detector with the antenna and the diode fabricated on the 3 μm GaAs membrane.

3.6.3 Combined Binary (Soret) and Grooved Dielectric FZP Lens.

The third and last proposal can be seen in Figure 3.38. It is similar to the second approach insomuch as the antenna and the diode are fabricated as an

integrated component on the GaAs membrane. However, the etching step in the silicon slab is exploited to perform a grooved Lens [Hri00] as a continuation of the planar metal lens. Therefore, the performance of the device in the IR range can be improved without affecting the SubMMW antenna performance.

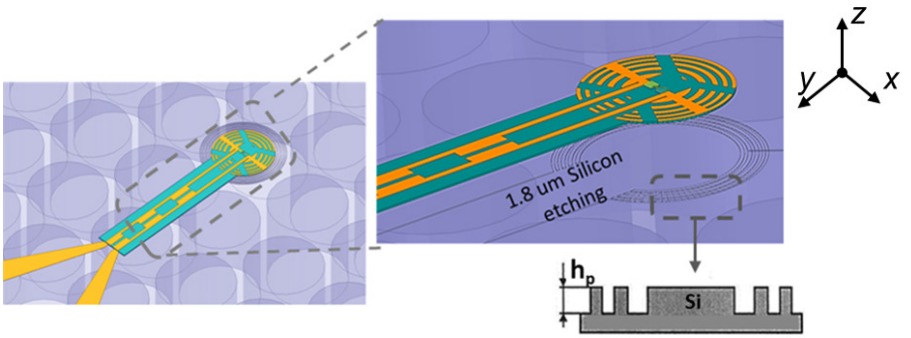

Figure 3.38: SubMMW detector with the antenna and the diode fabricated on the 3 μm GaAs membrane combined with a silicon etched grooved lens.

For simplicity, the grooved lens was designed with two phase levels (phase-reversal lens). The depth of the etching must be 1.8 μm (i.e. $\lambda/2(\sqrt{\epsilon_r}-1)$) [Hri00] to achieve a phase difference of 180 ° in the Fresnel Zones. In order to better understand and evaluate the advantages of the composite binary-grooved FZP lens, the structures where analytical simulated employing the KD theory method (Section 3.3). Figure 3.39 shows the simulated FG of two variations of the combined lenses, namely a Soret 10-FZPL followed by 10 additional zones of a grooved lens (blue line) and a Soret 6-FZPL followed by 14 extra zones of a grooved lens (green line). Additionally the FG of a conventional 10-FZPL (black continuous lines), 10 zones reversal-phase grooved lens (discontinuous black line) and 20 zones reversal-phase grooved lens (discontinuous red line) were simulated and included in Figure 3.39. The proposed combined lens would certainly increases the IR lens performance.

Concluding, the last approach is the most integrated and advanced idea. By going one step further, and taking advantage from the combination of lenses, the metallic parts of the amplitude binary lens that do not contribute to the performance of the SubMMW antennas may be totally replaced by grooved

zones. Nevertheless, it is challenging from the fabrication point of view, because of the assembly and because the silicon etching of structures with very different aspect ratio with the same rate of etching (i.e. etching exactly the same height in structures with different dimensions) is a difficult task.

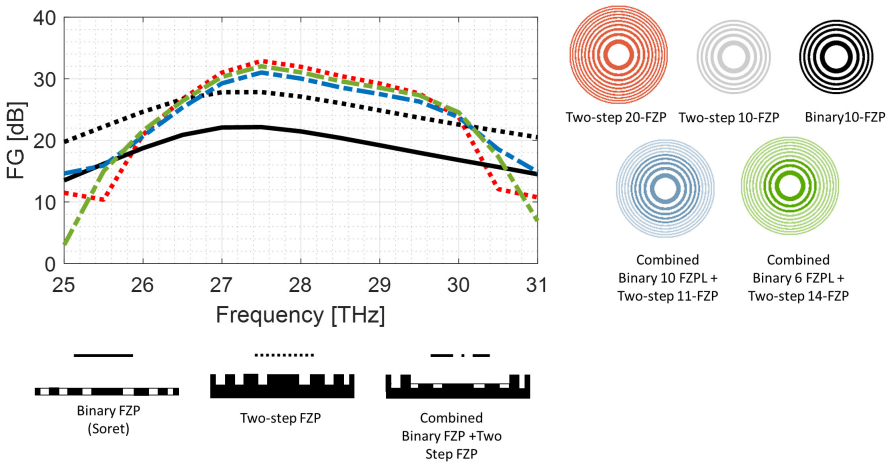

Figure 3.39: Focal Gain *vs* frequency calculated employing KD Theory for binary (Soret) lens, grooved dielectric lens and a combination of both. Black solid line represents the binary 10-FZP, discontinuous lines represents a grooved dielectric lens with two levels of phase correction and the dashed dot line are the combined binary-grooved lenses.

3.6.4 Simulated Final Detector Responsivities

Considering all the presented study up to here, three final devices were evaluated combining the input impedance results obtained with HFSS simulations and the non-linear ADS modelling. The loaded voltage responsivity results obtained with 10 kΩ output load can be seen in Figure 3.40. The discontinuous black line represents the maximum possible achievable responsivity under RF matching condition within the whole frequency band. A summary of the main dimensions of the designs presented in in Figure 3.40 can be found in Table 3.3.

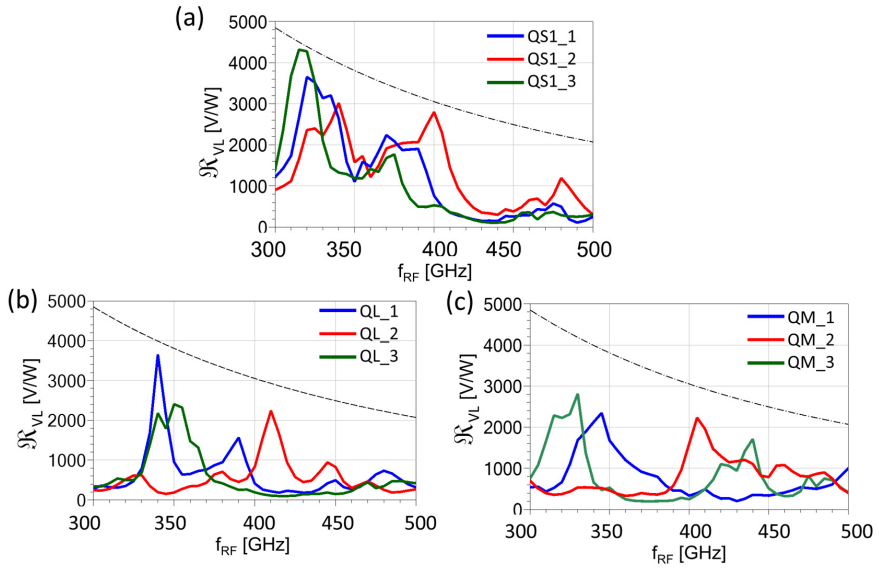

Figure 3.40: Simulated loaded voltage responsivity of final assembly detectors with R_L=10 kΩ including the PBG surrounding substrate and the RF-Choke. (a) Quasi-Spiral-1, (b) quasi-log and (c) quasi-meander based detector.

The first result (Figure 3.40(a)) corresponds to the simulation of three variations of the QS1 modified antenna based on the fabrication approach shown in Figure 3.37. Indeed, the simulation takes into account all the environment of the antenna-diode, namely, the diode layout, the surrounding PBG and the RF-Choke filter. Responsivities higher than 1000 V/W can be obtained in a fractional bandwidth around 30 % from 300 GHz to 400 GHz. Moreover, it

Table 3.3: Modified Lens-Antenna Dimensions

Model	Parameter	Description	Var 1	Var 2	Var 3
QS1	Angular connection	α_s	110°	95°	140°
	Feed Width	w	30μm	40 μm	30μm
QL	External Taper Angle	β_L	25°	25°	6°
	Internal Taper Angle	α_L	2°	2°	2°
	Feed Width	w	30μm	20 μm	5μm
	Distance to the 1^{st} filter section	d_f	70μm	160 μm	70μm
QM	Taper Angle	β_M	30°	30ree	10°
	Feed Width	w	20μm	20 μm	5μm
	Distance to the 1^{st} filter section	d_f	140μm	70 μm	90μm

is remarkable that perfect conjugate matching with associated responsivities higher than 4000 V/W can be achieved for a narrow frequency bandwidth.

The second and third simulated detectors are based on the antenna and the diode fabricated on the 3 μm GaAs membrane combined with a silicon grooved lens. Figure 3.40(b) presents the responsivities achieves for the variations of the Quasi-Log antenna listed in Table 3.3. No broadband behaviour can be obtained with this model. However, almost maximum responsivities can be obtained over a narrow frequency band. As a final result, the Quasi-Meander model was simulated and some of the interesting results can be found in Figure 3.40(c). Oppositely to the expected from the resonant folded dipole antenna, no matching condition was achieved although some acceptable responsivities higher than 1000 V/W can be obtained around 390-460 GHz in a 16 % bandwidth.

3.7 Conclusions

The integration of the IR and SubMMW wave ranges is highly attractive for many space and earth applications. Both frequency ranges provide complementary information that enhance the potential of such detector. Although some preliminary demonstrations of a dual-band detector based on a FZPL had already taken place, they were mainly focused on the study of the IR part of the detector.

In this chapter, the design of several SubMMW antennas, which also act as FZPL at IR frequencies ($\lambda_0 = 10.6$ μm) has been presented. Different variations of spirals, bow-tie and meander antennas suitable for the integrated detector were evaluated by means of a numerical analysis based on KD-Theory. From the comparison of the modified lenses with the conventional FZPL, we conclude that the quasi-spiral antennas are the ones that best emulate the lens performance. Two quasi-spiral variations, based on different ways to connect the rings, were addressed with no appreciable difference on its IR focusing performance. Moreover, the modifications based on bow-tie and meander antennas exhibited different levels of degradations of the focal gain accordingly with the obstruction made on the Fresnel zones. However, the achieved FG were always lower than the one obtained with the quasi-spiral modification and more pronounced undesired side lobes were found.

In the second part of the chapter, the modified antennas were analysed in the frequency range from 300 to 500 GHz in terms of both, input impedance and radiation properties. For each antenna, the influence of its main design variables on the input impedance was studied. Regarding to this, it can be said that the quasi-spiral designs act as a kind of wide band antenna where the input impedance can be modified with the variation of the angular position of the connection between the diode and the spiral. Furthermore, the tuneable inductive behaviour exhibited for both quasi-spiral designs made them suitable to be matched with the Schottky diode detector. Alternatively, the variations performed on the bow-tie and meander designs showed a resonant behaviour with good matching capabilities in narrower bandwidth. For these last antennas, an additional way to connect the DC lines was included. The RF-Choke planar filter was directly connected to the dipole terminals in a way that cuts the Fresnel rings. These major modifications in the lens were reflected in a lower and distorted focusing performance.

To complete the analysis of the overall detector behaviour, the radiation performance of the quasi-spiral antenna was evaluated. Firstly, it was shown that

the excitation of undesired surface wave modes degrades the radiation patterns in this device. Consecutively, to overcome this problem, a solution based on Photonic Band Gap structures surrounding the antenna was proposed. Finally, the general description of three fabrication approaches for a final prototype was presented. The projected designs take into account the state-of-the-art fabrication techniques and propose a promising approach that combines a silicon micromachine phase correcting lens with the metal lens. This way, the lens performance in terms of FG and efficiency can be highly improved. Lastly, based on all the results presented in this Chapter and in Chapter 2, the predicted responsivity of three example devices were evaluated by combining the results obtained with the 3D-EM full-wave simulations and the non-linear ADS modelling.

Some first fabrication test for the proposed devices were carried out in our facilities. Details of these preliminary fabrications can be found in the Appendix A. Nevertheless, the dimensions of the designed prototypes are in the limit of the photolithography process available in our clean room. The prototypes are still pending of fabrication in an external facility.

Chapter 4

Modified Soret Lenses for Dual Band Integrated Detectors at Millimetre and Submillimetre Wavelengths

4.1 Introduction

The design of an integrated dual-band detector for IR and SubMMW based on the modification of Fresnel Plate lenses was addressed in Chapter 3. Another potential application of this kind of integrated sensors may be the simultaneous detection of two closer frequency ranges, such as the millimetre (MMW) and submillimetre (SubMMW) wavelengths. As stated previously, these frequencies share many common characteristics that make them worthy for security, production technology, medical imaging and non-destructive inspection scanners. However, each range exhibits pros and cons, making their combination very attractive. On the one hand, the MMW range presents well-developed technologic solutions and allows integration with MMIC components [Yuj03]. This range provides good penetrability through some barrier materials compared to SubMMW, where the majority of the solid are less "transparent" [Fed05].

Furthermore, 30-300 GHz imaging systems both passive and active have been demonstrated and can be used in outdoor operation, as is the case of surveillance in poor weather condition [App07a]. On the other hand, the SubMMW range presents higher spatial resolution because of the smaller wavelength. This might be translated into the possibility of better identification of concealed threats based on their shape. Moreover, the SubMMW presents spectroscopic signatures for some explosives, biological and chemical agents and illegal drugs [App07b, Fed05], whereas there is no spectral information available to identify materials in the MMW waveband [App07a]. Finally, the atmosphere is strongly absorbing in the SubMMW, at 1 THz the attenuation is five order of magnitude higher than at 100 GHz. Therefore, the range of SubMMW applications is limited.

That is why multi-band imaging combining the MMW and SubMMW ranges can be of particular interest. The combination of the information at both frequency ranges might allow to enhance discrimination between different types of objects or materials, enabling the detection and identification even of concealed potential threats. Furthermore, compact multi-band detectors in the millimetre and terahertz ranges might find applications in radiometers for the study of several radioastronomical or meteorological events [NRC07].

In this chapter, we extend the study of the dual-band detectors to close frequency bands and analyse theoretically and experimentally the behaviour of new structures, which can serve as flat Soret-like lenses and antennas simultaneously. The standard Soret lens, working at 800-900 GHz, will be approximated by several W-band antenna shapes. This frequency band corresponds to one of the atmospheric window that permits ground-based observations and has been employed for earth exploration-satellite services, space research services and active imaging [NRC07, Han13] applications. The large spectral separation of the frequencies employed for the IR-SubMMW detector (Chapter 3) allows the design of the diffractive lens with a large focal distance. Conversely, the approach presented here implies a design based on a short focal length. Therefore, the fast scalar Kirchhoff's diffraction (KD) method is not accurate enough and 3D Full-Wave electromagnetic simulations must be employed. Finally, several prototypes were fabricated and their performance experimentally evaluated.

4.2 Detector Configuration

In the SubMMW range, direct detectors usually rely on quasi-optical antennas based on dielectric lenses or reflectors. Important improvements have been recently reported in this field, based on conventional silicon lenses. These have demonstrated bandwidth larger than one octave and dual-polarization operation with simple solutions [Yur16, Bue17]. Nevertheless, although silicon lenses have proven to be the best solution to the problems of low gain and high losses, they are bulky components, which increases the system cost and size. A possible solution to improve the gain and reduce the substrate associated losses is to use Fresnel Zone Plate lenses [Gou92, Pou18, Min17], which are based exclusively on planar elements.

Along the same lines as in Chapter 3, the goal is to combine two detectors in an integrated structure and the proposed solution is based on a modified FZPL printed on top of a silicon slab. First, a conventional FZPL in transmission mode is designed to operate in the SubMMW range, specifically centred around 850 GHz. This lens will focus the radiation onto the opposite side of the dielectric slab, where the detector would be placed

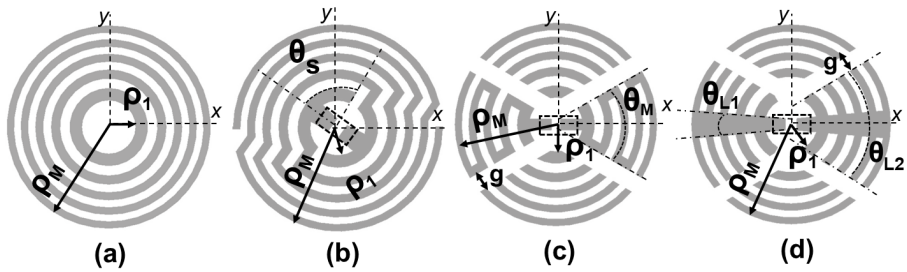

Figure 4.1: Proposed modified 10-FZPL that can act as antenna: (a) Conventional 10-FZPL; (b) quasi-spiral antenna; (c) quasi-meander antenna; (d) quasi-log antenna.

Afterwards, following the same criteria described in Charpter 3, the planar lens was modified to create a planar MMW antenna. Figure 4.1 shows the three evaluated modifications of the Soret lens (a), based on spiral (b), meander (c) and logarithmic (d) designs. In order to maintain the focusing properties of the planar lens we should not modify the radii of the Fresnel zones. Therefore, the antennas are constructed by connecting or opening the metal lens rings. The

dashed square in the centre of each antenna in Figure 4.1 represents the position and approximate dimensions of the direct detection element.

A commercial 520 μm thick high resistivity float zone silicon slab ($\epsilon_r = 11.67$; $\rho \sim 10^4\ \Omega \cdot cm$) is employed. The total number of zones (M_t) is chosen to be 10 and the focal distance (F) equals the thickness of the silicon slab, 520 μm ($\sim 5.03\ \lambda_d$). Employing equation (3.1) for the calculation of the lens radii, 10 zones lead to a lens diameter of 1800 μm. Thus, the focal-length-to-diameter ratio (F/D) is 0.29. The main goal in this approach is the analysis of the SubMMW modified lens and the evaluation of the feasibility of a design with such low focal number.

Nevertheless, it is important to keep in mind that the study of the impedance of the proposed modified lens antennas is necessary in order to maximize the low-frequency detector responsivity. A detailed analysis of the impedance requirements in a direct detector at 300-500 GHz based on a Schottky diode was given in Chapter 3. Even though a detailed study is not included in this work, we will discuss some basic properties of the input impedance of the modified antenna-lenses in the next section.

4.3 Low Frequency Band Antenna Performance Overview

It was shown that the antenna impedance is one of the most important parameters when optimizing the detector responsivity. To this aim, the impedance matching between the detection element and the antenna must be maximized. The reasons why Schottky barrier diode (SBD) are among the most employed uncooled sub-THz direct detection elements were exposed in Chapter 2. In terms of impedance, these devices have in common an internal resistive part (where the rectification occurs) and extra internal and external parasitic reactances (usually mainly capacitive) [Car15]. Therefore, the antennas should be designed to match these detection elements.

Figure 4.2 presents an example of the Load-Pull analysis performed for a commercial zero-bias Schottky diode [VDIa] in a direct detector configuration from 50 GHz to 100 GHz. The constant responsivity circuits represented in the Smith Chart serve as a reference to evaluate the required input impedance of the antennas.

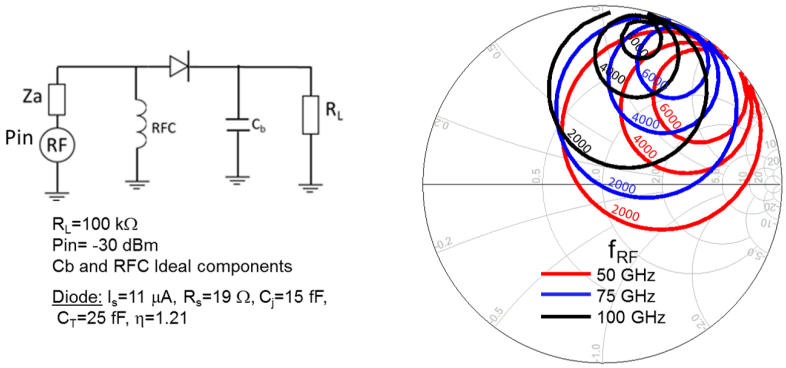

Figure 4.2: (a) Schematic circuit for the load-pull analysis performed with a commercial zero-bias diode for 50, 75 and 100 GHz. (b) 6000, 4000 and 2000 constant responsivity circles represented in the Smith chart.

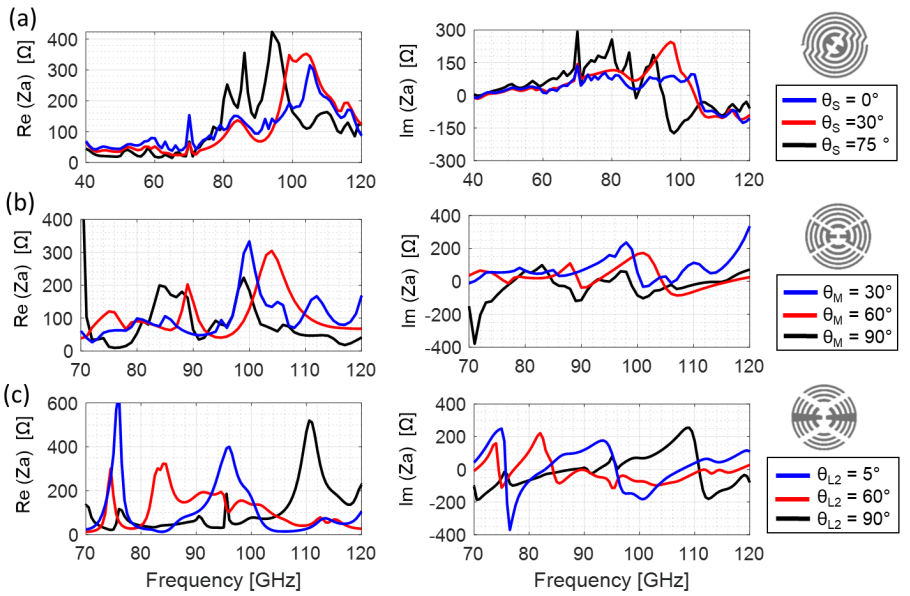

Figure 4.3: Real part (left) and imaginary part (right) of the input impedance of the modified antenna-lenses: (a) quasi-spiral antenna; (b) quasi-meander antenna; and (c) quasi-log antenna.

Figure 4.3 shows the simulated input impedance of the proposed antenna variations in the low-frequency band. Three variation of each design are presented just to describe the possibility of optimizing the mismatch factor in each case. Moreover, it must be taken into account that the MMW antenna operates on a high permittivity substrate with 0.65λ thickness at the upper edge of the W-band; thus, surface-wave contributions are not negligible. It was previously shown that a solution based on Photonic Band-Gap structures (PBG) would help to solve this problem. In this case, for simplification, instead of analysing the PBG, we simulate the substrate as a finite cylinder with 1500 μm radius. This set-up would emulate a PBG cavity of this size.

From Figure 4.3 (a) it can be seen that the input impedance of the quasi-spiral antennas is stable in frequency up to 80 GHz. This agrees with the theoretical highest operational frequency of a conventional spiral antenna with the same inner radius [Wat08]. Following the same line, the outer Fresnel ring

radius leads to a minimum operational frequency of 15 GHz in a frequency independent spiral antenna. The imaginary part of the impedance exhibits an inductive behaviour, which would be very attractive to optimize coupling to the detectors mentioned above. Therefore, this prototype could be used to cover the V and E-Bands and the lower part of the W-Band.

For the quasi-meander and quasi-log structures, multiple resonances associated with the excited dipoles can be seen in Figure 4.3 (b) and (c). In these two models, the non-exited sections of the lens would act as parasitic radiators. Finally, the performance of these antennas is similar to the one described in Section 3.5, where they were explored in more detail.

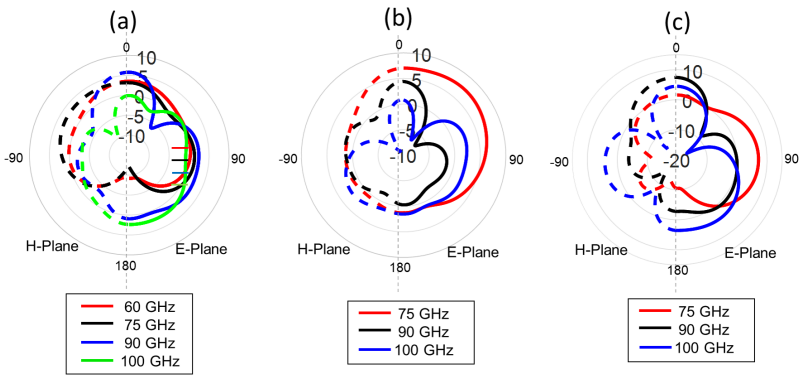

Figure 4.4: Gain radiation patterns of the modified antenna-lenses: (a) quasi-spiral antenna; (b) quasi-meander antenna; (c) and quasi-log antenna.

The gain radiation patterns of the three proposed modified antenna-lens with the dimensions presented in Table 4.1 are shown in Figure 4.4. Furthermore, the simulation of the radiation patterns includes the substrate, metal and matching losses.The simulated gain at the central frequency, i.e. 90 GHz, is 5.8, 4.53 and 7.47 dB for the quasi-spiral, quasi-meander and quasi-log model respectively. The corresponding radiation efficiency is 89 and 90 % (assuming $\tan\delta = 0.000154$, which results from the silicon resistivity $\rho = 10^5\ \Omega \cdot cm$).

There are multiple variables that can be varied in each design either to control the impedance or to optimize the performance of the modified lens-antenna in the low frequency band (preserving the main parameters of the FZPL). However, these initial variations were chosen because they correspond to substantial modifications of the lens that retain an acceptable impedance and

radiation performance in the low frequency band. The following sections will be devoted to the study of the modified lens antennas as focusing elements for the high frequency band.

Table 4.1: Dimensions of the modified lenses

Parameter	Description	Value
ρ_1	1^{st} Fresnel zone radius	237 μm
ρ_{10}	10^{th} Fresnel zone radius	896 μm
g	Gap	150 μm
θ_S	Quasi-spiral rotation	75°
θ_M	Quasi-meander angular size	63°
θ_{L1}	Quasi-log feed angular size	10°
θ_{L2}	Quasi-log angular size	60°

4.4 Modified Fresnel Plate Lens-Antennas Analysis

Conventionally, Soret lenses have been designed to operate as if immersed in air. Physically, they would be manufactured by printing the metallic pattern on a thin low-permittivity substrate and the feed element would be placed at a certain distance in other support structure. Therefore, one of the objectives of this analysis is the study of the effect on the lens performance of the high permittivity finite thickness substrate. The analysis of the semi-infinite substrate model is included to discern the influence of the lens modification and of the finite slab presence in a short focal number design.

The prototypes chosen for the analysis are those with the dimensions presented in Table 4.1. To start with, a numerical approximation based on the scalar KD theory was performed to obtain a first initial fast result. Afterwards, for a complete and accurate solution, the 3D full-wave electromagnetic simulation of the realistic model was done by means of the FDTD solver of the commercial software EMPro v.2019. The excitation was defined as a plane wave impinging normally on the lens-antenna side ($z = 0$) and the minimum and maximum mesh cell size employed was 5 μm ($0.014\lambda_0$) and 20 μm ($0.057\lambda_0$) respectively.

The focusing process can be visualized in a 2D map of the E-field distribution which is shown for the xz-plane (Figure 4.5) and yz-plane (Figure 4.6). In these plots, the analytical (a) and the simulated results at 840 GHz for a semi-infinite silicon slab (b and c) and for the 520 μm thick slab (d and e) are presented. Due to the non-symmetrical nature of the proposed modified lenses the full-wave simulation results were obtained for vertical and horizontal polarized incident plane-waves. So far, all the structures clearly keep on acting as lenses for both polarizations regardless of the introduced modifications. A clearly defined focus appears around $5\lambda_d$ (520 μm), which is the focus distance (F) in all designs. Analytical KD theory results in Figure 4.5 (a) and full-wave simulated results (b and c) are in good agreement, despite all the assumptions used for the KD based solution, validating it for a general initial fast analysis. The expected internal reflections in the dielectric slab and reflections at the dielectric-air interface due to the high index contrast, are plainly visible in Figure 4.5 (d and e). Their effect, simultaneously with the influence of the polarization, will be further studied.

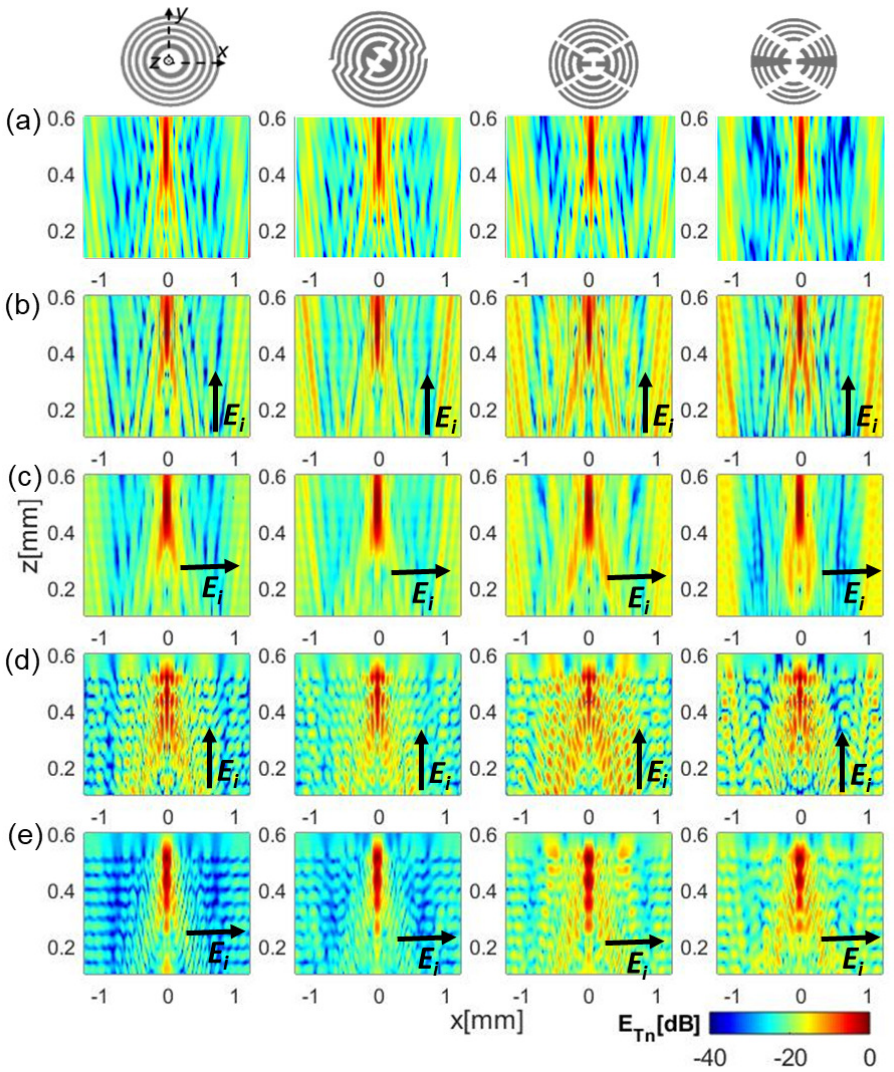

Figure 4.5: Normalized E-field distribution on the xz-plane at 840 GHz for: (a) KD theory results. (b) Full-wave simulated results for vertical polarization and (c) horizontal polarization with infinite substrate and for (d) vertical polarization and
(e) horizontal polarization with 520 μm thick substrate.

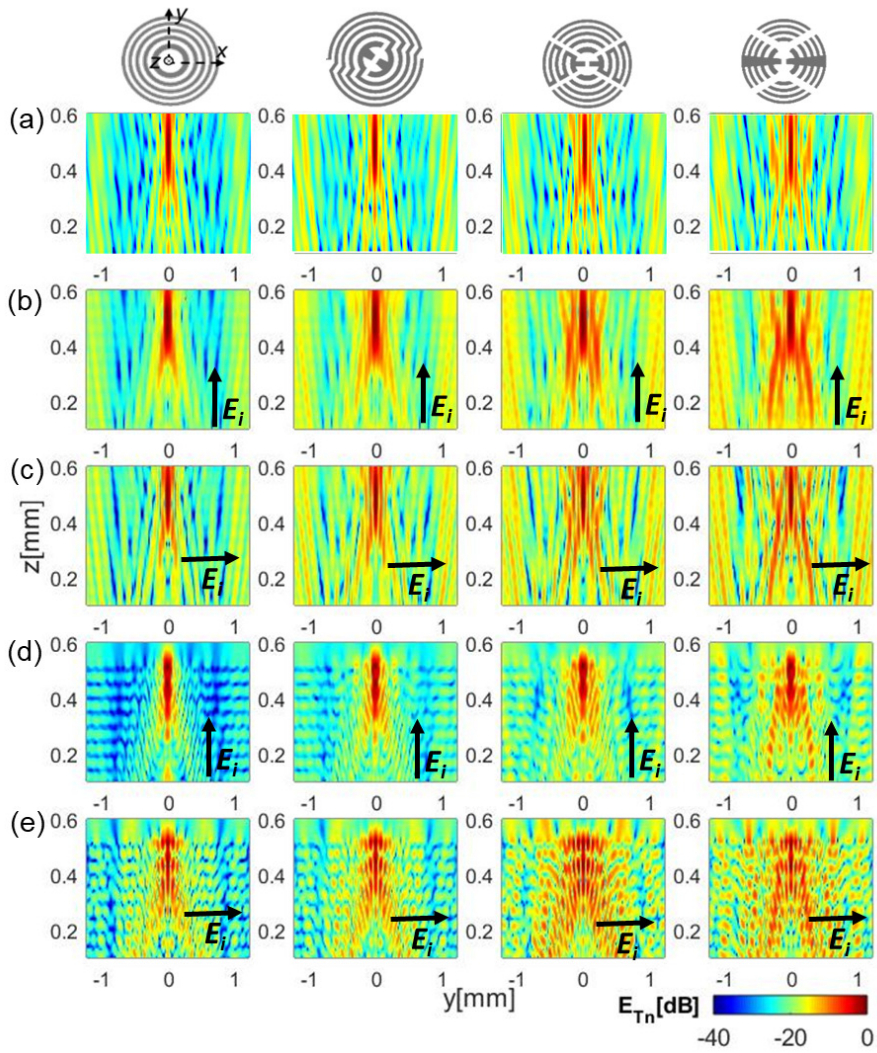

Figure 4.6: Normalized E-field distribution on the yz-plane at 840 GHz for: (a) KD theory results. (b) Full-wave simulated results for vertical polarization and (c) horizontal polarization with infinite substrate and for (d) vertical polarization and (e) horizontal polarization with 520 μm thick substrate.

Figure 4.7 shows the FG (defined in Equation 3.4) and E-field magnitude values at the focal point versus frequency for the case of semi-infinite silicon substrate and finite silicon slab (520 μm thickness) with vertical and horizontal polarizations, obtained with the full-wave simulations. KD theoretical results are also included in Figure 4.7. The maximum FG at 855 GHz for the 10-FZPL lens is 18.6 dB, whereas it is 17.1 dB for the quasi-spiral, 16 dB for the quasi-meander and 15.3 dB in the quasi-log design for the infinite substrate case. Thus, the predictable price paid for the modification performed in the lens geometry is a drop in the focal gain. The quasi-spiral design is the one that bears largest resemblance to the performance of the conventional lens, whilst the quasi-meander and quasi-log approaches reach comparable performance.

All the FZPL exhibit chromatic aberration (i.e the lens focusing quality is frequency dependent) [Hri00], which is an expected phenomenon in the flat lenses and the main cause of their limited bandwidth. For all the infinite slab cases the maximum FG is slightly shifted to higher frequencies than the design one (850 GHz). This frequency dependence and restricted bandwidth is even more pronounced in the finite slab case. The finite thickness of the dielectric slab causes that the internally reflected waves interact with the diffracted waves at the focal point leading to either constructive or destructive field interference depending on the frequency and the slab thickness. For the realistic finite slab models the maximum FG for the 10 zones Soret lens at 840 GHz is 24.7 dB, it is 23 dB for the quasi-spiral, 21 dB for the quasi-meander and 19.9 dB in the quasi-log design for horizontal polarization. These represent around 6 dB and 4.6 dB improvement of the FG for the best and the worst case respectively. Nevertheless, the FG response becomes frequency dependent and we can obtain higher gains but in narrower bandwidth. Due to this narrowband performance, they will not cover the full 800 - 900 GHz band, and the specific operation frequency should be selected according to the application. Note that there is another maximum value at frequencies higher than 900 GHz. However, this is at the border of the atmospheric window and we will focus the next studies and measurements on frequencies around 840 GHz.

Furthermore, as expected, the conventional FZPL is not affected by polarization changes; however, the asymmetries introduced in the modified lenses made them sensitive to it. The influence of the polarization is stronger for the quasi-meander and quasi-log models than for the quasi-spiral case.

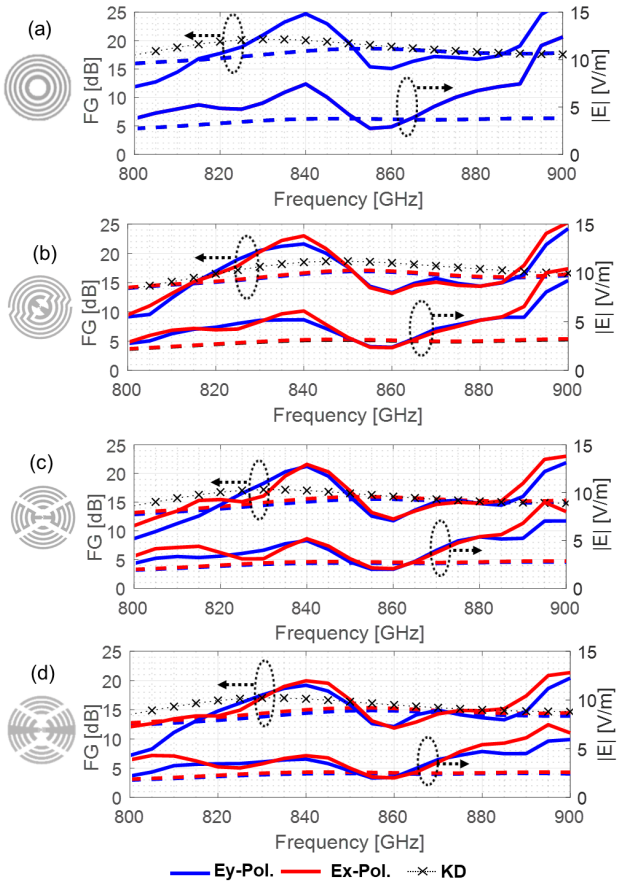

Figure 4.7: Focusing Gain and E-field magnitude at the focal point ($x = 0$, $y = 0$, $z = 520$ μm) *vs* frequency for infinite silicon substrate (dashed lines) and silicon slab (solid lines) with vertical (blue) and horizontal (red) polarized incident wave (FDTD simulation). KD theory result (x-marker). (a) 10-FZPL, (b) quasi-spiral, (c) quasi-meander and (d) quasi-log models.

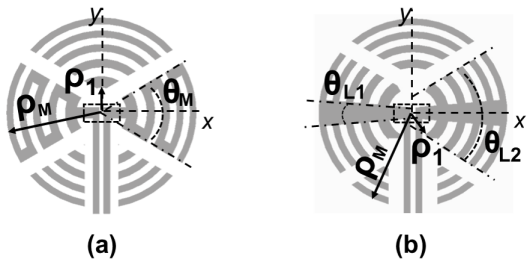

Figure 4.8: (a) Quasi-meander and (b) quasi-log modified lens models.

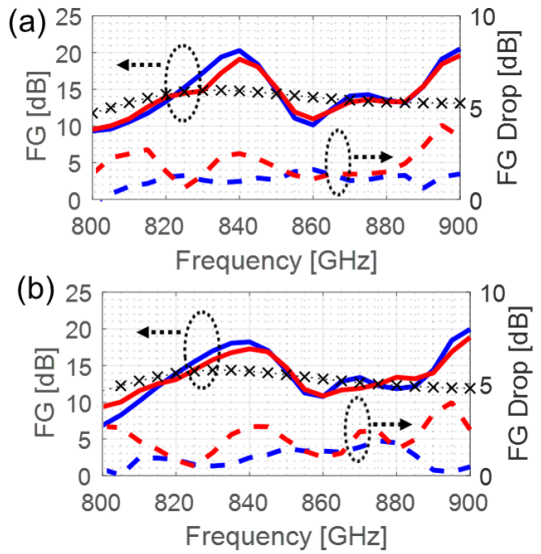

Figure 4.9: Focusing gain and focusing gain drop at the focal point ($x = 0$, $y = 0$, $z = 520$ μm) *vs* frequency with vertical (blue) and horizontal (red) polarized incident wave (FDTD simulation). KD theory result (x-marker) (a) quasi-meander and (b) quasi-log modified lens models.

Up to this point, the studied antennas were intended to work as direct detectors for the low frequency band. The read-out lines required to extract the envelope signal could be added to the outer rings of the spiral, or at the end of the meander or log dipoles [Sem10]. Nevertheless, more aggressive modifications might be made in the quasi-meander and quasi-log models to evaluate more complex designs which could be used as heterodyne receptors. To this end, feed lines would be connected to the non-linear element to get the IF signal. The new modified lens can be seen in Figure 4.8. The simulated FG of the new modified lenses as well as the focal gain reduction (w.r.t the quasi-meander and quasi-log designs in Figure 4.1) are shown in Figure 4.9. Around 2 dB deterioration of the FG due to the insertion of the read-out lines in the lower part of the lens can be seen. Nevertheless, the structures still act as focusing devices despite the major modifications in the lens geometry. A better understanding of the behaviour of the modified quasi-meander and quasi-log models can be obtained from Figure 4.10, where the E-field distributions are shown. The xz-plane field distribution is similar to that of the original models with higher side-lobe levels. However, in the yz-plane it can be observed that with the modified feed lines half of the structure barely contributes to the focusing process, which results in a significant field asymmetry.

A comparison between the simulated FG obtained with Full-Wave EM simulation for both infinite and finite substrate, and KD theoretical gain (at 840 GHz) is presented in Table 4.2. The focal size dimensions (defined as the separation in which the magnitude of the field decreases by 50 % (or -3 dB) from the peak focus intensity) are also included. From the comparison between the FG values for the full wave simulation in the finite slab and KD theory, we can observe a difference around 4.5 dB. As it was explained in Section 4.4, KD theory assumes an infinite medium. Thus, the multiple reflections in the finite substrate are not taken into account. Nevertheless, the FG values obtained with the KD method resemble those shown in Figure 4.7 for an infinite silicon. The focal size dimensions were obtained with 5 μm resolution in all cases and present slightly wider area for the full-wave slab simulations.

Summarizing, different kind of MMW antennas can be candidates to act as planar lenses at SubMMW, even with very short focal length. The quasi-spiral approach is the one with better performance, but other modified antennas can be employed depending on the application requirements. Even when major modifications are applied in the antenna-lenses, focusing properties can be obtained, which is a great advantage in order to perform a simultaneous optimization of the antenna and the lens properties.

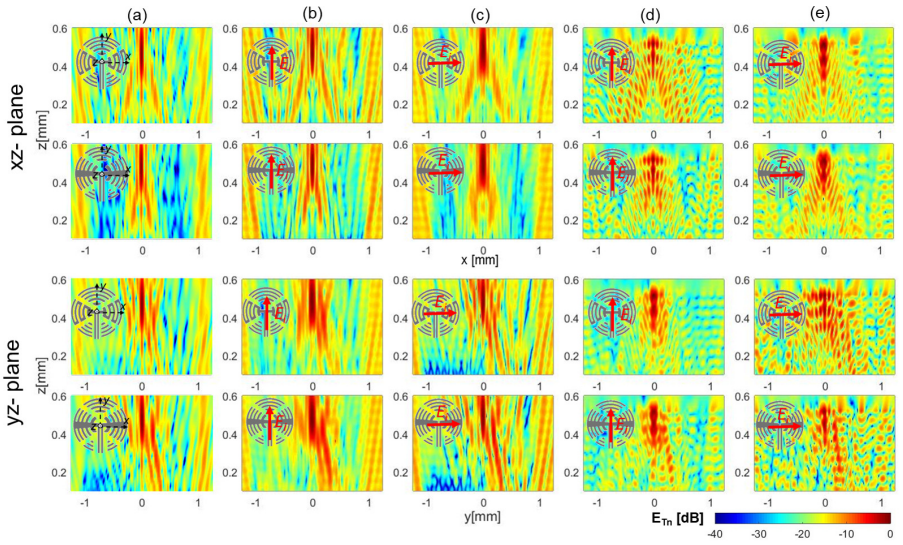

Figure 4.10: Normalized E-field distribution on the xz-plane and yz-plane at 840 GHz for: (a) KD theory results. (b) Full-wave simulated results for vertical polarization and (c) horizontal polarization with infinite substrate and for (d) vertical polarization and (e) horizontal polarization with 520 μm thick slab.

Table 4.2: Modified Lens Quantitative Comparison

	FD (KD)	FG (I-FW)	FG (Slab-FW)	Focal Size (KD)	Focal Size (Slab-FW)
FZPL	20	18.17	24.7	55x50	75x70
Q-Spiral	18.5	16.7	23	55x50	60x60
Q-Meander	17.3	15.6	21	55x40	70x60
Q-Log	16.8	15	20	55x40	70x60
Q-Meander-M	14.8	13.8	20.3	60x45	85x55
Q-Log-M	14.2	13.3	18.2	50x45	80x55

All gain values are in dB and Focal Sizes are in μm.

4.5 Efficiency

For a Fresnel lens antenna, the overall aperture efficiency (without including the radiation efficiency of the feeder) is the product of the spillover (η_s), taper (η_t) and phase efficiencies (η_p) [Bag92]:

$$\eta = \eta_s \eta_t \eta_p \tag{4.1}$$

The last one (i.e. η_p) is characteristic for this kind of lenses and can be defined as the ratio of the radiated power in the forward direction and the radiated power in the forward direction under the condition that the phase of the field in the antenna aperture is constant. The spillover and taper efficiencies are defined in the same way as in a conventional lens-antenna. Therefore, the spillover efficiency is the ratio of the power intercepted by the aperture to the total power radiated by the feed, whilst the illumination efficiency is determined by the distribution of the field on the antenna surface. Equation and definitions employed to calculate the individual and overall efficiencies can be found in [Kil85, Col84, Bag92].

Compared to hyperbolic dielectric lenses which reach around 50-60 % efficiency, absorbing/transparent FZP lenses have lower aperture efficiency (on the order of 10 %)[Hri00]. This is a result of the significant amount of energy blocked in the aperture by the metal zones and it is the prize to pay for the improvement in size and weight.

The theoretical total efficiency versus cos^n-like radiation pattern amplitude weighting can be analysed to obtain a feeder that uniformly illuminates the lens surface to maximize the efficiency [Col84]. The radiation pattern field of this feed, $G_f(\varphi, n)$, can be modelled by:

$$G_f(\varphi, n) = \begin{cases} 2(n+1)cos^n(\varphi) & 0 \leq \varphi \leq \pi/2 \\ 0 & \pi/2 < \varphi \leq \pi \end{cases} \tag{4.2}$$

For such an illumination, the overall efficiency (η) can be calculated as [Bag92]:

$$\eta = \left| \frac{1}{D} \sum_m \int_{\varphi_{m+1}}^{\varphi_m} (\cos(\varphi) + 1) \sqrt{2(n+1)cos^n(\varphi)} \frac{\sin(\varphi)}{\cos^2(\varphi)} F e^{-j(\frac{kF}{\cos(\varphi)} - \frac{m2\pi}{P})} d\varphi \right|^2 \tag{4.3}$$

where m is the number of the "open" Fresnel zones, P is the quantification level and F is the focal length:

- Binary amplitude zones (Soret Lens)→ P=2 → (m=0,2,4...Mt).
- Phase-correcting zones → P ≥ 2 (m=0,1,2...Mt).

Figure 4.11 shows the efficiency curves for different cos^n-like radiation pattern amplitude weighting versus the focal distances (F) with a fixed value of the lens diameter (D = 1800 μm). This means, the study of different silicon slabs thickness setting the value of the lens diameter to preserve the antenna for the low frequency band. Nevertheless, to keep a fixed diameter with larger focal distance, the total number of zones must be reduced. Thus, the low-band antenna should be modified accordingly. The steps appreciated in the curves correspond with the change in the number of zones. The efficiency results agree with the theory and show a maximum efficiency of 8 % for the presented design with a wide beam illumination (n = 2.5). Slightly higher efficiencies could be obtained for larger focal lengths with more directive illumination.

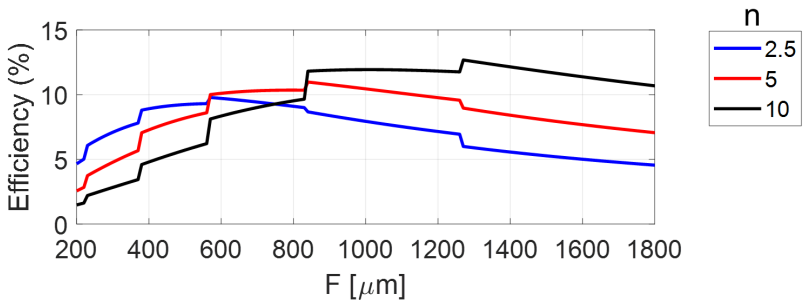

Figure 4.11: Total efficiency versus focal distance for different cos^n-like illuminations.

Figure 4.12 presents a similar analysis of the overall efficiency versus the amplitude weighting generated by a cos^n-like illumination for three different short focal length values with a fixed lens diameter ($D = 1800\ \mu$m). It is evident that narrower subtended angles require more directive patterns (i.e. higher n values) to obtain maximum efficiency. Nevertheless, for a binary amplitude lens the overall efficiency will be always limited to values lower than 10 %.

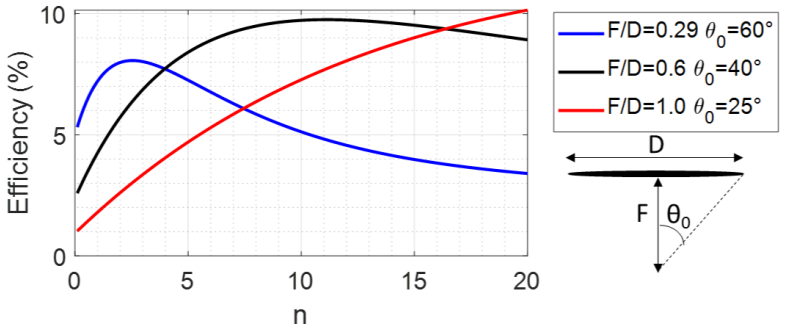

Figure 4.12: Total efficiency versus amplitude weighting generated by cos^n-like illumination.

A better insight of this limitation of the Soret lenses is obtained from the assess of the individual contribution of the involved efficiencies, namely, spillover, taper and phase efficiencies. The formulation employed for the calculation of each efficiency can be found at [Bag92]. Figure 4.13 shows the result of the referred analysis for two short F/D cases. It can be seen that the phase efficiency for two quantification levels ($P = 2$) is limited to around 40 %. However, the major constraints are imposed by the taper efficiency. This is not surprisingly because the illumination (taper) efficiency expresses how uniform the E-Field is across the plate lens aperture and in the binary amplitude lens a considerable part of the field is blocked in the obscure zones. A known solution to increase this efficiency is by increasing F/D, but this leads to a compromise with the decrease of the spillover efficiency.

Consequently, the only way to substantially rise the overall efficiency is by substituting the absorbing/transparent zones by phase correcting zones. Putting aside the modified Soret lenses and assuming the possibility of fabricating a multi-height design, the overall efficiency can be risen up to 75 % for

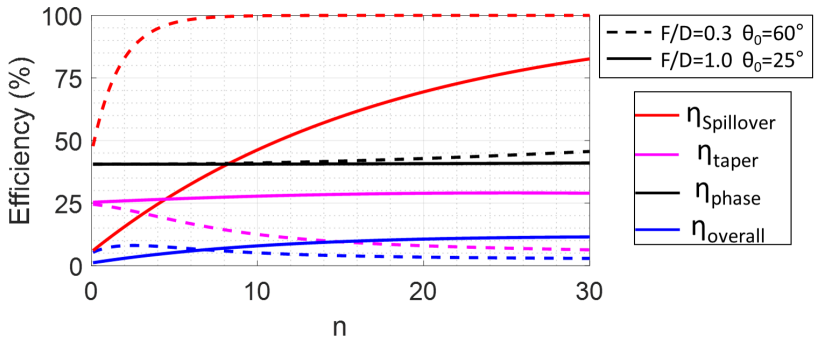

Figure 4.13: $\eta_{Spillover}$, η_{Taper}, η_{Phase} and $\eta_{Overall}$ efficiency versus the amplitude weighting generated by cos^n-like illumination of a Fresnel zone plate antenna with binary amplitude ($P = 2$).

$F/D = 1$ with eight phase-correcting levels ($P = 8$, blue discontinuous line), as can be seen in Figure 4.13. It can also be appreciated that for a phase-correcting lens, the major limitations come from the phase efficiency with a low number of quantification levels (e.g. $P = 2$). The same figure also shows the efficiencies related with two (blue continuous line) and four (blue dotted line) phase-correcting zones. Finally, it is important to highlight that this solution is compatible with the dual-band configuration since the plate lens can be designed as a combination of Soret and phase-correcting lens as in Section 3.6.3. Moreover, another solution could be the design of a plate lens individually as a phase-correcting element for the SMWW and later combine it with a MMW antenna (e.g. printed dipole) designed to obstruct as little as possible the area of the SubMMW lens. Nevertheless, we must recall that this improvement in the efficiency is at the expense of a more complex and expensive fabrication process.

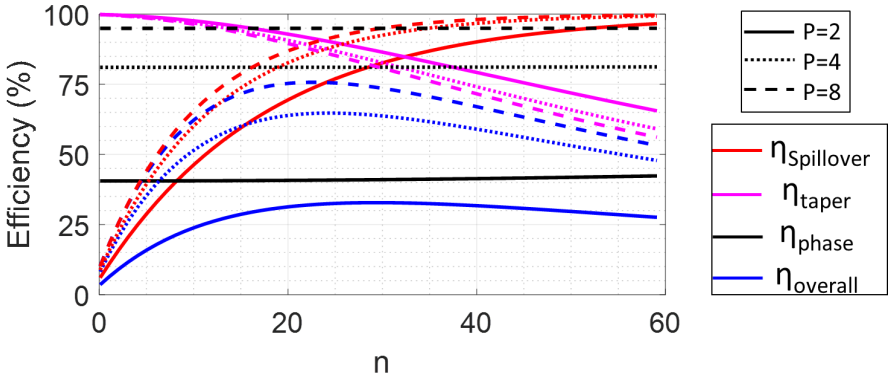

Figure 4.14: $\eta_{Spillover}$, η_{Taper}, η_{Phase} and $\eta_{Overall}$ efficiency versus the amplitude weighting generated by cos^n-like illumination of a Fresnel zone plate antenna with 2 (continuous line), 4 (dotted line) and 8 (discontinuous line) phase-correcting zones. $F/D = 1$.

4.6 Experimental Results and Discussion

To validate the previous results several prototypes were manufactured at the Public University of Navarra's facilities. The fabricated Soret lens and the modified lens-antennas are shown in Figure 4.15. They were made out of 2 μm of e-beam evaporated Cu on a 20 nm layer of Cr. The experimental characterization of the lenses was performed with an AB MillimetreTM quasi-optical vector network analyser using the setup illustrated in Figure 4.16.

To illuminate the prototypes, a WR 1.2-band diagonal horn antenna with 10.7 mm length, 25 dBi gain and 0.83 mm beam waist radius was place at a distance L=70 mm. At this distance, for a central operational frequency of 850 GHz ($\lambda_0 \sim 350\ \mu m$), the half beam diameter of the Gaussian beam is 9.4 mm which provides uniform illumination of the lens. Also, millimetre-wave absorbers were placed in the setup to mimic anechoic chamber conditions. To scan the focal plane field distribution, a rectangular WR-1.2 probe was used as detector and was moved from -800 to 800 μm along the x and y-axis in 20 μm steps. The probe detector was placed as close as possible to the dielectric-air interface, where the focus is located. However, there must be a minimum separation between them to allow the movement of the probe without touching the dielectric. Thus, the simulated and experimental results are compared for distances of 540 μm and 580 μm (20 μm and 40 μm separation between the silicon slab and the probe).

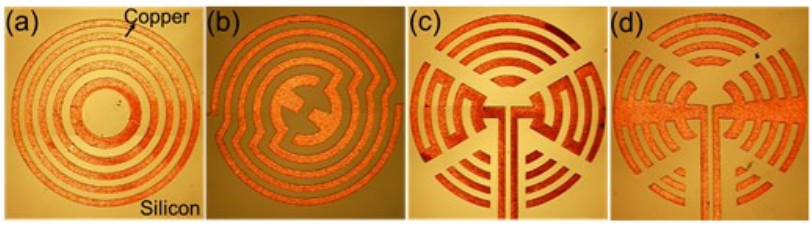

Figure 4.15: Fabricated W-Band antennas that can act as FZPL at 850 GHz: (a) 10-FZPL (b) quasi-spiral antenna, (c) quasi-meander antenna with read-out lines (d) quasi-log antenna with read-out lines.

The detection probe averages the detected field in its collecting area and, in consequence, the resolution of the measurements is limited by the probe dimensions. This effect was taken into account and introduced numerically in the

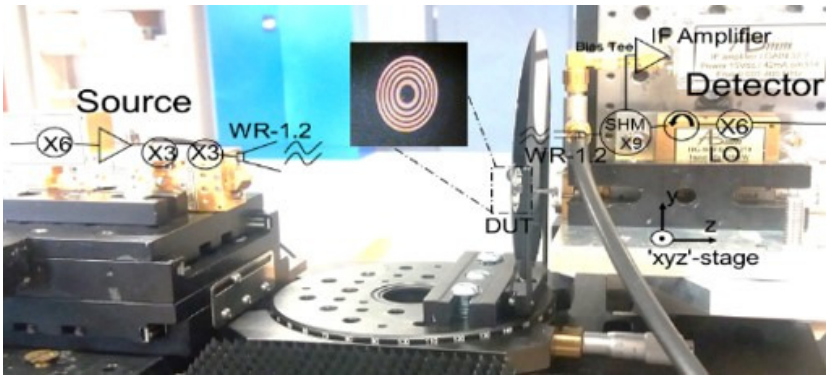

Figure 4.16: Scheme of experimental setup with a WR-1.2 waveguide probe as a receiver and a standard WR-1.2 high gain horn antenna as a transmitter.

simulations to perform a fair comparison between experimental and simulated results. To this end, the computed 2D E-Field distribution on the focal plane (obtained with full-wave simulations) was integrated with the TE10 mode field distribution on the aperture of the probe using the same sampling step as in the measurements.

The normalized power distribution in the xy–plane for all the fabricated prototypes can be seen in Figure 4.17. The raw data from the simulations at 520 μm (i.e. in the silicon-air interface) are shown in Figure 4.17(a). In addition, Figure 4.17(b) and (c) show the simulated field distribution at 540 μm and 580 μm respectively (i.e. 20 and 40 μm separation from the silicon slab) with the WR-1.2 probe as detector. The broadening of the focus as a consequence of the averaging introduced by the probe is clearly noticeable. For improved visibility, the E-Field intensity for the x=0 (black line) and y=0 (grey line) lines are also plotted on each figure. For the Soret lens and the quasi-spiral lens, the presence of the focus can be perceived up to 580 μm (Figure 4.17(c)), although the side lobe amplitudes are very high. Nevertheless, in the quasi-meander and quasi-log models, the already reduced focusing performance is more affected for this displacement of the measurement setup. The focal spot is additionally shifted in the y direction when the separation increases. A fast decrease of the focus intensity with the separation from the interface can also be noticed. Besides, as previously mentioned, at this frequency range any misalignment or tilt of the lens reduces the field intensity at the focus and therefore increases

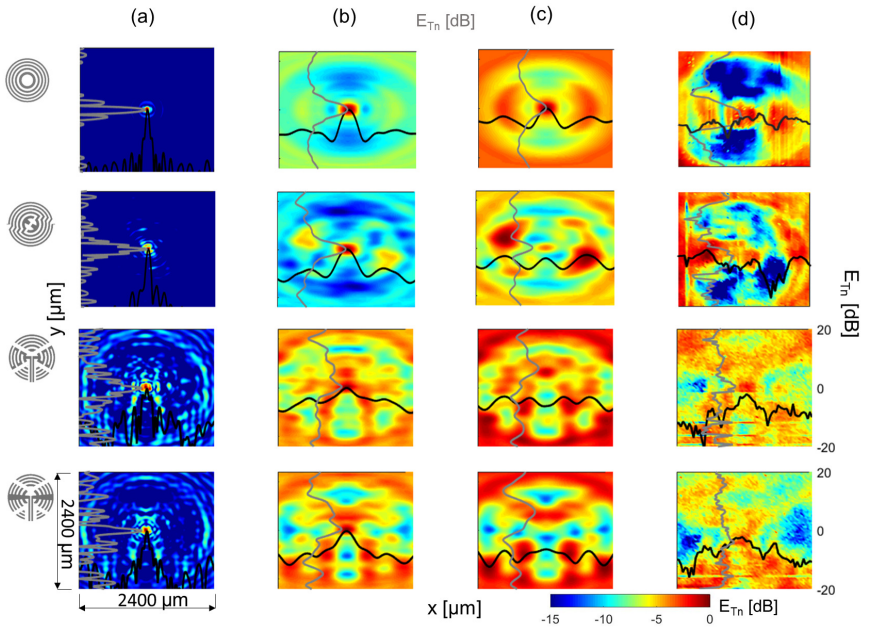

Figure 4.17: Normalized spatial power distribution on the xy-plane. (a) Simulation at the focal plane, $z = 520$ μm. (b) Simulation including the effect of the detection probe at $z = 540$ μm (20 μm away from the focal plane) and (c) at $z = 580$ μm (40 μm away from the focal plane) at 840 GHz for the 10 zones Soret Lens, quasi spiral, quasi-meander and quasi-log designs. (d) Experimental results. The E-field distribution at $x = 0$ (black curve) and $y = 0$ (grey curve) are also plotted for all the simulated and the measured results.

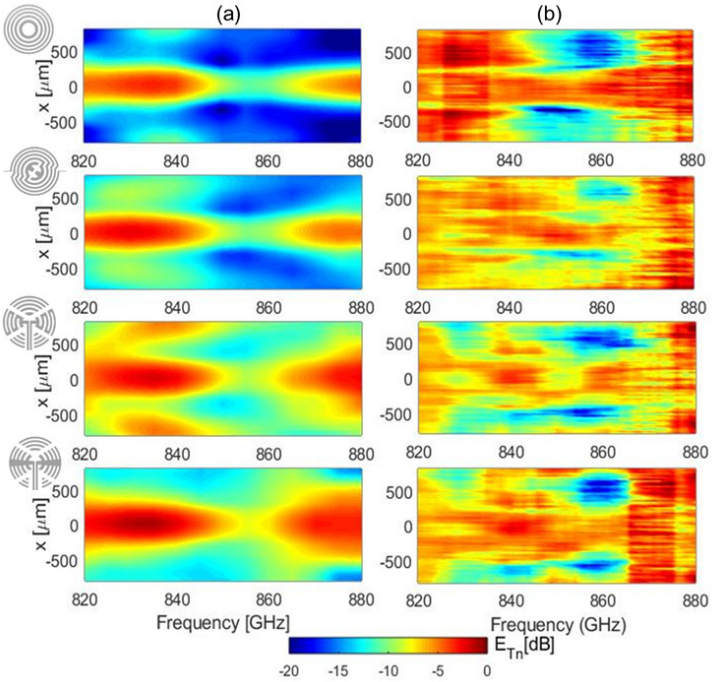

Figure 4.18: Normalized power distribution along the x-axis at $z = 540$ μm for the 820–880 GHz frequency range: (a) Simulation including the effect of the detection probe and (b) experimental results.

the relative amplitude of the side lobes. Nevertheless, this is only a problem for the measurement of the field distribution on the focal plane, since for the dual-band detector final assembly, the high frequency detector would be implemented directly on the silicon slab, where the focus is.

From the measured results, similar focusing behaviour between the Soret lens and the quasi-spiral antenna can be observed. The presence of the distorted focus can be intuited for both designs, particularly from the E-Field distribution lines (see Figure 4.17(d)). The measured results in the conventional lens and spiral cases agree with a measured position about 40 μm away from the silicon interface. The quasi-meander and quasi-log models were already poorer candidates, since both produce higher sidelobes, but nevertheless, both exhibit focusing properties up to 20 μm separation. Measured 2D results for these designs shown similar focusing performance than that observed in the simulations at 20 μm with the detector broadening effect (see Figure 4.17(b and c)). The field distribution in the x-line also confirms this focusing behaviour.

In the measurements of the power distribution at the focal plane as a function of frequency, the detector is placed in the $y = 0$ position and the x-axis (see Figure 4.18) was scanned from -800 μm to 800 μm for frequencies from 820 to 880 GHz with 100 MHz step. Figure 4.18) shows the comparison of these experimental results with the simulations (20 μm away from the focal plane and including the influence of the detection probe). Measured results are normalized with respect to the power received through a silicon slab without any lens.

Despite the shift in frequency, all models exhibit similar performance. The experimental results display the presence of the focus for all prototypes with a better definition in the Soret lens case. The focal point localization exactly at the dielectric-air interface, and the consequent small separation required between the probe and the silicon wafer make this measurement especially prone to present ripples in the experimental data. These are caused by the excitation of standing waves between the lens and the probe. For the same reason, the measurement is also very sensitive to any lens inclination.

Ultimately, a comparative table including the simulated Focusing Gain obtained with Full-Wave EM simulation, and the simulated absolute gain expected at the possible measured points with the WR-1.2 probe as detector is presented in Table 4.3 at 840 GHz. The highest gain values obtained out of the measurement results, Figure 4.18, are also included. The measured gain values are lower than the simulated ones and shifted to higher frequencies for the conventional Soret lens and quasi-spiral models. Nevertheless, the measured gain values follow a decreasing pattern similar to the predicted ones, with the exception of the quasi-spiral model. For this model the gain result agrees with a measure-

Table 4.3: Comparison Between Simulated and Measured Gain

	FG [dB]	Gain-20μm [dB]	Gain-40μm [dB]	Measured Gain[dB]
FZPL	25	9.4	2.2	6.7 @ 860 GHz
Q-Spiral	23	7.6	0	2.49 @ 847 GHz
Q-Meander-M	20	5.2	-3	3.5 @ 839 GHz
Q-Log-M	18	4	-4	1.73 @ 840 GHz

ment in a position farther than 30 μm form he interface, as was also intuited from Figure 4.17. Conversely, for the quasi-meander and the quasi-log lenses the agreement was better for 20 μm separation, and therefore the obtained gain is larger and closer to the theoretical value at this separation.

4.7 Conclusions

In this chapter, three different modification of a SubMMW FZP lens have been theoretical and experimentally evaluated. The analysis was based on both scalar Kirchhoff's diffraction (KD) method and FDTD full-wave simulations. The obtained results shown that the KD scalar method is useful for a fast prototyping, whereas a full-wave simulation is necessary to include all effects related to a lens operating with a short focal number on a high permittivity dielectric.

Out of the three analysed configurations, the quasi-spiral geometry shows the smallest degradation with respect to the initial Soret lens. Measurement of the field distribution 20 μm away from the focal plane and along the x-axis versus frequency confirms the focusing behaviour of this prototype. In addition, it is the less polarization sensitive. However, it is the most difficult to integrate with a read-out system for an integrated detector.

A theoretical analysis of the efficiency was included to assess the optimal feeder and its variation with the focal distance. Nevertheless, it was seen that the efficiency of a Soret lens will be greatly limited because of the energy blocked in the obscure zones. If high efficiency is required by the final application, the solution is a design based on phase-correcting zones. That is why, the efficiencies related with 2, 4 and 8 phase-correcting zones were also evaluated.

The proposed approach can be an alternative for compact integrated detectors, which are of great relevance to obtain in a single measurement information of different spectral ranges, reducing instrument cost, size, weight, and power consumption. Some of the work presented in this chapter has been published in [Tor19].

Chapter 5

Silicon Integrated Submillimetre Subharmonic Mixer

5.1 Introduction

The work presented in this chapter is based on concepts and technologies from both, electronic and photonic domains and may be a good starting point for the creation of new planar integrated devices.

At terahertz frequencies there have been significant advances in the development of planar direct detectors during the last years. Taking advantage from the development in terahertz CMOS technology and deeply cooled MMW and SubMMW detectors (e.g. different kind of bolometers), high-integrated FPA direct detectors have been reported [Han19, Rog10]. Nevertheless, direct detection can only recover the amplitude information. Heterodyne detection includes the use of an external Local Oscillator (LO), but allows recovering both, phase and amplitude information. However, the development of integrated planar heterodyne detectors working at room-temperature, suitable for high integrated multi-pixel configurations, is still a challenge [Chat04].

Multi-pixel heterodyne detection at SubMMW frequency range has been traditionally performed by stacked machined metallic waveguide housing modules. Nevertheless, this increases the complexity and cost whilst restricting the compactness and reliability of large arrays. Promising results have arisen from

silicon micro-machining fabrication [Rec12, LLo13, Rec15]. Multi-pixel arrays based on vertically stacked silicon layers have been demonstrated, increasing the density and uniformity of the array while lowering the cost compared to metal machining. However, the device assembly relies in a manual process whilst the alignment requirements increase exponentially with the frequency up scaling. Therefore, a monolithic heterodyne receiver that integrates a planar antenna and a mixer in a low profile easy to fabricate prototype is a very attractive solution.

The proposed design is based on a photonic crystal (PC) silicon platform. A PC waveguide terminated in a high Q-factor resonant cavity is created in the silicon to transmit the LO signal to a bow-tie antenna (which contains the mixer diode flip-chip). The design is optimized to achieve simultaneously high coupling and impedance matching. The use of the (PC) waveguide guiding possibilities, leads to several improvements. Firstly, although a single-pixel approach is presented, the design can be easily extended into a 2D multi-pixel array. PC waveguides have shown very high transmission even in very sharp bends [Mek96]. Therefore, a low-loss LO distribution network is fully feasible with PC waveguides. Additionally, high RF-LO and RF-IF isolation can be achieved. Lastly, this is a fully planar technology and dispenses the use of high precision milling metal housing-blocks which increase the cost and weight of the system.

Another notable benefit of terahertz silicon platforms comes from the use of slabs thicker than 100 μm at frequencies below 500 GHz (for single-mode operation). Therefore, contrary to its optical counterpart, the device can be manufactured as a self-supporting structure and does not require any cladding substrate, which could generate additional losses. Finally, an unintended benefit is that the silicon is an excellent heat sink due to its high thermal conductivity. Temperatures variations degrade the performance of active devices, and particularly of Schottky diodes. Therefore, thanks to the dissipation property of Si, more stable temperature performance can be obtained.

5.2 General Configuration

The 3D view of the proposed approach can be seen in Figure 5.1. It consists of an antiparallel Schottky diode pair connected to a Double Bow-Tie antenna and a coplanar stripline (CPS) filter, which provides the Intermediate Frequency (IF) output. The subharmonic mixer circuit is printed on a Silicon Dioxide (SiO_2) membrane on the top of a Photonic-Crystal (PC) Silicon slab. The Local Oscillator signal is guided within the PC waveguide and coupled to the diodes through a bow-tie antenna printed on the top of a PC cavity. The same printed antenna collects the RF signal coming from the air or from an external quasi-optical element (e.g. silicon lens). The LO signal pumps each diode of the antiparallel diode pair and the variation in the resistance of the mixer diode during forward conduction results in frequency mixing at any even multiple of the LO frequency. The proposed prototype is optimized to operate at LO frequency (f_{LO}) around 105 GHz and RF frequency (f_{RF}) bandwidth from 200-225 GHz; this leads to IF output frequencies (f_{IF}) around 0-15 GHz (*i.e* $f_{IF} = |(f_{RF} - 2f_{LO})|$).

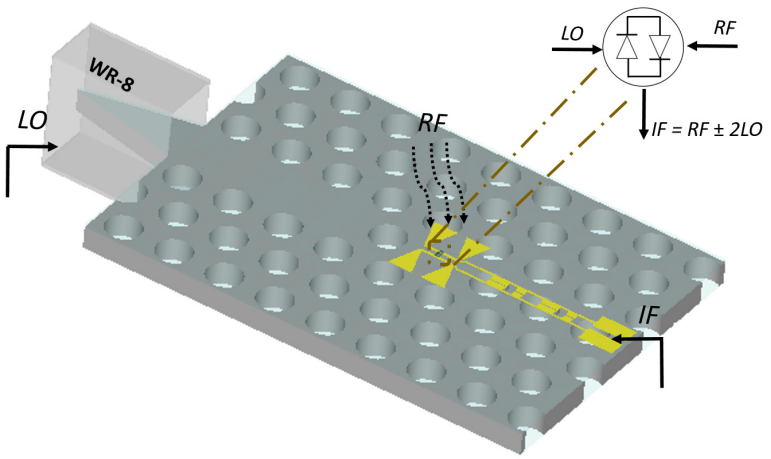

Figure 5.1: 3D perspective view of the Silicon Integrated Subharmonic Mixer.

The use of an antiparallel configuration is preferable in order to avoid the mixed even harmonics (i.e. all even LO ± even RF products and all odd LO ± odd RF products are cancelled; only odd LO ± even RF and even LO ± odd RF are generated). Theory about antiparallel diode configuration have been extensively studied and can be found in [Maas03].

Furthermore, the planar antenna shape and dimensions were selected within a compromise to achieve optimal coupling from the LO port to the diodes at LO frequency and optimal matching for the RF frequencies. The CPS filter rejects both, RF and LO frequencies and takes advantage of being placed on the PC (which perform alternating zones with low and high impedance as will be explained in Section 5.4.3) to improve the filter rejection. Thus, this filter lets only the IF frequency signal pass from the diodes to the IF port.

First and foremost, the 3 μm thick silicon dioxide (SiO_2) membrane is deposited on the top of the silicon slab to hold the printed antenna and IF output circuit. Another identical membrane is placed at the bottom of the silicon slab to preserve the symmetry in the PC structure. Nevertheless, the presence or absence of this symmetric layer does not create any difference, neither in the dispersion diagram of the Photonic Band-Gap (PBG) structure nor in the antenna/mixer full-wave simulation. The SiO_2 membrane thickness is too thin compared with the operational wavelength (0.001λ at 100 GHz) and has a relative low dielectric constant ($\varepsilon_r = 3.9$). Nonetheless, for the use of this model in higher frequency ranges, this symmetry factor must be included.

5.3 Photonic-Crystal Structure

The first step in the silicon integrated mixer design is the Photonic-Crystal study. Photonic-Crystals are artificial periodic dielectric, metallo-dielectric or even superconductor micro-structures where the periodicity can be defined in one, two, or three orthogonal directions. If the wavelength of the incident wave is of the same order of magnitude of the periodicity, and the difference between dielectric constants is large enough, a frequency range where the propagation is impossible (i.e. a photonic band gap) can happen in certain directions for certain polarizations [Joa08].

Although 3D and 2D infinitely-extended PCs have shown theoretical promising results [Bus06, Lai11, Gon02], there are extreme difficulties for their fabrication. The solution to successfully control the flow of the light in viable designs with Photonic-Crystals has come from combining 2D Photonic-Crystal guiding in the plane of the crystal periodicity with index guiding in the vertical direction provided by total internal reflection. Thus, PC waveguides can be constructed by creating defects (e.g. removing a cylinder, changing their radius ...) in a row of a 2D PC slab [Jam03]. These 2D PC waveguides have gained large attention in the last years and have enabled the development of complex Photonic Integrated Circuits (PICs). Furthermore, the results obtained in the optical field have been extended to the SubMMW range, allowing the integration of components based on PCs in the terahertz range [Wit18, Tsu15, Yu18].

The design of the line defect Photonic-Crystal waveguide, which will serve to guide the LO signal in the mixer, begins with the study of a PC structure with a band gap in the desired frequency range. Many periodic structures can obtain the desired prohibited band. However, to achieve a 2D PC waveguide that can be easily manufactured, only two approaches are possible: air holes in high dielectric material or high dielectric rods in air. Furthermore, the index contrast between the dielectric and the air must be large enough to guarantee confinement of the waves in vertical direction. In this work, high resistivity silicon is used as platform. It has been chosen because of its very low losses, easy etching, and maturity of silicon devices fabrication and integration in active devices.

From [Yar84], the maximum thickness of a dielectric slab satisfying the single mode condition is:

$$h_m = \frac{\lambda_0}{2\pi} \frac{1}{\sqrt{n^2 - n_2^2}} \left[\pi + \arctan \frac{\sqrt{n_2^2 - n_1^2}}{\sqrt{n^2 - n_2^2}} \right] \tag{5.1}$$

where λ_0 is the free space wavelength, n is the refractive index (RI) of the guiding layer and n_1 and n_2 are the RI of upper and lower cladding respectively. The cladding is almost imperative in the photonics field where single mode slabs are too thin and besides, supports for the structure are needed. On the contrary, scaling this technology to the SubMMW range implies the advantage of using thicker slabs, which can be used as self-supported structures. Therefore, in our case equation (5.1) reduces to $h_m = \lambda_0/(2\sqrt{n^2 - 1})$ and the value of h_m for single mode operation up to 105 GHz is 418 μm. Thinner slabs will provide weak wave confinement (i.e. the guided mode will be very close to the light cone) and thicker slabs could propagate higher order modes, which can eliminate the PBG. Thus, a commercial 400 μm thick silicon slab is selected.

The selected 3D geometry, lattice vectors, as well as the 2D irreducible Brilloin zone used for the analysis can be seen in Figure 5.2(a). Air holes ($\varepsilon_r = 1$) are etched in a silicon slab ($\varepsilon_r = 11.67$) arranged in a 2D periodical hexagonal lattice, with lattice constant a. The radius of the air cylinders (r) and the slab thickness (h_s) are 307 μm and 400 μm respectively.

The band diagram for the PC slab was obtained with the Plane Wave Expansion (PWE) solver of the commercial solver OptiwaveFDTD15 (see Figure 5.2(b)). For this analysis, the silicon slab was embedded in a $7a$ air box in the z-direction. The slab is in the xy-plane and the direction normal to the slab is z. With these coordinates, TE-like modes are those in which E_x, E_y and H_z are the dominant field components, whereas TM-like modes are those in which H_x, H_y, and E_z are the dominant field components. The dispersion diagram shows a band-gap for the TE-like modes (even modes) from 0.28 to 0.4 normalized frequency (a/λ).

5.3.1 Line Defect Waveguide Design

Once we have a structure with a band gap at certain frequencies, a row of air cylinders is completely removed from the 2D lattice plane to create a channel, which will act as a waveguide [Mea94]. Due to the introduced perturbation, some new defect states are created. If these states fall within the band gap, the periodic structure around the guiding channel will provide field confinement

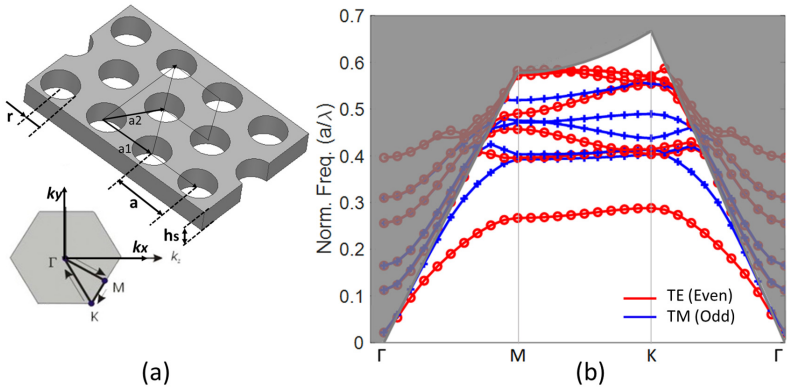

Figure 5.2: (a) 2D hexagonal lattice and its irreducible Brillouin zone.(b) Band diagram for a hexagonal lattice of air cylinders in silicon ($\varepsilon_r = 11.67$, $r = 0.33a, h_s = 0.43a$) for TE-like (red lines) and TM-like (blue lines) polarizations. The light grey color highlights the region outside the light cone.

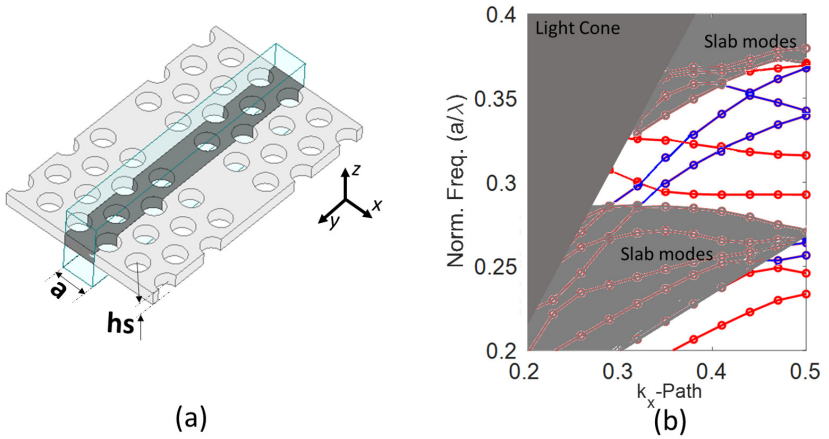

Figure 5.3: (a) Unit cell of the line defect PC slab. (b) Dispersion diagram of the TE-like (red lines) and TM-like (blue lines) modes of a 7×1 supercell in the line defect PC slab. The grey regions correspond to the slab bands.

in the waveguide in the 'xy'- plane in this frequency range [Joa08]. The field confinement in the vertical direction is achieved by total internal reflection at the Si-air interface.

For evaluation of the line defect, the PC waveguide dispersion diagram was computed using a 7×1 supercell shown in Figure 5.3(a). New guided modes appear within the frequency band gap of the original PC (Figure 5.3(b)). The TE-like mode bandgap is sufficient to confine these guided modes in the waveguide. In our case, only TE modes of the line defect waveguide will be excited, and they will not couple to the TM_z modes of the Photonic-Crystal structure due to field mismatch.

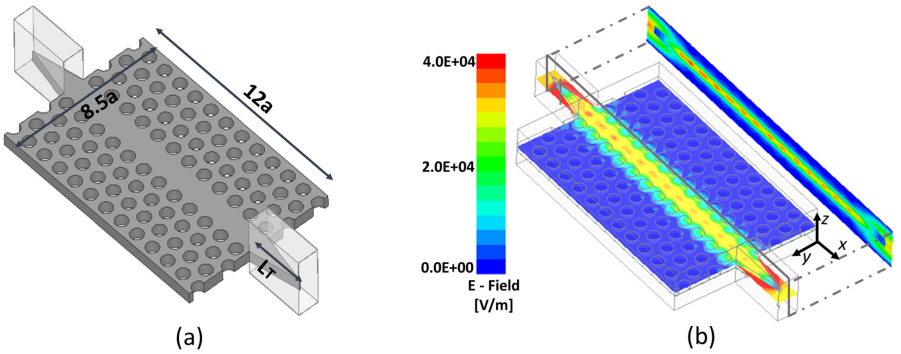

Figure 5.4: (a) Back-to-back WR-08 metallic waveguide to line defect PC waveguide. (b) Electric Field distribution showing the transmission through the back-to-back structure at 105 GHz.

A back-to-back structure (Figure 5.4(a)) was designed to evaluate the performance of the PC waveguide. To this aim, a transition from rectangular metallic waveguide to PC waveguide will be used. By means of this transition, the fundamental mode of a rectangular waveguide (TE_{10}) excites the dominant field components of TE-like modes in the PC waveguide. The silicon slab must be aligned with the rectangular waveguide E-Plane and a linear taper was created in the silicon slab to improve the coupling and matching. In addition, it helps to align and fit the PC waveguide and the WR-08 waveguide aperture. The silicon taper length (L_T) was optimized and the resulting optimum length was found to be 2.5 mm and its width 930 μm. With these dimensions, the fundamental mode of the metallic waveguide is adiabatically coupled to the PC

waveguide mode. The lattice constant (a) is chosen to be 930 μm, i.e. $0.33\lambda_0$ at 105 GHz. This will be the frequency for the LO signal. The air cylinder radius is $r = 306$ μm ($0.33a$), the total length of the analysed PC waveguide is 11.16 mm ($12a$) and the total width of the slab is 7.9 mm ($8.5a$). Finally, the HR-Si slab is 400 μm thick and its parameters are: $\varepsilon_r = 11.67$ and $\rho \simeq 10^4$ $\Omega \cdot cm$. Finally, the back-to-back transition was simulated with the 3D Electromagnetic Solver ANSYS HFSS. Figure 5.4(b) shows the electric field distribution at 105 GHz where the effective transmission of the expected TE polarized mode can be observed.

A parametric study for different lattice constant a (0.29-0.35λ) and different radius r ($0.29a - 0.35a$) of the back-to back transition was performed and the results of the S-Parameters can be seen in Figure 5.5. There is a transmission band with about 20 % 3 dB fractional bandwidth that can be optimized by varying the mentioned parameters r and a. Furthermore, losses are below 1 dB for the entire transmission band. The losses associated with the PC waveguide were estimated as 0.64 dB/cm from simulation whilst the transition from WR-08 to PC waveguide contributes with 0.005 dB. The losses of the evanescent modes above the light line are not appreciated in the transmission response due to the relatively short length ($\sim 3\lambda_0$) of the PC waveguide. Similar behaviours have been reported in [McN03, Ama17]. Note also that since the PC waveguide is intended for LO injection, narrow band is required. Therefore, even if a longer waveguide were required it would be broadband enough to accommodate the LO signal. Finally, the theoretical attenuation of the standard annealed copper and aluminium WR-8 rectangular waveguides are 0.06 dB/cm and 0.08 dB/cm respectively at 105 GHz. In this aspect, the performance of the conventional metallic waveguides is superior. Nevertheless, the PC waveguide could be a better option from the point of view of planarity and integrability.

The radius of the air cylinder is only varied up to $0.35a$ to guarantee the robustness of the structure. Larger holes in the silicon would make the device very fragile and would force the use of a cladding. Moreover, the presented study is also useful as a tolerance analysis for the subsequent fabrication.

Lastly, an analysis of the effect of the variation in the silicon resistivity on the PC waveguide losses was performed. The commercial silicon wafers which have been used for the fabrication present an uncertain bulk resistivity between 10^3 and 10^4 $\Omega \cdot cm$. Then and there, a simulation for fixed a and r with these two extremes values of silicon slab resistivity (which implies different dielectric loss tangent values) can be seen in Figure 5.6. The simulation of an ideal maximum resistivity of 10^5 $\Omega \cdot cm$ was also included for comparison. As expected, the losses increase to more than 2 dB for a 10^3 resistivity value. However, there is

hardly any difference between $10^4\ \Omega \cdot cm$ and $10^5\ \Omega \cdot cm$ resistivities.

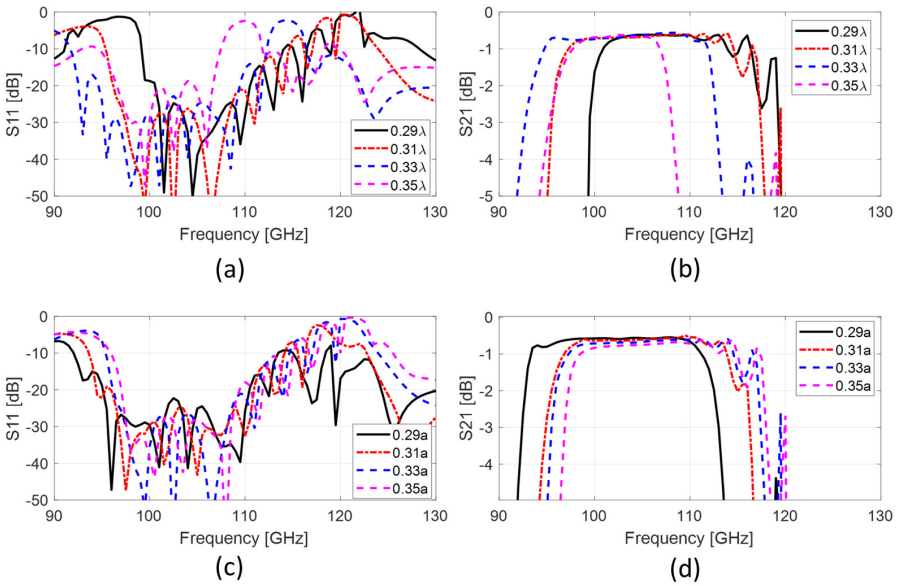

Figure 5.5: S-Parameters of the back-to-back transition for: (a and b) different lattice constant (a) with $r = 0.33a$ and (c and d) different radius with $a = 0.33\lambda$.

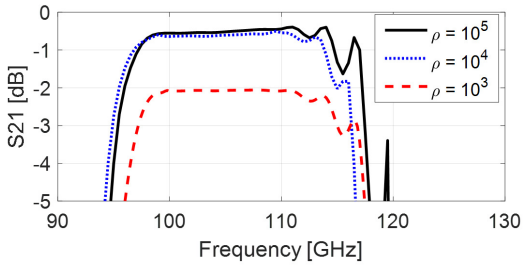

Figure 5.6: Simulated insertion losses of the back-to-back transition with different silicon resistivity values ($\Omega \cdot cm$).

Manufacturing and Experimental Validation

Finally, the back to back transition from WR-08 to PC waveguide was fabricated and measured at the Public University of Navarra's facilities. The details for the fabrication process can be found in Appendix A as part of the results of this work, since it involved the development of new fabrication techniques that had not been used before in our facilities and which required a large effort to achieve a reproducible and stable fabrication process. Additionally, to ensure a good alignment, a 3D printed housing block was also fabricated using the WR-08 metallic flange pins and screws as alignment guides. The fabricated silicon device and the 3D printed box are shown in Figure 5.7. Table 5.1 summarizes the designed and measured dimensions, so that the precision of the manufacturing process can be observed.

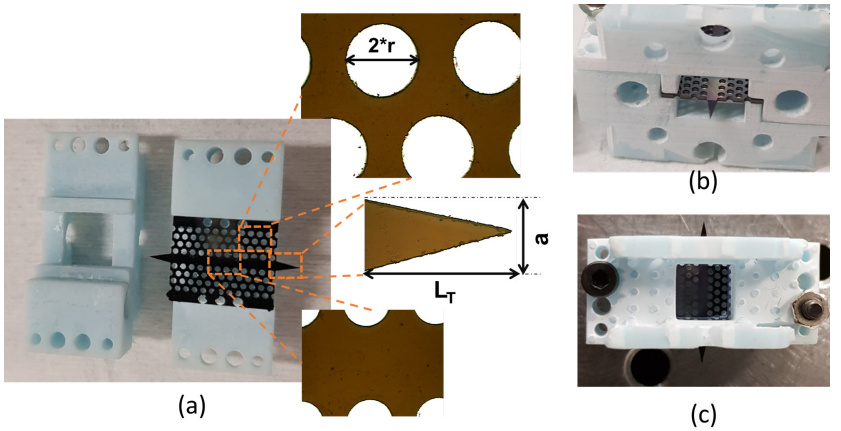

Figure 5.7: (a) Photograph of the back-to-back WR-08 waveguide excited line defect PC waveguide, with detail of the linear taper, the holes and the waveguide channel. (b) Perspective view of the flange of the 3D printed box and the PC waveguide. (c) Top view of the assembled component.

An Agilent PNA-X E3861 Microwave Network Analyser with two Keysight F-Band VNA Extenders (One Rx/Tx extender N5256A/B and one Rx only extender N5257A/B) was used for measurement. The equipment was calibrated using the standard F-Band SOL (Short-Open-Load) calibration for 1-Path 2-Port (forward or reverse). This allows us to measure S_{11} and S_{21} parameters. The manufactured back-to-back transition was connected in between the exten-

Table 5.1: Dimensions of the PC waveguide.

Parameter	Description	Designed	Measured
a	PC lattice constant	930 μm (0.31λ)	930±5 μm (0.31λ)
r	Air cylinder radio	307 μm (0.33a)	320±4 μm (0.34a)
L_T	Length of the silicon taper	2500μm	2450 μm

der waveguide ports and S-parameter measurements were carried out.

The measured transmission and reflection coefficient, presented in Figure 5.8, shows a very good agreement of the performance with respect to the simulation. There is a transmission band with about 18 % fractional bandwidth (from 98 to 117 GHz) and the insertion losses present very good results with measured values below 1 dB in the whole transmission band.

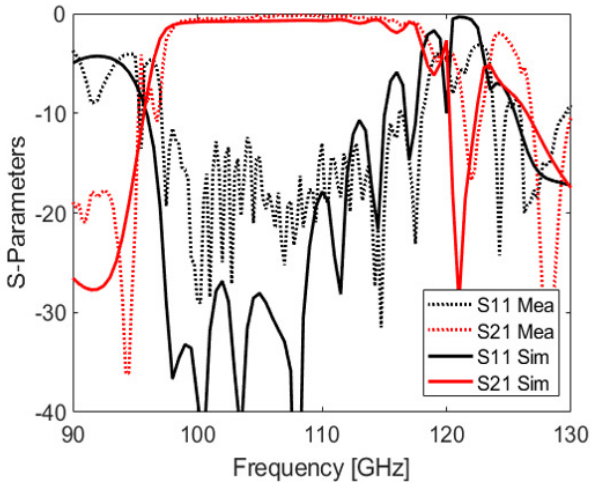

Figure 5.8: Back to back WR-8 waveguide to PC waveguide transition. S-Parameters comparison between simulated transition taking into account the fabricated value (solid line) and measurement results (dashed line).

5.3.2 Photonic Crystal Resonant Cavity

Reported studies in the state of the art of PC integration with active components highlight that the current challenge lies in mode and impedance matching between the active device and the photonic waveguide, for maximum coupling efficiency [Wit18]. Here, we propose a solution, which allows the whole receiver front-end integration in the same substrate with a high coupling efficiency, while preserving the planarity and guaranteeing compatibility with active semiconductor device fabrication.

In order to effectively couple the *LO* signal, guided through the PC waveguide, to the mixer diodes, the found solution was based on the design of a PC resonant cavity, which will be fed by the PC waveguide. The PC cavity was obtained by removing one air cylinder as shown in Figure 5.9(a). This cavity is separated from the PC waveguide by one air cylinder. By doing that, we introduce a new defect state in the PC where the field will be highly resonant. For the listed dimension in Table 5.2, the resonant behaviour of the cavity can be appreciated in the field distribution (Figure 5.9(b)).

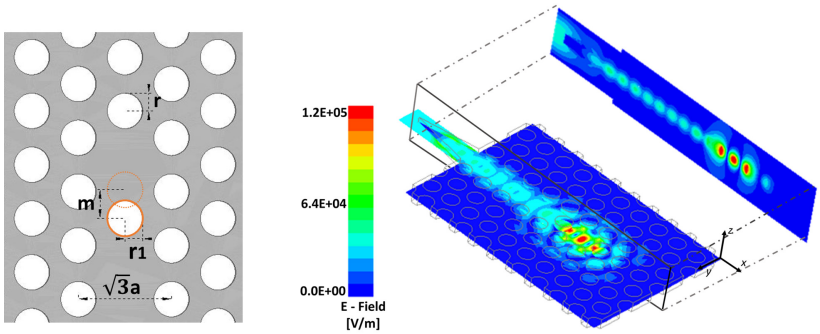

Figure 5.9: (a) Top view of the PC resonant cavity. (b) *E*-Field distribution in the PC waveguide coupled with the PC resonant cavity at 105 GHz.

The resonant frequency of the cavity can be controlled by changing the radius of the cylinders surrounding the cavity, as well as their position. Figure 5.10(a) shows the effect on the frequency response when the radius of the highlighted cylinder in Figure 5.9(a))(the one placed between the PC waveguide and the resonant cavity) is changed. Furthermore, Figure 5.10(b) shows the effect of

Table 5.2: Dimensions of the PC resonator shown in Figure 5.9.

Parameter	Description	Designed	Measured
a	PC lattice constant	930μm (0.31a)	930μm (0.31a)
r	Air cylinder radio	307μm (0.33a)	320$\pm$4 μm (0.34a)
$r1$	Highlighted air cylinder radio	307μm (0.33a)	320μm (0.34a)
m	(r_1) shifting	0μm	0μm

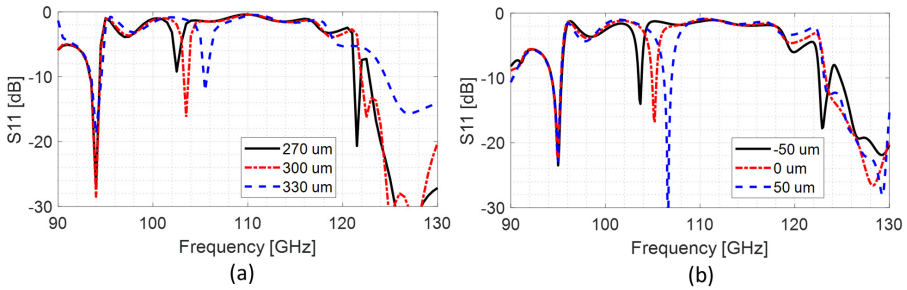

Figure 5.10: Simulated Return Loss for the PC resonant cavity with different (a) r_1 values and (b) m values.

slightly shift the same cylinder in the x-direction. It can be seen that the resonance frequency, as well as the return losses, can be optimized by means of the variation of these parameters.

In addition to the return loss simulations, the field distribution of the resonant response must be studied in detail to find the ideal planar antenna shape and orientation that maximizes the coupling. Thus, the vector field distribution at the resonant frequency (105 GHz), for E and $H-$planes can be seen in Figure 5.11. The observed field corresponds to the $HEM12\delta$ mode in a resonant cylindrical dielectric cavity. From the theory of dielectric resonant cavities [Kaj84], the first index denotes the number of full-period field variations in azimuthal direction and the second one, the number of radial variations. In classical waveguide cavities, the third index is used to denote the number of half-wavelength variations in the axial direction of the waveguide. Here, the third index, δ, denotes the fact that the dielectric resonator is shorter than one-half wavelength. This resonance will be used for the LO signal.

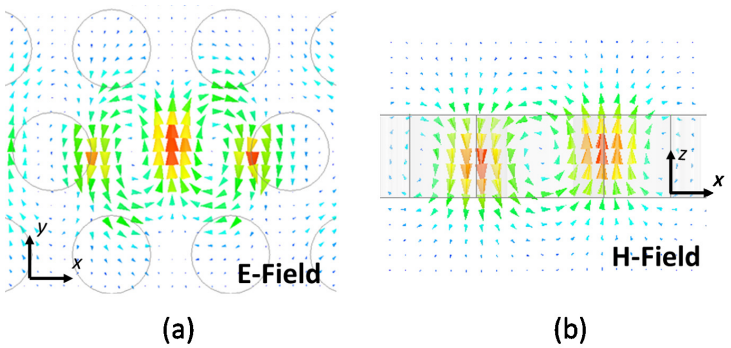

Figure 5.11: (a) Vector E-Field for the xy-equatorial plane (middle of the slab). (b) Vector H-Field for the yz-meridian plane of the cavity.

Manufacturing and Experimental Validation

To verify the performance of the PC cavity, a prototype with the dimensions listed in Table 5.2 was manufactured, packaged in a 3D printed housing block and measured. Details of the manufacturing process can also be found in Appendix A. Figure 5.12(a) shows the photograph of the assembled device connected to the metallic flange of the WR-08 waveguide for the return loss measurement. The silicon taper and the flange details can be seen in the perspective view in Figure 5.12(b).

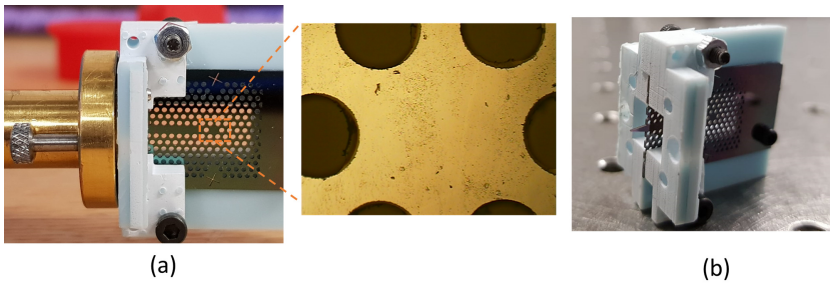

Figure 5.12: (a) Photograph of the fabricated structure connected to the WR-08 metallic waveguide with a zoom to the PC cavity. (b) Perspective view of the assembled device.

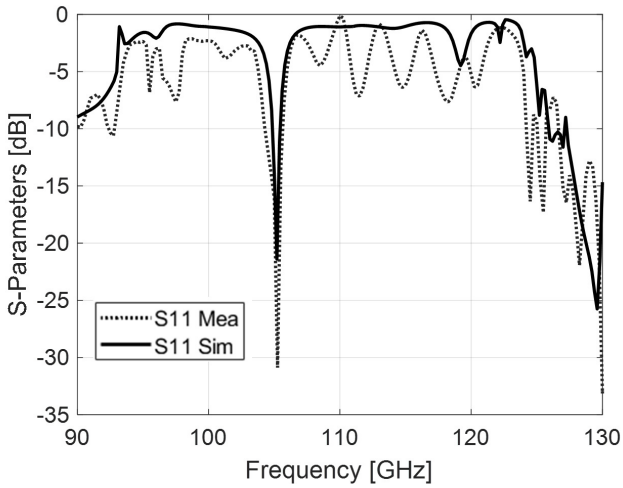

Figure 5.13: Comparison of the simulated and measured return loss of the PC cavity.

The measured return loss presented in Figure 5.13 exhibits very good agreement with the simulation. A resonant peak, with return loss higher than 20 dB at 105 GHz can be seen. This resonance frequency will be selected for the LO injection to the mixer.

5.4 Mixer topology

The general overview of the proposed mixer was introduced in Section 5.2. The antiparallel Schottky-diode pair (APD) is the selected mixer element and will be placed in the centre of the PC resonant cavity, connected to a planar antenna. It is known that if integrated diodes are used, better performance can be achieved, especially when the operating frequency increases. However, within our facilities we do not have the capability to fabricate diodes. This is why commercial discrete diodes have been used, namely the VDI SC1T2-D20 model [VDIa]. The main characteristics for the cited diode are: saturation current I_s= 0.2 fA, series resistance R_s= 13 Ω, ideality factor $\eta = 1.3$, zero voltage junction capacitance C_{jo}= 1.3 fF and diode forward voltage V_j= 0.73 V.

The ideal schematic of the antiparallel diode sub-harmonic mixer is shown in Figure 5.14(a). The HB parameters used for the simulation are: maximum mixing order equal to 8 for both LO and RF sources, $f_{LO} = 105$ GHz , $f_{RF} =$ 215 GHz and $f_{IF} = 5$ GHz ($f_{RF} - 2 * f_{LO}$). Besides, the VDI diode parameters are those mentioned above and the filters are ideal 2-ports S-Parameters Files. As a first approximation, the harmonic balance (HB) simulation of such ideal layout was performed and the output tones (V_{IF}) can be seen in Figure 5.14(b). The cancellation of the even harmonic mixing products for the antiparallel diode configuration is clear.

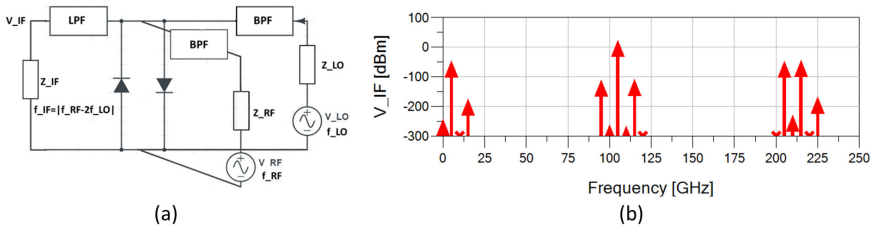

Figure 5.14: (a) Block diagram of a basic subharmonic mixer. (b) Cancellation of even harmonics using APD.

5.4.1 Load-Pull Analysis

The first step to achieve the best mixer performance is to find the optimum diodes embedding impedances, i.e. the impedances that provide the best con-

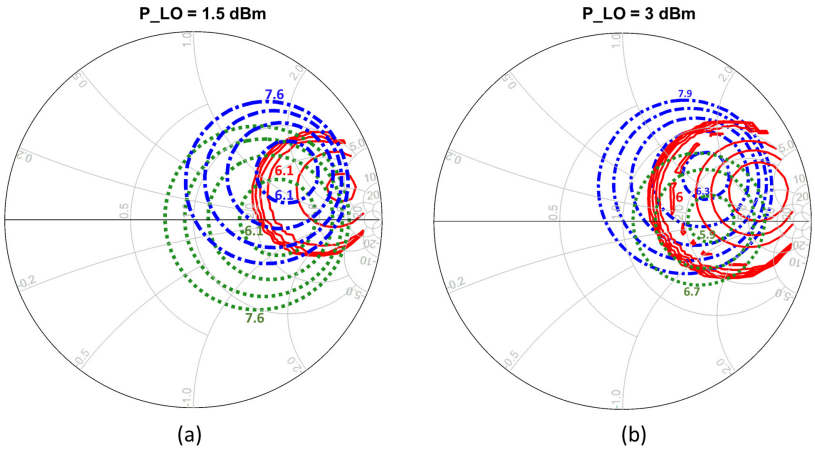

Figure 5.15: Smith Chart representation of constant conversion loss circles for different RF (dot-dashed blue), LO (continues red) and IF (dotted green) impedances with $P_{RF} = -30$ dBm for:
(a) $P_{LO} = 1.5$ dBm and (b)$P_{LO} = 3$ dBm.

version loss. Using the Load-Pull technique, the RF, LO and IF impedances are swept in an iterative process. This study offers the possibility to quickly know the optimum performance of the mixer and at which LO and RF source impedances it is reached. The HB parameters used are the same as in Figure 5.14. Likewise, the employed powers are: $P_{LO} = 1.5$ dBm and 3 dBm and $P_{RF} = -30$ dBm.

From this load-pull analysis, the best constant conversion loss circles obtained are shown in the Smith Chart in Figure 5.15 for the impedance variation of LO (red circles) and RF (blue circles) sources and for different IF output loads (green circles). Moreover, since the optimum diode embedding impedance is frequency and power dependent, the load-pull analysis is presented for two realistic input powers of the LO source.

Employing the best RF and LO impedance values from the Load-Pull simulations for $P_{LO} = 1.5$ dBm, shown in Figure 5.16(a), the simulated mixer conversion losses versus LO power are presented in Figure 5.16(b). Therefore, these impedances will be our design goal for the whole assembled mixer.

(a)

P_LO [dBm]	Z_RF [Ω]	Z_LO [Ω]	CL [dB]
1.5	138+j78	145+j23	5.9
3	111+j60	74+j50	6

(b)

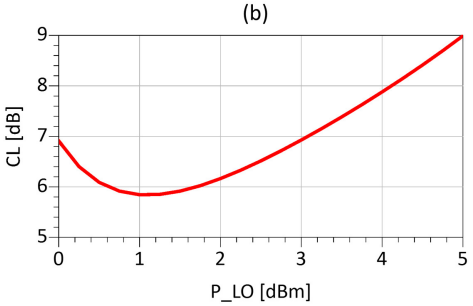

Figure 5.16: (a) Optimum RF and LO impedance values obtained from the Load-Pull simulations. (b) Conversion Loss versus LO input power for the impedance values listed in (a) for $P_{LO} = 1.5$ dBm with -30 dBm RF power.

5.4.2 3D Full-wave Simulation Considerations

It is important to point out that this study only takes into account the internal parameters of the diodes. Consequently, the impedances we are getting for best matching are the complex conjugate of the antiparallel diode impedances. However, to be able to accurately predict the discrete flip-chip diode optimum embedding impedances, the full 3D electromagnetic simulation of the diode in its circuit environment is necessary [Sob11, Wan09, Tho05, Per19]. For these suspended membrane and microstrip encapsulated mixers, the usual procedure is to simulate the 3D full diode model on the transmission line. Afterwards, two de-embedding waveguide ports at the extended reference planes in the microstrip line, and another coaxial or lumped port in the active junction of the diode are included. This way, the N-port S-Parameters, which include all the parasitic impedances, can be used in ADS non-linear simulations by just connecting the non-linear diode component model into the corresponding port.

For the proposed design, based on an integrated planar antenna, the analysis must be different. The diode flip-chip is directly connected to the antenna terminals. The LO and RF signals are transferred to the diode in a different manner than when the diode is on a microstrip line. The diode is oriented in the direction of the resonant E-field of the PC-cavity. This way, the diode itself acts as a probe receiving the LO signal from the back cavity. The planar antenna directly connected to the diodes helps to improve the coupling and impedance matching. Likewise, the planar antenna collects the RF signal into the APD. It can be seen that the structure must be simulated as a whole, since each

element directly influence the behaviour of the others. Therefore, in order to take into account the 3D full diode model in our design (which means including the parasitic impedances in the simulation), all the diode epitaxial layers and packaging structures are included in the HFSS full-wave simulation in a realistic environment taking into account the rest of the elements of the mixer, as can be seen in Figure 5.17. The 3D-model for the VDI antiparallel Schottky diodes have been previously created by the Antenna Group and it comprises the physical dimensions as well as the different layers that form a diode [Mae15]. Besides, a thin layer of silver epoxy (EPOTEK H20E) which has been used to weld the diodes is also included. Finally, it should be noted that the diode structure represents a small portion of the entire simulated structure. Accordingly, a mesh resolution of 0.01 μm was imposed for the air finger environment and 0.1 μm for the rest of the diode layers in HFSS to ensure an accurate simulation that takes into account the main parasitic impedances and coupling effects.

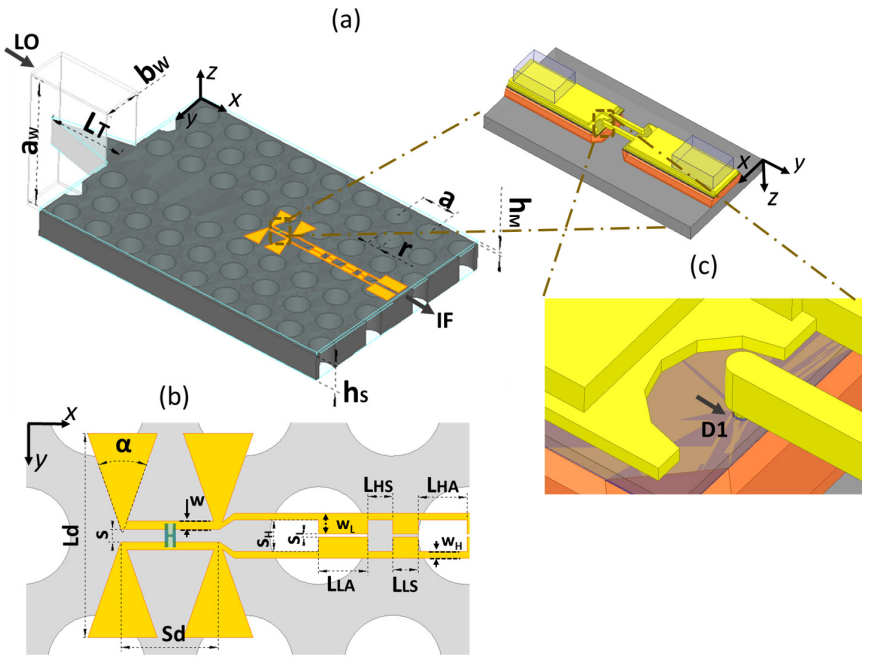

Figure 5.17: 3D perspective view of the silicon integrated subharmonic mixer and (b) its top view with (c) detail of the APD ports and epitaxial layers.

5.4.3 Filter Design

The low-pass filter is an essential component in the mixer. It must provide high rejection for the *LO* and *RF* frequency bands whilst it lets the IF signal go through. In our design, the filter runs on the PC substrate. By placing the CPS output lines on the PC substrate, an abrupt impedance change is obtained due to the changes in the dielectric permittivity. Therefore, the line will act as a low-pass filter by itself, due to the high/low impedance dielectric steps. The stop frequency band will depend on the PC periodicity and parameters.

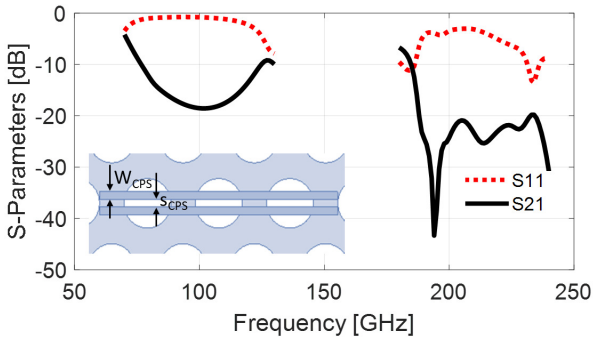

Figure 5.18: S-parameters of a CPS line running on the PC silicon substrate. $W_{cps} = 100$ μm, $s_{cps} = 90$ μm.

With the dimensions of the PC used in the presented design, alternate high/low impedance zones with lengths of 316 μm and 614 μm are formed. Figure 5.18 shows the S-parameters of a CPS line running on the PC silicon platform. It can be seen that this structure inherently rejects frequencies around 100 GHz and 200 GHz, which are the LO and RF frequency bands.

Finally, we designed a more complex low-pass filter by combining the intrinsic filtering property of the PC with a conventional CPS step impedance filter. The main dimensions of the new filter are listed in Table 5.3 (see Figure 5.17 for clarification). Furthermore, the simulated S-Parameters (with an inset figure of the filter layout) can be seen in Figure 5.19(a).

Table 5.3: CPS PBG based Filter.

Parameter	Description	Design
W_H	CPS High-Z sections width	40 μm
W_L	CPS Low-Z sections width	130 μm
s_H	CPS High-Z sections separation	200 μm
s_L	CPS Low-Z sections separation	20 μm
$L_{LA} = L_{HA}$	Length of Low/High-Z sections on SiO_2/Si	307 μm
$L_{LS} = L_{HS}$	Length of Low /High-Z sections on Si/SiO_2	158 μm

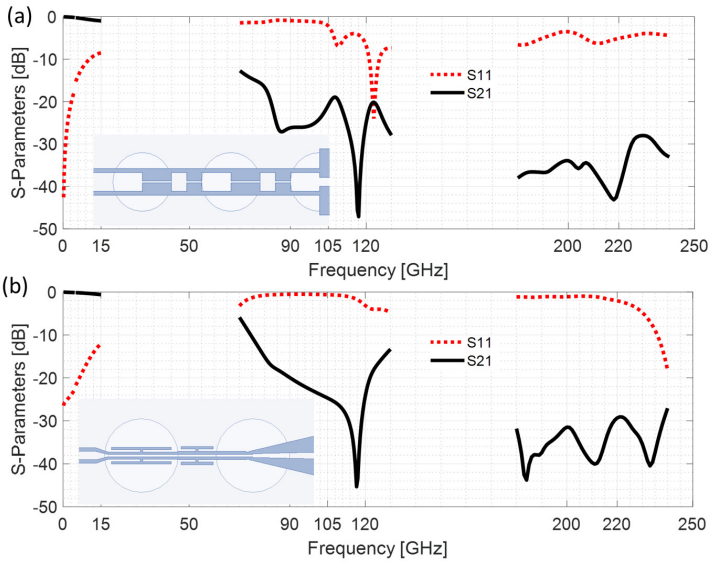

Figure 5.19: S-parameters of: (a) CPS step impedance filter on the PC silicon substrate. (b) CPS Open-T resonator filter on PC silicon substrate.

The step impedance filter successfully rejects the LO and RF frequencies, presenting insertion loss higher than 20 dB for both bands. However, even better results could be obtained from a filter based on CPS lines with small separation (s), since it should present better insertion loss. Therefore, another filter based on Open-Ended T-Strip resonators was designed and is presented in

Figure 5.19(b).

The T-Resonator filter also takes advantage from the PC substrate loading and uses two Open-Ended T-strips placed outside the central CPS to increase the rejection. The optimized lengths of the T-resonators in the silicon dioxide membrane were found to be $0.33\lambda_{eff}$@200 GHz ($\eta_{eff} = 1.1$) or 500 μm, while the length of the resonator on silicon is $0.32\lambda_{eff}$@105 GHz ($\eta_{eff} = 6.35$) or 370 μm. With those dimensions, the obtained response at *LO* frequencies is similar to the one of the step impedance filter, although in the *RF* band it is slightly better for the T-filter. Moreover, better insertion losses are obtained for the IF band. Unfortunately, fabricated prototypes were only successful with the step impedance filter. The T-resonator on the silicon dioxide membrane was founded to be more difficult to fabricate that the step impedance filter because of its fragility. Therefore, the following sections will be based on the step impedance approach.

5.5 Antenna Design

The core of an integrated planar receiver is the planar antenna and the antenna-mixer matching. The coupling efficiency between the planar antenna and the incoming radiation is the first loss the signal encounters in the receiver, which contributes directly to the noise figure (noise temperature in radiometry) [Reb92]. This topic has been extensively studied and a very good solution has arisen thanks to the use of dielectric lenses. High dielectric constant lenses offer a solution for the undesired surface wave modes and may increase the gain by a n^2 factor, where n is the refractive index. In this context, high gain lens antennas ($G >$ 30 dB) over large bandwidths ($>$ 20 %) can be found in [Fil93, Ala16, Net10]. However, this kind of antennas presents the disadvantage of having low aperture efficiency. A recently proposed solution can be found in the leaky-wave antennas (LWA) employed as lens illuminator. Thus, very high aperture efficiency and gaussianity up to 1.9 THz have been reported [Llo14, Llo11a, Llo11b].

Nevertheless, not much work has been found oriented to optimizing the antenna-mixer matching and the LO coupling in a planar configuration as is the one presented here. Therefore, the simultaneous RF and LO matching in the planar heterodyne mixer is the subject that will focus the major efforts in this investigation.

Most of the reported research about integrated planar mixers and detectors are based in Coplanar waveguide transmission line (CPW). With this technology, slot antennas radiate toward the substrate side where, usually, a high dielectric lens is integrated. The advantage of using CPW technology over microstrip or CPS (Coplanar stripline) in those designs is out of discussion. Nevertheless, in our proposed approach, a ground plane cannot be used. Another look into the field distribution in the waveguide (Figure 5.4) at the resonance frequency of the PC cavity (Figure 5.11) indicates that the E-Field is parallel to the slab and is not zero at the silicon-air interface. Therefore, the proposed design will be based on CPS technology.

In this planar integrated antenna mixer design, several factors must be taken into account. The geometry and orientation of the antenna must serve a double function. The first one is to effectively couple the LO signal from the cavity to the non-linear mixing element, namely the Schottky diodes. The second one is to couple the incoming RF signal to the same mixing element. The Load-Pull analysis in Section 5.4 shows that the selected antenna should present an inductive performance for both LO and RF frequencies to compensate the diode intrinsic capacitive behaviour.

Different dipole based antennas were studied keeping in mind all the conditions previously explained. Printed dipole antennas on a finite dielectric slab were the first option analysed. These antennas have been extensively studied for a long time [Kat83, Poz83] and the main constraint in their use is the excitation of surface wave modes in the slab, which degrade its radiation properties. Fortunately for us, one of the solutions to avoid these unwanted effects is to surround the antenna with a PC structure. However, the PC which has been used in the presented approach is designed for the *LO* frequency band and not for the *RF* band, where the antenna works. Nevertheless, it reduces the effective dielectric constant around the antenna and, therefore, the excitation of surface waves at RF frequency. A deeper insight into this fact will be given in section 5.5.2.

5.5.1 Input Impedance and Coupling

To start the analysis of the input impedance that can be obtained with a printed antenna on a Si substrate, we first simulate the simplest radiation element (w.r.t the printed dipole) on a 400 μm thick silicon substrate ($h = 0.14\lambda_0$@105 GHz) without ground plane. Figure 5.20 shows the input impedance of this element, where the dipole length is 1000 μm, its width is 100 μm and a generic lumped port excitation was used.

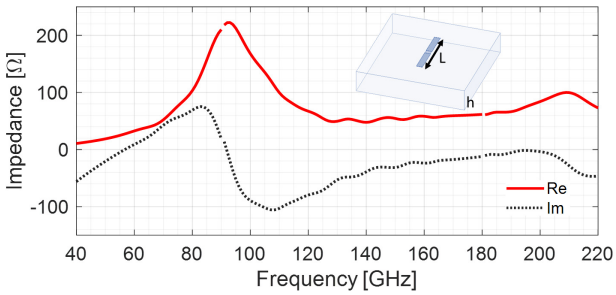

Figure 5.20: Input impedance of a printed dipole on a 400 μm thick silicon slab. L=1000 μm

From Figure 5.20 it can be seen that the resonant length of the half-wave printed dipole is around $0.19\lambda_0$ (57 GHz), while the full-wave resonance happens around $0.31\lambda_0$ (92 GHz). Besides, the input impedance is around 25 Ω and 200 Ω for a half-wave and full-wave dipole, respectively. Therefore, by choosing these length values for our planar antenna, impedance matching for *LO* and *RF* cannot be obtained simultaneously (i.e. from the load-pull analysis the antenna impedance must be higher than 100 Ω and present an inductive component to ensure matching). Nevertheless, for a resonant length of one λ at *LO* frequency, the *RF* resonance (around twice the *LO*) also exhibits high impedance values. Finally, it is known that in a final prototype, the PC substrate, the CPS filter and the diode flip-chip layers will influence the input impedance of the antenna. Therefore, the simulation of all the evaluated antennas include all these components.

In this framework, the first analysed antenna was a single printed dipole. The simulated antenna input impedance can be seen in Figure 5.21(a) for different dipole lengths from $0.18\lambda_0$ to $0.42\lambda_0$@105 GHz. Besides, not only the impedance, but also the *LO* coupling from the PC waveguide input to the antiparallel diode must be analysed. Therefore, Figure 5.21(b) shows the coupling from the *LO* waveguide port to the diode port. The conclusion from both results is that although the impedance values are not so deviated from the matching condition, the coupling of the electromagnetic field at LO frequency is very low. Therefore, this design is not suitable and other antenna configurations must be studied.

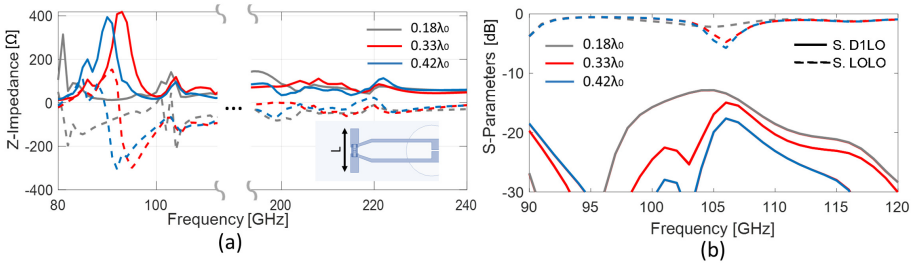

Figure 5.21: (a) Single dipole input impedance for different dipole lengths L (continuous lines represent the real part and discontinuous lines the imaginary part). (b) S-Parameters of the *LO* port and diode port ($D1$). ($w = 100$ μm and $h = 400$ μm).

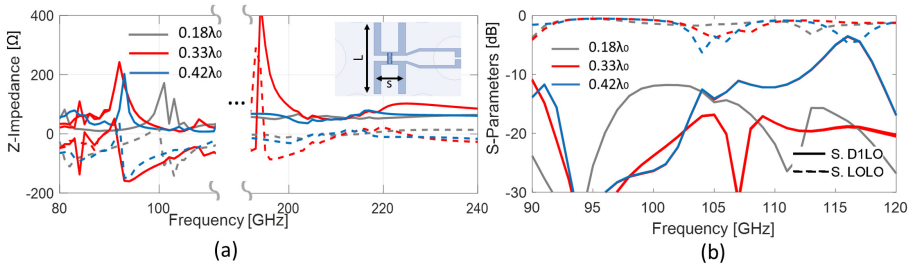

Figure 5.22: (a) Double dipole input impedance for different dipole length L and separations ($s = L/2$) (continuous lines represents real part and discontinuous line the imaginary part). (b) S-Parameters of the LO and diode (($D1$)) ports. ($w = 100$ μm and $h = 400$ μm)

The double dipole antenna is another configuration widely used in planar detectors. Double element antennas are usually preferred over single element antenna designs because they provide higher radiating resistance and more symmetric beam patterns, leading to higher Gaussian beam efficiency [Fil92]. Several variations of this structure were analysed and some of the impedance and coupling results are shown in Figure 5.22(a) and (b). From these results it can be seen that good LO-Diode coupling can be achieved for f_{LO} around 115 GHz, whereas the impedance values for the RF frequencies do not fulfil the initial requirements.

At this point, other modifications for the antenna were studied, including the bow-tie antenna. The bow-tie printed antenna is a natural modification of the dipole antenna and is commonly used when some characteristic or wider bandwidth input impedance are needed. Nevertheless, it must be said that, although this antenna has been widely used, some authors has shown objections by calling it a poor radiator [Com87]. However, in our case, the double-bow-tie antenna was the structure that showed the best coupling and impedance closest to our needs. Best results were obtained for the dimensions listed in Table 5.4.

The input impedance for the final double-bow-tie design can be seen in Figure 5.23. For the desired RF frequencies (200-220 GHz), similar values to those obtained in the Load-Pull analysis are achieved.

In Figure 5.24 we can see both, coupling and ports isolation. The LO-Diode coupling obtained from the S-parameters simulation is -6.3 dB, which means that approximately 23 % of the LO power is coupled to each diode. However, it

Table 5.4: Double Bow-tie Antenna Dimensions.

Parameter	Description	Design	Measured
L_d	Bow-Tie length	1280 μm	1274 μm
S_d	Bow-Tie separation	600 μm	605 μm
s	Feed separation	80 μm	82 μm
w	Feed width	50 μm	49 μm
α	Bow-Tie angle	40 °	40 °
h_m	Membrane thickness	3 μm	3.3 μm
h_s	Substrate thickness	400 μm	401 μm

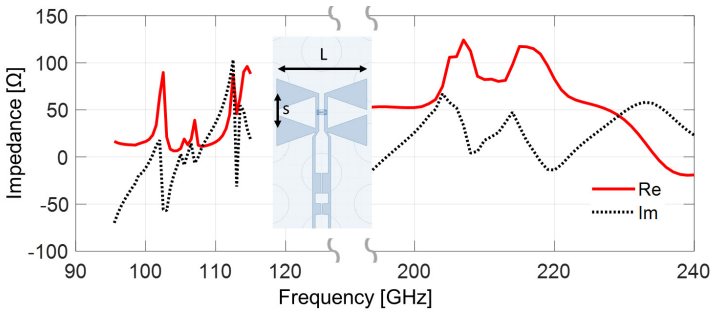

Figure 5.23: Double Bow-Tie, (see Figure 5.17), input impedance for the dimensions listed in Table 5.4.

must be pointed out that the simulations include the two diode ports. Thus, the LO power is divided between both diodes. The coupling efficiency between the bow-tie and the PC waveguide (considering the coupling of both diodes) is higher than 45 %. Furthermore, there is a high rejection ($\geq$ 24 dB) from the diodes to the IF output at both RF (210 GHz-230 GHz) and LO (105 GHz) frequencies. Besides, good isolation between the LO and the diodes ports (RF port) at RF frequency is achieved ($\geq$ 25 dB). Finally, the return losses of the antenna connected to the diode were obtained considering the diode impedance resulting from the non-linear analysis and are shown in Figure 5.24(b) (green line). Good matching bandwidth (S11< -10 dB) is achieved from 205 to 220 GHz, with a minimum, below -20 dB, obtained around 215 GHz.

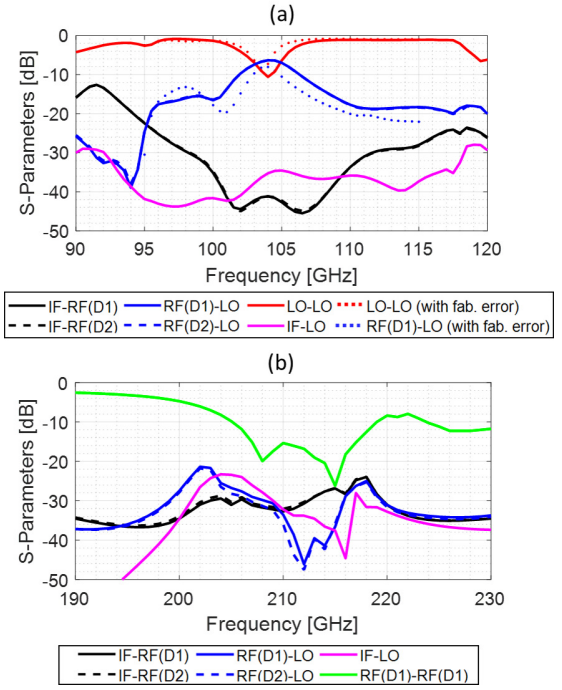

Figure 5.24: Coupling and isolation between the mixer ports at the (a) LO and (b) RF frequencies.

5.5.2 Radiation

The radiation performance of the double bow-tie on the PC cavity was evaluated. The power radiated by the structure is divided into two parts. One part propagates into the air, whilst the other part is radiated through the substrate as can be seen in Figure 5.25 (black lines) where the directivity *vs* frequency is shown. A back-metal reflector could be included at approximately $3/4\lambda_0@RF$ to improve the front to back radiation (it could not be placed closer not to affect the performance of the PC). With the back-metal plane, constant directivity values about 8 dB can be obtained for the RF frequency band as it is presented in Figure 5.25 (red lines). Nevertheless, it must be pointed out that the insertion of the metal reflector implies an extra layer in the design and could compromise the simplicity and planarity of the prototype.

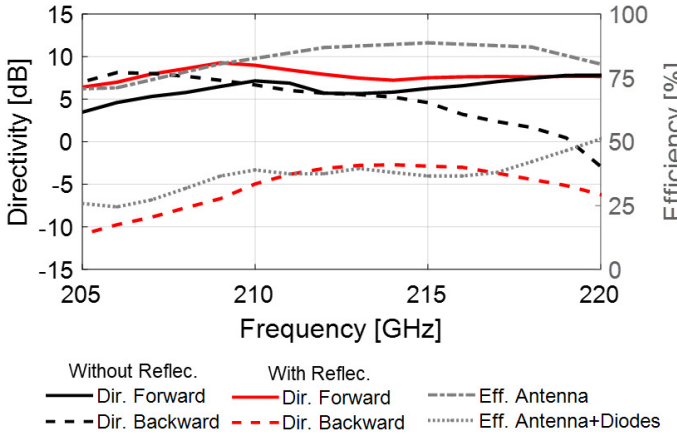

Figure 5.25: Simulated directivity *vs* *RF* frequency of the double-bow-tie on top of the silicon PC cavity without and with a back metal reflector (left axis). Radiation efficiency of the double-bow-tie on top of the silicon PC cavity without and with the diode (right axis).

Additionally, the simulated radiation efficiency of only the double bow-tie antenna on the PC platform was also included in Figure 5.25 and exhibits mean values of 85 %. The substrate modes, which do not contribute to the main radiation will deducted in its calculation. Furthermore, an extra simulation, taking into account the full structure of the diode, the silver epoxy material and the CPS filter was performed presenting a mean value of radiation efficiency of 43 % within the RF band. The new layout contains lossy materials around the port which introduce extra losses in the design. Nevertheless, this is a more realistic simulation of the mixer radiation performance.

The co-polar radiation patterns in the E-plane (yz-plane) and H-Plane (xz-plane) and the cross-polar radiation patterns in D-plane (45°-plane) are shown Figure 5.26 for $f_{RF} = 215$ GHz. According to the employed Ludwig third definition, the diagonal plane is the one that shows the worst cross-polar level with a critical point at $\phi = 45°$ and $\theta = 45°$. Ripples due to the existence of some substrate modes can be seen, emphasized in the H-Plane where the PC is not periodical, since it corresponds the plane of the defected PC line. However, even though the PC that surrounds the antenna is not designed to work in the RF band, it decreases the effective dielectric constant and reduces the excitation of

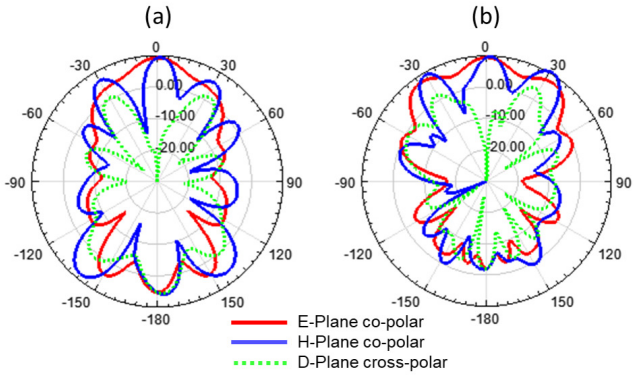

Figure 5.26: Simulations of the co-polar radiation patterns in the E-plane (yz-plane) and H-Plane (xz-plane) and cross-polar in D-plane (45 °-plane) according to Ludwig 3 definitions of the double-bow-tie on top of the silicon PC cavity at 215 GHz. (a) Without and (b) with a back-metal reflector.

substrate modes. The field distribution in Figure 5.27(a) shows the total surface wave suppression around the cavity at 105 GHz; while, in Figure 5.27(b and c) some attenuation after two PC periods is observed for RF frequencies.

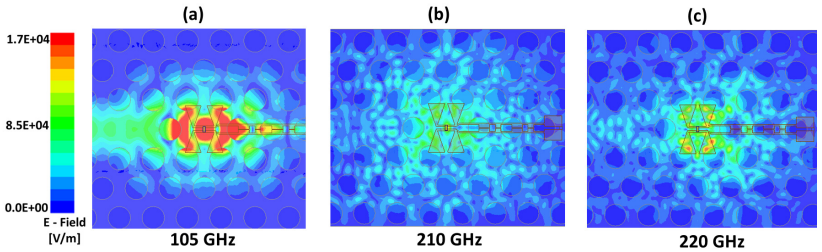

Figure 5.27: E-Field distribution at the middle of the silicon slab at: (a) 105 GHz (b) 210 GHz and (c) 220 GHz.

5.6 Silicon Integrated Subharmonic Mixer Performance

The S-Parameters obtained from the 3D full-wave simulated mixer (Figure 5.17) were imported to Keysight ADS software for the Harmonic Balance (HB) analysis. The schematic used in these simulations can be seen in Figure 5.28.

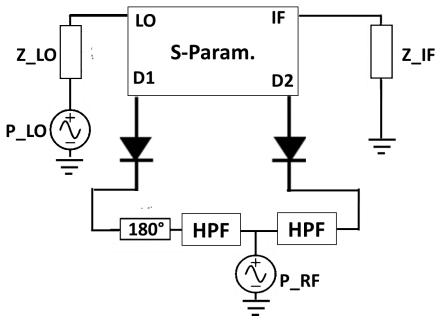

Figure 5.28: Schematic for the ADS simulated subharmonic mixer.

The RF power is injected in the mixer through the diode ports. Two ideal high-pass filters are placed to prevent any signal return to the RF source (which is impossible in reality). Furthermore, an ideal line with an electrical length of 180 degrees is placed to emulate the RF signal phase difference between the two diodes due to the antiparallel orientation. Conversely, since the S-Parameter block includes the 180 degree change in the phase of the LO signal, both diodes are connected with the same polarization. Finally, it is important to take into account the DC-return, either including it in the S-Parameter block component or as DC-feeds connected to the diodes.

The simulated Conversion Loss (CL) and the Equivalent Noise Temperature (ENT) of the whole sub-harmonic mixer are shown in Figure 5.29. The *LO* input power at 103.5 GHz (red lines) and 105 GHz (blue lines) has been swept from 6 dBm to 16 dBm, for different IF frequency values (namely, 2, 4 and 8 GHz).

Although the PC cavity was designed to maximize coupling at 105 GHz, when the bow-tie antenna is introduced the resonance is slightly shifted to lower frequencies. That is why the best coupling is obtained for $f_{LO} = 103.5$ GHz which implies that lower LO power is needed to pump the diodes as can be

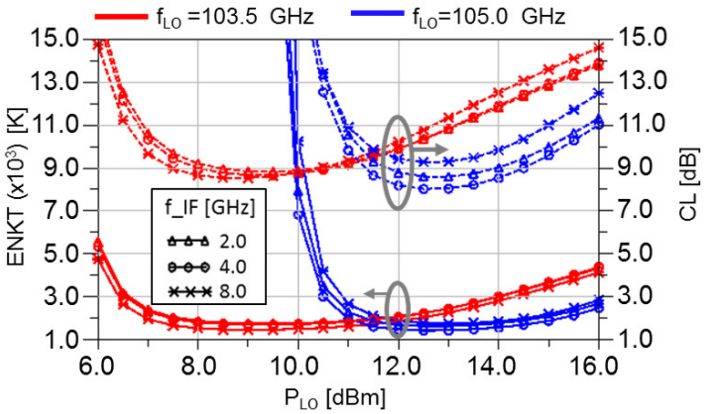

Figure 5.29: Simulated Conversion Loss (CL) and Equivalent Noise Temperature (ENT) vs P_{LO} with f_{LO} = 103.5 GHz (red lines) and f_{LO} = 105 GHz (blue lines) for three IF frequencies: 2 GHz (triangular marker), 4 GHz (circle marker) and 8 GHz (cross marker). The RF signal power was fixed to -30 dBm in all simulations.

seen in Figure 5.29. We can observe that the best absolute conversion loss value, 8 dB, is achieved for f_{LO}=105 GHz when the LO power is 13 dBm and f_{IF} = 4 GHz. Likewise, the best absolute equivalent noise temperature is 1438 K and is obtained for the same LO power and frequency values. Furthermore, for f_{LO}=103.5 GHz, better mean CL and ENT are achieved in a wider bandwidth. Additionally, from the non-linear analysis in ADS, the best coupling efficiency between the LO signal and the diodes is 54 % and was obtained with P_{LO} = 12 dBm and f_{LO} = 103 GHz.

The mixer RF bandwidth performance can be seen in Figure 5.30, where the CL and ENT are simulated for f_{LO}=103.5 GHz and f_{LO}=105 GHz, sweeping the f_{RF} with a P_{LO} variation from 7 to 12 dBm for the first f_{LO} frequency and from 11 to 15 dBm for the second one. For f_{LO}=103.5 GHz with 9 dBm LO power, the obtained 3-dB bandwidth is 5.6 % (between 207.5 GHz and 219.5 GHz); whilst, the mean CL is 9.6 dB and the mean ENT is 1816 K for the whole RF band. CL values lower than 11 dB and ENT lower than 2000 K are obtained for P_{LO} between 8 and 12 dBm. Moreover, for f_{LO}=105 GHz, better CL are achieved in a narrower bandwidth. At 214 GHz, 8 dB CL and 1438 K ENT are obtained with 12 dBm LO power. For the same LO frequency (105 GHz)

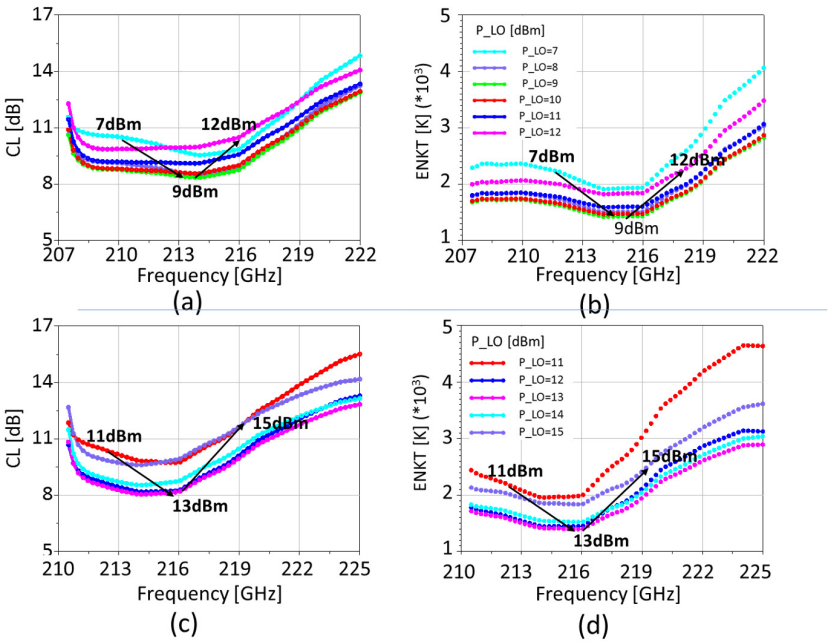

Figure 5.30: Simulated Conversion Loss (CL) and Equivalent Noise Temperature (ENT) for: (a,b) $f_{LO} = 103.5\ GHz$ and P_{LO} in the range between 7 dBm and 12 dBm and (c,d) $f_{LO} = 105\ GHz$ and P_{LO} in the range between 11 dBm and 15 dBm.

the 3-dB bandwidth is 10 GHz (between 210 and 220 GHz), which represents a 4.8 %. The mean equivalent noise temperature is around 2119 K and the mean conversion loss 10.1 dB within the whole IF bandwidth (0.1-15 GHz). Nevertheless, for $f_{LO} = 105$ GHz, a higher LO power is needed to obtain the same result (namely, from 12 to 14 dBm.)

5.7 Fabrication and Measurements

5.7.1 Fabrication

The mixer fabrication and assembly was carried out at the UPNA's facilities with the exception of the antiparallel diode that was fabricated by Virginia Diodes, Inc [VDIa].

The fabrication process for the silicon integrated subharmonic mixer includes:

1. **PC fabrication:**

   - For the PC fabrication, the first step is to deposit 3 μm of Silicon Dioxide (SiO_2) on the 400 μm thick high resistivity silicon wafer by means of evaporation using an Angstrom e-Beam evaporator.
   - The second step is to etch the alignment marks. These are required to align the printed metallic circuit (antenna and CPS filter) with the Photonic-Crystal structure. The alignment marks were etched using a positive photoresist mask in a 3 step-Bosch DRIE (Deep Reactive Ion Etching) procedure.
   - Afterwards, the antenna and CPS filter were fabricated by conventional photolithography with 20 nm of Cr, followed by 2 μm of Cu and 30 nm of Au, in order to avoid the oxidation.
   - The last step consists in etching the air cylinders backside, employing the same DRIE procedure used for the alignment marks. The SiO_2 membrane acts as a stopping layer in the Bosch silicon etching recipe, ensuring that the metal circuit is not affected by the DRIE.

     Detailed explanation and recipes of the manufacturing process can be found in Appendix A.

2. **Diode Welding**

   - The antiparallel VDI flip-chip Schottky diode was welded to the antenna pads using EPO-TEK-H20E silver loaded epoxy adhesive. This epoxy is specifically designed for microelectronics and optoelectronics applications. The epoxy and the diode were placed using a wire bonding and die placing machine (TPT HB16D). Figure 5.31 shows the details of the fabricated prototype.

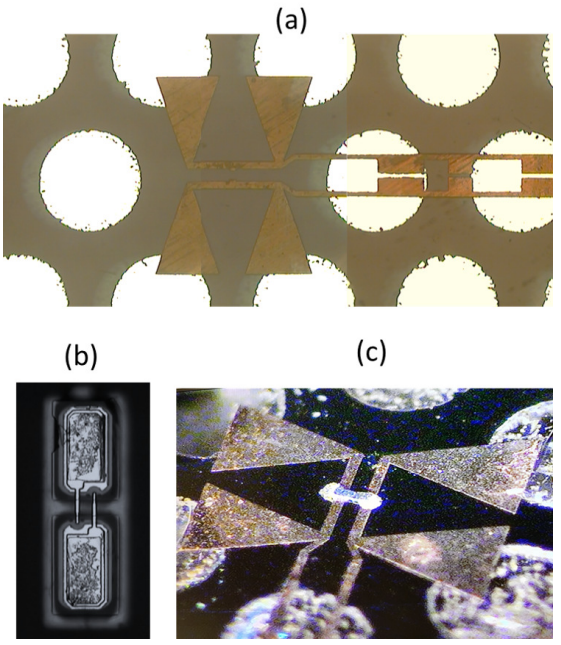

Figure 5.31: (a) Picture collage of the antenna at the microscope with back illumination. The silicon dioxide membrane is transparent and the suspended parts of the antenna and the filter can be seen. (b) 50X back-view of the VDI diode at the microscope before welding. (c) Picture of the welded diode.

3. **Device Assembly**

   - Finally, the silicon structure was assembled in a 3D printed housing box and the final result can be seen in Figure 5.32. The IF output consists of a SMA end launch connector attached to the silicon slab using two through holes.

The diode manual welding is the part of manufacturing process where the largest errors can be introduced. Nevertheless, it is still the most cost-effective solution in small facilities to design proof-of-concept first prototypes, as is the case of this work. Still, the whole fabrication procedure which has been described above is fully compatible with semiconductor active devices manufac-

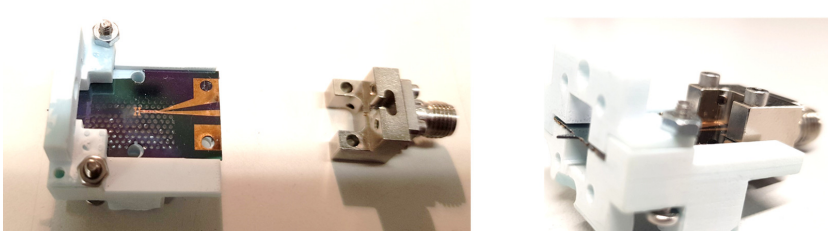

Figure 5.32: Picture of the mixer before the IF end-launcher connector assembly (left) and final assembled device (right).

turing process. Thus, the diode and the silicon PC structure could be fabricated altogether. Another approach to avoid the manual diode welding could be to use GaAs membrane beam-lead Schottky diode technology [Dra13, Zha12]. The antenna and diode may be fabricated on an insulated GaAs membrane, and after that, using the beam leads it is possible to fix the membrane onto the etched silicon wafer. Another advantage of this technology is that enables visual inspection of the circuit and diode anode since is based on a non-inverted circuit topology.

5.7.2 Measurements

The Y-Factor method is widely employed in the characterization of amplifiers and mixers in order to calculate its noise temperature [Agilent, RS17, Räi80]. A picture of the setup for the measurement of the presented subharmonic mixer, based on the Y-Factor gain method, is shown in Figure 5.33.

The IF chain consists of two LNA amplifiers (GAMP0100.0600SM10 [NeoTech]) with 35 dB gain and 1.8 dB Noise Figure (NF). The IF output power was measured from 1 to 7 GHz with 1 GHz step. The LO signal was generated with a millimetre wave generator (ELVA G4-143f) and the silicon integrated subharmonic mixer is directly connected to its WR-8 output waveguide.

First of all, the IF chain was characterized so that its noise temperature was obtained. A 50 Ω load was attached to the IF chain performing the hot load measurement, where $P_{hot,if}$ is measured. Then, the attached load was immersed into liquid nitrogen and the cold load is measured ($P_{cold,if}$). Afterwards, the subharmonic mixer is connected to the IF chain and to the LO source. The hot load is obtained by placing a piece of WAVASORB RAM material in front of the RF antenna ($P_{hot,s}$). For the cold load measurement, the absorbing mate-

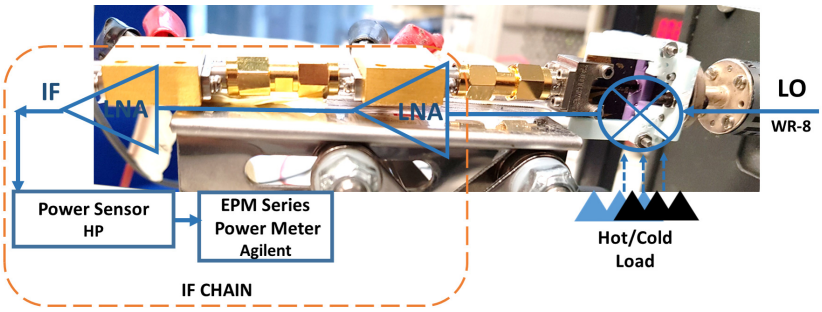

Figure 5.33: Mixer setup for Y-factor characterization.

rial is submerged in liquid nitrogen and subsequently placed in front of the RF antenna($P_{cold,s}$). These give us the receiver chain Y-factor. From these measurements, the mixer ENT and Noise Figure (NF) are calculated by removing the firstly measured IF chain contribution (see Equations below 5.2-5.6).

$$Y_{Rx} = \frac{P_{hot}}{P_{cold}} = \frac{T_{hot} + T_{Rx}}{T_{cold} + T_{Rx}} \tag{5.2}$$

$$T_{Rx} = \frac{T_{hot} - Y_{Rx}T_{cold}}{Y_{Rx} - 1} \tag{5.3}$$

$$L_{mix} = \frac{1}{L_{mix}} = \frac{P_{hot_{Rx}} - P_{Cold_{Rx}}}{P_{hot_{IF}} - P_{Cold_{IF}}} \tag{5.4}$$

$$T_{mix} = T_{Rx} - G_{mix}T_{IF} \tag{5.5}$$

$$\tag{5.6}$$

where IF refers to the isolated IF chain and s refers to the whole receiver.

The measured noise equivalent temperature for f_{LO}=105 GHz are shown in Figure 5.34 sweeping the LO power from 10 to 13.5 dBm. The IF frequency variation was limited to 6 GHz since this is the maximum operational frequency of the low noise amplifiers. Furthermore, the best mean ENT were measured at 4370 K and were obtained with $P_{LO} = 13$ dBm. For others LO powers (from 12 to 13.5 dBm) the ENT presents relatively stable performance from 2 to 6 GHz, varying from 4500 to 10000 K. For lower LO powers (namely, 10 and 11 dBm), the average measured ENT were higher than 30000 K. From the measures it was noted that they are similar to the simulated results with higher values of

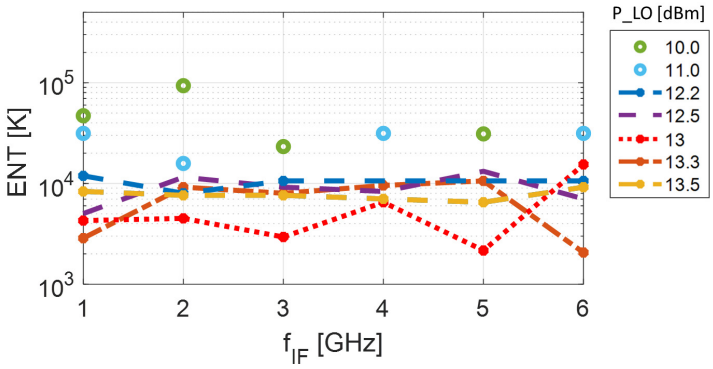

Figure 5.34: Measured Equivalent Noise Temperature for $f_{LO} = 105$ GHz with different LO powers.

ENT, which are achieved for higher LO powers. With regard to the latter, new simulations including a misalignment between the antenna and the PC slab during the fabrication process were done (i.e. the antenna is not exactly at the centre of the resonant cavity).

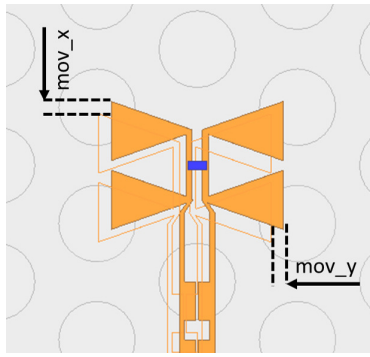

Figure 5.35: Antenna top-view showing the possible misalignments.

Figure 5.35 shows the mentioned misalignment, which was measured to be 10 and 12 μm in the x and y directions, respectively. Other dimensions, as can be those related directly with conventional photolithography and DRIE process, were measured and found to be in good agreement with their nominal

values (see Table 5.4). Thus, they are not source of the measurement deviations. The S-parameters related with the LO-Diode coupling taking into account the fabrication errors are included in Figure 5.24 (a) (dotted lines). They show certain decrease in the coupling efficiency which causes that higher LO power will be required.

The ENT and CL obtained from new simulation in HFSS and ADS including the fabrication misalignment can be seen in Figure 5.36. Additionally, the measured ENT for $f_{LO} = 103.5$ GHz and $f_{LO} = 105$ GHz with $P_{LO} = 13$ dBm are included in the same figure.

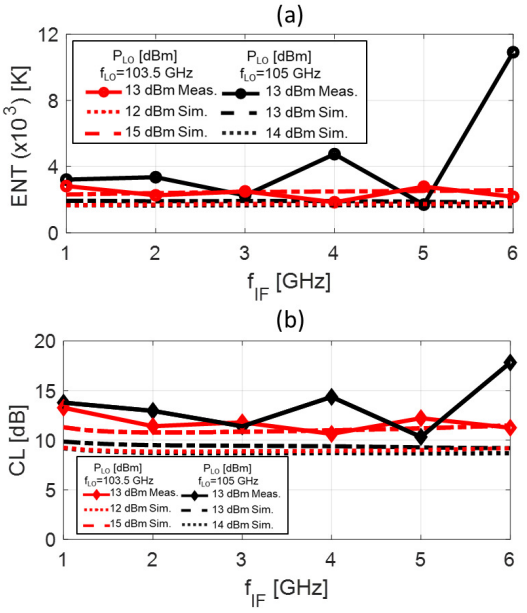

Figure 5.36: Comparison of measured and simulated (a) Equivalent Noise Temperature and (b) Conversion Losses including fabrication misalignments for $f_{LO} = 103.5$ GHz (red lines) and $f_{LO} = 105$ GHz (black lines).

For $f_{LO} = 103.5$ GHz the mean value for the whole measured IF band is 2400 K. As can be seen, the power needed to obtain the best ENT values is higher than the ideal one due to the *LO*-antenna coupling decrease caused by the misalignment. In particular, the best simulated results including the

fabrication deviation are obtained with $P_{LO} = 12$ dBm and $P_{LO} = 14$ dBm for $f_{LO} = 103.5$ GHz and $f_{LO} = 105$ GHz respectively (see Figure 5.36), whereas it was achieved for $P_{LO} = 9$ dBm and $P_{LO} = 13$ dBm in the ideal simulations (see Figure 5.29).

The respective simulated and measured CL can be seen in Figure 5.36(b). The measured mean CL is 11.8 dB for $f_{LO} = 103.5$ GHz (red line) and 13.5 dB for $f_{LO} = 105$ GHz (black line). Summarizing, the measured results are inferior to the expected ones although by introducing the fabrication misalignment errors, good agreement with the simulation is obtained.

5.8 Conclusions

The theory and demonstration of an integrated subharmonic mixer on a silicon PC platform have been presented in this chapter. Firstly, the PC platform, consisting of a PC waveguide coupled with a PC cavity was designed and measured. In this respect, very good agreement was obtained from the comparison of the simulated and measured devices. Afterwards, the efforts were focused on the design of a planar antenna suitable to effectively couple the LO signal from the cavity to the diodes and also the incoming RF signal to the same mixing element. Furthermore, two upgraded CPS filter were designed exploiting the potential of lying on the PC slab. This way their rejection properties were enhanced. The final design is based on a double-bow-tie antenna which offers good LO coupling (from the LO port to the diodes) and RF matching (between the antenna and the diodes). Furthermore, the planar subharmonic mixer achieves mean CL below 10 dB and mean ENT below 2000 K (with $P_{LO} = 9$ dBm).

Table 5.5 shows a comparison between this work and the state-of-the-art for room-temperature subharmonic mixers with different technologies. First references [VDIb, Cui19, And19, RadPhy, Mae11] correspond to conventional metallic block housings and metallic waveguides for LO and RF signals. The previously mention superiority of membrane Schottky integrated fabrication can be seen in [And19]. Until now, this technology has been the best proven solution to compensate the ohmic losses from metal-based transmission lines and passive components at high frequencies. However, such implementations increase the complexity and cost and restrict the compactness and reliability of terahertz integrated circuits.

Afterwards, the reported state-of-the-art for receivers based on planar antennas placed on silicon lenses [Kor93, Ali94] and on a 3D EBG structures [Ede07, Khr13] is presented. The LO and RF are external signals for these last ones. In those approaches, the requirement of an external high power LO source is an additional limitation.

From the previous comparison can be seen that, the results of this work are not far from the state-of-the-art. Nevertheless, additional advantages may be obtained with the presented approach from the point of view of weight, cost and full circuit integration. A monolithic heterodyne receiver, as the one presented here, is a very attractive solution, which may allow the realization of compact two-dimensional multi-pixel array. The main results and the experimental validation of this work were published in [Tor20].

Table 5.5: State-of-the-Art of Room-temperature Subharmonic Mixers Working at Similar Frequencies to this Work.

Ref. Ref.	RF (GHz)	ENT (K)	CL (dB)	P_{LO} (mW)	$IF(BW)$ (GHz)
[VDIb][a]	170-260	600-1200	8(mean)	3-6	<36
[Cui19][b]	198-238	1384-1848*	<7	3.1	-
[And19][c]	183	450-720	-	1	13.4
[RadPhy][a]	170-210	550	5.5	5	20
[Mae11][b]	210-220	> 1500	>8.4	10	-
[Ede07][d]	250	3000(m)	11.5	5-6	-
[Khr13][d]	90	3300-4000(m) <3500(s)	- -	+60 <7.1	- -
[Kor93]	182	1820	6.3	-	-
[Ali94]	335	1750	-	-	-
This Work	200-220	2400(m) 1450-2200(s)	11.8(m) 9.6(s)	20(m) <10(s)	1-6 (m) 0.1-15(s)

[a] Schottky diode, unspecified technology. $T_{DSB} = 2 * T_{SSB}$.
[b] Flip-Chip Schottky diode on suspended microstrip.
[c] GaAs membrane beam lead Schottky on suspended stripline.
[d] Flip-Chip Schottky diode on 3D EBG wood-pile based substrate.
* Converted from SSB where CL is usually 3 dB more than DSB CL

Chapter 6

Conclusions and Future Prospects

Remarkable progress has been achieved during the last years in the terahertz field approaching this technology closer to marketable applications. However, the cost and size of the components still limit its widespread deployment in many fields. In this thesis, the design and implementation of novel integrated compact terahertz detectors based on planar configuration have been proposed. The research work has been divided into two parts to cover solutions for both types of schemes of detection, namely, direct and heterodyne detection.

6.1 Planar Integrated Dual-Band Detectors

The combination of different spectral ranges is a very well-known solution and a widely employed technique to complement or increase the information in many detection systems. The first part of our research was dedicated to the design and study of integrated dual-band detectors for the MMW, SubMMW and IR ranges based on modified Fresnel zone plate lenses. The proposed prototypes were characterized by the combination of numerical methods with 3D EM full-wave simulations and non-linear analysis to fully comprehend its performance as integrated devices.

Specifically, two dual-band direct detectors were developed. These designs correspond to two different frequency ratios, namely $f_h/f_l > 70$ and $f_h/f_l < 10$. The first one was designed to operate around 400 GHz in the SubMMW range and in the mid-IR range (28 THz). The integration of those frequency ranges

combines the higher resolution provided by the IR waves with the higher penetration through obscurations of the SubMMW. The second dual-band detector was designed to operate simultaneously in the SubMMW range (850 GHz) and in the MMW range (100 GHz). The MMW allows better penetrability through some barrier materials compared with the SubMMW range and there is availability of MMIC components and amplifiers in this part of the spectrum, but the SubMM provides higher spatial resolution although it is more affected by the atmospheric attenuation.

In both designs, the SubMMW and MMW detectors have been intended to work as direct detector employing the Schottky diode as the detection element. Therefore, the main characteristics of the metal-semiconductor junction were initially described, alongside with the state of the art of GaAs Schottky diode planar detectors. The design guidelines for the evaluation of a planar direct detector based on a Schottky diode can be derived from the analysis and comparison performed in Chapter 2. Three planar GaAs Schottky diodes with different barrier height, based on different fabrication technologies, were selected to assess their performance as detection elements in the SubMMW range. The study was based on the diode internal parameters and the analysis of their responsivity and NEP giving especial attention to the role of the flicker noise. The low-barrier (or the "zero-bias") diodes exhibited reasonable NEP values in the order of $pW/(Hz)^{\frac{1}{2}}$ even under low-modulation video frequencies. Conversely, the high-barrier diode must be necessarily biased, which implies a degradation of the NEP as a consequence of the increase of the flicker noise. However, in a system with active illumination for modulation frequencies higher than the noise corner frequency the high barrier diode may also achieve a good NEP performance. Furthermore, it was shown that in a high input power scenario, the NEP of low-barrier diodes could be even more affected by the flicker noise contribution.

The key element in both dual-band detectors is the Fresnel zone plate lens. Different modifications of this lens have been evaluated in Chapter 3 and 4 to create planar antennas that work simultaneously as a lens for its designed frequency and as an antenna for a lower frequency band. Firstly, the modified lenses used for the SubMMW - IR detector were studied employing the scalar KD theory. The large electrical dimensions of this structure limit its simulation with a 3D full-wave EM simulator and furthermore, no symmetry-based simplification can be used. Oppositely, the MMW - SubMMW detector was designed with a very short focal number. Therefore, it was analysed with both, the scalar KD theory and full-wave simulations. The overall conclusion is that the scalar KD

analysis is accurate enough to be employed for a first design iteration, though it does not include neither the effects of polarization nor the resonances in the finite dielectric slab.

The modifications performed in the planar lens can be classified in three broad groups namely, bow-ties, meander and quasi-spirals. Among them, the quasi-spiral antenna was the one that exhibited the highest resemble with the performance of the Fresnel zone plate lens. The two studied variations of the spiral presented similar focusing performance in terms of both, focal gain (FG) and polarization response. Conversely, the modified bow-tie and meander designs exhibited lower FG values and higher level of secondary lobes. In all those first designs, the DC-output lines were connected to the outer point of the antennas to preserve the rings of the Fresnel zones. Additionally, an extra alternative for the connection of the DC read-out lines was considered. In this last approach, the read-out lines were directly connected to the centre of the antenna in a way that crosses the Fresnel rings. Even with these major modifications, the lenses achieved certain focusing behaviour, although the focal spot suffered from asymmetries and side lobes. To summarise, as long as the radii of the Fresnel zones are preserved, several modifications can be performed in the lenses without completely destroying the focusing properties.

Given the above, the modified lenses were studied in terms of its input impedances and radiation performance at the lower frequency range. As expected, modified bow-tie and meander variations exhibited resonant behaviour, whereas the modified spirals showed the potential to be matched in a wide frequency range.

For the SubMMW range detector, three different approaches for the manufacture and assembly were proposed based on discrete diodes and GaAs membrane integrated diodes. Moreover, one of the approaches combines the binary amplitude metal lens with a grooved dielectric (phase correcting lens). This last approach arises as a solution for the low efficiency, although it implies a more challenging fabrication. Finally, combining the non-linear analysis in ADS with the results obtained from the 3D full-wave software simulator, the predicted responsivity of three final assembly prototypes was obtained. Fabrication and measurement of these prototypes is pending.

Alternatively, the modified lenses from the MM - SubMMW detector were fabricated and measured. The E-field distribution close to the focal plane was mapped and compared with the one of a conventional FZPL. Despite the challenging measurements at 850 GHz, the focal behaviour was discerned. Moreover, it could be concluded that the modifications based on spiral prototypes are the most suitable to fulfil the dual function of operating as lens and antenna simul-

taneously.

6.2 Silicon Integrated Subharmonic Mixer.

Although direct detectors offer the advantage of simplicity and ease of integration, heterodyne detection is necessary if both, amplitude and phase information are needed. In heterodyne detection, the need of novel compact and efficient devices is a pressing demand of many THz applications. The second part of the thesis presents the design of a silicon integrated subharmonic mixer on a photonic-crystal platform. Our proposal combines solutions from the electronic and the photonic domains allowing the integration of existing techniques from both worlds. The LO power is injected through a 2D photonic crystal (PC) slab to a resonant cavity that effectively couples the signal to a planar bow-tie antenna which contains the antiparallel Schottky diode pair. To that end, the PC structure was first studied and optimized to operate within the required frequency range. Afterwards, the PC-waveguide and the PC cavity were fabricated and measured presenting very good agreement with the simulated results. The main challenge in this design was to achieve good LO coupling and simultaneously LO and RF matching. The large difference in the dimensions and operational mode between the PC waveguide and the mixing element (e.g. Schottky diode) complicates this coupling. A PC-cavity coupled to a planar bow-tie antenna was the best-found solution to overcome this issue. The double bow-tie element, which also acts as RF antenna, was optimized to be matched with the impedance of the diodes for the RF frequencies at the same time that improves the LO coupling.

Furthermore, an extra novelty in this design was the planar CPS filter. The output IF circuit runs on the PC platform, so the CPS line exhibits alternating low/high impedance sections with a periodicity determined by the PC lattice. Therefore, the line itself performs as a filter. For the PC dimensions employed in the design, the CPS line showed high rejection for both LO and RF frequencies. Additionally, two more advanced filters were proposed by combining the filtering response of the line itself with conventional high/low impedance CPS steps and T-resonator CPS filters. Finally, a proof-of-concept prototype was fabricated within our clean-room facilities. Although some previous work in silicon micromachining and silicon photolithography had been performed by our group, this fabrication involved a new combination of a multi-step process. This led us to a process of optimization of the recipes and the steps which are finally summarized in Apendix A. Finally, the assembly device was characterized

showing good performance and agreement with the simulated results.

6.3 Future Outlooks

First of all, although the binary amplitude modified lenses arise as the simplest solution to achieve the dual band behaviour, the implied low efficiency is a strong limitation for this design. The solution based on phase-correcting lens described in Section 4.5 and 3.6.3 is worthy to be further addressed as an improvement of the presented work. The antenna for the lower frequency detector can be combined with the phase-correcting lens in such a way that obstructs as less as possible the Fresnel zones.

Other aspects in the design of the dual-band detector that should be studied are those related with the integration of the lower band detector with another lens designed to enhance its radiation properties. The modified antennas presented in Chapter 3 and 4 may not be the optimum illuminator for a refractive silicon lens. However, the solution proposed above, based on phase-correcting design, provides the freedom of designing another type of illuminators suitable to be integrated with a refractive quasi-optical lens (e.g. Silicon hemispherical lens).

Nevertheless, following the same research line that had brought us up to here, the most consequent solution should be based on a planar lens. From the state-of-the-art of terahertz detectors, it has been shown that it is difficult to obtain wide bandwidth matching between the antenna and the non-linear element simultaneously with perfect radiation properties to illuminate the quasi-optical system. In this dissertation, it was also shown the importance of the RF matching to maximize the responsivity and hence to improve the NEP. Therefore, for applications where very wide bandwidth is not necessary, an attractive solution could be to dedicate prior efforts to achieve perfect matching and afterwards, design the planar lens adapted to the antenna radiation pattern.

This dissertation provided the design of compact integrated single pixel detectors. However, to achieve this integration in a large FPA there are several challenges that must be studied. For the dual-band detector, the large difference between both operational wavelength ranges implies different electrical separations between the elements of both bands. In this context, two combined solutions might be assessed. In the first place, planar lenses could be designed to focus, not into the optical axis, but pointing to certain angle below 50 degrees. Secondly, through all this research it has been proved that several modifications can be performed in the lenses without significant impact on its efficiency. Con-

sequently, several lens may be combined and partially overlapped. Figure 6.1 shows a possible design of an FPA based on both mentioned ideas.

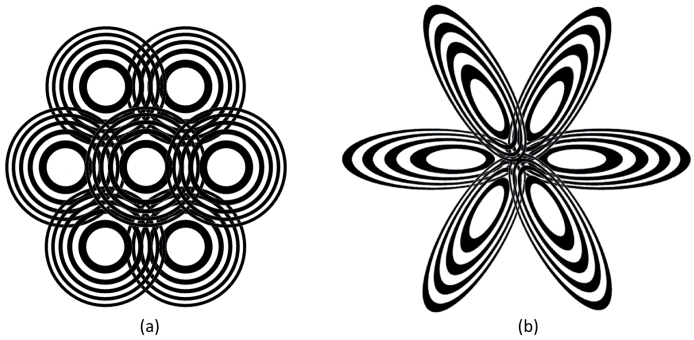

Figure 6.1: Possible FPA configurations

For the heterodyne detector, the planar integrated LO distribution network can be easily scaled to a multipixel array since PC waveguides can be designed to present very high transmission even in very sharp bends. However, the coupling efficiency between the LO port and the diode port obtained in this work is for the best case slightly higher than 53% (from the non-linear analysis in ADS). Therefore, the improvement of this coupling would be our next goal in this research. Until now, we had tried different antenna configurations, namely simple dipole, double dipoles and bow-ties antennas, obtaining the best results for the double bow-tie. Therefore, new configurations for the LO-diode coupling should be considered.

Appendix A

Fabrication

A.1 Fabrication of the Silicon Integrated Subharmonic Mixer on a Photonic Crystal Platform.

In this appendix we are going to describe the procedure we have followed in our facilities at Public University of Navarra for the fabrication of the silicon devices. The first step is to deposit the SiO_2 membrane on top and bottom of the silicon wafer. The main parameters of the HR-Si slab are: 400 μm thick, $\varepsilon_r = 11.67$, $\rho \simeq 10^4 \ \ \Omega - cm$, double-side polished, FZ $< 100 >$. The silicon dioxide was deposited by means of e-Beam evaporation following the next procedure:

1. $Si0_2$ membrane:

   (a) Surface treatment: To guaranty the adhesion of the $Si0_2$ material to the silicon wafer, the substrate must be cleaned to remove any organic and inorganic contamination and dehydrated to remove the water.

      i. O_2 clean for 10 minutes using Oxford Instruments Plasma Pro NGP80 ICP65. The chemical removal of hydrocarbons in the oxygen plasma is a standard treatment before coating, etching, printing or gluing.

ii. Acetone cleaning.
iii. IPA cleaning.
iv. Dehydration bake at 180°C for 2 minutes.

(b) $Si0_2$ e-Beam evaporation. The silicon dioxide is considered a very suitable material for e-Beam evaporation. However, some crucial factor must be considered to enhance its adhesion:
- Temperature: In our design the first nanometres were deposit at 200°C. Afterwards, the heater source was turned off and the rest of the thickness was deposited with the own heat produced by the process. The temperature of the wafer was higher than 180°C during the whole process. Usually the deposition is recommended to start at much higher temperatures, in the order of 350°C. Nevertheless, we tried lower temperatures to evaluate the adhesion in the scenario where photoresist from a previous photolithography process had been employed. The conclusion was that with a good surface treatment and heating the substrate up to 200°C, good adhesion results were obtained. However, we also tried to intersperse the photolithography process between surface cleaning and $Si0_2$ deposition. This results in a worse membrane adhesion.

- Power of deposition: It is recommended sweeping the e-Beam at low power to uniformly fuse the surface of the pieces and to avoid hole drilling. For our fabrication, the deposition rate was 2 Angstroms per second and the shape of the beam was a sinuous with low barrier velocity. The $Si0_2$ material does not melt, but it sublimes. Therefore, high ratios (which implies high power) may cause the material to spill over. What is more, the pockets should not be neither overfilling nor too empty since other inconveniences may arise. To sum up, high temperatures, low powers and pocket filling around 70 % are advisable. Finally, to deposit the required 3 μm membrane, 3 pockets (70 % filled) were employed.

2. Two-sides alignment marks. For the proposed design the top and backside alignment must be ensured since the back-etched PC cavity must be aligned with the planar antenna. Therefore, the alignment marks were firstly etched through the silicon wafer. This step can be avoided if a backside alignment MLA is available.

(a) Photolithography of the alignment marks.

i. Surface cleaning (Acetone and IPA)
ii. A10XT Positive photoresist (10 μm in the spin coater at 2000 rpm.)
iii. MLA Dose: 1500 mJ/cm^2.
iv. Development in AZ400(1:3) 5 min.

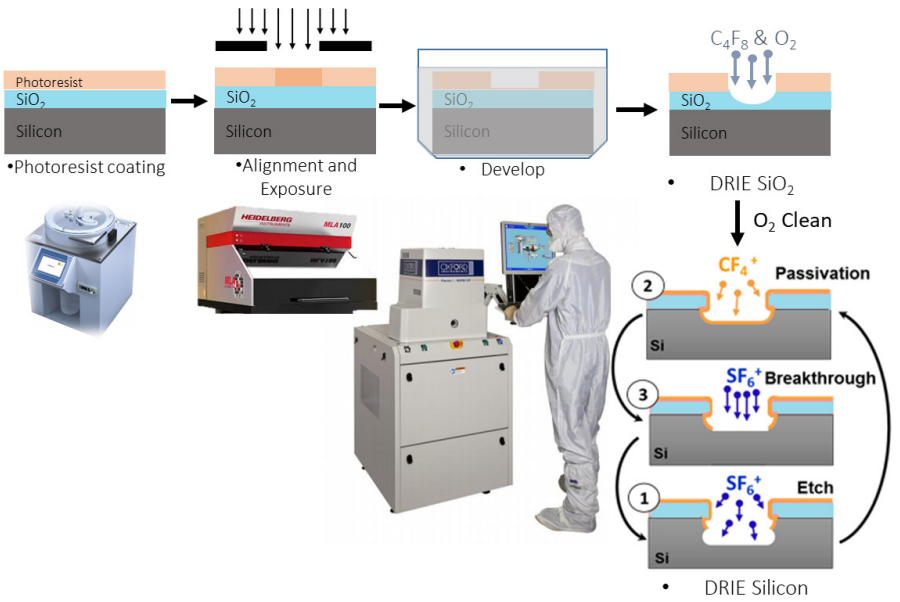

Figure A.1: (a) Schematic of the photolithography and DRIE procedure at the Public University of Navarra's facilities.

(b) Alignment marks etching (Bottom-Side)
The etched was performed with the Deep Reactive Ion Etching (DRIE) procedure employing the Oxford Instruments Plasma Pro NGP80 ICP65. This is a complex process where a material is exposed to a plasma of certain gases in a high vacuum environment. The etching is achieved because chemically reactive radical is formed in the plasma and it is accelerated towards the substrate (physical bombardment). Therefore, different materials can be etched depending on the combination of gases, RF and ICP powers and temperature.

In the presented fabrication process, two different recipes were employed. A C_4F_8/O_2 based recipe to etch the thin $Si0_2$ membrane followed by a three-step-Bosh to etch the silicon.

i. $Si0_2$ etching at 10°C:
The etching in silicon dioxide increase the wafer temperature significantly. This extra heat could damage the photoresist. Therefore, 5 minutes pauses were including after 5 minutes of process to cool the wafer.
Etch recipe: C_4F_8 27 sccm, O_2 3 sccm, HF 50 W, ICP 500 W, 5'.
Finally, 20 minutes of etching were employed to etch the 3 μm SiO_2. After any silicon dioxide etching, an O_2 plasma cleaning is recommended because of the residual dirt.

ii. Silicon etching: The next step consists in the silicon etching. The $Si0_2$ acts as a mask for the following 400 μm silicon DRIE. This can be done since the recipes employed to etch the silicon barely affect the $Si0_2$. In the same way, the bottom membrane will act as a stop layer protecting the metal circuits.
Classical silicon etching consists on two main steps which are: the isotropic silicon etch and the fluorocarbon film deposition (known as passivation). However, higher etch selectivity with respect to the masking material can be obtained by subdividing the etch step into two parts. The first part is the selective removal of the fluorocarbon film deposited at the bottom of the trench, whereas the second part is a fast isotropic etching. This gives rise to a so called three step DRIE process (or 3-Step-Bosh). The following 3-step-bosh was used:
1-Passivation: C_4F_8 100 sccm, SF_6 1sccm, HF 0 W, ICP 220 W, 4".
2-Breakthrough: C_4F_8 1 sccm, SF_6 100 sccm, HF 15 W, ICP 220 W, 5".
3-Etch: C_4F_8 1 sccm, SF_6 100 sccm, HF 0 W, ICP 220 W, 3".
Figure A.1 displays the overall schematic of the photolithography process followed by the dry etching.
As was shown in Section 5.7, the dimensions of the fabricated PC are in good agreement with the theoretical ones. Nevertheless, there are some aspects that we are working to improve. The most important one is the side-wall verticality since we are getting an

over-etching with 1.8 ° inclination. Figure A.2 presents a picture taken in the optical microscope of the same device area with top-side and back-side illumination. The different radii of the holes are appreciated. This is a known problem in the silicon etching and it could be sorted out employing a cryogenic dry etching.

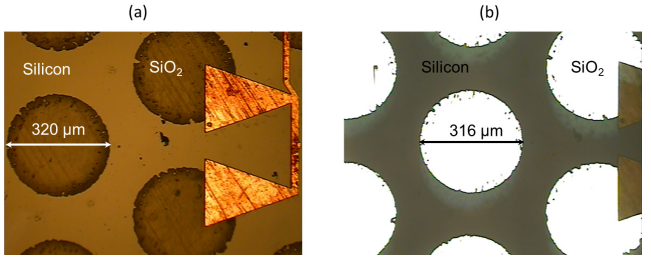

Figure A.2: Optical microscope picture of the PC platform with (a) top-side and (b) back-side illumination. The suspended SiO_2 membrane can be also seen.

3. Antenna and filter photolithography (Top-side):

   The antenna and the filer were fabricated in a conventional photolithography process following the next steps:

   (a) Surface cleaning.

   (b) Ti Prime Adhesion Promoter (Spin coater at 3000 rpm).

   (c) AZ1518 Positive photoresist (2 μm Spin coater at 3000 rpm).

   (d) MLA Dose: 30 mJ/cm^2.

   (e) Development AZ400(1:4) 2min.

   (f) Metal deposition: e-Beam evaporation of Cr 20 nm (100°C), Cu 2 μm and Au 30 nm. Deposition Rate: Cr 1 A/s, Cu 3 A/s and Au 1 A/s.

   (g) Lift-off: TechniStrip NI555.

   Figure A.3 presents the pictures of the fabricated antennas and the back-side etched marks employed for the alignment.

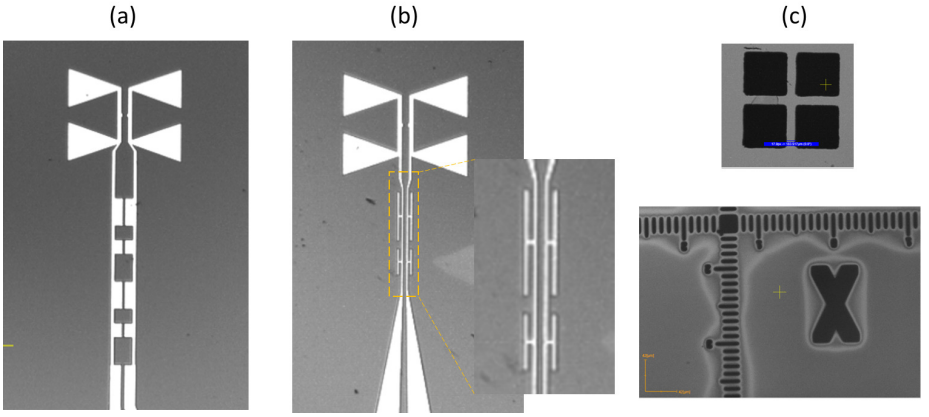

Figure A.3: (a-b) Pictures of the fabricated antennas. (c) Back-etched marks used for the alignment. (Images taken by the MLA microscope).

4. Photonic-crystal etching (back-side): The last step is the photonic crystal etching. For that purpose, it was employed the same photolithography and DRIE procedures that the ones for the alignment marks described above. But firstly, (before the etching) the top-side metallized circuits (antenna+filter) must be protected. To that end, the AZ520D protective coating was used. Secondly, the back-side photolithography process was carried out and subsequently the back 3 μm $Si0_2$ etching was performed. The final step is the 400 μm PC silicon etching. Although the top $Si0_2$ membrane (which in this etching step is the down-side) is supposed to acts as a barrier, the silicon etch-rate in the wafer is not uniform. The central area of the wafer is etched faster than the borders. Therefore, some areas of the top membrane might break because of the over-etching. In such case the metallic base of the DRIE instrument would be exposed which is strongly not recommended. Therefore, the silicon wafer was attached to a dummy wafer employing a thermal tape. This tape adheres tightly at room temperature and can easily be release just by heating up to certain temperature (120 °C for our case) without damaging the substrates upon tape removal.
   It can be pointed out that in the first tries, the PC was etched in the same step that the alignment marks. However, many drawbacks were found because of the difficulty to achieve the vacuum for a holey wafer in the

spinning and in the MLA. To sum up, as happens in all the multi-step photolithography process, it is advantageous to preserve the planarity of the wafer up to the end.
Other approach for etching the alignment marks and the PC structure was tested. This time, the bottom $Si0_2$ layer was dismissed and a thick layer (24 μm) of positive photoresist was employed instead. With this thickness, the silicon/photoresist selectivity was enough to break through the 400 μm silicon wafer. Although this method leads to a lower aspect ratio performance, the whole process became simpler. Furthermore, the aspect ratio is not a critical factor in this design since the PC dimensions are in the order of the etched height. Furthermore, from the point of view of the PC waveguide, the SiO_2 membrane is electrically very thin and presents a low refractive index, so that can be removed without creating any asymmetry in the field distribution. Nevertheless, this aspect must be carefully analysed if the design is intended to be scaled to higher frequencies.

To avoid an extra shaping process in a dicing machine we took advance of the same PC etching to erode the profile of the PC platform circuit including the silicon taper and the holes for the alignment pins and screws. These marks were used to align the circuit with the printed jig box and for the screws that fix the IF connector.

A.2 Reproducibility of the Photonic Crystal's Fabrication Method

Additionally, to evaluate the stability and reproducibility of the manufacturing process, three identical designs were fabricated and measured. The results can be seen in Figure A.4 where an accurate and repeatable manufacturing process can be intuited from the similarity of the curves.

A.3 Possible Causes of Fabrication Failures

The etching may be affected by several factors. In our case, one of the main possible causes of failure, in this specific part of the manufacturing, was the dirtiness associated with the SiO_2 etching.

Usually, two separate machines are used for SiO_2 and Si etching. In our case we perform a 2 hours chamber clean and a 30 min O_2 clean between both

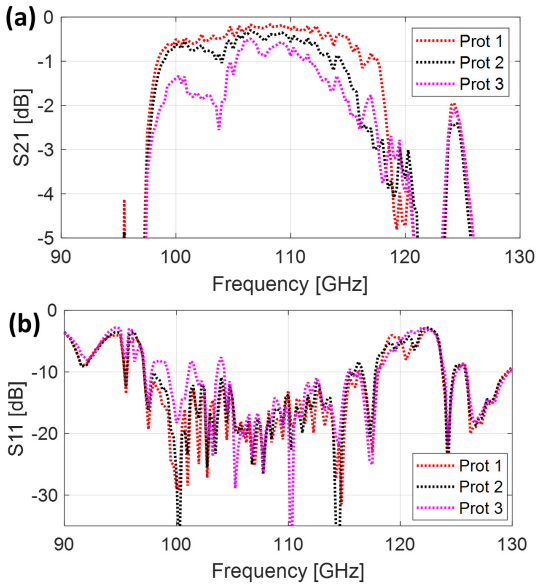

Figure A.4: Comparison between three measured PC waveguides: (a) Insertion Loss and (b) Return Loss.

processes. However, if the chamber is not clean enough or the pumping is not capable to extract all the material and gases residuals of the etching process, some part of this "dirt" may be redeposited on the silicon interfering the etching. Figure A.5(a) shows an image obtained with the optical microscope, focusing on the bottom of an incomplete silicon etching where the redeposited dirt stopped the etching when approximately half of the height had been eroded.

The residual water, solvent and nitrogen formation might be also a source of failures. All they create bubbles in the photoresist that react during the etching and can destroy the process as in the example presented in Figure A.5 (b). In this case, an abrupt increase of the temperature also burns the photoresist.

Some things can be done to avoid bubble formation and increase the thermal stability.

- The first one is to ensure a sufficient softbake and maybe introduce a ramped soft bake temperatures for very thick photoresists, because bubbles can be formed by rapid outgassing of solvents.

- Other trick is to introduce a hard-baking step after the development below the resist softening point to reduce the water concentration.

- Moreover, if not all the photoinitiators are converted in the photolithography process, large amount of nitrogen can be formed in the resist during dry etching. Therefore, it is also recommended to perform a flood exposure (without mask) and to wait until the nitrogen formed has gone before starting the DRIE.

-Finally, a combination of solutions was performed to guaranty the temperature stability. The first one is the hard-backing mentioned above, which helps to prevent the thermal deformation of the resist structure. Furthermore, a good Helium flux from the chuck, which guaranties a good cooling, must be verified before each etching process. Finally, if two wafers are attached, it is important to avoid the formation of any bubble in the thermal tape that could affect the cooling transfer.

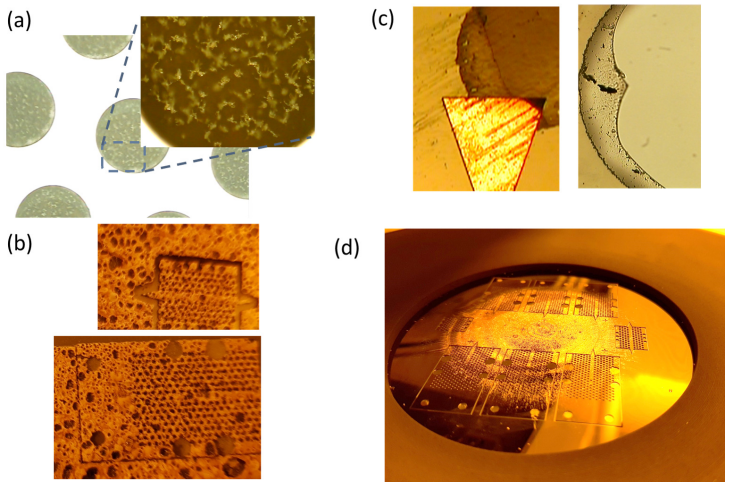

Figure A.5: Pictures of possibles sources of errors during the fabrication. (a) Grass (dirtiness) on the bottom of the PC. (b) Broken membrane. (c) Bubbles in a burned photoresist. (d) Non-uniform etching.

We found another possible point of failure in the release of the substrate from the thermal tape. Some areas of the protective photoresist coating resulted damaged during the etching, sticking the tape and the wafer. The SiO_2 membrane in these areas was broken upon tape removal. Figure A.5 (c) presents some examples of the broken membrane. The degradation of the resist might be

due to an overheating in those areas as a consequence of a bad cooling transfer from the chuck. Once again, the temperature proved to be a critical factor in the success of the fabrication.

Lastly, another factor that could cause a thinning or weakening of the membrane is over-etching. The Bosch recipe presents ideally an etching ratio higher than 450 ($Si : SiO_2$) for a thermal grown SiO_2 mask. For the e-Beam evaporated SiO_2 we assume a selectivity around 100 (Si : SiO2) from previous designs carried out in our facilities. The selectivity displays the ratio of the etching rate of two materials that are simultaneously exposed to the etching. Nevertheless, this parameter is not homogeneous over the entire substrate since the selectivity in the center is much lower than in the borders. Figure A.5(d) presents a picture of a partially etched wafer employing a photoresist mask where it can be easy appreciated the mentioned inhomogeneity. Therefore, it is recommended to dispose the designs in a way that uniform etching rate is obtained avoiding the over-etching of some areas and the implicit membrane thinning.

A.4 3D-Printed Housing Blocks

The ceramic housing jigs were fabricated with the 3D printer DWS 028J which is based on laser stereolithography (SLA). This technology combines fast prototyping with good resolution (in the order of 200 μm). Furthermore, the dielectric constant of the photoresist employed was measured to be around 3. This low value is advantageous to avoid undesired reflections and diffraction effects that are commonly found in metallic jigs. Lastly, the housing blocks were designed to allow proper alignment and easy connection between the flange of the metal waveguide and the PC waveguide. Figure A.6 shows some of the fabricated designs.

A.5 Fabrication of the Modified Lens-Antennas

The modified antenna lens presented in Chapters 3 and 4 were fabricated following a similar photolithography process than the one presented above. The main difference was the use of negative photoresist and a mask aligner with a chromium hard mask. The overall schematic of the process and the pictures of the employed equipment can be seen in Figure A.7. Furthermore, the recipe is described below:

1. Modified Lens-Antennas 100-850 GHz detector:

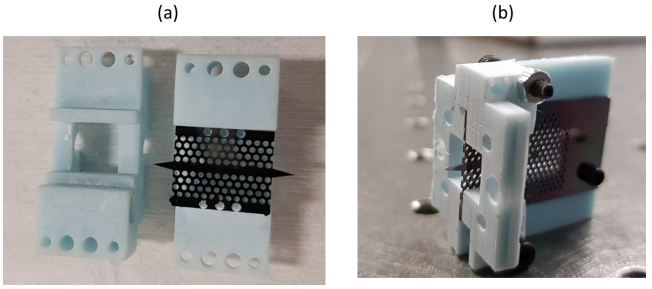

Figure A.6: Pictures of the fabricated 3D printed housing jigs: (a) Top view of the split housing block and (b) perspective view of the mounted silicon circuit in housing block.

(a) Surface cleaning.

(b) Ti Prime Adhesion Promoter (Spin coater at 3000 rpm).

(c) AZ nLof2070 negative photoresist (7 μm Spin coater at 2500 rpm) followed by 90" 110°C baking.

(d) Mask Aligner 14"(186 mJ/cm^2) exposition followed by 90" post-exposure bake at 110°C.

(e) Development AZ726mif.

(f) Metal deposition: e-Beam evaporation of Cr 20 nm (100°C), Cu 2 μm and Au 10 nm to avoid oxidation. Deposition Rate: Cr 1 A/s, Cu 3 A/s, Au 3 1/s.

(g) Lift-off: TechniStrip NI555.

2. Modified Lens-Antennas 400 GHz - 28 THz detector:

(a) Surface cleaning

(b) Ti Prime Adhesion Promoter (Spin coater at 3000 rpm).

(c) AZ nLof2020 negative photoresist (2 μm Spin coater at 3000 rpm) followed by 60" 110°C baking.

(d) Mask Aligner 5" exposition (66 mJ/cm^2) followed by 60" post-exposure bake at 110 °C.

(e) Development AZ726mif

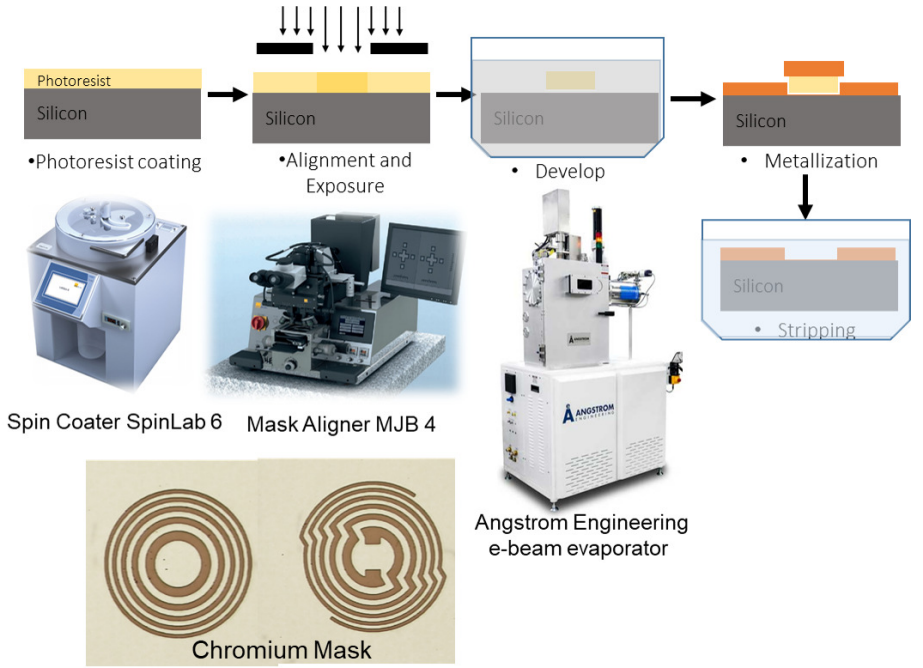

Figure A.7: Schematic of the photolithography process used to fabricate the modified antenna-lens at the Public University of Navarra's facilities.

(f) Metal deposition: e-Beam evaporated Cr 20 nm (100 °C), Cu 2 μm. Deposition Rate: Cr 1 A/s, Cu 3 A/s.

(g) Lift-off: TechniStrip NI555

Some pictures of the fabricated prototypes can be seen in Figures A.8, A.9 and A.10.

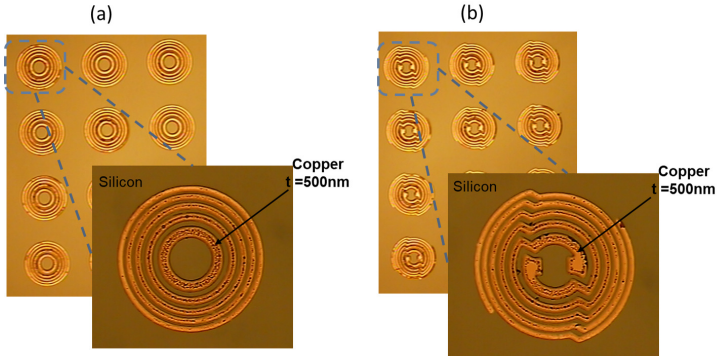

Figure A.8: Pictures of the fabricated (a) FZPL and (b) modified quasi-spiral antenna-lens for the SubMMW-IR detector.

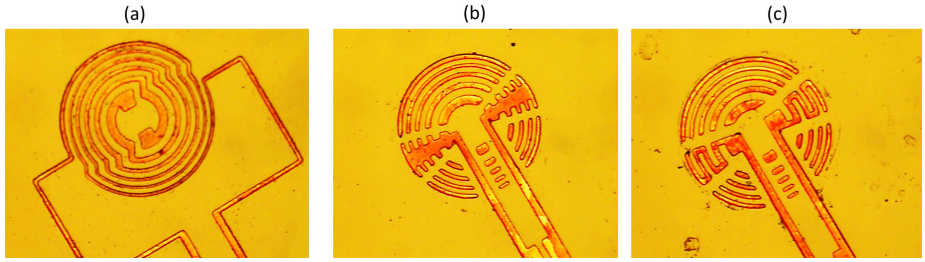

Figure A.9: (a) Pictures of the fabricated modified quasi-spiral, (b) quasi-bow-tie and (c) quasi-meander antenna-lens for the SubMMW-IR

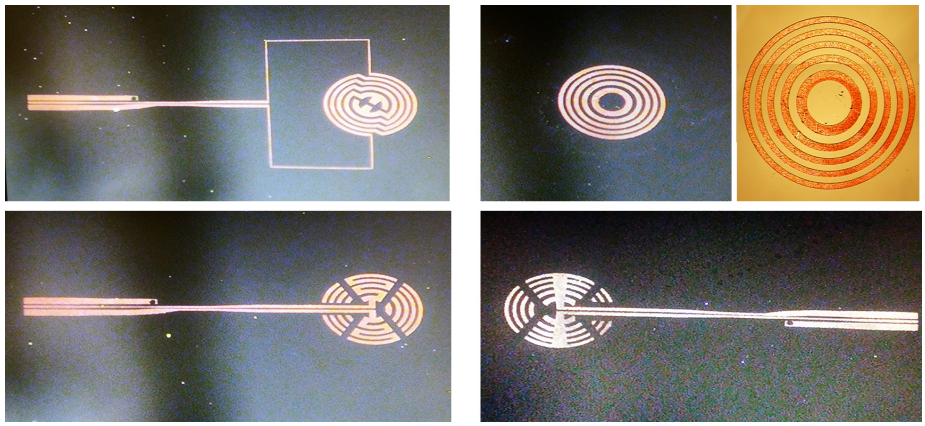

Figure A.10: Pictures of the fabricated and measured modified antenna-lenses for the MM-SubMMW detector described in Chapter 4.

Bibliography

[Ali94] W. Y. Ali-Ahmad and G. M. Rebeiz, "A 335 GHz quasi-optical Schottky receiver.", *IEEE Microwave and Guided Wave Letters*, vol. 4, pp. 37–39, 1994.

[ACS] ACST. "Advanced Compound Semiconductor." http://www.acst.de/.

[Ade14] P. Ade, N. Aghanim, M. Alves, C. Armitage-Caplan, M. Arnaud, M. Ashdown, F. Atrio-Barandela, J. Aumont, H. Aussel and C. Baccigalupi et al., "Planck 2013 results. I. Overview of products and scientific results.", *Astronomy & Astrophysics*, vol. 571, p. A1, 2014.

[ADS] Keysight ADS. "Advanced Design System." https://www.keysight.com/en/pc-1375582/advanced-design-system-ads-simulation-elements?cc=US&lc=eng.

[Afs19] L. Afsah-Hejri, P. Hajeb, P. Ara and R.J. Ehsani, "A comprehensive review on food applications of terahertz spectroscopy and imaging.", *Comprehensive Reviews in Food Science and Food Safety*, vol. 18, no. 5, pp. 1563–1621, 2019.

[Ala16] A. J. Alazemi, H. H. Yang and G.M. Rebeiz, "Double bow-tie slot antennas for wideband millimeter-wave and terahertz applications.", *IEEE Transactions on Terahertz Science and Technology*, vol. 6, no. 5, pp. 682–689, 2016.

[Ald09] J. Alda and F. J. González, "Fresnel zone antenna for dual-band detection at millimeter and infrared wavelengths.", *Optics letters*, vol. 34 6, pp. 809–11, 2009.

[Ali15] N. Alijabbari, M. F. Bauwens and R. M. Weikle, "Design and Characterization of Integrated Submillimeter-Wave Quasi-Vertical Schottky Diodes.", *IEEE Transactions on Terahertz Science and Technology*, vol. 5, no. 1, pp. 73–80, 2015.

[ALMA] ALMA and (ESO/NRAO/NAOJ). "How does ALMA see?" https://www.almaobservatory.org/en/about-alma-at-first-glance/how-alma-works/how-does-alma-see/.

[Ama17] H. Amarloo and S. Safavi-Naeini, "Terahertz Line Defect Waveguide Based on Silicon-on-Glass Technology.", *IEEE Transactions on Terahertz Science and Technology*, vol. 7, no. 4, pp. 433–439, 2017.

[And19] M. Anderberg, P. Sobis, V. Drakinskiy, J. Schleeh, S. Dejanovic, A. Emrich and J. Stake, "A 183-GHz Schottky Diode Receiver with 4 dB Noise Figure.", *2019 IEEE MTT-S International Microwave Symposium (IMS)*, pp. 172–175, 2019.

[App07a] R. Appleby and R.N. Anderton, "Millimeter-wave and submillimeter-wave imaging for security and surveillance.", *Proceedings of the IEEE*, vol. 95, no. 8, pp. 1683–1690, 2007.

[App07b] R. Appleby and H. B. Wallace, "Standoff detection of weapons and contraband in the 100 GHz to 1 THz region.", *IEEE transactions on antennas and propagation*, vol. 55, no. 11, pp. 2944–2956, 2007.

[Bag92] L.C.J. Baggen. "The Fresnel zone plate antenna: Design and analysis." Ph.D. thesis, MSc. thesis, Eindhoven University of Technology, 1992.

[Bah03] I. Bahl and P. Bhartia. *Microwave solid state circuit design*. John Wiley & Sons, 2003.

[Bas17] J.A. Baselmans, J. Bueno, S.J.C. Yates, O. Yurduseven, N. Llombart, K. Karatsu, A.M. Baryshev, L. Ferrari, A. Endo and D.J. Thoen et al., "A kilo-pixel imaging system for future space based far-infrared observatories using microwave kinetic inductance detectors.", *Astronomy & Astrophysics*, vol. 601, p. A89, 2017.

[Bis90] W. L. Bishop, E. R. Meiburg, R. J. Mattauch, T. W. Crowe and L. Poli. "A micron-thickness, planar Schottky diode chip for terahertz applications with theoretical minimum parasitic capacitance." *IEEE International Digest on Microwave Symposium*, pp. 1305–1308 vol.3. 1990.

[Mae15] I. Maestrojuan Biurrun. "Development of Terahertz Systems for Imaging Applications." Ph.D. thesis, Universidad Publica de Navarra, 2015.

[Blu92] R. Blundell, "Submillimeter receivers for radio astronomy.", *Proceedings of the IEEE*, vol. 80, no. 11, pp. 1702–1720, 1992.

[Bro03] E.R. Brown, "Fundamentals of terrestrial millimeter-wave and THz remote sensing.", *International journal of high speed electronics and systems*, vol. 13, no. 04, pp. 995–1097, 2003.

[Bue17] J. Bueno, O. Yurduseven, N. Llombart, S.J.C Yates, A. Neto and J.J.A Baselmans. "Experimental validation of an mkid coupled dual polarized leaky lens antenna." *2017 42nd International Conference on Infrared, Millimeter, and Terahertz Waves (IRMMW-THz)*, pp. 1–2. IEEE, 2017.

[Bus61] L. Van Buskirk and C. Hendrix, "The zone plate as a radio-frequency focusing element.", *IRE Transactions on Antennas and Propagation*, vol. 9, no. 3, pp. 319–320, 1961.

[Bus06] K. Busch, S. Lölkes, R.B. Wehrspohn and H. Föll. *Photonic crystals: advances in design, fabrication, and characterization*. John Wiley & Sons, 2006.

[Car15] G. Carpintero, E. Garcia-Munoz, H. Hartnagel, S. Preu and A. Raisanen. *Semiconductor teraHertz technology: devices and systems at room temperature operation*. John Wiley & Sons, 2015.

[Chat04] G. Chattopadhyay, I. Mehdi, J.S. Ward, E. Schlecht, A. Skalare and P.H. Siegel et al. "Development of multi-pixel heterodyne array instruments at submillimeter wavelengths." *Proceedings of the Asia Pacific Microwave Conference*. 2004.

[Chat13] G. Chattopadhyay, T. J. Reck, C. Jung-Kubiak, J. V. Siles, C. Lee, R. Lin and I. Mehdi. "Silicon micromachining for terahertz component development." *IEEE MTT-S International Microwave and RF Conference*, pp. 1–4. 2013.

[Coj05] O. Cojocari, C. Sydlo, H.L Hartnagel, S. Biber, J. Schür and L.P. Schmidt. "Schottky-structures for THz-applications based on quasi-vertical design-concept." *International Symposium on Space Terahertz Technology, Göteborg, Sweden*. 2005.

[Col84] R. Collin, "Aperture efficiency for paraboloidal reflectors.", *IEEE transactions on antennas and propagation*, vol. 32, no. 9, pp. 997–1000, 1984.

[Col07] R. E. Collin. *Foundations for microwave engineering*. John Wiley & Sons, 2007.

[Com87] R. Compton, R. McPhedran, Z. Popovic, G. Rebeiz, P. Tong and D. Rutledge, "Bow-tie antennas on a dielectric half-space: Theory and experiment.", *IEEE transactions on antennas and propagation*, vol. 35, no. 6, pp. 622–631, 1987.

[Cor09] R. Cory and Skyworks Solutions, "Schottky Diodes.", *Microwave Product Digest*, pp. 1–5, 2009.

[NRC07] National Research Council et al. *Handbook of Frequency Allocations and Spectrum Protection for Scientific Uses*. National Academies Press, 2007.

[Cow65] A.M. Cowley and S.M. Sze, "Surface states and barrier height of metal-semiconductor systems.", *Journal of Applied Physics*, vol. 36, no. 10, pp. 3212–3220, 1965.

[Cow66] A. M. Cowley and H. O. Sorensen, "Quantitative Comparison of Solid-State Microwave Detectors.", *IEEE Transactions on Microwave Theory and Techniques*, vol. 14, no. 12, pp. 588–602, 1966.

[Cro91] T. W. Crowe. "GaAs Schottky diodes for mixing applications beyond 1THz." *International Conference on Infrared and Millimeter Waves*. 1991.

[Cui19] J. Cui, Y. Zhang, D. Xia, Y. Xu, F. Xiao, B. Yan and R. Xu, "A 220 GHz Broadband Sub-Harmonic Mixer Based on Global Design Method.", *IEEE Access*, vol. 7, pp. 30067–30078, 2019.

[Dec16] T. Decoopman, M. Trier, N. Martin, D. Boisbunon, A. Lemasson, J. Tailhades, P. Frijlink, M. Hoefle, O. Cojocari, P. Piironen and M. Périchaud. "Millimetre-wave detectors for direct detection radiometers." *2016 Global Symposium on Millimeter Waves (GSMM) ESA Workshop on Millimetre-Wave Technology and Applications*, pp. 1–4. 2016.

[Dhi17] S.S Dhillon, M.S Vitiello, E.H. Linfield, A.G. Davies, M. C. Hoffmann, J. Booske, C. Paoloni, M. Gensch, P. Weightman and G.P. Williams et al., "The 2017 terahertz science and technology roadmap.", *Journal of Physics D: Applied Physics*, vol. 50, no. 4, p. 043001, 2017.

[Alo13] M. Alonso del Pino, N. Llombart, G. Chattopadhyay, C. Lee, C. Jung-Kubiak, L. Jofre and I. Mehdi, "Design guidelines for a terahertz silicon micro-lens antenna.", *IEEE Antennas and Wireless Propagation Letters*, vol. 12, pp. 84–87, 2013.

[Dra13] V. Drakinskiy, P. Sobis, H. Zhao, T. Bryllert and J. Stake. "Terahertz GaAs Schottky diode mixer and multiplier MIC's based on e-beam technology." *Conference Proceedings - International Conference on Indium Phosphide and Related Materials*, pp. 1–2. may 2013.

[Ede07] I. Ederra, L. Azcona, B.E.J. Alderman, A. Laisné , R. Gonzalo, C.M. Mann, D.N. Matheson and P. de Maagt, "A 250 GHz Sub-Harmonic Mixer Design Using EBG Technology.", *IEEE Transactions on Antennas and Propagation*, vol. 55, pp. 2974–2982, 2007.

[Ede10] I. Ederra, I. Khromova, R. Gonzalo, N. Delhote, D. Baillargeat, A. Murk, B.E.J. Alderman and P. de Maagt, "Electromagnetic Band Gap Waveguide for the Millimeter Range.", *IEEE Transactions on Microwave Theory and Techniques*, vol. 58, pp. 1734–1741, 2010.

[Eta14] D. Etayo, I. Ederra and R. Gonzalo, "Analysis of square Fresnel Zone Plate Lens for dual band detectors.", *Journal of Infrared, Millimeter, and Terahertz Waves*, vol. 35, pp. 525–535, 2014.

[Fed05] J. F. Federici, B. Schulkin, F. Huang, D. Gary, R. Barat, F. Oliveira and D. Zimdars, "THz imaging and sensing for security applications—explosives, weapons and drugs.", *Semiconductor Science and Technology*, vol. 20, no. 7, p. S266, 2005.

[Fil92] D.F. Filipovic, Y. W. Ali-Ahmad and G.M. Rebeiz, "Millimeter-wave double-dipole antennas for high-gain integrated reflector illumination.", *IEEE transactions on microwave theory and techniques*, vol. 40, no. 5, pp. 962–967, 1992.

[Fil93] D. F. Filipovic and G. M. Rebeiz, "Double-slot antennas on extended hemispherical and elliptical quartz dielectric lenses.", *International Journal of Infrared and Millimeter Waves*, vol. 14, pp. 1905–1924, 1993.

[Fuk15] R Fukasawa, "Terahertz imaging: Widespread industrial application in non-destructive inspection and chemical analysis.", *IEEE Transactions on Terahertz Science and Technology*, vol. 5, no. 6, pp. 1121–1127, 2015.

[Gon01] R. Gonzalo, I. Ederra, C.M. Mann and P. De Maagt, "Radiation properties of terahertz dipole antenna mounted on photonic crystal.", *Electronics Letters*, vol. 37, no. 10, pp. 613–614, 2001.

[Gon02] R. Gonzalo, B. Martinez, C. M. Mann, H. Pellemans, P. H. Bolivar and P. de Maagt, "A low-cost fabrication technique for symmetrical and asymmetrical layer-by-layer photonic crystals at submillimeter-wave frequencies.", *IEEE Transactions on Microwave Theory and Techniques*, vol. 50, no. 10, pp. 2384–2392, 2002.

[Gon05] F. González, B. Ilic, J. Alda and G. D. Boreman, "Antenna-coupled infrared detectors for imaging applications.", *IEEE Journal of Selected Topics in Quantum Electronics*, vol. 11, pp. 117–120, 2005.

[Gou92] M. Gouker and G.S. Smith, "A millimeter-wave integrated-circuit antenna based on the Fresnel zone plate.", *IEEE transactions on microwave theory and techniques*, vol. 40, no. 5, pp. 968–977, 1992.

[Gra13] O. Grasset, M.K. Dougherty, A. Coustenis, E.J. Bunce, C. Erd, D. Titov, M. Blanc, A. Coates, P. Drossart and L. N. Fletcher et al., "JUpiter ICy moons Explorer (JUICE): An ESA mission to orbit

Ganymede and to characterise the Jupiter system.", *Planetary and Space Science*, vol. 78, pp. 1–21, 2013.

[Gra15] U. Graf, C. Honingh, K. Jacobs and J. Stutzki, "Terahertz heterodyne array receivers for astronomy.", *Journal of Infrared, Millimeter, and Terahertz Waves*, vol. 36, no. 10, pp. 896–921, 2015.

[Gut19a] J. Gutiérrez, K. Zeljami, T. Fernández, J.P. Pascual and A. Tazón, "Accurately Modeling of Zero Biased Schottky-Diodes at Millimeter-Wave Frequencies.", *Electronics*, vol. 8, no. 6, p. 696, 2019.

[Gut19b] J. Gutiérrez, K. Zeljami, J.P. Pascual, T. Fernández and A. Tazón, "Comparison of Microstrip W-Band Detectors Based on Zero Bias Schottky-Diodes.", *Electronics*, vol. 8, no. 12, p. 1450, 2019.

[Han13] R. Han, Y. Zhang, Y. Kim, D. Y. Kim, H. Shichijo, E. Afshari and K. K. O, "Active Terahertz Imaging Using Schottky Diodes in CMOS: Array and 860-GHz Pixel.", *IEEE Journal of Solid-State Circuits*, vol. 48, no. 10, pp. 2296–2308, 2013.

[Han19] R. Han, Z. Hu, C. Wang, J. W. Holloway, X. Yi, M. Kim and J. Mawdsley, "Filling the Gap, Silicon Terahertz Integrated Circuits Offer Our Best Bet.", *IEEE Microwave Magazine*, vol. 20, pp. 80–93, 2019.

[Hea18] D. Headland, Y. Monnai, D. Abbott, C. Fumeaux and W. Withayachumnankul, "Tutorial: Terahertz beamforming, from concepts to realizations.", *Apl Photonics*, vol. 3, no. 5, p. 051101, 2018.

[Hes07] J. Hesler and T.W. Crowe, "Responsivity and noise measurements of zero-bias Schottky diode detectors.", *Proc. ISSTT*, pp. 89–92, 2007.

[Hoe11] M. Hoefle, A. Penirschke, O. Cojocari and R. Jakoby. "Advanced RF characterization of new planar high sensitive zero-bias Schottky diodes." *2011 6th European Microwave Integrated Circuit Conference*, pp. 89–92. 2011.

[Hoe13] M. Hoefle, A. Penirschke, O. Cojocari, A. Amrhein, T. Decoopman, P. Piironen and R. Jakoby. "1/f-noise prediction in millimeter wave detectors based on quasi vertical Schottky diodes." *2013 38th International Conference on Infrared, Millimeter, and Terahertz Waves (IRMMW-THz)*, pp. 1–3. 2013.

[Hri00] H.D. Hristov. *Fresnal Zones in Wireless Links, Zone Plate Lenses and Antennas*. Artech House, Inc., 2000.

[Hro13] M. Hrobak, M. Sterns, M. Schramm, W. Stein and L. Schmidt. "Planar zero bias schottky diode detector operating in the E- and W-band." *2013 European Microwave Conference*, pp. 179–182. 2013.

[ITU16] ITU. "Regulations Radio-ITU, Edition of 2016."

[Jam79] J.R. James and A. Henderson, "High-frequency behaviour of microstrip open-circuit terminations.", *IEE Journal on Microwaves, Optics and Acoustics*, vol. 3, no. 5, pp. 205–218, 1979.

[Jam03] C. Jamois, R.B. Wehrspohn, L.C. Andreani, C. Hermann, O. Hess and U. Gösele, "Silicon-based two-dimensional photonic crystal waveguides.", *Photonics and Nanostructures: Fundamentals and Applications*, vol. 1, no. 1, pp. 1 – 13, 2003.

[Ji20] G. Ji, D. Zhang, J. Meng, S. Liu and C. Yao, "Design and Measurement of a 0.67 THz Biased Sub-Harmonic Mixer.", *Electronics*, vol. 9, no. 1, p. 161, 2020.

[Joa08] J. Joannopoulos, S.G. Johnson, J.N. Winn and R. D. Meade. *Molding the flow of light*. Princeton Univ. Press, Princeton, NJ [ua], 2008.

[Joh99] SG Johnson and JD Joannopoulos. "MIT Photonic Bands (MPB).", 1999.

[Kaj84] D. Kajfez, A. W. Glisson and J. James, "Computed Modal Field Distributions for Isolated Dielectric Resonators.", *IEEE Transactions on Microwave Theory and Techniques*, vol. 32, no. 12, pp. 1609–1616, 1984.

[Kat83] P. Katehi and N. Alexopoulos, "On the effect of substrate thickness and permittivity on printed circuit dipole properties.", *IEEE Transactions on Antennas and Propagation*, vol. 31, no. 1, pp. 34–39, 1983.

[Khr13] I. Khromova, R. Gonzalo, I. Ederra, N. Delhote, D. Baillargeat, A. Murk, B. Alderman and P. de Maagt, "Subharmonic Mixer Based on EBG Technology.", *IEEE Transactions on Terahertz Science and Technology*, vol. 3, pp. 838–845, 2013.

[Kil85] P.S. Kildal, "Factorization of the feed efficiency of paraboloids and Cassegrain antennas.", *IEEE Transactions on Antennas and Propagation*, vol. 33, no. 8, pp. 903–908, 1985.

[Kim05] T.Y. Kim, Y. Kagawa and L.Y. Chai, "Modelling of a circular Fresnel zone plate lens for electromagnetic wave antenna application.", *International Journal of Numerical Modelling: Electronic Networks, Devices and Fields*, vol. 18, no. 6, pp. 429–439, 2005.

[Kim17] D. Y. Kim and K. 0. Kenneth, "Reduction of Low Frequency Noise Impact to Terahertz Detectors in CMOS.", *IEEE Microwave and Wireless Components Letters*, vol. 27, no. 2, pp. 150–152, 2017.

[Kim17] D. Y. Kim and K.O. Kenneth, "Reduction of NEP variations for terahertz detectors using Schottky barrier diodes in CMOS.", *Electronics Letters*, vol. 53, no. 11, pp. 732–734, 2017.

[Kor93] B. Kormanyos, P. Ostdiek, W.L. Bishop, T.W. Crowe and G.M. Rebeiz, "A planar wideband 80-200 GHz subharmonic receiver.", *IEEE transactions on microwave theory and techniques*, vol. 41, no. 10, pp. 1730–1737, 1993.

[Kow14] M. Kowalski, M. Kastek, H. Polakowski, N. Palka, M. Piszczek and M. Szustakowski. "Multispectral concealed weapon detection in visible, infrared, and terahertz." *Terahertz Physics, Devices, and Systems VIII: Advanced Applications in Industry and Defense*, vol. 9102, p. 91020T. International Society for Optics and Photonics, 2014.

[Kow19] M. Kowalski, "Hidden object detection and recognition in passive terahertz and mid-wavelength infrared.", *Journal of Infrared, Millimeter, and Terahertz Waves*, vol. 40, no. 11-12, pp. 1074–1091, 2019.

[Lai11] N.D. Lai, J.H. Lin, D.B. Do, W.P. Liang, Y. Di, T. S. Huang, Y. Huang and C.C. Hsu. "Fabrication of Two-and Three-Dimensional Photonic Crystals and Photonic Quasi-Crystals by Interference Technique." *Holography, Research and Technologies*. IntechOpen, 2011.

[Lam03] J-M. Lamarre, J.L. Puget, F. Bouchet, P. Ade, A. Benoit, J.P. Bernard, J. Bock, P. De Bernardis, J. Charra and F. Couchot et al., "The Planck High Frequency Instrument, a third generation CMB experiment, and a full sky submillimeter survey.", *New Astronomy Reviews*, vol. 47, no. 11-12, pp. 1017–1024, 2003.

[Lec07] S. Leclercq, "Discussion about Noise Equivalent Power and its use for photonnoise calculation.", *Report On FOV Optics And Bolometer Projects For The 30m Telescope, International Research Institute For Radio Astronomy (IRAM)*, pp. 1–15, 2007.

[Lew19] R.A. Lewis, "A review of terahertz detectors.", *Journal of Physics D: Applied Physics*, vol. 52, no. 43, p. 433001, 2019.

[Llo11a] N. Llombart, G. Chattopadhyay, A. Skalare and I. Mehdi, "Novel Terahertz Antenna Based on a Silicon Lens Fed by a Leaky Wave Enhanced Waveguide.", *IEEE Transactions on Antennas and Propagation*, vol. 59, no. 6, pp. 2160–2168, 2011.

[Llo11b] N. Llombart, G. Chattopadhyay, A. Skalare and I. Mehdi, "Novel Terahertz Antenna Based on a Silicon Lens Fed by a Leaky Wave Enhanced Waveguide.", *IEEE Transactions on Antennas and Propagation*, vol. 59, no. 6, pp. 2160–2168, 2011.

[LLo13] N. Llombart, C. Lee, M. Alonso del Pino, G. Chattopadhyay, C. Jung-Kubiak, L. Jofre and I. Mehdi, "Silicon Micromachined Lens Antenna for THz Integrated Heterodyne Arrays.", *IEEE Transactions on Terahertz Science and Technology*, vol. 3, no. 5, pp. 515–523, 2013.

[Llo14] N. Llombart, M. Alonso-delPino, C. Lee, G. Chattopadhyay, C. Jung-Kubiak and I. Mehdi. "On the development of silicon micromachined lens antennas for THz integrated heterodyne arrays." *2014 39th International Conference on Infrared, Millimeter, and Terahertz waves (IRMMW-THz)*, pp. 1–2. 2014.

[Luc10] F. C. De Lucia, "The submillimeter: A spectroscopist's view.", *Journal of Molecular Spectroscopy*, vol. 261, no. 1, pp. 1–17, 2010.

[Luh79] N. C. Jr. Luhmann. "Instrumentation and techniques for plasma diagnostics-An overview." *imw*, vol. 2, pp. 1–65. 1979.

[Maa03] P.de Maagt, R. Gonzalo, Y. Vardaxoglou and J-M Baracco, "Electromagnetic bandgap antennas and components for microwave and (sub) millimeter wave applications.", *IEEE Transactions on Antennas and Propagation*, vol. 51, no. 10, pp. 2667–2677, 2003.

[Maas03] S.A. Maas. *Nonlinear Microwave and RF Circuits*. Artech House, 2003.

[Mac15] V. Mackowiak, J. Peupelmann, Y. Ma and A. Gorges, "NEP: noise equivalent power.", *Thorlabs, Inc., Newton, NJ, USA, White Paper*, 2015.

[Mae10] A. Maestrini, B. Thomas, H. Wang, C. Jung-Kubiak, J. Treuttel, Y. Jin, G. Chattopadhyay, I. Mehdi and G. Beaudin, "Schottky diode-based terahertz frequency multipliers and mixers.", *Comptes Rendus Physique*, vol. 11, no. 7-8, pp. 480–495, 2010.

[Mae11] I. Maestrojuán, I. M. Palacios, A. Rebollo, D. Etayo, J. Teniente, I. Ederra and R. Gonzalo, "Development of a sub-harmonic mixer working at 220 GHz.", *IEEE MTT-S International Microwave Workshop Series on Millimeter Wave Integration Technologies*, pp. 77–80, 2011.

[McN03] Sharee J. McNab, Nikolaj Moll and Yurii A. Vlasov, "Ultra-low loss photonic integrated circuit with membrane-type photonic crystal waveguides.", *Optics express*, vol. 11 22, pp. 2927–39, 2003.

[Mon13] J. Montero-de Paz, I. Oprea, V. Rymanov, S. Babiel, L.E. García-Muñoz, A. Lisauskas, M. Hoefle, A. Jimenez, O. Cojocari, D. Segovia-Vargas, M. Palandöken, T. Tekin, A. Stöhr and G. Carpintero, "Compact Modules for Wireless Communication Systems in the E-Band (71–76 GHz).", *Journal of Infrared, Millimeter, and Terahertz Waves*, vol. 34, pp. 251–266, 2013.

[Mea94] R.D. Meade, A. Devenyi, J. Joannopoulos, O.L. Alerhand, D.A. Smith and K. Kash, "Novel applications of photonic band gap materials: Low-loss bends and high Q cavities.", *Journal of applied physics*, vol. 75, no. 9, pp. 4753–4755, 1994.

[Mek96] A. Mekis, J.C. Chen, I. Kurland, S. Fan, R. Villeneuve and J. D. Joannopoulos, "High Transmission through Sharp Bends in Photonic Crystal Waveguides.", *Physical review letters*, vol. 77 18, pp. 3787–3790, 1996.

[Mel00] G. J. Melnick, J. R. Stauffer, M. Ashby, E.A Bergin, G. Chin, N. Erickson, P.F. Goldsmith, M. Harwit, J. E. Howe and S. C. Kleiner et al., "The submillimeter wave astronomy satellite: Science objectives and instrument description.", *The Astrophysical Journal Letters*, vol. 539, no. 2, p. L77, 2000.

[Min11] I. Minin and O. Minin, "Reference phase in diffractive lens antennas: A review.", *Journal of Infrared, Millimeter, and Terahertz Waves*, vol. 32, no. 6, p. 801, 2011.

[Min17] L. Minkevivcius, S. Indrivsiunas, R. Sniaukas, B. Voisiat, V. Janonis, V. Tamovsiunas, I. Kavsalynas, G. Ravciukaitis and G. Valuvsis, "Terahertz multilevel phase Fresnel lenses fabricated by laser patterning of silicon.", *Optics letters*, vol. 42, no. 10, pp. 1875–1878, 2017.

[Mit18] D. M. Mittleman, "Twenty years of terahertz imaging.", *Optics express*, vol. 26, no. 8, pp. 9417–9431, 2018.

[Moh16] N. Mohammad, M. Meem, B. Shen, P. Wang and R. Menon, "Broadband imaging with one planar diffractive lens.", *Scientific reports*, vol. 8, no. 1, pp. 1–6, 2018.

[Nea12] D.A. Neamen. *Semiconductor physics and devices: basic principles*. New York, NY: McGraw-Hill, 2012.

[NeoTech] NeoTech, 2019. Http://www.myneotech.com/products/gamp0100-0600sm10/.

[Net10] A. Neto, "UWB Non Dispersive Radiation From the Planarly Fed Leaky Lens Antenna— Part 1: Theory and Design.", *IEEE Transactions on Antennas and Propagation*, vol. 58, pp. 2238–2247, 2010.

[Nie74] B. Niemann, D. Rudolph and G. Schmahl, "Soft x-ray imaging zone plates with large zone numbers for microscopic and spectroscopic applications.", *Optics Communications*, vol. 12, no. 2, pp. 160–163, 1974.

[Agilent] Agilent Application Note, "Noise Figure Measurement Accuracy–The Y-Factor Method.", *Agilent Technology, Palo Alto, CA*, 2001.

[Öhr10] L. Öhrström, A. Bitzer, M. Walther and F. J. Rühli, "Terahertz imaging of ancient mummies and bone.", *American journal of physical anthropology*, vol. 142, no. 3, pp. 497–500, 2010.

[Oka17] K. Okamoto, K. Tsuruda, S. Diebold, S. Hisatake, M. Fujita and T. Nagatsuma, "Terahertz Sensor Using Photonic Crystal Cavity and Resonant Tunneling Diodes.", *Journal of Infrared, Millimeter, and Terahertz Waves*, vol. 38, pp. 1085–1097, 2017.

[Ott14] W. J. Otter, S. M. Hanham, N. M. Ridler, G. Marino, N. Klein and S. Lucyszyn, "100 GHz ultra-high Q-factor photonic crystal resonators.", *Sensors and Actuators A-physical*, vol. 217, pp. 151–159, 2014.

[Pag03] L. Pagani, A.O. Olofsson, P. Bergman, P. Bernath, J. H. Black, R. S. Booth, V. Buat, J. Crovisier, C. L. Curry and P. J.Encrenaz et al., "Low upper limits on the O2 abundance from the Odin satellite.", *Astronomy & Astrophysics*, vol. 402, no. 3, pp. L77–L81, 2003.

[Per19] J.M. Pérez-Escudero. "Development of sub-millimetre wave band subsystems and packaging techniques." Ph.D. thesis, Universidad Pública de Navarra, 2019.

[Phi92] T.G. Phillips and J. Keene, "Submillimeter astronomy (heterodyne spectroscopy).", *Proceedings of the IEEE*, vol. 80, no. 11, pp. 1662–1678, 1992.

[Pou18] J. Pourahmadazar and T.A. Denidni, "Towards Millimeter-wavelength: Transmission-Mode Fresnel-Zone Plate Lens Antennas using Plastic Material Porosity Control in Homogeneous Medium.", *Scientific reports*, vol. 8, no. 1, pp. 1–14, 2018.

[Poz83] D. Pozar, "Considerations for millimeter wave printed antennas.", *IEEE Transactions on Antennas and Propagation*, vol. 31, no. 5, pp. 740–747, 1983.

[Räi80] A. Räisänen, "Experimental studies on cooled millimeter wave mixers.", *Acta Polytechnica Scandinavica 46*, 1980.

[Reb92] G. M. Rebeiz, "Millimeter-wave and terahertz integrated circuit antennas.", *Proceedings of the IEEE*, vol. 80, no. 11, pp. 1748–1770, 1992.

[Rec12] T. Reck, J. Siles, C. Jung, J. Gill, C. Lee, G. Chattopadhyay, I. Mehdi and K. Cooper. "Array technology for terahertz imaging." *Passive and Active Millimeter-Wave Imaging XV*, vol. 8362, p. 836202. International Society for Optics and Photonics, 2012.

[Rec15] T. J. Reck, C. Jung-Kubiak, J. V. Siles, C. Lee, R. Lin, G. Chattopadhyay, I. Mehdi and Ken B. Cooper, "A Silicon Micromachined Eight-Pixel Transceiver Array for Submillimeter-Wave Radar.", *IEEE*

Transactions on Terahertz Science and Technology, vol. 5, pp. 197–206, 2015.

[Rei06] D. R. Reid and G. S. Smith, "A Full Electromagnetic Analysis for the Soret and Folded Zone Plate Antennas.", *IEEE Transactions on Antennas and Propagation*, vol. 54, no. 12, pp. 3638–3646, 2006.

[Rie15] G. Rieke, G.S. Wright, T. Böker, J. Bouwman, L. Colina, A. Glasse, K.D. Gordon, T.P. Greene, M. Güdel and T.H Henning et al., "The mid-infrared instrument for the james webb space telescope, I: Introduction.", *Publications of the Astronomical Society of the Pacific*, vol. 127, no. 953, p. 584, 2015.

[Riz93] B. Rizzi, T.W. Crowe and N.R. Erickson, "A high-power millimeter-wave frequency doubler using a planar diode array.", *IEEE Microwave and Guided Wave Letters*, vol. 3, no. 6, pp. 188–190, 1993.

[Rog10] A. Rogalski and F. Sizov, "Terahertz detectors and focal plane arrays.", *Opto-Electronics Review*, vol. 19, pp. 346–404, 2010.

[RS17] Rohde and Schwarz, "The Y Factor Technique for Noise Figure Measurements.", *Applicat. Note 1MA178-1E*, jul 2012.

[RadPhy] Radiometer Physics GmbH RPG. "Subharmonic Mixer narrowband 170-210 GHz." https://www.radiometer-physics.de/products/mmwave-and-terahertzproducts/mixers/mixers-subharmonic-and-harmonic-mixers/highperformance-subharmonic-mixers1/subharmonic-mixer-narrowband170-210-ghz/#tabs-container-0, 2018.

[Sat98] K. F. Sato, C. W. Chan, K. Najita, M. P. DeLisio, Y. H. Chung, J. Cowles, P. C. Grossman, R. Lai, A. K. Oki, D. C. Streit and H. Wang. "Low-frequency noise in GaAs and InP Schottky diodes." *1998 IEEE MTT-S International Microwave Symposium Digest (Cat. No.98CH36192)*, vol. 3, pp. 1695–1698 vol.3. 1998.

[Sem10] A. Semenov, O. Cojocari, H.-W. Hubers, F. Song, A. Klushin and A.-S. Muller, "Application of zero-bias quasi-optical Schottky-diode detectors for monitoring short-pulse and weak terahertz radiation.", *IEEE Electron Device Letters*, vol. 31, no. 7, pp. 674–676, 2010.

[Sen18] K. Sengupta, T. Nagatsuma and D. M. Mittleman, "Terahertz integrated electronic and hybrid electronic–photonic systems.", *Nature Electronics*, vol. 1, no. 12, pp. 622–635, 2018.

[Sie07] P.H. Siegel, "THz instruments for space.", *IEEE Transactions on Antennas and Propagation*, vol. 55, no. 11, pp. 2957–2965, 2007.

[Sie12] P. H. Siegel, "Terahertz Pioneer: Frank C. De Lucia "The Numbers Count".", *IEEE Transactions on Terahertz Science and Technology*, vol. 2, no. 6, pp. 578–583, 2012.

[Sie19] A. Siemion, "Terahertz diffractive optics—smart control over radiation.", *Journal of Infrared, Millimeter, and Terahertz Waves*, vol. 40, no. 5, pp. 477–499, 2019.

[Sim93] A. Simon, A. Grub, V. Krozer, K. Beilenhoff and H.L. Hartnagel. "Planar THz Schottky diode based on a quasi vertical diode structure." *Proc. 4th Int. Symp. Space Terahertz Technol*, pp. 392–403. 1993.

[Sim17] F. Simoens, J. Meilhan, L. Dussopt, J.-A. Nicolas, N. Monnier, G. Sicard, A. Siligaris and B. Hiberty. "Uncooled Terahertz real-time imaging 2D arrays developed at LETI: present status and perspectives." *Micro-and Nanotechnology Sensors, Systems, and Applications IX*, vol. 10194, p. 101942N. International Society for Optics and Photonics, 2017.

[Sob11] P. Sobis. "Advanced Schottky Diode Receiver Front-Ends for Terahertz Applications." Ph.D. thesis, Chalmers University of Technology, 2011.

[Son15] H-J. Song and T. Nagatsuma. *Handbook of terahertz technologies: devices and applications*. Jenny Stanford Publishing, 2015.

[Sus14] J. Suszek, A. M. Siemion, N. Blocki, M. Makowski, A. Czerwinski, J. Bomba, A. Kowalczyk, I. Ducin, K. Kakarenko, N. Palka, P. Zagrajek, M. Kowalski, E. Czerwinska, C. Jastrzebski, K. Switkowski, J.-L. Coutaz, A. Kolodziejczyk and M. Sypek, "High order kinoforms as a broadband achromatic diffractive optics for terahertz beams.", *Opt. Express*, vol. 22, no. 3, pp. 3137–3144, feb 2014.

[Tan11] A. Y. Tang and J. Stake, "Impact of Eddy Currents and Crowding Effects on High-Frequency Losses in Planar Schottky Diodes.", *IEEE Transactions on Electron Devices*, vol. 58, no. 10, pp. 3260–3269, 2011.

[Tan13] A. Y. Tang. "Modelling and Characterisation of Terahertz Planar Schottky Diodes." Ph.D. thesis, Chalmers University of Technology, 2013.

[Tan15] B. K. Tan. *Development of coherent detector technologies for sub-millimetre wave astronomy observations*. Springer, 2015.

[Tor17] A. E. Torres García, I. Ederra and R. Gonzalo. "Implementation of a THz quasi-spiral antenna for THz-IR detector." *2017 11th European Conference on Antennas and Propagation (EUCAP)*, pp. 2526–2529. 2017.

[Tor19] Alicia Elena Torres-García, José M Pérez-Escudero, Iñigo Ederra and Ramón Gonzalo, "Modified Soret Lenses for Dual-Band Integrated Detectors at Millimetre and Submillimetre Wavelengths.", *IEEE Transactions on Terahertz Science and Technology*, vol. 10, no. 2, pp. 107–117, 2019.

[Tho05] B. Thomas, A. Maestrini and G. Beaudin, "A low-noise fixed-tuned 300-360-GHz sub-harmonic mixer using planar Schottky diodes.", *IEEE Microwave and Wireless Components Letters*, vol. 15, no. 12, pp. 865–867, dec 2005.

[Tor20] A. E. Torres-Garcia, J. M. M. Perez Escudero, J. Teniente, R. Gonzalo and I. Ederra, "Silicon Integrated Subharmonic Mixer on a Photonic-Crystal Platform.", *IEEE Transactions on Terahertz Science and Technology*, pp. 1–1, 2020.

[Tsu15] K. Tsuruda, M. Fujita and T. Nagatsuma, "Extremely low-loss terahertz waveguide based on silicon photonic-crystal slab.", *Optics express*, vol. 23, no. 25, pp. 31977–31990, 2015.

[Tur58] E.M. Turner. "Spiral slot antenna.", 1958. US Patent 2,863,145.

[Uen08] Y Ueno and K Ajito, "Analytical terahertz spectroscopy.", *Analytical Sciences*, vol. 24, no. 2, pp. 185–192, 2008.

[UMS] UMS. "United Monolithic Semiconductors." https://www.ums-gaas.com/wp-content/uploads/2018/01/2018-Fall-UMS-proposes-a-shared-foundry-run-on-BES-process_Euro2.pdf.

[VDIa] VDI. "Virginia Diodes, Inc." https://www.vadiodes.com/en/products/w-and-g-band.

[VDIb] VDI. "Virginia Diodes, Inc." https://www.vadiodes.com/en/products/mixers-shm-ehm-and-fm?id=129.

[Zie70] A. van der Ziel, "Noise in solid-state devices and lasers.", *Proceedings of the IEEE*, vol. 58, no. 8, pp. 1178–1206, 1970.

[Wal02] G.C. Walker, E. Berry, N. Zinovev, A. J. Fitzgerald, R. E. Miles, J.M. Chamberlain and M.A. Smith. "Terahertz imaging and international safety guidelines." *Medical Imaging 2002: Physics of Medical Imaging*, vol. 4682, pp. 683–690. International Society for Optics and Photonics, 2002.

[Wan09] H. Wang. "Conception et modélisation de circuits monolithiques à diode Schottky sur substrat GaAs aux longueurs d'onde millimétriques et submillimétriques pour des récepteurs hétérodynes multi-pixels embarqués sur satellites et dédiés à l'aéronomie ou la planétologie." Ph.D. thesis, Université Pierre Et Marie Curie, may 2009.

[Wan16] P. Wang, N. Mohammad and R. Menon, "Chromatic-aberration-corrected diffractive lenses for ultra-broadband focusing.", *Scientific reports*, vol. 6, p. 21545, 2016.

[Wat06] J W Waters, L Froidevaux, R S Harwood, R F Jarnot, H M Pickett, W G Read, P H Siegel, R E Cofield, M J Filipiak, D A Flower et al., "The earth observing system microwave limb sounder (EOS MLS) on the Aura satellite.", *IEEE Transactions on Geoscience and Remote Sensing*, vol. 44, no. 5, pp. 1075–1092, 2006.

[Wat08] R. Waterhouse. *Printed antennas for wireless communications*, vol. 19. John Wiley & Sons, 2008.

[Wau96] R. Waugh and R. Buted. "The zero bias schottky diode detector at temperature extremes-problems and solutions." *Proceedings of the WIRELESS Symposium*, pp. 175–183. 1996.

[Wil99] J.C. Wiltse. "History and evolution of Fresnel zone plate antennas for microwaves and millimeter waves." *IEEE Antennas and Propagation Society International Symposium. 1999 Digest. Held in conjunction with: USNC/URSI National Radio Science Meeting (Cat. No. 99CH37010)*, vol. 2, pp. 722–725. IEEE, 1999.

[Wil04] J. C. Wiltse. "Diffraction optics for terahertz waves." *Terahertz for Military and Security Applications II*, vol. 5411, pp. 127–135. International Society for Optics and Photonics, 2004.

[Win96] G. Winnewisser, "Spectroscopy among the stars.", *Fresenius' journal of analytical chemistry*, vol. 355, no. 5-6, pp. 571–575, 1996.

[Wit18] W. Withayachumnankul, M. Fujita and T. Nagatsuma, "Integrated Silicon Photonic Crystals Toward Terahertz Communications.", *Advanced Optical Materials*, vol. 6, no. 16, pp. 1–7, 2018.

[Woo03] R.M Woodward, V.P. Wallace, D.D Arnone, E.H. Linfield and M. Pepper, "Terahertz pulsed imaging of skin cancer in the time and frequency domain.", *Journal of Biological Physics*, vol. 29, no. 2-3, pp. 257–259, 2003.

[Yan11] R. Yang, W. Tang and Y. Hao, "A broadband zone plate lens from transformation optics.", *Optics express*, vol. 19, pp. 12348–55, jun 2011.

[Yar84] A. Yariv and P. Yeh. *Optical waves in crystals*, vol. 5. Wiley New York, 1984.

[Yat16] M. Yata, M. Fujita and T. Nagatsuma, "Photonic-crystal diplexers for terahertz-wave applications.", *Optics express*, vol. 24 7, pp. 7835–49, 2016.

[You65] D.T. Young and J.C Irvin, "Millimeter frequency conversion using Au-n-type GaAs Schottky barrier epitaxial diodes with a novel contacting technique.", *Proceedings of the IEEE*, vol. 53, no. 12, pp. 2130–2131, 1965.

[Yu18] X. Yu, R. Yamada, J. Kim, M. Fujita and T. Nagatsuma, "Integrated Circuits Using Photonic-Crystal Slab Waveguides and Resonant Tunneling Diodes for Terahertz Communication.", *2018 Progress in Electromagnetics Research Symposium (PIERS-Toyama)*, pp. 599–605, 2018.

[Yu19a] X. Yu, Y. Hosoda, T. Miyamoto, K. Obata, J. Kim, M. Fujita and T. Nagatsuma, "Terahertz fibre transmission link using resonant tunnelling diodes integrated with photonic-crystal waveguides.", *Electronics Letters*, vol. 55, no. 7, pp. 398–400, 2019.

[Yu19b] X. Yu, J. Kim, M. Fujita and T. Nagatsuma, "Efficient mode converter to deep-subwavelength region with photonic-crystal waveguide platform for terahertz applications.", *Optics Express*, vol. 27, no. 20, pp. 28707–28721, 2019.

[Yu20] X Yu, T Ohira, J-Y Kim, M Fujita and T Nagatsuma, "Waveguide-input resonant tunnelling diode mixer for THz communications.", *Electronics Letters*, vol. 56, no. 7, pp. 342–344, 2020.

[Yua03] T. Yuan, H. Liu, J. Xu, F. Al-Douseri, Y. Hu and X.-C. Zhang. "Terahertz time-domain spectroscopy of atmosphere with different humidity." *Terahertz for Military and Security Applications*, vol. 5070, pp. 28–37. International Society for Optics and Photonics, 2003.

[Yuj03] L. Yujiri, M. Shoucri and P. Moffa, "Passive millimeter wave imaging.", *IEEE microwave magazine*, vol. 4, no. 3, pp. 39–50, 2003.

[Yur16] O. Yurduseven, Juan, N. Llombart and A. Neto, "A dual-polarized leaky lens antenna for wideband focal plane arrays.", *IEEE Transactions on Antennas and Propagation*, vol. 64, no. 8, pp. 3330–3337, 2016.

[Zel13] K. Zeljami. "Caracterización y modelado de dispositivos semiconductores para uso en sistemas de telecomunicaciones a frecuencias de terahercios." Ph.D. thesis, Universidad de Cantabria, 2013.

[Zha12] H. Zhao, V. Drakinskiy, P. Sobis, J. Hanning, T. Bryllert, and J. Stake. "Development of a 557 GHz GaAs monolithic membrane-diode mixer." *2012 International Conference on Indium Phosphide and Related Materials*, pp. 102–105. aug 2012.

[Zha13] Y. Zhang, R. Han, Y. Kim, D. Y. Kim, H. Shichijo, S. Sankaran, C. Mao, E. Seok, D. Shim and K.O. Kenneth. "Schottky diodes in CMOS for terahertz circuits and systems." *2013 IEEE Radio and Wireless Symposium*, pp. 43–45. IEEE, 2013.

[Zho18] Z. Zhou, T. Zhou, S. Zhang, Z. Shi, Y. Chen, W. Wan, X. Li, X. Chen, C. Gilbert, N. Stephanie and Z. Fu et al., "Multicolor T-ray imaging using multispectral metamaterials.", *Advanced Science*, vol. 5, no. 7, p. 1700982, 2018.

Author's merit

Scientific production of this Thesis

Journal Papers

Generated by this Thesis:

1. Alicia Torres-Garcia, José M. Pérez Escudero, Ramón Gonzalo, Iñigo Ederra. "Modified Soret Lenses for Dual-Band Integrated Detectors at Millimeter and Submillimeter Wavelengths". IEEE Transactions on Terahertz Science and Technology, Vol. 10, no. 2, pp.107-117, mar 2020)

2. Alicia Torres-Garcia, José M. Pérez Escudero, Ramón Gonzalo, Iñigo Ederra. "Silicon Integrated Subharmonic Mixer on a Photonic-Crystal Platform". IEEE Transaction on Terahertz Science and Technology. DOI: 10.1109/TTHZ.2020.3020699

3. Alicia Torres-Garcia, José M. Pérez Escudero, Ramón Gonzalo, Iñigo Ederra."1/f noise in Sub-mm Direct Detectors based on GaAs Schottky diodes" Electronics in preparation.

Additional Publication:

1. Dayan Pérez-Quintana, Alicia E. Torres-García , Iñigo Ederra , Miguel Beruete. "Compact Groove Diamond Antenna in Gap Waveguide Technology With Broadband Circular Polarization at Millimeter Waves" IEEE Transaction on Antennas and Propagation, Vol. 68, no. 8, aug 2020

2. José M. Pérez Escudero, Alicia E. Torres-García, Ramón Gonzalo, Iñigo Ederra. "A Chebyshev Transformer Based Microstrip to Groove Gap Waveguide Inline Transition for MMIC Packaging". IEEE Transactions on Components, Packaging and Manufacturing Technology, Vol. 9, no. 8, pp.1595-1602, 2019.

3. José M. Pérez Escudero,Alicia E. Torres-García, Ramón Gonzalo, Iñigo Ederra. "A simplified design inline microstrip to waveguide transition". Electronics, Vol. 7, no.10, 2018.

4. Unai Beaskoetxea, Alicia Elena Torres-García ; Miguel Beruete. "Ku-Band Low-Profile Asymmetric Bull's-Eye Antenna with Reduced Sidelobes and Monopole Feeding" IEEE Antennas and Wireless Propagation Letters, Vol. 17, no. 3, march 2018

International Conferences

Generated by this Thesis:

1. Alicia E. Torres-García, José M. Pérez-Escudero, Ramóon Gonzalo, I˜nigo Ederra "Comparison of Modified Soret Lenses for Dual Band Integrated Detectors" 2020 14th European Conference on Antennas and Propagation (EuCAP)

2. Alicia E. Torres-Garcia, Bakhtiyar Orazbayev, Inigo Ederra, Ramon Gonzalo. "IR-Fresnel zone plate lens acting as THz antenna". 2017 10th Global Symposium on Millimeter-Waves

3. Alicia E. Torres-García, Bakhtiyar Orazbayev, Ramón Gonzalo, Iñigo Ederra Dual-band integrated detector for THz and IR based on quasi-spiral antenna coupled to schottky diode. 2016 IEEE International Symposium on Antennas and Propagation (APSURSI)

4. Alicia E. Torres-García, Bakhtiyar Orazbayev, Ramón Gonzalo, Iñigo Ederra. "A quasi-spiral antenna for THz-IR dual-band sensors" 2016 Global Symposium on Millimeter Waves (GSMM) & ESA Workshop on Millimetre-Wave Technology and Applications (**Best Student Paper Award)**

Additional Publication:

5. Dayan Pérez-Quintana, Alicia Torres-García, Iñigo Ederra, Miguel Beruete A Gap Waveguide Fed Circular Polarization Antennas in the Millimeter

Wave Range 2020 14th European Conference on Antennas and Propagation (EuCAP)

6. José M. Pérez Escudero, Alicia E. Torres-García, Ramón Gonzalo, Iñigo Ederra. "Design of a Groove Gap Waveguide to Microstrip Inline Transition". 13th European Conference on Antennas and Propagation, EuCAP 2019.

7. Unai Beaskoetxea ; Alicia Elena Torres-Garcia ; Miguel Beruete "Monopole fed grounded dielectric slab leaky wave Bull's-Eye antenna". 2018 15th European Radar Conference (EuRAD)

8. A. Torres-García, F. Marante, A. Tazón, J. Vassal'lo, J. Teniente, M. Beruete. "Broadband circular polarized field generation in single layer microstrip patch antennas". 2016 10th European Conference on Antennas and Propagation (EuCAP)

National Conferences

Generated by this Thesis:

1. Alicia E. Torres-García, Bakhtiyar Orazbayev, Ramón Gonzalo, Iñigo Ederra. "An Integrated Detector for Submillimeter and Infrared Ranges based on a modified Planar Fresnel Zone Lens Antenna". XXXI Simposium Nacional de la Unión Científica Nacional de Radio, URSI 2016, Madrid.

Additional Publication:

2. José M. Pérez Escudero, Alicia Torres García, Javier Chocarro Álvarez, Adrián Gómez-Torrent. "Micromachining of High Frequency Components at ISC/UPNA". XXXIII Simposium Nacional de la Unión Científica Nacional de Radio, URSI 2018, Granada.

3. Jorge Teniente-Vallinas, Marta Melero Frago, Carlos Biurrun Quel, Alicia E. Torres García, José M. Pérez Escudero. "Millimetre and sub-millimetre wave electronic circuit manufacture with micron precision by means of photolithography techniques". XXXIV Simposium Nacional de la Unión Científica Nacional de Radio, URSI 2019, Sevilla.

Other Merits

Research Stay

Research Stay at Terahertz and Millimetre Wave Laboratory. Chalmers University of Technology. August 2017-November 2017. Göteborg, Sweden.